

AD-A151 731

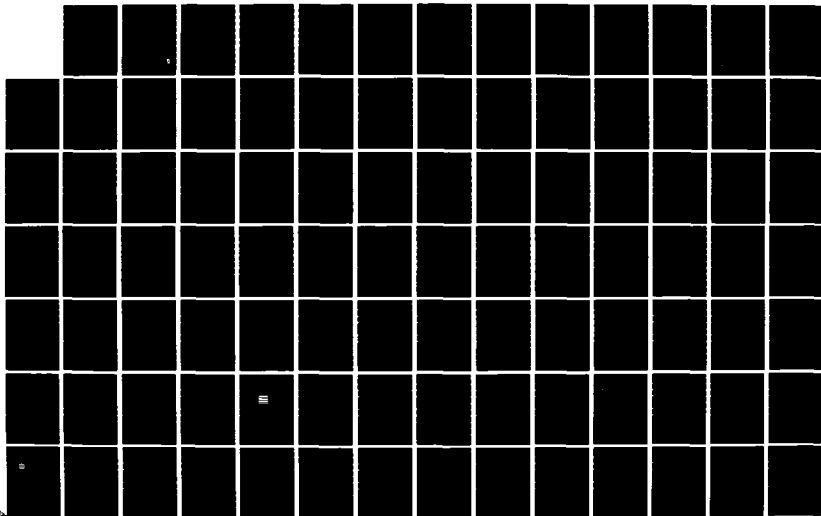
SPECTROSCOPIC INVESTIGATION OF MATERIALS FOR FREQUENCY  
AGILE LASER SYSTEMS(U) OKLAHOMA STATE UNIV STILLWATER  
DEPT OF PHYSICS R C POWELL JAN 85 ARO-18677.11-PH  
DAG29-82-K-0041

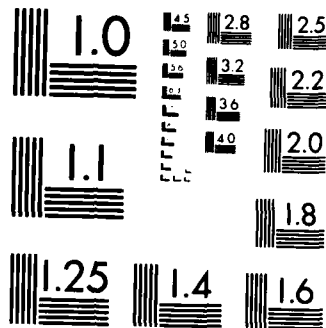
1/2

UNCLASSIFIED

F/G 20/5

NL





MICROCOPY RESOLUTION TEST CHART  
NATIONAL BUREAU OF STANDARDS-1963-A

ARO 18677.118H

(2)

SPECTROSCOPIC INVESTIGATION OF MATERIALS FOR  
FREQUENCY AGILE LASER SYSTEMS

Richard C. Powell, Ph.D.  
Principal Investigator

Department of Physics  
OKLAHOMA STATE UNIVERSITY  
Stillwater, Oklahoma 74078

AD-A151 731

FINAL REPORT

U.S. Army Research Office  
Research Triangle Park, North Carolina 27709

Contract Number DAAG29-82-K-0041  
ARO Proposal Number 18677-PH

January 13, 1982 - January 14, 1985

DTIC FILE COPY

DTIC  
ELECTE  
MAR 25 1985  
S E D

85 03 06 142

UNCLASSIFIED

SECURITY CLASSIFICATION OF THIS PAGE (When Data Entered)

REPORT DOCUMENTATION PAGE		READ INSTRUCTIONS BEFORE COMPLETING FORM
1. REPORT NUMBER ARO 18677.11-PH	2. GOVT ACCESSION NO. N/A	3. RECIPIENT'S CATALOG NUMBER N/A
4. TITLE (and Subtitle) Spectroscopic Investigation of Materials for Frequency Agile; Laser Systems		5. TYPE OF REPORT & PERIOD COVERED 15 Jan 82 - 14 Jan 85 Final Report
		6. PERFORMING ORG. REPORT NUMBER
7. AUTHOR(s) Richard C. Powell		8. CONTRACT OR GRANT NUMBER(s) DAAG29-82-K-0041
9. PERFORMING ORGANIZATION NAME AND ADDRESS Oklahoma State Univ		10. PROGRAM ELEMENT, PROJECT, TASK AREA & WORK UNIT NUMBERS
11. CONTROLLING OFFICE NAME AND ADDRESS U. S. Army Research Office Post Office Box 12211 Research Triangle Park, NC 27709		12. REPORT DATE Jan 85
		13. NUMBER OF PAGES
14. MONITORING AGENCY NAME & ADDRESS (if different from Controlling Office)		15. SECURITY CLASS. (of this report) Unclassified
		15a. DECLASSIFICATION/DOWNGRADING SCHEDULE
16. DISTRIBUTION STATEMENT (of this Report)  Approved for public release; distribution unlimited.		
17. DISTRIBUTION STATEMENT (of the abstract entered in Block 20, if different from Report)  NA		
18. SUPPLEMENTARY NOTES  The view, opinions, and/or findings contained in this report are those of the author(s) and should not be construed as an official Department of the Army position, policy, or decision, unless so designated by other documentation.		
19. KEY WORDS (Continue on reverse side if necessary and identify by block number) Agile Laser Systems Laser Systems Tunable Lasers Laser Materials		
20. ABSTRACT (Continue on reverse side if necessary and identify by block number)  This research involves the use of laser spectroscopy techniques such as four-wave mixing, multiphoton absorption, time-resolved site-selection spectroscopy, and holography to characterize dynamical optical processes such as energy transfer, exciton migration, radiation-		

UN 1 JAN 73 1973

UNCLASSIFIED

UNCLASSIFIED

SECURITY CLASSIFICATION OF THIS PAGE (When Data Entered)

## ABSTRACT

This report summarizes the research done in the Department of Physics of Oklahoma State University supported by the U.S. Army Research Office under contract number DAAG29-82-K-0041 from January 15, 1982 through January 14, 1985. The research involves the use of laser spectroscopy techniques such as four-wave mixing, multiphoton absorption, time-resolved site-selection spectroscopy, and holography to characterize dynamical optical processes such as energy transfer, exciton migration, radiationless relaxation, and the photorefractive effect. In addition, a significant effort was spent in the synthesis and characterization of new types of materials for tunable laser applications. The materials investigated include alexandrite, titanium doped sapphire, lithium niobate, neodymium pentaphosphate, rhodium doped rubidium calcium fluoride, manganese silicate, and neodymium doped garnet crystals and glasses. Some of the results of major importance from this work are: (1) The demonstration of  $\text{RbCaF}_3:\text{Rh}^{2+}$  as a high gain tunable laser material; (2) The characterization of the spectral pumping and decay dynamics of  $\text{Y}_3\text{Al}_5\text{O}_{12}:\text{Nd}^{3+}$  under high power, picosecond pulse excitation; (3) The characterization of exciton dynamics in  $\text{NdP}_5\text{O}_{14}$  crystals with four-wave mixing; (4) The development of a model based on trap modulated mobility of two types of charge carriers to explain the photorefractive effect in  $\text{LiNbO}_3$ ; and (5) The demonstration of third order susceptibility effects in  $\text{BeAl}_2\text{O}_4:\text{Cr}^{3+}$ .

less relaxation, and the photorefractive effect. In addition, a significant effort was spent in the synthesis and characterization of new types of materials for tunable laser applications. The materials investigated include alexandrite, titanium doped sapphire, lithium niobate, neodymium pentaphosphate, rhodium doped rubidium calcium fluoride, manganese silicate, and neodymium doped garnet crystals and glasses.

Accession For	
NTIS GRA&I	<input checked="" type="checkbox"/>
DTIC TAB	<input type="checkbox"/>
Unannounced	<input type="checkbox"/>
Justification	
By	
Distribution/	
Availability Codes	
Avail and/or	
Dist	Special
A-1	



## CONTENTS

### I. INTRODUCTION

#### I.1 Summary of Research Accomplishments

#### I.2 Publications and Personnel

### II. CHARACTERIZATION OF EXCITON DYNAMICS IN STOICHIOMETRIC LASER MATERIALS

#### II.1 Transient Grating Investigation of Exciton Diffusion and Fluorescence Quenching in $\text{Nd}_x\text{La}_{1-x}\text{P}_5\text{O}_{14}$ Crystals

#### II.2 Temperature Dependence of the Exciton Diffusion in $\text{Nd}_x\text{La}_{1-x}\text{P}_5\text{O}_{14}$ Crystals

#### II.3 Investigation of Four-Wave Mixing in $\text{Nd}_x\text{La}_{1-x}\text{P}_5\text{O}_{14}$

### III. DEVELOPMENT OF NEW VIBRONIC LASER CRYSTALS

#### III.1 Spectroscopy of 4d and 5d Transition Metal Ions in Alkali Halide Crystals

#### III.2 Stimulated Emission and Tunable Gain From $\text{Rh}^{2+}$ Ions in $\text{RbCaF}_3$ Crystals

#### III.3 Recent Results on the Spectroscopy of Transition Metal Ions for Tunable Solid State Lasers

#### III.4 Spectroscopic Evaluation of $\text{Mn}_2\text{SiO}_4$ as a Possible Tunable Laser Material

#### III.5 Four-Wave Mixing in Alexandrite Crystals

### IV. INVESTIGATION OF THE SPECTRAL DYNAMICS OF LASER MATERIALS UNDER MULTIPHOTON EXCITATION

#### IV.1 Spectroscopy of $\text{Y}_3\text{Al}_5\text{O}_{12}:\text{Nd}^{3+}$ Under High Power, Picosecond Pulse Excitation

### V. DETERMINATION OF CHARGE RELOCATION DYNAMICS IN PHOTOREFRACTIVE CRYSTALS

#### V.1 Analysis of the Decay Dynamics of Laser-Induced Gratings in $\text{LiNbO}_3$

### APPENDIX: Derivation of the Susceptibility for a Three-Level System

## I. INTRODUCTION

Laser-based electro-optic technology in the military is especially important in areas of target acquisition and recognition, guidance, surveillance and night vision, rangefinders, communications, and countermeasures. Each different application requires a laser system with specific operational parameters. Thus there is an important demand for developing new materials for laser systems having device properties that are optimum for specific types of applications. In order to develop the ability to tailor make materials with desired device characteristics, it is important to fully understand and characterize the fundamental physical processes underlying the optical pumping and emission dynamics of the material.

The purpose of the research on this contract was to enhance our understanding of the spectral dynamics of materials used in laser systems and to develop new materials for laser applications. The major research goals stated in the original proposal have all essentially been accomplished. The important results obtained during the three years of this contract are briefly outlined in this section and presented in detail in the remainder of the report.

This research project benefited greatly from additional support provided by a DoD University Research Instrumentation grant. The equipment purchased with these funds permitted the establishment of five independently operating laser stations. These are utilized for four-wave mixing spectroscopy, transient holography spectroscopy, multiphoton absorption spectroscopy, time-resolved site-selection spectroscopy, and picosecond spec-



troscopy. Block diagrams of these experimental setups are shown in Figs. 1 - 5. This expansion of the solid state physics of the OSU Laser Spectroscopy Facility increased the operational capabilities and efficiency of our research program. This unique facility allows us to attack a research problem with a variety of different laser spectroscopy techniques and to train students with state-of-the-art equipment so they are prepared for jobs in high technology industries.

### 1.1 Summary of Research Accomplishments

The research performed under this contract can be divided into five thrust areas. The first is characterizing exciton dynamics in stoichiometric laser crystals. These crystals are useful in applications requiring low threshold, high gain "mini-lasers" and exciton migration plays an important roll in determining the level of concentration quenching which affects the quantum efficiency of the material. We used the technique of four-wave mixing spectroscopy to characterize the properties of exciton migration in  $\text{Nd}_x\text{La}_{1-x}\text{P}_5\text{O}_{14}$  crystals. This provided the first measurement of the exciton diffusion coefficient in this class of material. In addition, we demonstrated the conditions necessary for vibronically enhanced exciton diffusion and for partially coherent exciton migration.

The second thrust area is the development of new vibronic laser materials. This work focused on the synthesis and spectroscopic characterization of 4d and 5d transition metal ions as dopants in crystalline hosts. Techniques were demonstrated for minimizing charge transfer emission and maximizing d-d emission.

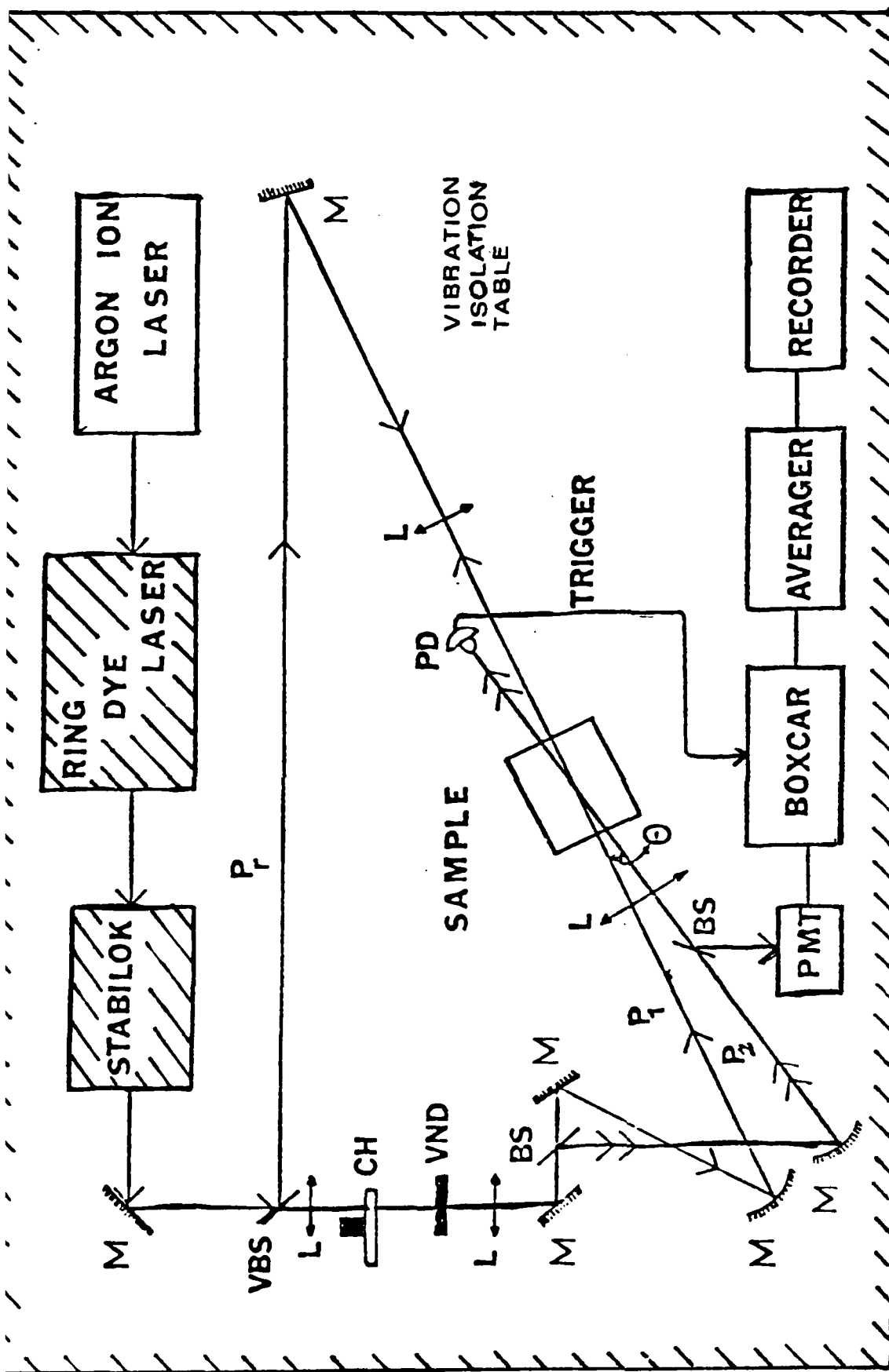


Figure 1 . Four-Wave Mixing experimental configuration .

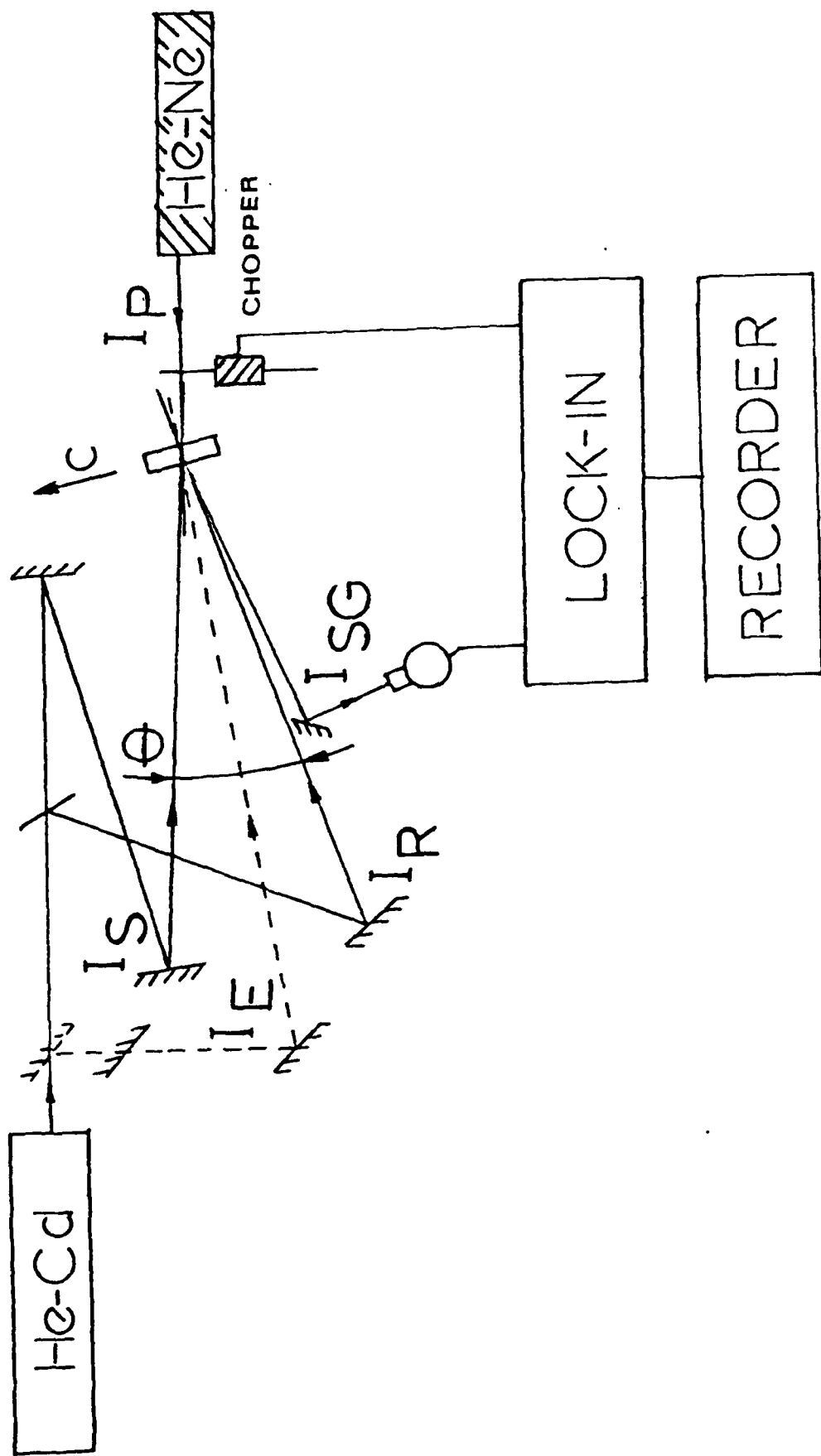


Figure 2. Holographic grating experimental configuration.

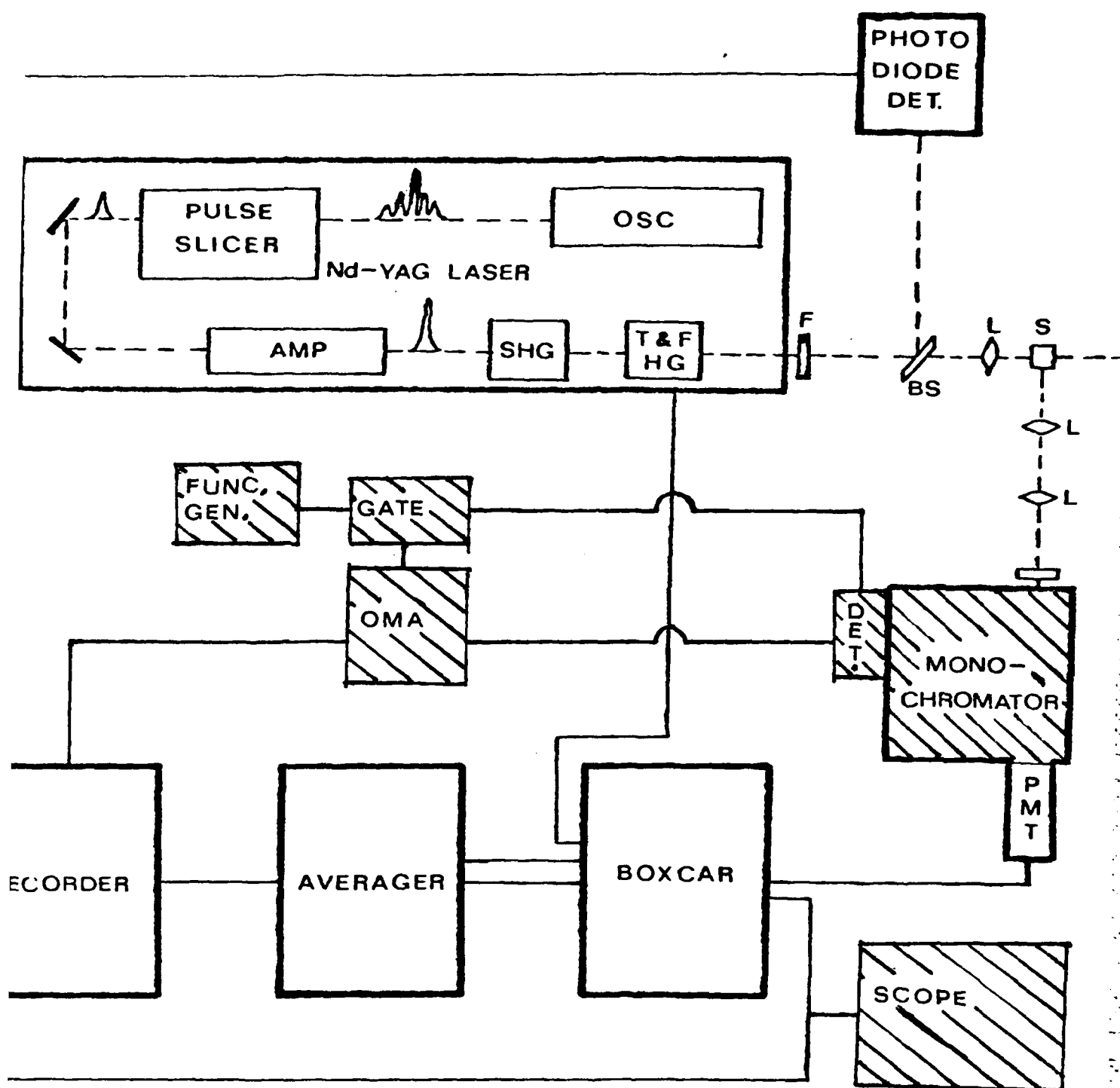


Figure 3. Multiphoton spectroscopy experimental configuration.

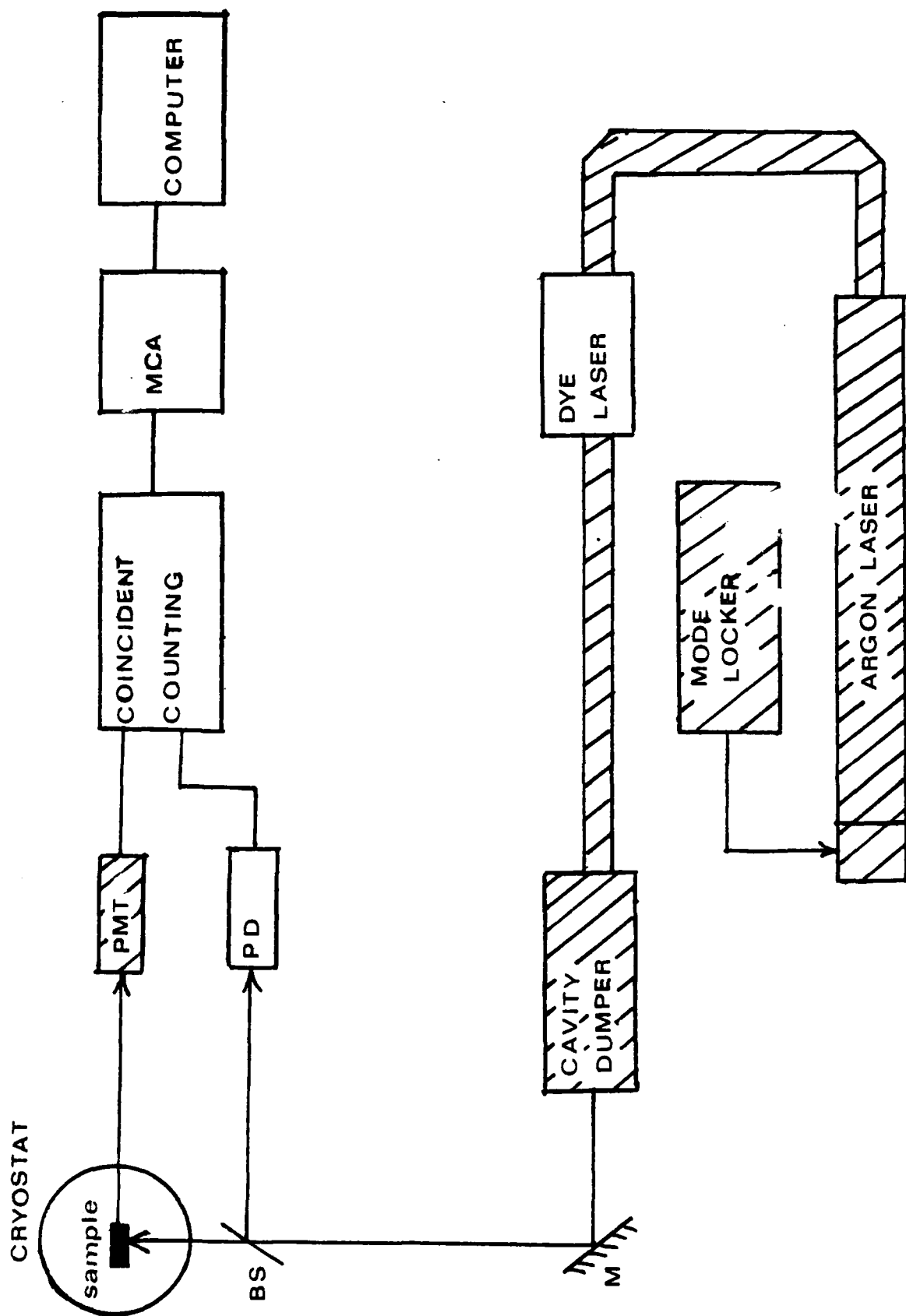


Figure 4. Picosecond spectroscopy experimental configuration.

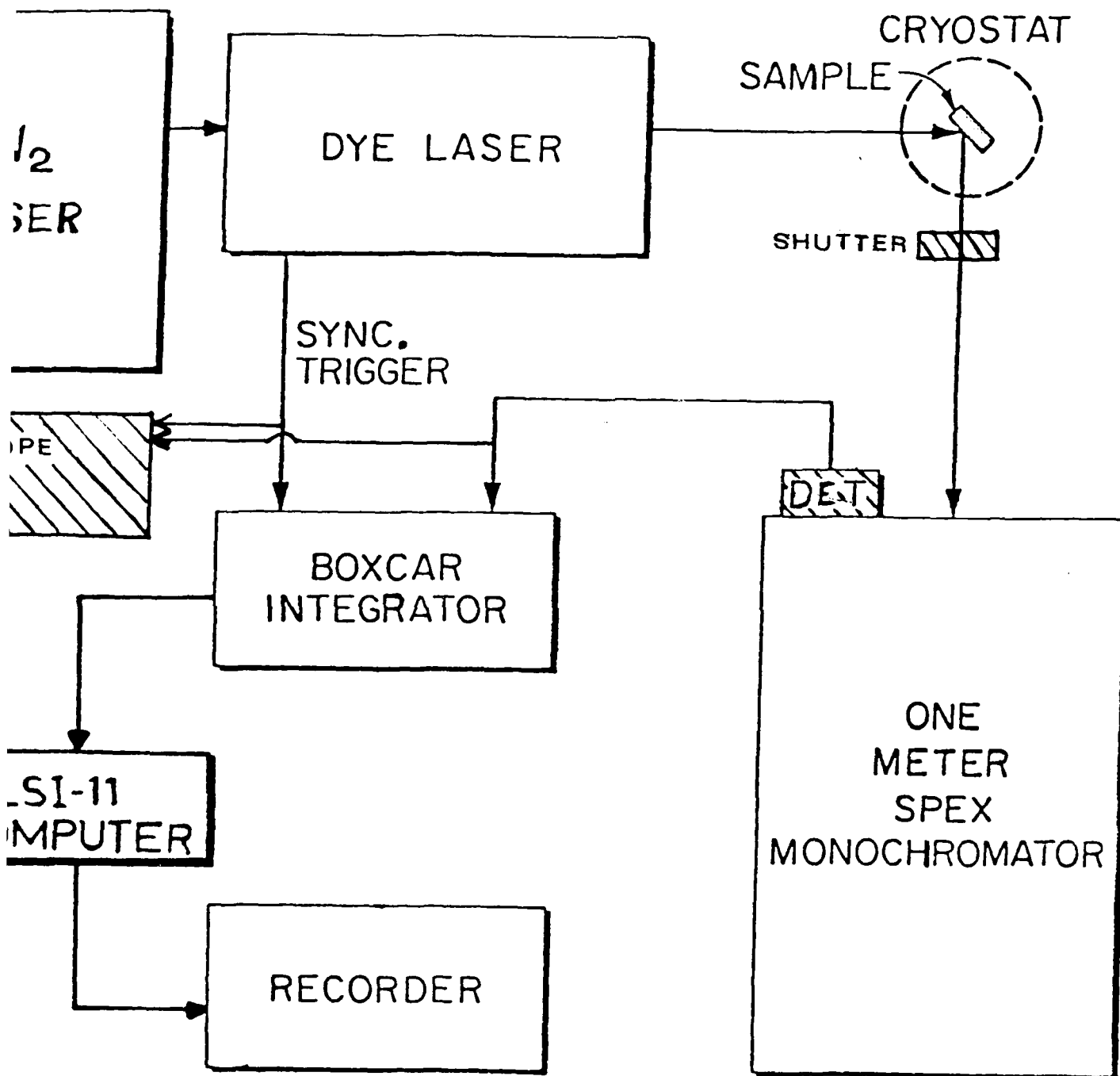


Figure 5. Time-resolved site-selection spectroscopy experimental configuration.

Experimentally, one usually works with crossing angles large enough that case I applies and Eqs. (13), (14), or (15) will be applicable. However, it is of interest to derive the expression for scattering efficiency for very small crossing angles in certain limiting cases to discover what new effects should be expected in this situation.

#### Case II: $\theta$ is small

If  $\theta$  is very small, then  $A_p(z)$  and  $A_s(z)$  do change appreciably over  $\lambda_{\text{ex}}$ . Equations (7) and (8) cannot

be solved exactly in this case. However, they can be solved approximately whenever the pump beams are well below saturation intensity.

Defining  $\alpha$  as

$$\alpha = \frac{\alpha_0(i - i\delta)}{(1 + \delta^2)} [1 + (I_b + I_a)/I_S]^{-2},$$

the output intensity of the signal beam can be formed from the solution of Eqs. (7) and (8) (Ref. 15) to first order in  $|A_b A_a|/I_S$ ,

$$\begin{aligned} |A_s(0)|^2 = L |\alpha|^2 \frac{I_b I_a}{I_S^2} |A_p(L)|^2 e^{-2\alpha_R L} \\ \times \left\{ L + \frac{2|A_b A_a|L}{k(1 - \cos\theta)I_S} \{ 3\alpha_R \sin[k(1 - \cos\theta)L + \Delta] - \alpha_i \cos[k(1 - \cos\theta)L + \Delta] \} \right. \\ \left. - \frac{12|A_b A_a|\alpha_R}{k^2(1 - \cos\theta)^2 I_S} \sin \left[ \frac{k(1 - \cos\theta)L}{2} + \Delta \right] \sin \left[ \frac{k(1 - \cos\theta)L}{2} \right] \right. \\ \left. - \frac{4|A_b A_a|}{k(1 - \cos\theta)I_S} \left[ 4 - \frac{\alpha_i}{k(1 - \cos\theta)} \right] \left| \sin \left[ \frac{k(1 - \cos\theta)L}{2} \right] \cos \left[ \frac{k(1 - \cos\theta)L}{2} + \Delta \right] \right| \right\}. \end{aligned} \quad (16)$$

The scattering efficiency is then

$$\begin{aligned} \eta = L |\alpha|^2 (I_b I_a / I_S^2) \exp[2\alpha_0 L / (1 + \delta^2)] \exp(-2\alpha_R L) \\ \times \left\{ L + \frac{2|A_b A_a|L}{k(1 - \cos\theta)I_S} \{ 3\alpha_R \sin[k(1 - \cos\theta)L + \Delta] - \alpha_i \cos[k(1 - \cos\theta)L + \Delta] \} \right. \\ \left. - \frac{12|A_b A_a|\alpha_R}{k^2(1 - \cos\theta)^2 I_S} \sin \left[ \frac{k(1 - \cos\theta)L}{2} + \Delta \right] \sin \left[ \frac{k(1 - \cos\theta)L}{2} \right] \right. \\ \left. - \frac{4|A_b A_a|}{k(1 - \cos\theta)I_S} \left[ 4 - \frac{\alpha_i}{k(1 - \cos\theta)} \right] \left| \sin \left[ \frac{k(1 - \cos\theta)L}{2} \right] \cos \left[ \frac{k(1 - \cos\theta)L}{2} + \Delta \right] \right| \right\}. \end{aligned} \quad (17)$$

Important information about the type of effects expected at small crossings angles can be obtained by examining Eqs. (16) and (17). One can see that all of the terms that are first order in  $|A_b A_a|/I_S$  vary sinusoidally with the phase mismatch  $\Delta$  of the two pump beams. If the pump beams are within the coherence length of each other, then  $\Delta = (2\pi/\lambda)\Delta L$  where  $\Delta L$  is the difference in path length. All terms that are first order in  $|A_b A_a|/I_S$  will therefore be exceptionally sensitive to vibrations and to precise alignment of the pump beams. Thus at very small angles, Eqs. (16) and (17) predict the observed signal beam to have a component that oscillates very rapidly due to vibrations or minor

adjustments superimposed on an "envelope signal" that is insensitive to vibrations and precise alignments. The observation of this type of behavior is discussed in the following section.

#### IV. EXPERIMENTAL RESULTS AND INTERPRETATION

Information about spatial energy migration in  $\text{Nd}_x\text{La}_{1-x}\text{P}_5\text{O}_{14}$  crystals at room temperature was obtained using the FWM configuration described previously and observing the decay of the Bragg diffracted signal beam. Useful data was obtained

$$A_p(z) = A_p(L) \exp[\xi \sec\theta(z-L)] , \quad (9)$$

where  $A_p(L)$  is the incident probe-beam amplitude and  $\xi$  is the complex absorption coefficient given by

$$\xi = \frac{\alpha_0(1-i\delta)}{(1+\delta^2)} \left[ \frac{1+(I_b/I_S)+(I_a/I_S)-2I_bI_a/I_S^2}{\{[1+(I_b/I_S)+(I_a/I_S)]^2-4I_bI_a/I_S^2\}^{3/2}} \right] . \quad (10)$$

With the use of the boundary condition that there is no incident signal beam, i.e.,  $A_s(0)=0$ , the solution to Eq. (8) is

$$A_s(z) = - \frac{-A_p(L)}{\sec\theta - 1} \left[ \frac{|A_b A_a| e^{i\Delta}}{I_S} \left[ \frac{[1+(I_b+I_a)/I_S]}{[1+(I_b+I_a)/I_S-2I_bI_a/I_S^2]} \right] \right] \\ \times \{ \exp[\xi \sec\theta(z-L)] - \exp[\xi(z-L)] \} . \quad (11)$$

One quantity of interest is the signal-beam intensity as it exits the sample  $|A_s(0)|^2$ , since this is an experimentally measureable quantity.

$$|A_s(0)|^2 = \frac{(I_b I_a / I_S^2) [1 + (I_b / I_S) + (I_a / I_S)]^2}{[1 + (I_b / I_S) + (I_a / I_S) - 2 I_b I_a / I_S^2]^2} [ |A_p(L)|^2 / (\sec\theta - 1)^2 ] \\ \times \{ \exp(-2\xi_R L) + \exp(-2\xi_R \sec\theta L) - 2 \exp[-\xi_R(1 + \sec\theta)L] \cos[\xi_i(1 - \sec\theta)L] \} , \quad (12)$$

where  $\xi_R$  and  $\xi_i$  are the real and imaginary parts of Eq. (10), respectively. Normally in a degenerate FWM experiment the two pump beams and the probe beam are obtained by splitting one laser beam into three parts. When this is the case, one sees from Eq. (12) that the output signal-beam intensity will vary as the cube of the laser power.

A good measure of the "scattering efficiency"  $\eta$  of the FWM processes is the ratio of the exciting signal beam  $|A_s(0)|^2$  to the exiting probe beam in the absence of the pump-beam interactions. With the use of Eqs. (9) and (10), we have

$$|A_p(0)|^2_{E_0=0} = |A_p(L)|^2 \exp\{-[2\alpha_0/(1+\delta^2)]L\} .$$

The scattering efficiency  $\eta$  is then given by

$$\eta = \frac{(I_b I_a / I_S^2) [1 + (I_b / I_S) + (I_a / I_S)]^2 \exp[2\alpha_0 L / (1 + \delta^2)]}{\{[1 + (I_b / I_S) + (I_a / I_S) - 2 I_b I_a / I_S^2]^2 (\sec\theta - 1)^2\}} \\ \times \{ \exp(-2\xi_R L) + \exp(-2\xi_R \sec\theta L) - 2 \exp[-\xi_R(1 + \sec\theta)L] \cos[\xi_i(1 - \sec\theta)L] \} . \quad (13)$$

The dependence of the scattering efficiency on crossing angle can be clarified somewhat whenever  $\xi L(1 - \sec\theta)$  is small. This will usually be true since the experiment does not work well if

- (i)  $\xi L$  is large since the beams are then essentially extinguished in the crystal.
- (ii)  $\theta$  is very large since the output signal-beam intensity decreases with increasing  $\theta$ .

Thus under this condition, to first order in  $|\xi L(1 - \sec\theta)|$ , Eq. (13) becomes

$$\eta = \frac{\alpha_0^2}{1 + \delta^2} \left[ \frac{(I_b I_a / I_S^2) [1 + (I_b + I_a) / I_S]^2 L^2 \exp(-2\xi_R L) \exp[2\alpha_0 L / (1 + \delta^2)]}{\{[1 + (I_b + I_a) / I_S]^2 - 4 I_b I_a / I_S^2\}^3} [1 + \xi_R L(1 - \sec\theta)] \right] . \quad (14)$$

Equation (14) shows that the scattering efficiency decreases strongly with increasing crossing angle  $\theta$ .

Whenever the pump intensity is well below the saturation intensity, to lowest order in  $(I_b + I_a) / I_S$  the scattering efficiency reduces to

$$\eta = \frac{\alpha_0^2 L^2}{1 + \delta^2} (I_b I_a / I_S^2) \left[ 1 + \frac{\alpha_0 L}{1 + \delta^2} (1 - \sec\theta) \right] . \quad (15)$$



$$2ike^{i\omega t} \left[ \cos\theta e^{-i\vec{k}_p \cdot \vec{r}} \frac{\partial A_p(z)}{\partial z} + e^{-i\vec{k}_s \cdot \vec{r}} \frac{\partial A_s(z)}{\partial z} \right] = -k^2 e^{i\omega t} \chi(E_0) \left[ E_0 + \Delta E - \frac{(E_0^2 \Delta E^* + E_0^{-2} \Delta E)}{I_S + |E_0|^2} \right], \quad (5)$$

where  $k^2 = |\vec{k}_p|^2 = |\vec{k}_s|^2$ .

The only terms of interest on the right-hand side are those that satisfy the phase matching condition, i.e. those terms that synchronously drive the left-hand side as either  $\exp[i(\omega t - \vec{k}_s \cdot \vec{r})]$  or  $\exp[i(\omega t - \vec{k}_p \cdot \vec{r})]$ . Defining the pump-beam intensities as  $I_b = |A_b|^2$  and  $I_a = |A_a|^2$ , Eq. (5) becomes

$$\begin{aligned} \left[ \cos\theta e^{-i\vec{k}_p \cdot \vec{r}} \frac{\partial A_p(z)}{\partial z} + e^{-i\vec{k}_s \cdot \vec{r}} \frac{\partial A_s(z)}{\partial z} \right] &= \frac{\alpha_0 |E_s|^2 (1-i\delta)}{(I_S + |E_0|^2)^2} \\ &= ((I_S + |E_0|^2)(A_p e^{-i\vec{k}_p \cdot \vec{r}} + A_s e^{-i\vec{k}_s \cdot \vec{r}}) \\ &\quad - (I_b + I_a)(A_p e^{-i\vec{k}_p \cdot \vec{r}} + A_s e^{-i\vec{k}_s \cdot \vec{r}}) - A_p A_b A_a^* e^{-i\vec{k}_s \cdot \vec{r}} \\ &\quad - A_s A_b^* A_a e^{-i\vec{k}_p \cdot \vec{r}} - \{A_b^* A_a \exp[-i(\vec{k}_p - \vec{k}_s) \cdot \vec{r}]\} A_p e^{-i\vec{k}_p \cdot \vec{r}} \\ &\quad - \{A_b A_a^* \exp[i(\vec{k}_p - \vec{k}_s) \cdot \vec{r}]\} A_s e^{-i\vec{k}_s \cdot \vec{r}}). \end{aligned} \quad (6)$$

The phase mismatch  $\Delta$  of the two pump beams is given by  $\Delta = \phi_b - \phi_a$ , where  $A_b = |A_b| \exp(i\phi_b)$  and  $A_a = |A_a| \exp(i\phi_a)$ . Since the signal beam is much weaker than the probe beam for this type of FWM experiment, Eq. (6) leads to two coupled wave equations. Along the  $z$  axis, these are

$$\frac{\partial A_p(z)}{\partial z} + p(z) A_p(z) = 0, \quad (7)$$

$$\frac{\partial A_s(z)}{\partial z} + P(z) A_s(z) = Q(z), \quad (8)$$

where

$$\begin{aligned} p(z) &= \frac{-\alpha_0 |E_s|^2 (1-i\delta)}{\cos\theta} \left[ \frac{I_S + |A_b A_a| \exp\{+i[k(1-\cos\theta)z + \Delta]\}}{\{I_S + I_b + I_a + 2|A_b A_a| \cos[k(1-\cos\theta)z + \Delta]\}^2} \right], \\ P(z) &= -\alpha_0 |E_s|^2 (1-i\delta) \left[ \frac{I_S + |A_b A_a| \exp\{-i[k(1-\cos\theta)z + \Delta]\}}{\{I_S + I_b + I_a + 2|A_b A_a| \cos[k(1-\cos\theta)z + \Delta]\}^2} \right], \end{aligned}$$

and

$$Q(z) = \frac{-\alpha_0 |E_s|^2 (1-i\delta) |A_b A_a| e^{i\Delta} A_p(z)}{\{I_S + I_b + I_a + 2|A_b A_a| \cos[k(1-\cos\theta)z + \Delta]\}^2}.$$

It can be seen that  $p(z)$ ,  $P(z)$ , and  $Q(z)$  each oscillate with  $z$  with oscillation wavelength  $\lambda_{\text{osc}} = \lambda/(1-\cos\theta)$ . The solutions to Eqs. (7) and (8) fall into two categories, depending on whether or not  $p(z)$ ,  $P(z)$ , and  $Q(z)$  oscillate rapidly over distances where  $A_p(z)$  and  $A_s(z)$  change appreciably. These will be treated separately.

#### Case I: $\theta$ is not small

If  $\theta$  is not small, then  $A_p(z)$  and  $A_s(z)$  do not change appreciably over  $\lambda_{\text{osc}}$ . Since  $p(z)$ ,  $P(z)$ , and  $Q(z)$  then oscillate many times over distances where  $A_p(z)$  and  $A_s(z)$  change appreciably, they may be averaged over an oscillation wavelength. The solution to Eq. (7) is then

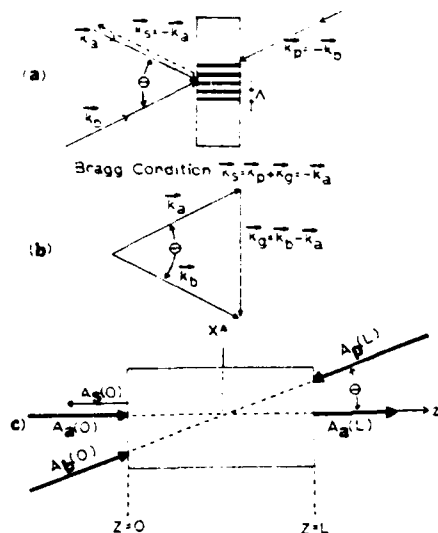


FIG. 2. (a) Grating formation geometry. (b) Conservation of wave vector and the Bragg condition. (c) Sample and electric field geometry.

observed signal properties. No attempt is made to relate these results to specific material properties since important properties such as dispersion in the excited state are not included in this simple model.

In the FWM configuration generally used to study energy migration, a laser beam is split into two strong "pump" beams of wave vectors  $\vec{k}_a$  and  $\vec{k}_b$ , and a weaker "probe" beam of wave vector  $\vec{k}_p$  which counterpropagates against one of the pump beams. This is shown in Fig. 2. The two pump beams interfere in the medium and optical absorption by the active ions creates a spatial distribution of excited states with a sinusoidal pattern of wave vector  $\vec{k}_g = \vec{k}_b - \vec{k}_a$ . Corresponding to the grating wave vector  $\vec{k}_g$  is the grating wavelength given by  $\Lambda = \lambda / (2 \sin \theta / 2)$ , where  $\lambda$  is the laser wave length and  $\theta$  is the crossing angle of the two pump beams. The depth of the grating can then be ascertained by Bragg diffraction of the probe beam. With the probe beam counterpropagating against the pump beam which has wave vector  $\vec{k}_b$ , the Bragg condition requires the scattered signal beam to have wave vector  $\vec{k}_s = \vec{k}_p + \vec{k}_g = -\vec{k}_a$ , which implies that the signal beam counterpropagates back against the pump beam with wave vector  $\vec{k}_a$  (see Fig. 2).

The assumptions will be made that all beams are linearly polarized in the same direction, with the pump beam electric field given by  $E_b(\vec{r}, t)$  and  $E_a(\vec{r}, t)$ , the probe field as  $E_p(\vec{r}, t)$ , and the signal beam as  $E_s(\vec{r}, t)$ . If the  $z$  axis is taken to be along the pump beam with electric field  $E_s$ , then the configuration will be as shown in Fig. 2 which is similar to the geometry of Refs. 7 and 9. By making the "parametric approximation" that the pump beams are undepleted in the media, then the four electric fields are given as

$$E_p(\vec{r}, t) = A_p(z) e^{i\omega t} e^{-i\vec{k}_p \cdot \vec{r}},$$

$$E_s(\vec{r}, t) = A_s(z) e^{i\omega t} e^{-i\vec{k}_s \cdot \vec{r}},$$

$$E_b(\vec{r}, t) = A_b e^{i\omega t} e^{i\vec{k}_b \cdot \vec{r}},$$

$$E_a(\vec{r}, t) = A_a e^{i\omega t} e^{i\vec{k}_a \cdot \vec{r}}.$$

The wave equation that these fields must obey in the material is

$$\nabla^2 E - \epsilon_0 \mu_0 \frac{\partial^2 E}{\partial t^2} = \mu_0 \frac{\partial^2 P}{\partial t^2}, \quad (1)$$

where  $\epsilon_0$  is the permittivity constant,  $\mu_0$  is the permeability constant, and  $P$  is the polarization. The polarization  $P$  may be expressed in terms of the susceptibility as

$$P(E) = \epsilon_0 \chi(E) E. \quad (2)$$

The media can be modeled as two-level system with the susceptibility given by<sup>9,14</sup>

$$\chi(E) = -\frac{2\alpha_0}{k} \left[ \frac{i + \delta}{1 + \delta^2 + |E/E_S|^2} \right], \quad (3)$$

where  $\delta$  is the normalized detuning from line center,  $|E_S|^2$  is the saturation intensity, and  $\alpha_0$  is the line center small-signal field attenuation coefficient. The total pump-beam electric field  $E_0 = E_a + E_b$  will have a much larger amplitude than the sum of the electric fields of the probe beam and the signal beam  $\Delta E = E_p + E_s$ . Thus the polarization can be expanded to first order in  $\Delta E/E_0$  to obtain<sup>9</sup>

$$P(E_0 + \Delta E) = e^{i\omega t} \epsilon_0 \chi(E_0) \left[ E_0 + \Delta E - \frac{(E_0^2 \Delta E^* + |E_0|^2 \Delta^2 E)}{I_S + |E_0|^2} \right], \quad (4)$$

where  $I_S = E_S^2 (1 + \delta^2)$ .

With the use of the slowly varying envelope approximation,  $|\partial^2 A_i / \partial z^2| \ll |k_i \partial A_i / \partial z|$ ,  $i = p, s$ , Eq. (1) becomes

acid.<sup>13</sup> The crystals grown were greater than 4 cm in cross section, which allowed samples of various crystallographic orientations to be cut and polished. The three samples studied had fractional concentrations of  $\text{Nd}^{3+}$  of  $x=0.2$ ,  $x=0.6$ ,  $x=1.0$ .

The experimental configuration used for this work is shown in Fig. 1. The 5145-Å line of an argon laser was used because it falls on the edge of one of the absorption bands of  $\text{Nd}^{3+}$ . The beam is sent through a 1-m focal length lens and then split into three beams. The weak probe beam (labeled  $p$  in the figure) is split off using a variable beam splitter. The two pump beams (labeled  $a$  and  $b$  in the figure) are split off using a 50-50 beam splitter. The path lengths of the pump beams must be within the coherence length of the laser, but the probe beam path length is purposely made much different to discourage gratings formed through the interference of the probe beam with one of the pump beams. The probe beam is aligned counterpropagating to pump beam  $b$ . This probe beam is then Bragg diffracted off the interference grating formed by the interaction of two pump beams in the sample so that the diffracted signal beam (label  $s$ ) counterpropagates back along pump beam  $a$ . The signal beam is then picked off using a beam splitter and directed into a photomultiplier tube. To analyze the transient behavior of the grating decay both of the pump beams are mechanically chopped, and the decay of the signal beam is monitored using a boxcar integrator and x-y recorder. The optics are slightly misaligned to prevent feedback into the laser. In addition, various orientations of polarizers have been used to decrease background light levels and an LSI-11 computer system has been used to analyze the data.

The laser directly pumps a  $\text{Nd}^{3+}$  absorption band

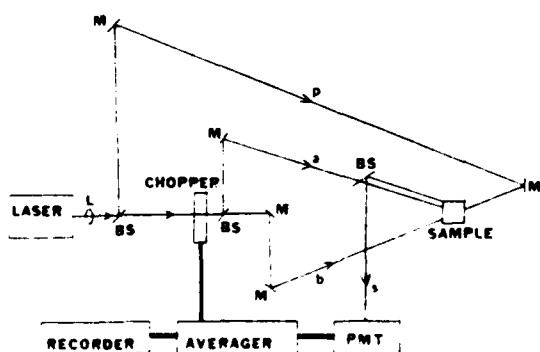


FIG. 1. Experimental configuration for transient grating measurements. Beams  $a$  and  $b$  are the pump beams, beam  $p$  is the probe beam, and beam  $s$  is the signal beam.

made up of overlapping  $^2G_{9/2}$  and  $^4G_{7/2}$  levels. There is then rapid radiationless relaxation to the  $^4F_{3/2}$  metastable state from which the fluorescence emission occurs to the various components of the  $^4I$  ground state term. The excited-state relaxation occurs on a time scale too rapid to be detected by this experiment. The energy migration occurs while the ions are in the metastable state, and it is the diffusion coefficient of this mobile excited state which is measured by this experiment.

### III. THEORY

The theory of FWM has recently been addressed in several papers<sup>6-12</sup> using two fundamentally different approaches. References 6 and 8 model the system as the probe beam Bragg diffracting off of a sinusoidally varying complex index of refraction grating. This is useful in studying the physical processes that destroy the grating in time. This is especially important in exciton-migration studies, and the results of this theory will be used in Sec. IV to analyze experimental data. References 7, 9, and 10 model the system by explicitly considering the nonlinear wave equations where the electric fields are coupled by the nonlinear susceptibility in the material. Furthermore, Refs. 9 and 10 consider the mechanisms creating this nonlinear susceptibility by modeling the system as an ensemble of two- and three-level atoms, respectively. This approach yields important information about the steady-state scattering efficiency. In interpreting FWM data it is important to understand the signal properties as fully as possible, and thus in discussing the results in Sec. IV theoretical predictions of both approaches are utilized. The Bragg scattering approach is used to directly determine information on exciton diffusion,<sup>6,11</sup> and the nonlinear interaction model is used to explain the dependence of signal strength and stability on alignment characteristics. Previous work with the latter model assumed phase-matched, counterpropagating pump beams. The FWM scattering efficiency is rederived below, modeling the media as a two-level system as in Ref. 9 but including important extensions to the theory consistent with the configuration used for exciton-migration studies. It is recognized that this treatment using interacting plane waves in a two-level system must be considered only a rough approximation to the real case of focused Gaussian beams<sup>7</sup> in a multilevel system ( $\text{Nd}^{3+}$ ). However, the general features of the signal intensity predicted by the simplified model are still useful in understanding the

# Transient grating investigation of exciton diffusion and fluorescence quenching in $\text{Nd}_x\text{La}_{1-x}\text{P}_5\text{O}_{14}$ crystals

Christopher M. Lawson and Richard C. Powell

*Physics Department, Oklahoma State University, Stillwater, Oklahoma 74078*

Walter K. Zwickler

*Philips Laboratories, Briarcliff Manor, New York 10510*

(Received 29 March 1982; revised manuscript received 15 June 1982)

The use of degenerate four-wave-mixing techniques to investigate exciton migration in highly concentrated laser materials is discussed. A theoretical derivation is presented of the signal beam intensity for this technique using the geometric arrangement common for energy-transfer studies. The results demonstrate effects that occur when the pump beams are not exactly phase matched and the instabilities encountered for very small pump-beam-crossing angles. Applying this technique to crystals of  $\text{Nd}_x\text{La}_{1-x}\text{P}_5\text{O}_{14}$  shows that exciton diffusion takes place in a given direction with diffusion lengths between 0.18 and  $0.36\ \mu\text{m}$  for samples with  $x$  ranging from 0.2 to 1.0, respectively. Fluorescence quenching is shown to vary linearly with concentration at high values of  $x$  and quadratically at low values of  $x$ . This is consistent with an exciton migration and trapping mechanism at high concentrations and cross relaxation at low concentrations.

## I. INTRODUCTION

We report here the results of an investigation of the properties of exciton diffusion in  $\text{Nd}_x\text{La}_{1-x}\text{P}_5\text{O}_{14}$  crystals using degenerate four-wave-mixing (FWM) techniques. Preliminary results of this work were given in Ref. 1. This paper presents a detailed derivation of some of the theoretical aspects of FWM, as well as extending the experimental data to an additional mixed crystal with a different composition and discussing the relevance of these results to the understanding of the concentration quenching characteristics of this material.

Investigating the optical properties of the so called "stoichiometric rare-earth laser materials" has been a topic of great interest in recent years, due to their possible important applications as "mini-lasers."<sup>2,3</sup> Understanding the concentration quenching in these materials is of specific interest since it is quite different from other rare-earth laser materials. Past work involving both site-selection spectroscopy<sup>4</sup> and fluorescent line narrowing spectroscopy<sup>5</sup> has shown that at low temperatures spectral diffusion of energy does not take place. However, spatial migration of energy has been observed over long distances at room temperature,<sup>1</sup> and the details of this process are described here. These measurements were made by degenerate FWM spec-

troscopy techniques in which an excited-state population grating is established and probed by chopped laser excitation. This form of transient grating spectroscopy has been shown to be an important method of determining exciton diffusion lengths in organic solids,<sup>6</sup> and has the important property of being able to detect spatial migration of energy without spectral diffusion.

Although the theory of FWM has been developed by several authors,<sup>6-12</sup> the form of the expression describing the scattering efficiency is different depending on the specific experimental orientation used. In Sec. III a derivation is presented of the FWM scattering efficiency expression assuming the experimental arrangement important for exciton migration studies. Several aspects of this expression are discussed which have not previously been addressed in other theoretical treatments. In Sec. IV the experimental results obtained from FWM measurements on  $\text{Nd}_x\text{La}_{1-x}\text{P}_5\text{O}_{14}$  crystals are discussed and the properties of concentration quenching in this type of material are investigated.

## II. SAMPLES AND EXPERIMENTAL APPARATUS

Large size single crystals of high optical quality  $\text{Nd}_x\text{La}_{1-x}\text{P}_5\text{O}_{14}$  were grown by the previously described flux technique from hot phosphoric

## II. CHARACTERIZATION OF EXCITON DYNAMICS IN STOICHIOMETRIC LASER MATERIALS

The following three manuscripts describe the results of characterizing the properties of exciton dynamics in  $\text{Nd}_x\text{La}_{1-x}\text{P}_5\text{O}_{14}$  crystals. These materials are important for applications as low threshold, high gain "minilasers". The results of this work are of practical importance since they demonstrate the role of exciton diffusion in concentration quenching which affects the quantum efficiency of these materials. From the point of view of fundamental physics, these results are exciting in several respects. They provide the first measurement of the exciton migration properties of this type of material and the first observation of vibronically enhanced and partially coherent exciton migration. Some of the mathematical background for interpreting the properties of four-wave mixing signals in multilevel systems is developed in the Appendix.

in the Excited States of Ions and Molecules in Solids,  
Stanford, July 1983.

G.E. Venikouas and R.C. Powell, "Spectroscopy of YAG:Nd Under  
High Power, Picosecond Pulse Excitation", Optical Society of  
America Meeting, New Orleans, October 1983.

J.K. Tymiński and R.C. Powell, "Transient Grating Studies of  
NdP<sub>5</sub>O<sub>14</sub>", Midwest Solid State Conference, Fayetteville,  
October 1983.

G.E. Venikouas and R.C. Powell, "Picosecond Spectroscopy of  
YAG:Nd", Oklahoma Academy of Sciences Meeting, Tulsa,  
November 1983.

J.K. Tymiński, K.L. Sweeney, L.H. Halliburton, and R.C. Powell,  
"Dependence of the Photorefractive Effect in LiNbO<sub>3</sub> on  
Annealing Temperature", American Physical Society Meeting,  
Detroit, March 1984.

G.J. Quarles, G.E. Venikouas, and R.C. Powell, "Pulse Width  
Dependence of Two-Photon Absorption Cross Sections in  
Y<sub>3</sub>Al<sub>5</sub>O<sub>12</sub>:Nd<sup>3+</sup>", Optical Society of America Meeting, San  
Diego, October 1984.

---

September 1983.

-North Texas State University, November 1983.

-Universidad Autonoma de Madrid, January 1984.

-University of Arkansas, January 1984.

-Central State University, November 1984.

R.C. Powell, Research Colloquium on "Oklahoma State University Materials Research Program" presented at:

-North American Philips Research Laboratory, June 1983.

-Allied Research Laboratories, June 1983.

-Union Carbide, October 1984.

-Air Force Office of Scientific Research, December 1984.

R.C. Powell, "Transition Metal Ion Tunable Laser Materials", Tunable Laser Workshop, NVEOL, Ft. Belvoir, VA, June, 1983.

R.C. Powell, "Recent Results on the Spectroscopy of Transition Metal Ions for Tunable Solid State Lasers", Tunable Solid State Lser Conference, La Jolla, CA, June 1984.

C.M. Lawson, R.C. Powell, and W.K. Zwicker, "Four-Wave Mixing in  $\text{Nd}_x\text{La}_{1-x}\text{P}_5\text{O}_{14}$  Crystals", American Physical Soc. Meeting, Dallas, March 1982.

J.K. Tyminski, R.C. Powell, and W.K. Zwicker, "Four-Wave Mixing in  $\text{Nd}_x\text{La}_{1-x}\text{P}_5\text{O}_{14}$  at Low Temperatures", Optical Soc. of America Meeting, Tucson, October 1982.

J.K. Tyminski, R.C. Powell, and W.K. Zwicker, "Temperature and Power Variation of Four-Wave Mixing in  $\text{Nd}_x\text{La}_{1-x}\text{P}_5\text{O}_{14}$ ", American Physical Society Meeting, Los Angeles, March 1983.

J.K. Tyminski, R.C. Powell, and W.K. Zwicker, "Variation of Transient Grating Decay Rate with Pump Wavelength and Power in  $\text{Nd}_x\text{La}_{1-x}\text{P}_5\text{O}_{14}$ ", Fourth Int. Conf. on Dynamical Processes

J.K. Tymiński and R.C. Powell, "Analysis of the Decay Dynamics of Laser-Induced Gratings in  $\text{LiNbO}_3$ ", to be published in the March issue of J. Opt. Soc. Am. B.

R.C. Powell, "Recent Results on the Spectroscopy of Transition Metal Ions for Tunable Solid State Lasers", Proc. of First Annual Conference on Tunable Solid State Lasers, edited by A. Pinto, A. Budgor, and P. Hammerling, (Springer-Verlag, Berlin, 1984) to be published.

L. Xi, R.H. Schweitzer, R.C. Powell, G.M. Loiacono, and G. Mizell, "Spectroscopic Evaluation of  $\text{Mn}_2\text{SiO}_4$  As a Possible Tunable Laser Material", Proc. Int. Conf. on Lasers '84, edited by W.A. Stwalley (STS Press, McLean, VA, 1985), to be published.

R.C. Powell, G.J. Gries, J.J. Martin, C.A. Hunt, and W.A. Sibley, "Stimulated Emission and Tunable Gain From  $\text{Rh}^{2+}$  Ions in  $\text{RbCaF}_3$  Crystals", submitted to Optics Letters.

## II. Doctoral Thesis

J.K. Tymiński, "Energy Migration Processes in Rare Earth Pentaphosphates", Oklahoma State University, Department of Physics, July 1983.

## III. Presentations

R.C. Powell, Research Colloquium on "Laser Spectroscopy of Solids" presented at:

-University of Rochester, February 1983.

-Texas Tech University, April 1983.

-Oklahoma State University (Sigma Xi Honor Lecture),



TABLE I

## PUBLICATIONS, THESES, AND PRESENTATIONS

## I. Publications

- C.M. Lawson, R.C. Powell, and W.K. Zwicker, "Transient Grating Investigation of Exciton Diffusion and Fluorescence Quenching in  $\text{Nd}_x\text{La}_{1-x}\text{P}_5\text{O}_{14}$  Crystals", *Phys. Rev. B* **26**, 4836 (1982).
- J.K. Tyminski, R.C. Powell, and W.K. Zwicker, "Temperature Dependence of the Exciton Diffusion in  $\text{Nd}_x\text{La}_{1-x}\text{P}_5\text{O}_{14}$  Crystals", *Proc. of Int. Conf. on Lasers '82*, edited by R.C. Powell (STS Press, McLean, VA, 1983), p. 245.
- J.K. Tyminski, R.C. Powell, and W.K. Zwicker, "Investigation of Four-Wave Mixing in  $\text{Nd}_x\text{La}_{1-x}\text{P}_5\text{O}_{14}$ ", *Phys. Rev. B* **29**, 6074 (1984).
- R.C. Powell, R.H. Schweitzer, J.J. Martin, G.E. Venikouas, and C.A. Hunt, "Spectroscopy of 4d and 5d Transition Metal Ions in Alkali Halide Crystals", *J. Chem. Phys.* **81**, 1178 (1984).
- G.E. Venikouas, G.J. Quarles, J.P. King, and R.C. Powell, "Spectroscopy of  $\text{Y}_3\text{Al}_5\text{O}_{12}:\text{Nd}^{3+}$  Under High Power, Picosecond Pulse Excitation", *Phys. Rev. B* **30**, 2401 (1984).
- R.C. Powell, J.J. Martin, R.H. Schweitzer, B.C. Gilliland, G.E. Venikouas, and C.A. Hunt, "Spectroscopic Analysis of 4d and 5d Transition Metal Ions for Tunable Solid State Laser Materials", *Proc. Int. Conf. On Lasers '83*, edited by R.C. Powell (STS Press, McLean, VA, 1984), p. 285.
- A.M. Ghazzawi, J.K. Tyminski, R.C. Powell, and J.C. Walling, "Four-Wave Mixing in Alexandrite Crystals", *Phys. Rev. B* **30**, 7182 (1984).

Jose Cabrera of the Universidad Autonoma de Madrid, John King of Central State University, and George Dixon of Oklahoma State University each spent one Summer working on this research. Dr. J.K. Tyminski made significant contributions to this work, first as a graduate research assistant and then as a post doctoral research associate. Graduate students supported in part by this contract include B. Quarles, X. Gang, M. Kleiwer, and L. Xi.

It is a pleasure to acknowledge the collaboration with a number of colleagues. First, many of the samples used in this research were obtained from the Oklahoma State University Crystal Growth Laboratory under the supervision of Prof. J.J. Martin. Second, we have benefited greatly from discussions with Profs. W.A. Sibley and L.E. Halliburton concerning the results of their optical and electron paramagnetic resonance studies on materials of interest to our research. In addition, we have worked closely with Dr. John Walling of Allied Chemical Laboratories on the studies of alexandrite; with Dr. J.L. Caslavsky of the Army Materials and Mechanics Research Center on the studies of titanium doped sapphire; and with Drs. Walter Zwicker and Gabe Loiacono at North American Philips Laboratories on the investigations of neodymium pentaphosphate and manganese silicate. Finally, we have benefited from helpful discussions with Dr. Al Pinto of the army Night Vision Electro-Optics Laboratory.

branching ratios, lifetimes, and quantum efficiencies were determined for these metastable states. Multiphoton absorption cross sections were determined for two types of transitions and radiationless relaxation rates were obtained for several decay processes including the 5d-4f transition.

The final thrust area involved a determination of the photorefractive properties of  $\text{LiNbO}_3$  using holographic grating techniques. The most important results were found from monitoring the changes in the erasure decay patterns of the gratings as a function of thermal annealing treatments. This led to the development of a model to describe the charge relocation dynamics involved in producing the photorefractive effect. This is based on the presence of trap modulated mobility of two types of charge carriers. Charge carrier densities, relocation rates, and relative trap concentrations were determined from analyzing the results using this model.

## 1.2 Publications and Personnel

The work performed during the three years of this contract resulted in eleven publications, one doctoral thesis, and numerous unpublished presentations and colloquia. These are listed in Table I.

The personnel making major contributions to this work include the Principal investigator, Richard C. Powell, and several visiting professors, post doctoral associates, and graduate students. Dr. George Venikouas worked on this project for two years before becoming a scientific staff member at the Electro-Optics Materials Division of Union Carbide. Professors

The most important result of this work was the demonstration of tunable single pass gain in  $\text{RbCaF}_3:\text{Rh}^{2+}$  crystals. The peak gain coefficient is significantly higher than that of other transition metal ion vibronic laser materials.

The goal of the third thrust area was to improve materials already demonstrated to be useful in tunable vibronic laser systems. The first project in this area involved characterizing the nonlinear optical properties of alexandrite crystals ( $\text{BeAl}_2\text{O}_4:\text{Cr}^{3+}$ ). The signal beam efficiency and decay rates from four-wave mixing were determined as a function of laser power. The results are consistent with scattering from excited state population gratings related to the difference in dispersion of the  $\text{Cr}^{3+}$  ions in the ground and metastable states. These gratings can be selectively established with  $\text{Cr}^{3+}$  ions in the inversion or mirror sites of the host lattice depending on the excitation wavelength. The second project in this thrust area was the investigation of inclusions appearing in  $\text{Al}_2\text{O}_3:\text{Ti}^{3+}$  crystals. These act as a loss mechanism for the material due to the scattering of laser light. Using laser Raman microprobe techniques, we identified these inclusions as  $\text{TiO}_2$ . This information was useful in improving the optical quality of this material.

The fourth thrust area was studying the response of laser materials to high power, fast pulse pumping. The most important results in this area focused on the multiphoton absorption and decay dynamics of  $\text{Y}_3\text{Al}_5\text{O}_{12}:\text{Nd}^{3+}$  crystals. Fluorescence emission lines were assigned to three different metastable states and the

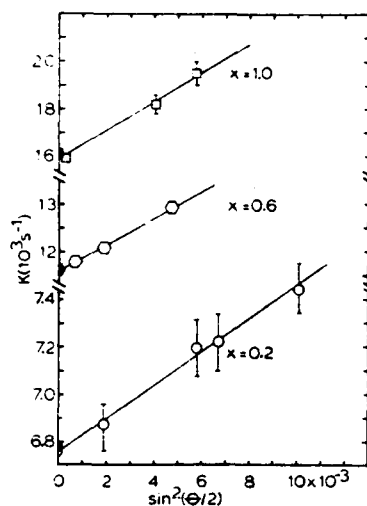


FIG. 3. Variation of grating decay constant with the square of the sine of half the pump-beam crossing angle at room temperature. The shaded points are twice the fluorescence decay rates.

only for  $\theta \geq 2^\circ$  since the signal beam was found to be extremely unstable at smaller crossing angles. The signal had two components at these small angles. One component was exceptionally sensitive to vibrations and to the exact alignment of the experiment, and underwent many oscillations whenever slight alignment changes were made. This component was superimposed on another much stabler component. This small-angle behavior is exactly what is predicted by Eqs. (16) and (17).

Whenever the pump beams are chopped and the grating is destroyed by fluorescence decay and exciton diffusion, the signal beam is predicted to decay exponentially with decay constant  $K$  given by<sup>6,11</sup>

$$K = (32\pi^2 D / \lambda^2) \sin^2(\theta/2) + 2/\tau. \quad (18)$$

Here  $D$  is the diffusion coefficient,  $\tau$  is the fluorescence lifetime of the excited state, and both  $\theta$  and  $\lambda$  have been corrected for the index of refraction of the sample.

In all three samples, double exponential decays were observed. The fast component had a decay constant that was independent of  $\theta$  and did not extrapolate to twice the fluorescence decay rate. Since

TABLE I. Exciton diffusion parameters in  $\text{Nd}_x\text{La}_{1-x}\text{P}_5\text{O}_{14}$  crystals.

$x$	$\tau$ ( $\mu\text{sec}$ )	$D$ ( $\text{cm}^2/\text{sec}$ )	$l_d$ ( $\mu\text{m}$ )
0.2	294	$5.2 \times 10^{-7}$	0.18
0.6	174	$2.5 \times 10^{-7}$	0.30
1.0	124	$5.1 \times 10^{-7}$	0.36

this is not consistent with the predictions of Eq. (18), the mechanism causing this component is scattering from something other than a simple population grating. It is not particularly surprising that other mechanisms create an optical Kerr effect in a birefringent, ferroelastic crystal such as  $\text{Nd}_x\text{La}_{1-x}\text{P}_5\text{O}_{14}$ , and these mechanisms will be studied in future experiments. The slower component of the double exponential decay had a decay constant that followed the predictions of Eq. (18) very closely and is therefore identified as being due to scattering from an excited-state population grating. It is this component of the total decay constant that is of interest in characterizing spatial energy migration.

The decay constant  $K$  is plotted versus  $\sin^2(\theta/2)$  in Fig. 3. With each sample, it is seen that  $K$  varies linearly with  $\sin^2(\theta/2)$  and extrapolates to twice the fluorescence decay rate for  $\theta=0$  as predicted by Eq. (18). By calculating the slope of the theoretical fit to the data, Eq. (18) can be used to obtain the diffusion coefficient  $D$ . Table I lists the values of  $D$  determined for the three samples. These are for energy migration along approximately the crystallographic  $a$  direction. It was more difficult to obtain data along other crystallographic directions due to higher background scattering, but in the  $\text{Nd}_{0.2}\text{La}_{0.8}\text{P}_5\text{O}_{14}$  sample the diffusion coefficient along the  $b$  direction was found to be the same as along the  $a$  direction within experimental error.

The exciton migration length in the grating direction  $l_i$  can be defined as  $l_i = \sqrt{2D\tau_0}$ . The values obtained for  $l_i$  are listed in Table I.

In order to identify the microscopic interaction causing the exciton migration, the concentration dependence of the diffusion coefficient must be ascertained. For a random walk resulting from electric dipole-dipole interaction<sup>10</sup>

$$D = \frac{1}{2} [(4\pi/3) N_{so}]^{4/3} R_0^6 / \tau_0 x^{4/3}, \quad (19)$$

where  $R_0$  is the critical interaction distance,  $\tau_0$  is the intrinsic fluorescence lifetime,  $N_{so}$  is the concentration of ions on the exciton lattice for  $\text{NdP}_5\text{O}_{14}$ , and  $x$  is the normalized Nd concentration. Figure 4 shows a plot of  $D$  vs  $x^{4/3}$ . The linear variation of  $D$  with  $x^{4/3}$  is consistent with Eq. (19). The use of values of  $\tau_0 = 350 \mu\text{sec}$  and  $N_{so} = 4 \times 10^{21} \text{ cm}^{-3}$  and fitting the data in Fig. 4 with Eq. (19) gives a value of  $R_0 = 45 \text{ \AA}$ . This long-range interaction distance will overcome any crystal anisotropy which is consistent with the observation that the diffusion coefficient is the same along the  $a$  and  $b$  directions.

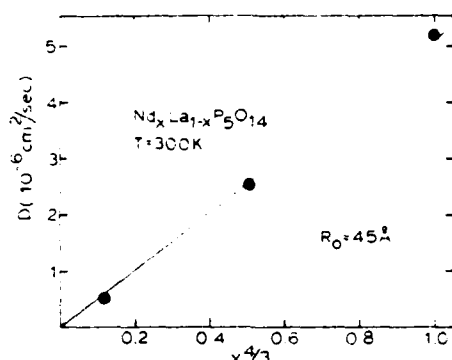


FIG. 4. Concentration dependence of the exciton diffusion coefficient at room temperature.

Next, it is important to determine the role played by the exciton migration in the concentration quenching properties of the material. The quenching rate is given by

$$W_Q = \tau^{-1} - \tau_0^{-1}, \quad (20)$$

where  $\tau$  is the measured fluorescence decay time and  $\tau_0$  is the intrinsic fluorescence lifetime in the absence of concentration quenching. Again taking  $\tau_0 = 350 \mu\text{sec}$  the fluorescence lifetime and quenching rate plotted versus concentration in Fig. 5. At high concentrations the quenching rate varies linearly with concentration as shown in Fig. 5. This linear concentration dependence of the quenching rate together with the long exciton migration lengths listed in Table I indicate that the dominant quenching process in the higher concentration  $\text{Nd}_x\text{La}_{1-x}\text{P}_5\text{O}_{14}$  crystals is an exciton diffusion and trapping mechanism. At low concentrations the quenching rate no longer varies linearly with concentration as can be seen in Fig. 5. This region is expanded in Fig. 6 where the quenching rate is plotted both versus concentration and the square of the

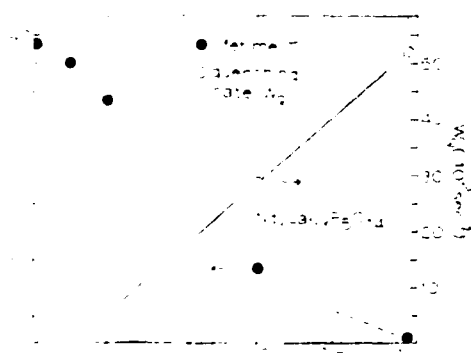


FIG. 5. Concentration dependence of the fluorescence lifetime and quenching rate at room temperature.

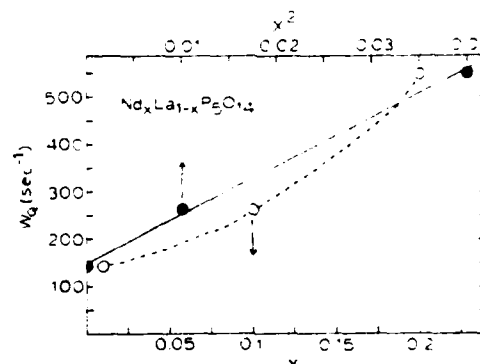


FIG. 6. Concentration dependence of the quenching rate at room temperature for samples with low Nd concentrations.

concentration for the three samples with smallest values of  $x$ . It is seen that for these low-concentration samples, the quenching rate varies approximately quadratically with concentration, which is consistent with an ion pair cross-relaxation quenching mechanism.

## V. SUMMARY AND CONCLUSIONS

Three important results have been described in the preceding sections. The first is the derivation of the expression describing the intensity of the FWM signal beam in the typical configuration used for studies of exciton dynamics. This shows the effects of not having the beams exactly phase matched and the instabilities that arise for very small write beam crossing angles. The latter effect was encountered experimentally. The second is the demonstration that excitons diffuse over an average distance of  $0.36 \mu\text{m}$  in a specific direction in  $\text{NdP}_5\text{O}_{14}$  at room temperature. The third is the implication obtained from the concentration dependence of the fluorescence quenching that at very low concentrations quenching occurs through cross relaxation while at high concentrations the quenching mechanism is exciton migration to sinks.

There has been significant controversy in the literature concerning the concentration quenching mechanism in stoichiometric laser materials and whether exciton diffusion occurs in these materials or not. The arguments on these subjects have been discussed elsewhere and will not be repeated here.<sup>4,17</sup> Some of the discrepancies in data reported previously may be due to differences in sample quality since it has only been recently that it has been possible to obtain good single crystals of large size and high optical quality.<sup>13</sup>

The results reported here showing that different quenching mechanisms are active in high- and low-concentration samples are consistent with the observed differences of the effects of high pressure on the optical spectra of stoichiometric rare-earth materials.<sup>18</sup> The exponential shape of the population grating FWM signal decay indicates that exciton motion is diffusive at room temperature.<sup>6,11</sup> The nature of the trapping sites and quenching interaction has not yet been determined. The sample surface has been shown to play some role in the quenching but it does not appear to be the dominant quenching site.<sup>5</sup> Also it is important to note that hydroxyl radicals which were known to cause quenching in early materials of this type are not present in the high quality samples used in this study.

The observation of long-range exciton diffusion in  $\text{NdP}_5\text{O}_{14}$  at room temperature is consistent with the recent low-temperature photon-echo results ob-

tained on similar  $\text{EuP}_5\text{O}_{14}$  crystals which show the excitons to be delocalized.<sup>19</sup> Attempts are currently underway to repeat these FWM experiments at low temperatures to determine the role played by phonons in the exciton migration and trapping process. However, additional experimental complications such as added background scattering from dewar windows and reduced absorption of the signal beams have so far inhibited low-temperature measurements of this type. These will be pursued further in the future as well as additional investigations into the nature of the unexplained angular-independent scattering mechanism.

#### ACKNOWLEDGMENTS

This work was supported by the U.S. Army Research Office and National Science Foundation Grant No. DMR-7916152.

- <sup>1</sup>C. M. Lawson, R. C. Powell, and W. K. Zwicker, *Phys. Rev. Lett.* **46**, 1020 (1981).
- <sup>2</sup>H. G. Danielmeyer, in *Festkörperprobleme*, edited by H. J. Queisser (Pergamon, New York, 1975), Vol. 15, p. 253.
- <sup>3</sup>H. P. Weber, *Opt. Quantum Electron.* **7**, 431 (1975).
- <sup>4</sup>J. M. Flaherty and R. C. Powell, *Phys. Rev. B* **19**, 32 (1979).
- <sup>5</sup>R. C. Powell, D. P. Neikirk, J. M. Flaherty, and J. G. Gualtieri, *J. Phys. Chem. Solids* **41**, 345 (1980).
- <sup>6</sup>J. R. Salcedo, A. E. Siegman, D. D. Diott, and M. D. Fayer, *Phys. Rev. Lett.* **41**, 131 (1978).
- <sup>7</sup>A. Yariv and D. M. Pepper, *Opt. Lett.* **1**, 16 (1977).
- <sup>8</sup>A. E. Siegman, *J. Opt. Soc. Am.* **67**, 545 (1977).
- <sup>9</sup>R. L. Abrams and R. C. Lind, *Opt. Lett.* **2**, 94 (1978); **3**, 205 (1978).
- <sup>10</sup>P. F. Liao and D. M. Bloom, *Opt. Lett.* **3**, 4 (1978).
- <sup>11</sup>V. M. Kenkre, *Phys. Rev. B* **18**, 4064 (1978); Y. M.

- Wong and V. M. Kenkre, *ibid.* **22**, 3072 (1980); V. M. Kenkre, *Phys. Lett. A* **82**, 100 (1981).
- <sup>12</sup>H. Kogelnik, *Bell Sys. Tech. J.* **48**, 2909 (1969).
- <sup>13</sup>R. D. Plattner, W. W. Kruhler, W. K. Zwicker, T. Kovats, and S. R. Chinn, *J. Cryst. Growth* **49**, 274 (1980).
- <sup>14</sup>A. Yariv, *Quantum Electronics* (Wiley, New York, 1975), p. 149.
- <sup>15</sup>C. M. Lawson, doctoral dissertation, Oklahoma State University, 1981 (unpublished).
- <sup>16</sup>Th. Förster, *Ann. Phys.* **2**, 55 (1948).
- <sup>17</sup>W. Lenth, G. Huber, and D. Fay, *Phys. Rev. B* **23**, 3877 (1981); D. Fay, G. Huber and W. Lenth, *Opt. Commun.* **28**, 117 (1979).
- <sup>18</sup>L. D. Merkle, I. L. Spain, and R. C. Powell, *J. Phys. C* **14**, 2027 (1981).
- <sup>19</sup>R. M. Shelby and R. M. Macfarlane, *Phys. Rev. Lett.* **45**, 1098 (1980).

TEMPERATURE DEPENDENCE OF THE EXCITON DIFFUSION IN  $\text{Nd}_x\text{La}_{1-x}\text{P}_5\text{O}_{14}$  CRYSTALS

Jacek K. Tymiński and Richard C. Powell

Oklahoma State University, Stillwater, OK 74078

and

Walter K. Zwicker

Philips Laboratories, Briarcliff Manor N.Y. 10510

Abstract

Recent results are presented on the exciton dynamics of  $\text{Nd}_x\text{La}_{1-x}\text{P}_5\text{O}_{14}$  crystals obtained using four-wave mixing spectroscopy.

I. Introduction

We have been characterizing the spatial migration of energy in mixed neodymium-lanthanum pentaporphosphate crystals using degenerate four-wave mixing spectroscopy techniques in which an excited state population grating is established and probed by chopped laser excitation.<sup>1,2</sup> The results show that diffusive exciton migration takes place over long distances in these systems and that the effects of phonons in limiting the diffusion process are quite different in stoichiometric materials versus mixed crystals.

The experimental setup used for this work is described in ref. 2. An argon laser-pumped tunable dye laser with rhodamine 6G was used as the excitation source. The dye laser was tuned to the peak of a  $\text{Nd}^{3+}$  absorption line and the output was split into three beams, two strong pump beams (a and b) which enter the sample from the front and a weak probe beam p which enters the back of the sample conjugate to one of the pump beams. The scattered probe beam is detected as a signal s by a RCA 1P28 photomultiplier tube. By mechanically chopping the pump beams the decay curve of the signal beam can be measured using a boxcar integrator and signal averager. The sample is mounted in a cryogenic refrigerator capable of temperature variation between 10 K and room temperature.

The interacting pump beams form a sine wave pattern which creates a population grating of  $\text{Nd}^{3+}$  ions. There are a high density of excited ions at the peak regions of the grating and a low density of excited ions at the valley regions of the grating. Because of the differences in polarizability in the ground and excited states, the probe beam Bragg diffracts off this grating. When the pump beams are cut off, the signal beam decays as the grating decays for two reasons: the fluorescence decay of the excited ions and the migration of the excitation (or excitons) from the peak to the valley regions of the grating. The equation describing this decay is

$$I_s(t) = I_p I_e^2 e^{-Kt} \quad (1)$$

where

$$K = 2/\tau + (32\pi^2 D/\lambda^2) \sin^2(\theta/2). \quad (2)$$

Here  $\tau$  is the intrinsic fluorescence decay time,  $D$  is the exciton diffusion coefficient, and  $\theta$  is the crossing angle of the pump beams. If the exciton motion is not diffusive, it has been shown that the equation describing the signal decay is quite different from this and specifically is not purely exponential as predicted here.<sup>3</sup>

II. Results

Using relatively low laser powers the signal decays as a pure exponential and with the use of the signal averager we achieve excellent signal to noise ratios. The observed exponential decays indicate that the exciton migration is diffusive at all temperatures between 10 and 300 K for samples with  $\text{Nd}^{3+}$  concentrations between 20 and 100%.

Figure 1 shows the measured values of the grating decay rate plotted versus the sine squared of half the pump beam crossing angle for samples with two different  $\text{Nd}^{3+}$  concentrations at 26K. The solid points represent one half the fluorescence decay rates obtained by independent measurements. The straight lines are the best fits to the data using Eq. (2). As predicted, the data plotted this way vary linearly and extrapolate to half the decay rates at zero crossing angle. The exciton diffusion coefficients can be obtained from the slopes of the lines.

The values of the diffusion coefficients obtained by this technique are listed Table 1. In the 100% sample the diffusion length is of the order of half a micron. The values of  $D$  are significantly higher than those usually measured for exciton migration among rare earth



ions in solids, but this is consistent with the much higher concentration of ions in these systems compared to the usual lightly doped materials.

The temperature dependence of the diffusion coefficients are shown in Fig. 2. Obviously the temperature dependence is quite different in the 100% sample and the 20% sample. In the former D is essentially independent of temperature while in the latter there is a significant increase in D going from about 100 K down to about 10 K. These observations of the differences in temperature dependence are difficult to understand.

### III. Discussion

The diffusion coefficient can be expressed in terms of the exciton velocity and either the mean free path or scattering time,

$$D = 1/3 \langle A_m v \rangle = 1/3 \langle t_{sv}^2 \rangle. \quad (3)$$

One special case which is generally true for lightly doped rare earth systems is the nearest neighbor hopping model in which the mean free path is just the distance between rare earth ions and the velocity can be expressed in terms of the ion-ion energy transfer rate. The temperature dependence of D is contained on this latter factor which is proportional to the oscillator strength of the transitions f and the spectral overlap integral  $\Omega$ ,

$$D = 1/3 (a^2/t_h) = 1/3 (a^2 w) \quad (4)$$

where

$$W(T) \propto f_i f_j \Omega. \quad (5)$$

The latter factor increases as temperature increases which is not consistent with the data in this case. The oscillator strengths have been shown to be independent of concentration in this system<sup>4</sup> and thus any temperature dependent changes in f should be the same for both samples which is again inconsistent with experimental observations. Thus we can rule out the nearest neighbor hopping model as a way of interpreting data for these highly concentrated systems.

In the general case, the scattering time or mean-free-path of migration of excitons can be limited by several different types of scattering events the most common of which are listed in Table 2. Agronovitch and co-workers<sup>5</sup> have derived the temperature dependences associated with each of these mechanisms. Obviously a variety of temperature dependences are possible depending on the type of phonons or defects which dominate the scattering process. However, both because of the various assumptions which had to be made about the electron-phonon coupling in deriving these equations, and because several mechanisms may be active simultaneously, it is difficult to do any quantitatively fitting between theory and experiment.

However we can formulate some general assumptions of a model which gives a consistent interpretation of the observed results and is the only model we have found for doing this. The first assumption is that only optical phonons are effective in scattering the excitons. This is reasonable since in these highly concentrated materials energy will move between ions within the wave length of acoustic phonons and thus the energy levels of both ions will be modulated simultaneously by these phonons. In contrast, optical phonons will modulate the position and energy of one ion with respect to its nearest neighbor and thus be effective in exciton scattering. Thermal diffusivity measurements<sup>6</sup> indicate that the Debye temperature is around room temperature in these crystals and thus lattice phonons should be contribute to a temperature dependence of the diffusion coefficient. The excitons in the 100% sample are then limited by boundary scattering and thus D is independent of temperature. These boundaries may be surfaces, grain boundaries, or ferroelastic domain boundaries. Previous measurements have shown an increase in energy migration rate with increasing hydrostatic pressure which may be due to decreasing the number of grain boundaries in the crystal.<sup>7</sup> The final assumption is that the dominant scattering in the 20% sample is by thermally activated defects. These can be thought of as localized phonons around the lanthanum impurity ions distributed randomly in the lattice. This type of scattering center predicts the type of temperature dependence of D observed in the sample.<sup>5</sup>

Although we have no conclusive proof of the validity of this model, it is the only method we have been able to find for interpreting the observed temperature dependences of the exciton diffusion coefficient in these crystals.

### Acknowledgments

This work was supported by the U.S. Army Research Office and National Science Foundation Grant No. WMR-7916152.

# References

1. C.M. Lawson, R.C. Powell, and W.K. Zwicker, Phys. Rev. Lett. **46**, 1020 (1981).
2. C.M. Lawson, R.C. Powell, and W.K. Zwicker, Phys. Rev. B **26**, 4836 (1982).
3. V.M. Kenkre, Phys. Rev. B **18**, 4064 (1978); Phys. Lett. A **82**, 100 (1981).
4. F. Auzel, IEEE J. Quantum Electronics **12**, 258 (1976).
5. V.M. Agranovich and Yu. V. Konobeev, Sov. Phys. Solid State **5**, 999 (1963); *ibid* **6**, 644 (1964); Phys. Stat. Sol. **27**, 435 (1968); and Opt. and Spect. **6**, 155 (1959).
6. S.R. Chinn and W.K. Zwicker, J. Appl. Phys. **49**, 5892 (1979).
7. L.D. Merkle, I.L. Spain and R.C. Powell, J. Phys. C **14**, 2027 (1981).

Table 1: Diffusion Coefficient In  $\text{Nd}_x\text{La}_{1-x}\text{P}_5\text{O}_{14}$

T(K)	D( $10^{-6}\text{cm}^2\text{s}^{-1}$ )	
	X=0.2	X=1.0
295	2.3	8.4
12	5.2	8.2

Table 2: Temperature Dependences Of Exciton Mean Free Paths

Scattering Mechanism	$\lambda(T)$
Acoustic Phonons	$T^{-1}$
Optic Phonons	$T^{-1}$ , $T > T_D$ $C$ , $T < T_D$
Boundaries	$L$
Thermal Defects	$\exp(u/kT)$

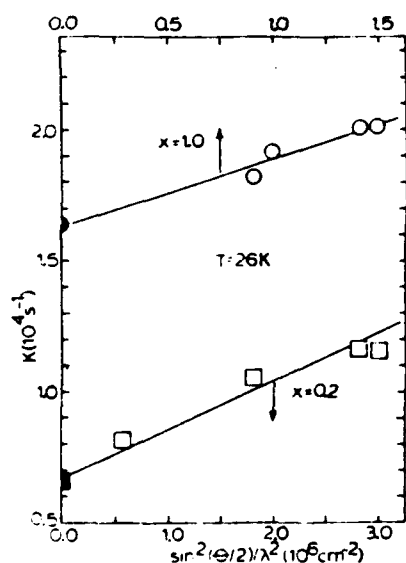


Fig. 1. Grating decay constant as a function of pump beam crossing angle for two samples at low temperature. (See text for explanation of experimental points and theoretical lines.)

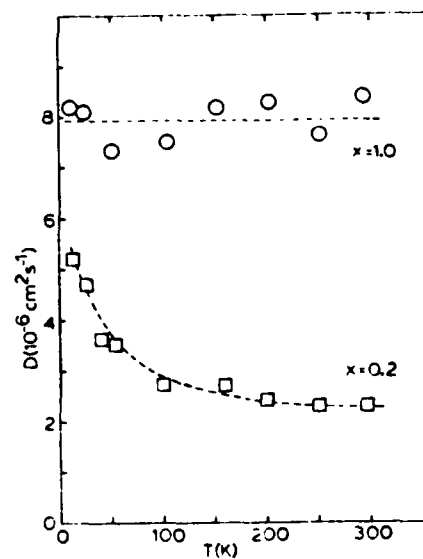


Fig. 2. Temperature dependence of the exciton diffusion coefficient for two samples.

Investigation of four-wave mixing in  $\text{Nd}_x\text{La}_{1-x}\text{P}_5\text{O}_{14}$ 

Jacek K. Tyminski and Richard C. Powell

*Physics Department, Oklahoma State University, Stillwater, Oklahoma 74078*

Walter K. Zwicker

*Philips Laboratories, Briarcliff Manor, New York 10510*

(Received 7 November 1983)

Four-wave mixing has been investigated in  $\text{Nd}_x\text{La}_{1-x}\text{P}_5\text{O}_{14}$  crystals as a function of temperature, laser excitation wavelength, and power. The results are interpreted in terms of scattering from a population grating, and the relative intensity of the scattered signal is investigated as well as the grating decay time. The power dependence of the scattered intensity is explained by a model involving interaction with a three-level system, and the properties of the grating decay are associated with the exciton dynamics of the ions in the excited state. Decay patterns characteristic of both incoherent and partially coherent exciton migration can be observed under different experimental conditions. Enhanced migration due to vibronic generation of phonons resonant with the metastable state splitting is also observed. The temperature dependence of the results shows a weak coupling between the excitons and the acoustic phonons of the host. Local heating effects are found to affect the ion-ion and ion-phonon interaction parameters and produce a thermal grating under certain experimental conditions.

## I. INTRODUCTION

The dynamics of quasiparticle transport has long been a topic of fundamental interest in solid-state physics. Exciton migration among ions and molecules in highly concentrated crystals represents an important special case of this type of problem. Two of the most important questions which have been extensively addressed theoretically concern the distinction between coherent and incoherent motion<sup>1-3</sup> and spectral variations in migration efficiency.<sup>4-6</sup> It has proven to be quite difficult to find the appropriate experimental techniques and crystal systems to provide the data necessary to verify the theoretical predictions. We report here the results of using four-wave-mixing transient-grating spectroscopy to characterize the properties of  $\text{Nd}_x\text{La}_{1-x}\text{P}_5\text{O}_{14}$  crystals. This work demonstrates the powerful capabilities of this experimental technique for studying exciton-transport properties.

The technological potential of rare-earth pentaphosphates as minilasers has made it imperative to understand the basic optical properties of this class of materials.<sup>7</sup> An interesting dichotomy has developed in comparing the results obtained from site-selection laser spectroscopy techniques<sup>8-10</sup> which monitor spectral energy migration with results obtained from coherent transient techniques<sup>11</sup> which probe the spatial delocalization of the energy. The former indicate that weak spectral transfer occurs, while the latter show the excitation energy to be spatially delocalized. Our initial investigation using four-wave-mixing transient-grating spectroscopy produced results which demonstrated the existence of long-range exciton diffusion in  $\text{Nd}_x\text{La}_{1-x}\text{P}_5\text{O}_{14}$  crystals at room temperature.<sup>12</sup> In this paper we present the results of an investigation of the exciton-diffusion coefficient as a function of temperature, laser-pump power, and excitation wavelength. Also the

variation of scattering efficiency as a function of pump power is reported. The results show that either incoherent or partially coherent exciton migration can occur depending on the initial excitation conditions. They also show the effects of local thermal heating on excitation-migration parameters.

The details of crystal growth and sample properties were described previously.<sup>13</sup> Figure 1 shows the pertinent energy levels and transitions for this study. The dye laser with Rhodamine-6G pumps the  $\text{Nd}^{3+}$  ions in the region of the absorption band consisting of overlapping levels of the  $^2G_{7/2}$  and  $^4G_{5/2}$  manifolds. With high-energy vibronic excitation a photon is absorbed and a phonon is emitted. Rapid radiationless relaxation to the  $^4F_{3/2}$  metastable

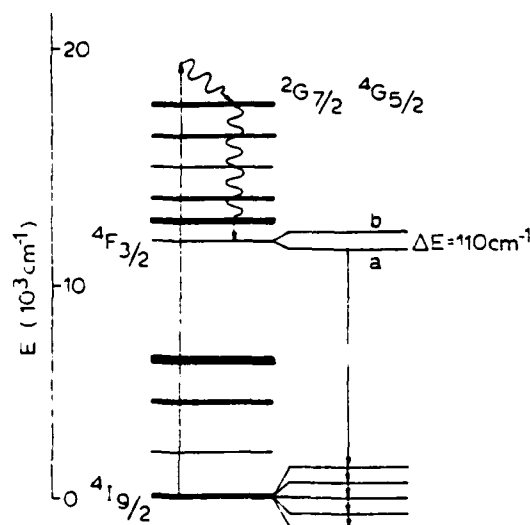


FIG. 1. Partial energy-level diagram for  $\text{Nd}^{3+}$  showing the excitation and emission transitions of interest to this work.

state then occurs. Fluorescence occurs from this level to the various components of the  $^4I$  term. An extensive amount of work has been reported on the conventional optical spectroscopy of this material.<sup>14-16</sup> The energy in the metastable state can be transferred from one  $\text{Nd}^{3+}$  ion to another and this mobile excitation energy is treated as a Frenkel exciton.

## II. FOUR-WAVE-MIXING TRANSIENT-GRATING SPECTROSCOPY

Figure 2 shows a block diagram of the experimental setup used for four-wave-mixing measurements. The output of an argon-ion laser-pumped tunable dye laser with Rhodamine-6G dye was split into three beams. By using a variable beam splitter and a variable neutral-density filter the power in each of these beams was controlled. Beams *a* and *b* are the pump beams. They are chopped and weakly focused inside the sample. Care was taken to ensure that the difference in their optical path lengths was less than the coherence length of the laser. The probe beam *p* enters the opposite side of the sample conjugate to pump beam *a* and the signal beam *s* exits the sample conjugate to pump beam *b*. Another beam splitter was used to send part of the signal beam to a photomultiplier tube. The time decay of the signal beam was processed by both a boxcar integrator and a signal averager before being displayed on a recorder. This double averaging technique gave excellent signal-to-noise-ratio results. The sample was mounted in a cryogenic refrigerator with a temperature controller which varied the temperature selectively between about 10 K and room temperature.

Four-wave mixing occurs through the third-order component of the susceptibility tensor. This can be related to local changes in the refractive index induced by the interacting laser pump beams. These changes can be produced by several physical mechanisms including thermal effects, photoconductive effects, and changes in electronic state populations. Each of these has specific characteris-

tics different from the others, and thus it is generally possible to determine the dominant physical mechanism giving rise to the scattering for a specific system under given experimental conditions. There are two different approaches to describing this physical process.<sup>17-19</sup> One is through the use of Maxwell's equations and the susceptibility of the material to account for the nonlinear interaction of the laser beams in the solid. This method is generally used to determine the signal-generation efficiency as discussed in Sec. VI. The other approach is to treat the process as the scattering of the probe beam from a grating formed by the interfering pump beams.<sup>19</sup> This method is generally used to study the physical properties of the material which produce and destroy the grating. For the case of interest here, the scattering is due to a population grating. The interference pattern of the two pump beams is a sine wave. This results in the creation of a high density of  $\text{Nd}^{3+}$  ions in the metastable state in the peak regions of the sine wave and a low density of excited  $\text{Nd}^{3+}$  ions in the valley regions. Figure 3 schematically depicts this population grating.<sup>20</sup> The difference in the refractive index of the ions in the ground and excited states causes the scattering of the probe beam. The Bragg-diffraction condition is satisfied with the probe beam directed conjugate to one of the pump beams and scattering in the direction of the other pump beam.

The two primary experimental parameters to be measured are the scattering efficiency and the decay pattern of the signal beam when the pump beam is chopped off. The former information is of greatest interest in the practical application of four-wave mixing to optical data processing, while the latter information is useful in understanding the physical mechanisms which cause the destruction of the grating pattern. Both types of measurements are discussed in the following sections, but the latter is most important in using this technique to study exciton dynamics. As shown in Fig. 3, the grating is destroyed by the normal radiative and radiationless relaxation processes, and, in addition, by the migration of exci-

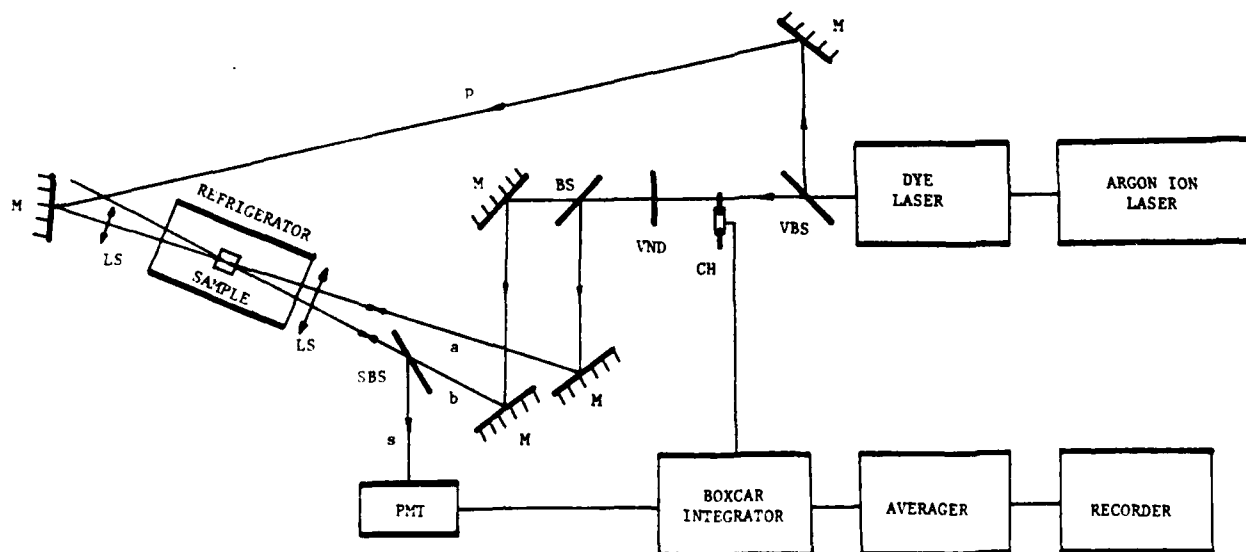


FIG. 2. Block diagram of the experimental apparatus. *M*, mirror; *LS*, lens; *BS*, *VBS*, and *SBS*, beam splitters; *CH*, chopper; *PMT*, photomultiplier tube.

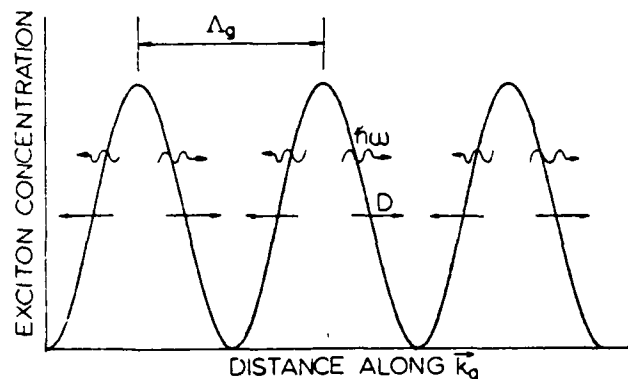


FIG. 3. Schematic representation of the population grating (Ref. 20).  $\Lambda$  is the grating wavelength.

tation energy from the peak to the valley regions of the population distribution. It is this last process of exciton migration which is of interest here, and the relationship between the properties of this migration and the measured experimental characteristics are discussed in the following section.

### III. CHARACTERISTICS OF GRATING DECAY PATTERNS

Figure 4 shows the absorption spectrum of  $\text{NdP}_3\text{O}_{14}$  in the region of the laser wavelength at 77 K. This type of stoichiometric rare-earth material has high optical densities in the regions of peak absorption, and therefore the pump, probe, and signal beams are strongly depleted for this type of excitation. Strong beam depletion makes it difficult to perform four-wave-mixing experiments and to interpret the results. Therefore these experiments were performed by exciting into the high-energy wing of the absorption transition or by using Stokes vibronic excitation. Each point in the figure represents the results of determining the exciton-diffusion coefficients for  $\text{Nd}_x\text{La}_{1-x}\text{P}_3\text{O}_{14}$  samples with  $x = 1.0$  and  $0.2$  using transient-grating data as described below. These measurements were made at 12.5 K using weakly focused laser beams.

Figure 5 shows examples of the three different types of

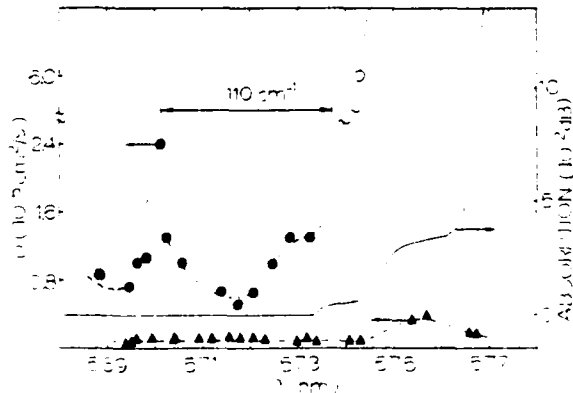


FIG. 4. Excitation wavelength dependence of the exciton-diffusion coefficient with respect to the absorption spectrum for  $P_p = 0.18$  W. Absorption spectrum taken at 77 K and values for  $D$  obtained at 12.5 K.  $\circ$  represents data for the  $x = 1.0$  sample and  $\triangle$  represents data for the  $x = 0.2$  sample.

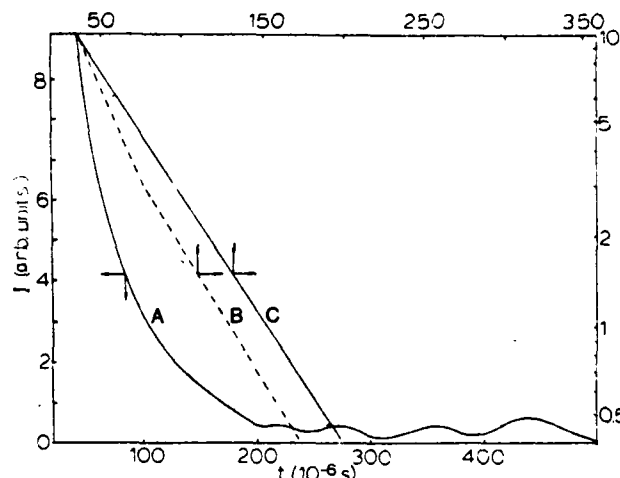


FIG. 5. Examples of signal decay patterns observed at 12.5 K at  $\theta = 10^\circ$ . A,  $\lambda_{\text{exc}} = 5745$  Å;  $P_p = 0.03$  W. B,  $\lambda_{\text{exc}} = 5745$  Å;  $P_p = 0.18$  W. C,  $\lambda_{\text{exc}} = 5724$  Å;  $P_p = 0.18$  W.  $x = 1.0$ .

grating decay patterns that were observed for different types of experimental conditions. These traces show the excellent signal-to-noise ratio obtained with the dual-averaging technique. Under most conditions the single exponential decay is observed, which is consistent with results of previous work of this type.<sup>12,20-24</sup> This pattern is always observed for the  $x = 0.2$  sample. It is also always observed for the  $x = 1.0$  sample when vibronic excitation is used. However, for resonant excitation into the wing of the absorption band of the  $x = 1.0$  sample, the other two types of decay patterns can be observed. The oscillatory pattern was observed at low temperatures using total laser-pump powers of less than 30 mW. If the temperature is raised to about 100 K, the oscillatory pattern disappears and a single exponential pattern is observed. If the power is increased, the double exponential decay pattern is seen. The physical significance of these different types of grating decay patterns is discussed below.

Since the use of transient-grating techniques to study exciton migration is fairly recent, there has been little work done in developing and testing theoretical models for interpreting experimental results. Several different types of approaches to this problem have been employed. The two most useful formalisms for developing specific expressions describing population grating decay patterns are due to Fayer<sup>20</sup> and to Wong and Kenkre.<sup>25</sup> Fayer's results have been derived for the two limiting cases of purely incoherent and purely coherent exciton migration. In his formalism, the latter case is applicable for the initial experimental conditions of direct, resonant excitation into the exciton band leading to strongly delocalized states. The Wong and Kenkre approach has been developed for the general case of partially coherent exciton migration as well as the two limiting cases. The Fayer and the Wong and Kenkre results have been shown to be equivalent in the purely incoherent migration limit if the continuum approximation is made in both cases. However, the Fayer and the Wong and Kenkre formalisms lead to quite different results in the purely coherent migration limit. The reason is that the latter is based on a generalized master-

equation approach which requires the initial density matrix for the system to be diagonal. Physically, this restricts the applicability of the approach to initial experimental conditions of highly localized exciton states or complete phase randomness among the wave functions. This condition can be achieved experimentally by excitation into a higher-lying energy level followed by fast radiationless relaxation into the exciton band. As described in Sec. I, these are exactly the experimental conditions of the work described here. Therefore, the Wong-Kenkre theory is outlined below and their results are used to interpret the experimental data. The validity of this theory and other possible theoretical interpretations of the data are discussed further in Sec. VII.

Starting from a generalized master-equation approach, Wong and Kenkre<sup>25</sup> express the probability of finding an exciton on lattice site  $m$  at time  $t$  as  $p_m(t)$  and its time

evolution is described by

$$\frac{dp_m(t)}{dt} = \int_0^t dt' \left[ \sum_n V_{m,n}(t-t') P_n(t') - V_{n,m}(t-t') P_m(t') \right] - P_m(t)/\tau. \quad (1)$$

Here  $\tau$  is the exciton lifetime and  $V_{m,n}(t)$  gives the rate of energy transfer from the  $m$ th to the  $n$ th site. This latter parameter is called the "memory function" since it reflects the degree of coherence influencing the energy-migration process. This function has been computed using a one-dimensional model with a time-independent, nearest-neighbor ion-ion-interaction matrix element  $j$  and a single, time-independent, randomized parameter  $\alpha$  describing the exciton interaction with the phonon bath,<sup>24</sup>

$$V_{n,m}(t) = 2j^2 e^{-\alpha t} [J_{m-n+1}^2(2jt) + J_{m-n-1}^2(2jt) + 2J_{m-n+1}(2jt)J_{m-n-1}(2jt) - \{2J_{m-n}^2(2jt) + J_{m-n}(2jt)[J_{m-n+2}(2jt) + J_{m-n-2}(2jt)]\}], \quad (2)$$

where  $J_l(x)$  is the Bessel function of the first kind and  $l$ th order. Substituting Eq. (2) into Eq. (1) and using Laplace-transform techniques gives<sup>25</sup>

$$I_s(t) = I_s(0) e^{-2t/\tau} \left[ 1 - e^{-\alpha t} 4j \sin(k_g d/2) \int_0^t du J_1(4ju \sin(k_g d/2)) e^{\alpha(u^2 - t^2)^{1/2}} \right], \quad (3)$$

where  $d$  is the lattice constant in the grating direction.

This expression describes the time decay of the grating signal intensity in the presence of partially coherent exciton migration within the limitations of the model. Simpler expressions can be obtained from Eq. (3) for the limiting cases of purely coherent or purely incoherent exciton migration. The latter is the most important case since it is most commonly observed experimentally. The limiting conditions for this case are  $\alpha \rightarrow \infty$  as  $j^2/\alpha$  remains constant. The expression for the time dependence of the scattered-beam intensity becomes<sup>25</sup>

$$I_s(t) = I_s(0) \exp\{-2t[4F \sin^2(k_g d/2) + 1/\tau]\} \\ = I_s(0) e^{-Kt}, \quad (4)$$

where  $F$  is the transfer rate given by  $F = 2j^2/\alpha$ , and

$$K = 2[4F \sin^2(k_g d/2) + 1/\tau]. \quad (5)$$

In the continuum approximation which usually applies, the exciton motion is considered to be diffusive with the diffusion coefficient given by

$$D = Fd^2 = 2j^2 d^2/\alpha, \quad (6)$$

and so the decay rate in this case reduces to

$$K = 2(k_g^2 D + 1/\tau). \quad (7)$$

For the case of greater than nearest-neighbor ion-ion interaction,  $F/2\alpha \rightarrow 0$ , and Eq. (1) reduces to yield an exponential decay pattern

$$I_s(t) = I_s(0) \exp\{-2t[\alpha^2 + 16j^2 \sin^2(k_g d/2)]^{1/2} + \alpha + 1/\tau\} = I_s(0) e^{-Kt}, \quad (8)$$

TABLE I. Exciton-diffusion coefficient in  $\text{Nd}_x\text{La}_{1-x}\text{P}_2\text{O}_{14}$  crystals.

Excitation condition ( $T = 12.5$ K, $P_p = 0.18$ W)	$D$ ( $10^{-5}$ cm <sup>2</sup> s <sup>-1</sup> )	
	$x = 0.2$	$x = 1.0$
Vibronic	0.1	0.8
Enhanced vibronic	0.1	2.4
Direct	0.4	6.0*

\*Obtained from Eq. (6) with the short-time value of  $j$  and low value of  $\alpha$  found from fitting the data obtained using a pump power of 0.03 W.

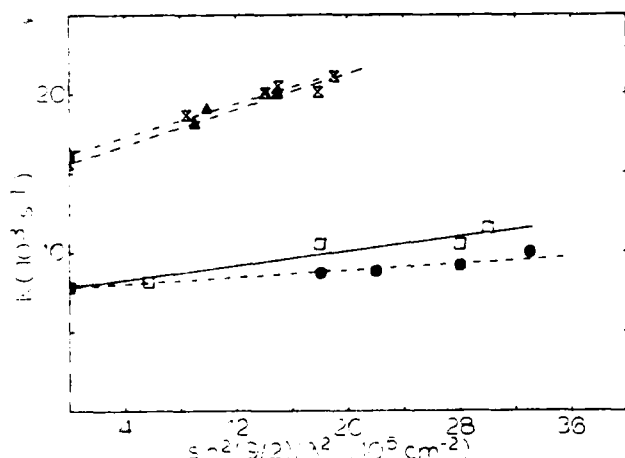


FIG. 6. Dependence of signal decay rate on crossing angle.  $\Delta$  and  $\times$  are for  $x = 1.0$  with  $\lambda_{exc} = 5699$  Å where the former corresponds to  $T = 23$  K and the latter to 300 K.  $\square$  and  $\bullet$  are for  $x = 0.2$  with  $\lambda_{exc} = 5749$  Å where the former corresponds to  $T = 28$  K and the latter to  $T = 300$  K.

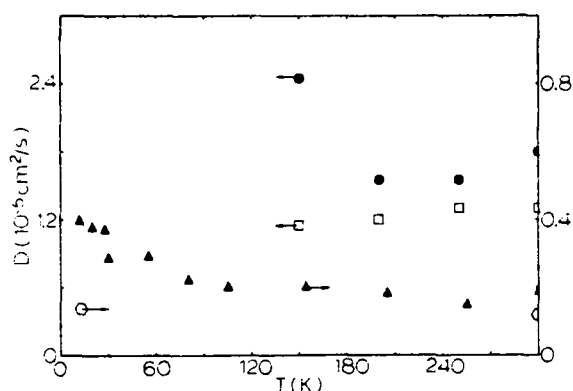


FIG. 7. Temperature dependence of the exciton diffusion coefficient for incoherent motion.  $\bullet$  and  $\square$  are for  $x=1.0$ ,  $\lambda_{\text{exc}}=5746$  Å, with laser-pump powers of 0.18 and 0.03 W, respectively.  $\triangle$  and  $\circ$  are for  $x=0.2$ ,  $\lambda_{\text{exc}}=5749$  Å, with laser-pump powers of 0.18 and 0.03 W, respectively.

where

$$K = 2\{[\alpha^2 + 16j^2 \sin^2(k_g d/2)]^{1/2} - \alpha + 1/\tau\}. \quad (9)$$

In the following work we use Eq. (3) in fitting the data to determine the microscopic interaction parameters  $j$  and  $\alpha$ . Then  $D$  is determined from Eq. (6) as a phenomenological parameter to characterize the macroscopic exciton migration. It must be emphasized that, in general, only the microscopic parameters have real physical meaning, whereas the parameter  $D$  only has an exact physical meaning within the limiting conditions discussed in deriving Eq. (6), and in other cases it should only be considered as a parameter used for comparative purposes to characterize the mobility of the excitons. An oscillatory grating decay pattern is predicted by Eq. (3), although an exact fit to the experimentally observed shape is not possible due to the limitations of the theoretical model as discussed in the following sections. The double exponential decay pattern shown in Fig. 5 cannot be theoretically described with a simple grating decay expression and is attributed to

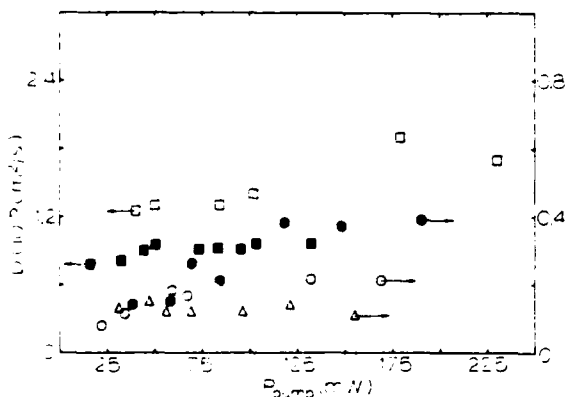


FIG. 8. Pump-power dependence of the exciton diffusion coefficient for incoherent motion.  $\bullet$  is for  $x=0.2$ ,  $T=12.5$  K, and  $\lambda_{\text{exc}}=5756$  Å.  $\circ$  is for  $x=0.2$ ,  $T=300$  K, and  $\lambda_{\text{exc}}=5718$  Å.  $\triangle$  is for  $x=0.2$ ,  $T=300$  K, and  $\lambda_{\text{exc}}=5749$  Å.  $\square$  is for  $x=1.0$ ,  $T=300$  K, and  $\lambda_{\text{exc}}=5743$  Å.  $\blacksquare$  is for  $x=1.0$ ,  $T=300$  K, and  $\lambda_{\text{exc}}=5688$  Å.

scattering from two types of gratings.

Figure 6 shows examples of results obtained by plotting the measured signal decay rate versus the crossing angle of the pump beams under the conditions giving single exponential decays. For each set of measurements the results vary as  $\sin^2(\theta/2)$ , and are extrapolated to independently measured values of  $2/\tau$ , as predicted by the simplified form of Eq. (3) given in Eq. (7). The diffusion coefficients found from fitting these data are listed in Table I. Their variations with excitation wavelength, temperature, and pump power are shown in Figs. 4, 7, and 8, respectively.

#### IV. CHARACTERISTICS OF THE EXCITON-DIFFUSION COEFFICIENT

Figure 4 shows three interesting features in the dependence of  $D$  on excitation wavelength. First, for direct excitation into the absorption-band edge of the  $x=1.0$  sample, nonexponential decay patterns are observed. This may be associated with partially coherent exciton migration and is discussed in the next section. The other two features are the enhancement of  $D$  after direct excitation of the  $x=0.2$  sample and after vibronic excitation  $110$   $\text{cm}^{-1}$  above the absorption-band edge for the  $x=1.0$  sample. These effects can be attributed to enhancement of the ion-ion-interaction processes giving rise to incoherent exciton migration. In the latter case, this enhancement is associated with the creation of phonons of energy of  $110$   $\text{cm}^{-1}$  in the vibronic excitation process. As seen in Fig. 1, this is the same energy as the crystal-field splitting of the  $^4F_{3/2}$  metastable level, and thus the generation of  $110$ - $\text{cm}^{-1}$  phonons will cause an increase in the population of excited ions in the upper component of this manifold. The verification of this nonequilibrium population distribution is given by the emission spectra shown in Fig. 9. As the excitation wavelength is scanned into the region of vibronic enhancement increased emission from the upper level ( $b$ ) of the metastable state can be distinctly seen. It is known from the absorption spectrum<sup>14</sup> that the transition between the  $b$  level and the ground state has a higher oscillator strength than the transition between the lower level ( $a$ ) and the ground state.

For both cases of interest here (direct excitation of the  $x=0.2$  sample and vibronic excitation of the  $x=1.0$  sample), the assumptions leading to Eq. (6) are valid, and thus this expression can be used for the diffusion coefficient where  $j$  contains the matrix element for the interaction,  $\alpha^{-1}=\tau$ , is the exciton scattering time, and  $d$  is the lattice spacing. The matrix element depends on the oscillator strengths and the spectral overlaps of the transitions involved in the interaction. The scattering time has different properties depending on the mechanism limiting the exciton mean free path.<sup>27,28</sup> Thus the diffusion coefficient will increase with an increase in the oscillator strengths of the transitions involved in the energy transfer. The lack of increase in  $D$  in the  $110$ - $\text{cm}^{-1}$  phonon vibronic excitation region for the  $x=0.2$  sample may be due to two reasons. The first is the generation of fewer phonons in the more lightly doped sample. The second is

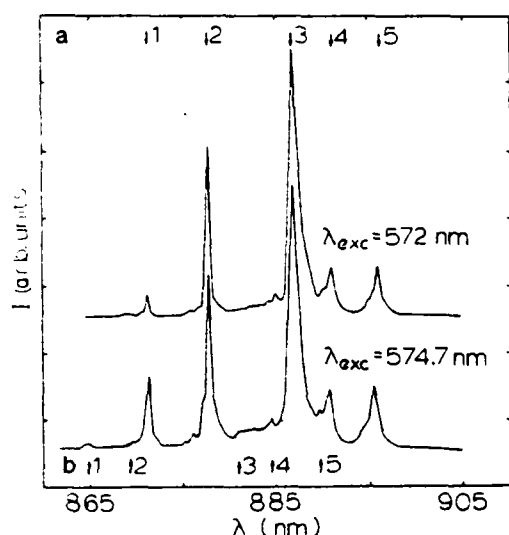


FIG. 9. Fluorescence emission of the  $x = 1.0$  sample at 12.5 K and a pump power of 0.18 W for two different excitation wavelengths.

the greater distance between  $\text{Nd}^{3+}$  ions which reduces the number of ions available for absorbing the  $110\text{-cm}^{-1}$  phonons.

The increase in  $D$  in the region of direct excitation for the  $x = 0.2$  sample can be explained through the properties of site selection. The excitation transitions are inhomogeneously broadened due to random perturbations in the local crystal-field sites of the  $\text{Nd}^{3+}$  ions. The narrow-line laser excitation selectively excites the subset of ions having transitions in resonance with the excitation wavelength. As the laser is scanned toward the center of a transition, the concentration of ions in the resonant subset increases. This results in an increase in  $D$  because of the increase in the density of lattice sites involved in the exciton migration. For the particular case of interest here, there is a significant amount of structure within the absorption band associated with the overlap of several different discrete transitions. This structure is partially reflected in the variation of  $D$  with excitation wavelength as seen in Fig. 4.

Figure 7 shows the variation of  $D$  with temperature for an excitation wavelength just on the edge of the resonant absorption region and different laser powers. For low laser power, the value of  $D$  for the  $x = 0.2$  sample remains constant as temperature is lowered from room temperature to 12.5 K, while for the  $x = 1.0$  sample  $D$  is constant between room temperature and about 100 K, below which nonexponential decay patterns are observed. At high laser powers the room-temperature values of  $D$  are approximately the same as those obtained with lower powers, but a significant increase in  $D$  occurs at lower temperatures. As shown in Fig. 7,  $D$  increases continuously as temperature is lowered to 12.5 K, where it reaches a value which is approximately equal to that obtained with lower powers exciting in the peak region of resonant excitation shown in Fig. 4. The  $x = 1.0$  sample again exhibits nonexponential behavior below about 100 K.

There are several different types of physical processes which can affect the temperature dependence of the diffusion coefficient. With reference to Eq. (9), these processes can be separated into two categories: those that change the group velocity  $v_g$  of the excitons, and those that alter the scattering time of the excitons. The fact that  $D$  is independent of temperature for low-pump-power conditions implies that the exciton-phonon scattering rate which contributes to  $t_s$  must be independent of temperature. For this to be true there must be weak coupling between the excitons and acoustical phonons which are present at low temperatures.<sup>28</sup> Strong scattering may occur from optical phonons, but at the temperatures of interest in this study, which range from slightly above to well below the Debye temperature, too few phonons of this type will be available for this to be an effective mechanism for limiting the exciton mean free path. Thus the major mechanism for exciton scattering must be lattice defects and boundaries which give a temperature-independent  $t_s$ . This implies that the parameter  $\alpha$  from Eq. (3) in this case is dominated by exciton-defect interactions instead of exciton-phonon interactions. Therefore the origin of the observed temperature dependence at high powers must be due to processes affecting  $v_g$ . These cannot be intrinsic changes in parameters such as transition oscillator strengths and spectral overlaps since they do not occur with low excitation power. The most probable explanation appears to be a power broadening combined with the site-selection characteristics of laser excitation. At low temperatures the laser excitation is just on the edge of the resonant transition and the low value of  $D$  is associated with the low concentration of the subset of ions excited. As power is increased this subset is saturated and ions in other subsets having Lorentzian wings overlapping the laser-excitation area become excited. This results in a power broadening of the excitation spectrum so that subsets having higher concentrations of ions take place in the exciton-migration process. Activating these higher-concentration subsets creates an increase in  $D$  similar to that observed when the laser excitation is scanned closer to the center of the resonant transition. As the temperature is raised, the spectral lines shift to lower energies so that the laser-excitation wavelength employed is no longer on the edge of the absorption transition, but rather is in the vibronic sideband area. In this case, saturation and power broadening is less effective and there is a decrease in the enhancement of  $D$ . Thus the observed temperature dependence of  $D$  for the  $x = 0.2$  sample at high laser powers is essentially associated with the temperature shift of the spectral line out of resonance with the laser-excitation wavelength. The same may be true for the  $x = 1.0$  sample, but it is difficult to tell since the region of nonexponential decay occurs as  $D$  begins to vary strongly with  $T$ .

Figure 8 shows the change in  $D$  with pump power. For the majority of the experimental conditions investigated  $D$  did not vary with pump power. However, as shown in the figure, for the  $x = 0.2$  sample at 12.5 K with excitation in the area of the resonant transition, the value of  $D$  increases from its normal low value to its resonantly enhanced value as power is increased. Coupled with the



characteristics described above, this can again be attributed to a power-broadening effect.

### V. CHARACTERISTICS OF EXCITON MIGRATION AFTER DIRECT EXCITATION

Next, we consider the results obtained on the  $x = 1.0$  sample at low temperatures for direct excitation into the absorption band. For low-laser-pump powers the oscillatory decay pattern shown in Fig. 5 is observed. The source of these oscillations is unknown and may be associated with several different types of physical processes. One possibility is the destruction of the grating through partially coherent exciton migration. In order to test this possibility, the results are analyzed in terms of a partially coherent exciton-migration model as discussed below. Oscillatory patterns of the grating decay are predicted by Eq. (3) from the model developed by Wong and Kenkre<sup>25</sup> for certain values of the parameters  $j$  and  $\alpha$ . However, it was not possible to obtain a close fit to the decay patterns observed experimentally using Eq. (3) for two reasons. First, the frequency of the observed oscillations decreases with time, whereas the predicted value is a constant given by  $4j \sin(k_g d/2)$ . Second, the magnitudes of the oscillation peaks increase with time before damping out, instead of showing a uniform exponential decrease with time as theoretically predicted. These variations are shown graphically in Fig. 10. Both quantities exhibit a similar exponential variation with time.

An important physical process which can affect these results is local heating. As the excited  $\text{Nd}^{3+}$  ions relax radiationlessly to the metastable state, phonons are given off which produce a thermal grating pattern which follows the population grating. This local heating can produce three effects. The first is the variation of the ion-ion-interaction parameter  $j$ . The magnitude of  $j$  can be enhanced both by thermal broadening of the interaction transitions and by thermally populating higher crystal-

field levels with stronger interaction properties. This enhancement of  $j$  should decrease with time as the phonons diffuse away from the locally heated region. This is confirmed by the results in Fig. 10 which show the oscillation frequency to decrease exponentially with the same decay time as the thermal grating, as discussed below.

The second possible effect of local heating is the modulation of the exciton scattering rate  $\alpha$ . As discussed in the preceding section, acoustic phonons do not appear to be effective in scattering the excitons so any variation of  $\alpha$  due to local heating would occur only if optical phonons are generated in the radiationless relaxation process. If this occurs,  $\alpha$  would decrease with time as the optical phonons diffuse away from the locally heated area. According to Eq. (3) this change in  $\alpha$  would decrease the rate of decay of the grating, but would not cause the peak magnitudes of the oscillations to increase with time. The latter may be associated with the decrease in  $j$  with time, which can be seen from Eq. (3) to cause an increase in signal intensity. Although it is tempting to interpret the results in this way, because of the similar time-dependent changes in the magnitude and frequency of the oscillations as shown in Fig. 10, there is no way to rule out the presence of more complex interference effects similar to those observed in coherent transient experiments.<sup>29</sup>

The third possible effect of local heating is probe-beam scattering from the thermal grating due to thermally induced changes in the refractive index. There is no evidence of contributions to the detected signal beam due to this effect at low-laser-pump powers where the oscillatory decay patterns are observed. However, at high pump powers the oscillations disappear and are replaced by a double exponential decay pattern. This can be attributed to simultaneous scattering of the probe beam from the thermal and population gratings. The slower decay rate is consistent with those extracted from the observed single exponential decay patterns of population gratings. Scattering from the thermal grating obscures the observation of any coherent oscillations which may be present. The decay pattern of the thermal grating is given by<sup>30</sup>

$$I_s(t) = I_s(0)e^{-2K_T t}, \quad (10)$$

where

$$I_s(0) = \frac{1}{4} I_p T_\lambda \left[ \frac{2\pi d'}{\lambda} \frac{dn}{dt} \hat{T} \right]^2$$

and

$$K_T = 16\pi^2 \sin^2(\theta/2) D_T / \lambda^2. \quad (11)$$

Here,  $\hat{T}$  is the spatial temperature amplitude,  $D_T$  is the thermal diffusion coefficient,  $d'$  is the sample thickness, and  $T_\lambda$  is the transmission. The thermal properties of neodymium pentaphosphate crystals<sup>31</sup> predict a value of  $D_T \leq 1 \times 10^{-2} \text{ cm}^2 \text{ s}^{-1}$ , which is consistent with the rough estimate of  $D_T = 3 \times 10^{-3} \text{ cm}^2 \text{ s}^{-1}$  obtained from the leading part of the double exponential decay.

Despite the complexities discussed above, it is possible to obtain numerical values for  $j$  from the observed frequencies of the oscillations and for  $\alpha$  from fitting the initial decay of the signal shape. This gives a value of

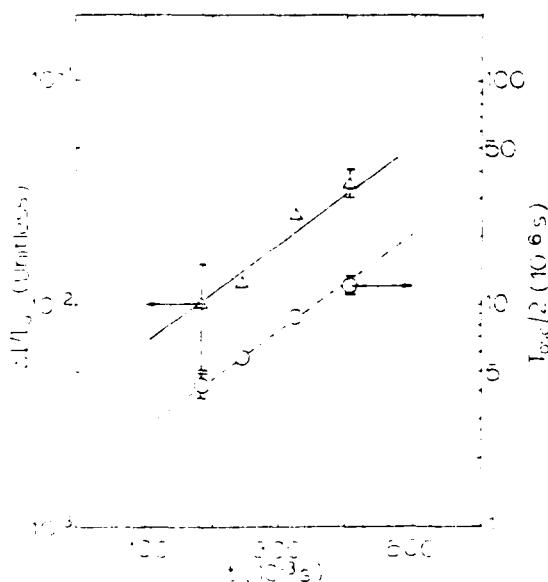


FIG. 10. Time dependence of the relative peak intensities and half-periods of the signal oscillations for  $x = 1.0$ ,  $T = 12.5$  K,  $P_p = 0.03$  W, and  $\lambda_{exc} = 5745$  Å.  $T_{osc}$  is the period of the oscillations.

$j = 1.2 \times 10^7 \text{ s}^{-1}$  at short times and a much smaller value at long times, as seen in Fig. 10. Unfortunately, Eq. (3) is much less sensitive to the parameter  $\alpha$ , and so the best fit to the experimental data can be obtained with any value of  $\alpha$  between  $10^4$  and  $3 \times 10^6 \text{ s}^{-1}$ . By using the experimentally obtained values of  $j$  and  $\alpha$  in Eq. (6), an estimate for the diffusion coefficient for partially coherent exciton motion can be obtained. This analysis, with the short-time value for  $j$  and the smallest value in the range of  $\alpha$ , is the origin of the point plotted in the direct excitation region in Fig. 4 for the  $x = 1.0$  sample and the value of  $D$  listed in Table I. Note that this value of  $D$  is much greater than the values obtained for vibronic excitation, but it decreases significantly for long-time values of  $j$  or higher values in the range of  $\alpha$ . The fact that partially coherent exciton migration was not observed for the  $x = 0.2$  sample implies the need for a high concentration of active ions to produce this type of motion. This can be attributed to the increase in the separation of  $\text{Nd}^{3+}$  ions which decreases the ion-ion-interaction rate.

## VI. POWER DEPENDENCE OF SCATTERING EFFICIENCY

Another experimental measurement of interest is the power dependence of the scattering efficiency. Although this does not contain specific information concerning exciton dynamics, it does provide additional information concerning the characteristics of the four-wave-mixing interaction in the material. This type of information is especially useful in the application of this technique to areas such as optical data processing or phase conjugation. The experimental beam geometry used for these types of applications is different from the geometry used for studying exciton dynamics,<sup>12,19,32-35</sup> and this leads to different mathematical expressions for the scattering efficiency. The detailed outline of the mathematical development of the expression for scattering efficiency is given in Ref. 12. An extension of this development is presented below, in which some of the simplifying assumptions made previously are no longer used. In addition, in previous work the mechanism of field coupling is modeled by analyzing the response of a two-level system to the perturbations of the electric fields, whereas in the treatment outlined below an attempt is made to better model the true multilevel nature of the material by treating the susceptibility as the linear combination of the susceptibilities of two two-level systems, which has been suggested previously.<sup>23</sup>

The polarization of the medium is given by  $P(E) = \epsilon_0 \chi(E)E$ , where  $\epsilon_0$  is the dielectric constant of free space and  $\chi(E)$  is the dielectric susceptibility. The electric field in the medium can be separated into two parts,  $E = E_0 + \Delta E$ , where the first part represents the contribu-

tion due to the two strong pump beams, while  $\Delta E$  is the contribution due to the weak probe and signal beams. The susceptibility of the multilevel system is approximated by

$$\chi = \frac{R}{R+1} \chi_1 + \frac{1}{R+1} \chi_2, \quad (12)$$

where  $\chi_1$  is the susceptibility of the system with the ions in the ground state and  $\chi_2$  is the susceptibility of the system with the ions in the metastable state.  $R = n_1/n_2$  where  $n_1$  is the number of ions in the ground state and  $n_2$  is the number of ions in the metastable state. Expanding the polarization to first order in  $\Delta E/E_0$  gives

$$P(E_0 + \Delta E) = \epsilon_0 e^{i\omega t} \sum_{i=1,2} R_i \chi_{0i}(E_0) \times \left[ E_0 + \Delta E - \frac{E_0 \Delta E + |E_0|^2 \Delta E}{I_{si} + |E_0|^2} \right], \quad (13)$$

where  $R_1 = R/(R+1)$ ,  $R_2 = 1/(R+1)$ , and

$$\chi_{0i}(E_0) = \frac{-2\alpha_{0i}}{k} \frac{I_{si}(i + \delta_i)(1 + \delta_i^2)}{I_{si} + |E_0|^2}. \quad (14)$$

Here, the  $i = 1, 2$  subscripts refer to the ions in ground and metastable states, respectively.  $\alpha_0$  is the line-center small-signal field-attenuation coefficient,  $\delta_i$  is the detuning parameter, and  $I_{s0}$  is the saturation intensity.

The key approximations used in deriving the expression for the four-wave-mixing signal intensity are  $\Delta E \ll E_0$ , that the pump and probe beams are undepleted in traveling through the medium (parametric approximation), and the slowly varying envelope approximation.<sup>12</sup> By using these approximations and solving the wave equation in the medium, expressions can be obtained for the magnitudes of the electric field components at different positions along the direction of propagation. The square of these amplitudes gives the beam intensities. The quantity of greatest interest is the scattering efficiency defined as the ratio of the signal-beam intensity as it leaves the sample to the probe-beam intensity as it leaves the sample in the absence of pump beams. The general expression for this is quite complicated<sup>18</sup> and it is usually more convenient to simplify the expression by making appropriate assumptions. For interpreting data on the power dependence of the scattering efficiency, the least restrictive assumption<sup>12</sup> to make is that the crossing angle of the pump beams is sufficiently large that the amplitudes of the pump and signal fields do not change appreciably over the distance  $\lambda_{cs} = \lambda/(1 - \cos\theta)$ . This approximation holds for the angles used in the experiments described here. The resulting expression for scattering efficiency is

$$\eta = \frac{\rho}{\zeta} \frac{\exp(\Psi_{E_0})}{(\cos^{-1}\theta - 1)^2} \left| \exp(-2\zeta_R L) + \exp(-2\zeta_R L \cos^{-1}\theta) - 2 \exp[-\zeta_R L(1 + \cos^{-1}\theta)] \cos[\zeta_I L(1 - \cos^{-1}\theta)] \right|, \quad (15)$$

where

Tunable solid state lasers are potentially important for various electro-optic systems applications. This has generated significant interest in developing new vibronic laser materials.<sup>1</sup> Most research in this area has centered around 3d transition metal ions.<sup>2-7</sup> However, it was shown recently that the spectroscopic properties of 4d and 5d transition metal ions make them possible candidates for vibronic lasers.<sup>8</sup> We report here the first tunable laser action in materials of this type using  $\text{RbCaF}_3:\text{Rh}^{2+}$  as an example.

The Rh-doped  $\text{RbCaF}_3$  crystal was grown by the Bridgman method in the OSU Crystal Growth Laboratory. Stoichiometric amounts of "Optran zone refined"  $\text{RbF}$  and  $\text{CaF}_2$ , and 0.1 at. % of 99.9 %  $\text{RhCl}_3$  were loaded in the platinum crucible. The growth run was done in a gettered Ar atmosphere. The host crystal has a cubic perovskite structure at room temperature<sup>9</sup> and the  $\text{Rh}^{2+}$  ions substitute for the  $\text{Ca}^{2+}$  ions with no charge compensation or size mismatch problems. Thus they occupy a site with  $O_h$  symmetry and six-fold coordination of the  $\text{F}^-$  ligands. The sample used for this work was cleaved from the boule along (100) planes and was about 1.0 cm in diameter and 0.45 cm thick. It contained a high density of scattering centers which do not greatly affect its use in spectroscopic studies but do produce significant losses which affect the accurate determination of laser parameters.

$\text{Rh}^{2+}$  ions have a  $4d^7$  electronic configuration. Previous spectroscopic investigations<sup>8</sup> have demonstrated the existence of strong charge transfer absorption bands in the near u.v. spectral region between 300 and 400 nm. The fluorescence emission can occur either from the Stokes shifted charge transfer transition

STIMULATED EMISSION AND TUNABLE GAIN FROM  $\text{Rh}^{2+}$  IONS  
IN  $\text{RbCaF}_3$  CRYSTALS

Richard C. Powell, Greg J. Quarles, Joel J. Martin,  
Charles A. Hunt and William A. Sibley  
Department of Physics, Oklahoma State University,  
Stillwater, OK 74078

Stimulated emission was detected in  $\text{RbCaF}_3:\text{Rh}^{2+}$  crystals through the observation of power dependent shortening of the fluorescence lifetime and narrowing of the emission band with a distinct threshold. In addition, single pass gain was observed to be tunable between about 700 and 720 nm.

wavelength. To test these materials as lasers, crystal growth techniques are being developed to incorporate an order of magnitude higher concentration of dopant ions in the host crystals. No evidence for emission from the low energy states with spin forbidden transitions was observed in these host crystals. There is some evidence that intersystem crossing to these levels is more efficient in oxide crystal hosts<sup>5</sup> and samples of this type are under preparation. These transitions should have millisecond lifetimes and be better suited for flashlamp pumped laser applications.

In conclusion, this work demonstrates the existence of both charge transfer and *d* level fluorescence emission from 4d and 5d transition metal ions in alkali halide crystals. It also shows how the *d* emission can be enhanced through thermal or radiation treatments resulting in broad fluorescence bands throughout the visible region of the spectrum. These materials may be useful in tunable laser applications if samples can be prepared with high enough levels of doping.

#### ACKNOWLEDGMENTS

This research was supported by the Office of Naval Research and the U.S. Army Research Office. The authors express their appreciation to L. E. Halliburton, Z. F. Al Shaieb, and G. D. Gilliland for technical assistance in this

work and to W. A. Sibley for helpful discussions concerning the interpretation of the results.

<sup>1</sup>G. A. Crosby, W. G. Perkins, and D. M. Klassen, *J. Chem. Phys.* **43**, 1498 (1965); K. W. Hipps, G. A. Merrell, and G. A. Crosby, *J. Phys. Chem.* **80**, 2232 (1976); J. N. Demas and G. A. Crosby, *J. Am. Chem. Soc.* **92**, 7262 (1970); **93**, 2841 (1971); W. A. Fordyce and G. A. Crosby, *ibid.* **21**, 1455 (1982).

<sup>2</sup>R. J. Watts and G. A. Crosby, *J. Am. Chem. Soc.* **94**, 2606 (1972); T. R. Thomas, R. J. Watts, and G. A. Crosby, *J. Chem. Phys.* **59**, 2123 (1973); R. J. Watts and D. Missimer, *J. Am. Chem. Soc.* **100**, 5350 (1978).

<sup>3</sup>W. Halper and M. K. DeArmond, *J. Lumin.* **5**, 225 (1972).

<sup>4</sup>F. Diomedei Camassei, L. Ancarani-Rossello, and F. Castelli, *J. Lumin.* **8**, 71 (1973).

<sup>5</sup>G. Blasse and A. Bril, *J. Electrochem. Soc.* **114**, 1306 (1967).

<sup>6</sup>C. D. Plint and A. G. Poulusz, *Mol. Phys.* **41**, 907 (1980).

<sup>7</sup>W. Holzapfel, H. Yersin, and G. Gliemann, *J. Chem. Phys.* **74**, 2124 (1981).

<sup>8</sup>S. Sugano, Y. Tanabe, and H. Kamimura, *Multiplets of Transition-Metal Ions in Crystals* (Academic, New York, 1970).

<sup>9</sup>A. E. Hughes, D. Pooley, H. U. Rahman, and W. A. Runciman, United Kingdom Atomic Energy Research Establishment Report R5604, 1967.

<sup>10</sup>A. S. Chakravarty, *Introduction to the Magnetic Properties of Solids* (Wiley, New York, 1980); see also S. Basu and A. S. Chakravarty, *Phys. Rev. B* **26**, 4327 (1982); **27**, 6495 (1983); V. P. Desai and A. S. Chakravarty, *Proc. Nucl. Phys. Solid State Phys. Symp.* **14c**, 563 (1972).

<sup>11</sup>M. G. Townsend, *J. Chem. Phys.* **41**, 3149 (1964).

#### IV. DISCUSSION AND CONCLUSIONS

Table I summarizes the spectral properties of the four samples studied in this work. The results indicate that the energy levels and dynamics of 4*d* and 5*d* transition metal ions in alkali halide crystals are quite complex. The spectra shown in Figs. 2, 4, 6, and 8 show structure indicating the existence of several different types of excited state levels and the significant changes observed with variations in temperature or different types of sample treatment indicate that the population dynamics of these levels is extremely sensitive to the local environment of the dopant ion and to lattice vibrations. The simplified configuration coordinate model proposed here is useful in interpreting some of the general spectral properties but additional, systematic studies are necessary to gain a complete understanding of these materials.

The identification of the peaks appearing in the near UV spectral region as being due to charge transfer transitions and the peaks in the visible spectral region as being due to spin-allowed *d-d* transitions is somewhat arbitrary. However these assignments are consistent with the observed strengths of these peaks in absorption and with their fluorescence lifetimes as compared to the values of these parameters generally measured for these different types of transitions. In addition, the overall spectral properties of these materials are similar to those observed for these ions in chemical complexes<sup>1-4</sup> where much work has been done to unambiguously identify the bands belonging to charge transfer and *d-d* transitions. A similar definitive assignment for the materials investigated here must await further experiments to provide conclusive information about the local structure and ligand interactions in these crystalline environments. Since the materials investigated here contain lattice vacancies necessary for charge compensation of the doping ions, and since radiation treatment is used to alter the spectral characteristics of the samples, it is important to note that the spectral properties of color centers in these alkali halide host crystals are well known,<sup>9</sup> and none of the reported spectral features are consistent with color center transitions.

The general location of the charge transfer bands is approximately the same for both of the 4*d* and both of the 5*d* transition metal ions in the two types of alkali halide host crystals. However, the exact peak positions, widths, and structure of these bands are different for each sample. For example, the ct bands in both KCl samples appear as two extremely narrow transitions, whereas in both KBr samples they are broader, single transitions. This demonstrates the general similarity of the host-impurity ion systems and the effects of different ligands on the spectral details. These results are again similar to those obtained on chemical complexes of these ions.<sup>1-4</sup>

For a detailed spectral analysis of these 4*d* and 5*d* transition metal ions in solids, it would be desirable to obtain specific information on the local crystal field at the site of the ions. In this case it is difficult to do for two reasons: the very weak *d-d* absorption transitions and the lack of complete crystal field diagrams for these types of ions. The Sugano-Tanabe diagrams such as those shown in Fig. 1 work well for ions of the 3*d* transition metal series but the increased spin-

orbit interaction causes a breakdown of the Russell-Saunders coupling for 4*d* and 5*d* ions. Although some work has been done in treating these types of ions in an intermediate coupling scheme,<sup>10</sup> complete crystal field energy level diagrams are not yet available for *d*<sup>6</sup>, *d*<sup>7</sup>, and *d*<sup>8</sup> ions. Therefore the diagrams in Fig. 1 are used to estimate the values of *Dq* but the results should be taken as only rough approximations to be used for comparative purposes. Considering that the broad, overlapping bands give only approximate values for the energy level positions, that the Stokes shifts of the *d* levels between absorption and emission are unknown, and that local charge compensation produces a strong deviation from an octahedral crystal field, it is not possible at the present time to do a more exact theoretical analysis of the specific systems investigated here.

Only the structure of the spectra of Pt<sup>2+</sup> and Rh<sup>2+</sup> in Figs. 2 and 4, respectively, is detailed enough to use in crystal field analysis. The free ion Racah parameters *B* for these ions are 699 cm<sup>-1</sup> for Pt<sup>2+</sup> and either 438 or 458 cm<sup>-1</sup> for Rh<sup>2+</sup> depending on the wave functions used in the calculations.<sup>10</sup> The structure in the spectra of Fig. 2 can be interpreted as due to transitions from the components of the <sup>3</sup>T<sub>2</sub> and <sup>3</sup>T<sub>1</sub> split by spin-orbit interaction and low symmetry contributions to the crystal field. The average value of the three lowest energy peak positions can be used as an estimate of the position of the <sup>3</sup>T<sub>2</sub> energy level in an octahedral field. Dividing this energy by *B* provides a value for *E/B* to use the crystal field diagram for *d*<sup>8</sup> ions shown in Fig. 1. This leads to a cubic crystal field parameter of *Dq* = 1188 cm<sup>-1</sup>. A similar analysis relating the structure of the Rh<sup>2+</sup> spectra to transitions from the split components of the <sup>2</sup>T<sub>1</sub> and <sup>2</sup>T<sub>2</sub> levels results in a value of *Dq* = 1230 cm<sup>-1</sup>. The only published value of *Dq* for Rh<sup>2+</sup> is 1600 cm<sup>-1</sup> in ZnWO<sub>4</sub> crystals.<sup>11</sup> This is consistent with the lower bound, Stokes shifted value of *Dq* given above. More accurate crystal field analysis of these materials requires samples with higher concentrations of doping ions so that the positions of *d-d* absorption transitions can be accurately determined.

The broad *d* emission bands for these materials are attractive possibilities for tunable laser applications. One critical parameter for this consideration is the peak emission cross section given by

$$\sigma_p = \{0.02\lambda_p^2\eta\}/\{n^2\Delta\nu\tau_f\}, \quad (4)$$

where  $\lambda_p$  is the peak wavelength of the emission band and  $\Delta\nu$  is its frequency half-width.  $\eta$  is the quantum efficiency. The latter quantity is difficult to determine accurately since no temperature dependent intensity quenching is observed in the temperature region studied. In calculating  $\sigma_p$ , a value of 0.5 was used for  $\eta$  which should be a good approximation in comparison to previous results on chemical complexes of these ions. The values obtained for the cross sections are listed in Table I and are all of the order of 10<sup>-21</sup> cm<sup>2</sup> which is similar to  $\sigma_p$  for 3*d* ion transition metal vibronic laser materials. The lifetimes of the order of tens of microseconds indicate that fast laser pumping would be better than flash-lamp pumping of these materials. This type of pumping should be very efficient since these materials have strong charge transfer absorption band coincident with the Nd laser

where the  $W_i$  represent the pumping rates, the  $\tau_i$  are the fluorescence lifetimes, and  $\beta$  is the radiationless relaxation rate between the two sets of levels. These equations can be solved simultaneously and the resulting expressions for the time dependences of the excited state populations are directly proportional to the measured fluorescence intensities. This procedure provides equations for fitting the experimental data on the temperature variations of the fluorescence lifetimes and relative intensities.

The temperature dependencies of the ratios of fluorescence intensities at a specific time after the excitation pulse can be expressed as

$$I_d/I_{ct} = A + B \exp(-\Delta E_1/kT). \quad (2)$$

The temperature independent coefficients  $A$  and  $B$  contain factors describing the ratios of the initial pumping rates and the radiative decay rates of the two types of levels as well as a correction factor for the detection sensitivity in the different spectral ranges of the two types of emissions and an exponential time factor. The exponential temperature dependence comes from expressing the parameter  $\beta$  as the ratio of the rates of absorption and emission of phonons coupling the charge transfer and  $d$  states.

The solid line in Fig. 3 represents the best fit to the temperature dependent intensity data for KBr:Pt using Eq. (2) and treating  $A$ ,  $B$ , and  $\Delta E_1$  as adjustable parameters. This fit was obtained for  $A = 1.69$ ,  $B = 240$ , and  $\Delta E_1 = 398 \text{ cm}^{-1}$ . The simple model used here can not explain the peak in the intensity ratios at 250 K which is associated with the redistribution of energy among the several different ct and  $d$  levels which are present in the sample.

Similar good fits to the observed temperature dependences of the intensity ratios could not be obtained for the other samples. In the case of KBr:Rh the peak at 250 K is too dominant to allow the simplified model to be a good approximation. For KCl:Ir the strong increase with temperature begins to occur near 300 K. This indicates a higher value of  $\Delta E_1$  but the measurements do not extend to high enough temperatures to obtain an accurate theoretical fit. The temperature dependence of the intensity ratios for KCl:Ru is the opposite of that predicted by the simple model used here which is probably due to redistribution of the energy among different types of charge transfer states with different radiative emission rates. Some evidence for this can be seen in the spectra shown in Fig. 8.

The temperature dependencies of the fluorescence lifetimes of the  $d$  emission bands can be interpreted by a model assuming the presence of two  $d$  levels with different intrinsic decay times  $\tau_{LT}$  and  $\tau_{HT}$  separated by an energy barrier,  $\Delta E_2$ , and connected by efficient radiationless processes so that the populations of the levels are in thermal equilibrium. For this situation the observed fluorescence decay time will be the weighted combination of the two intrinsic decay times

$$\tau = \{1 + G \exp(-\Delta E_2/kT)\} / \{1/\tau_{LT} + (1/\tau_{HT})G \exp(\Delta E_2/kT)\}, \quad (3)$$

where  $G$  is the ratio of the degeneracies of the two states. This equation gives a reasonably good fit to the lifetime data for all four samples as shown in Figs. 3, 5, 7, and 9. The solid lines are obtained treating  $G$ ,  $\Delta E_2$ , and the two intrinsic lifetimes as adjustable parameters. The numerical results for these parameters are listed in Table I. The values obtained are physically reasonable except for the value of  $G = 50$  for KBr:Pt. This high value indicates that the structure of the  $d$  manifold of levels is more complex than the simple model employed here.

The changes in sample properties after various types of treatments are associated with the defect structure of the material. When divalent ions are incorporated in alkali halide crystals, charge compensation is necessary. Usually this takes the form of alkali ion vacancies which are not necessarily located close to the dopant ions. These defects are mobile and aging, annealing, and radiation treatments can cause the formation and redistribution of defect centers. The spectral changes observed for the samples studied here due to these types of treatments can be attributed to the effects of the interaction of the dopant ion with near neighbor lattice defects. The position and shape of the charge transfer potential well is especially sensitive to changes in the ligand structure in the environment of the transition metal ion. Shifting this potential well can significantly change the efficiency of radiationless transfer from the charge transfer state to the  $d$  levels. The spectra shown in Figs. 3 and 5 indicate that local charge compensation greatly enhances the crossover to the  $d$  levels. Similar results were observed on other samples such as KCl:Ru. However, no significant changes in the spectrum were observed in a sample of KMgF<sub>3</sub>:Rh after annealing. This is due to the fact that the defect mobility in KMgF<sub>3</sub> crystals is greatly reduced compared to alkali halides.

TABLE I. Spectroscopic parameters.

Parameter	Crystal			
	KCl:Ru (4d <sup>6</sup> )	KBr:Rh (4d <sup>7</sup> )	KCl:Ir (5d <sup>7</sup> )	KBr:Pt (5d <sup>8</sup> )
$\lambda_p$ (nm)	588	650	636	660
$\Delta\lambda$ (nm)	268	270	226	216
$\tau_{ct}$ ( $\mu$ s)	46	25	35	23
$\sigma_p$ ( $10^{-21} \text{ cm}^2$ )	1.16	2.10	2.50	3.27
$\Delta E_1$ ( $\text{cm}^{-1}$ )	275	355	350	700
$\tau_{LT}$ ( $\mu$ s)	99	80	78	110
$\tau_{HT}$ ( $\mu$ s)	19	13	12.4	13.7
$G$	5	3.75	2.5	50

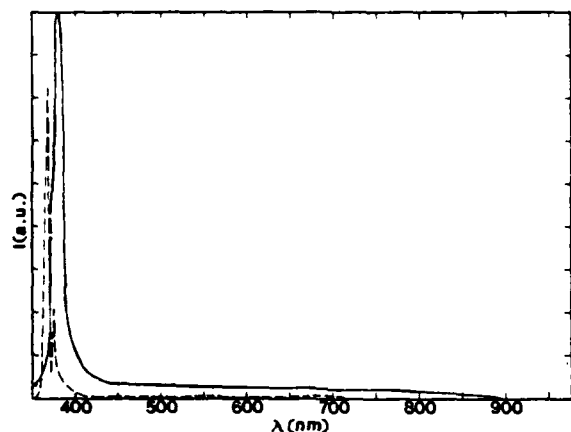


FIG. 8. Fluorescence spectra of KCl:Ru after pulsed  $N_2$  laser excitation at 10 K (---) and room temperature (—) of a freshly cleaved, unirradiated sample.

dependencies of the lifetimes and relative intensities for KCl:Ir $^{2+}$  crystals. The results are similar to those observed in the other samples except that the  $d$  emission intensity is much weaker in comparison to the charge transfer bands.

#### D. KCl:Ru $^{2+}$

Figures 8 and 9 show the results obtained for KCl:Ru $^{2+}$  crystals. This case shows the weakest  $d$  emission compared to the charge transfer emission at room temperature. Unlike the other samples, this material shows a slight increase in the intensity ratios as temperature is lowered.

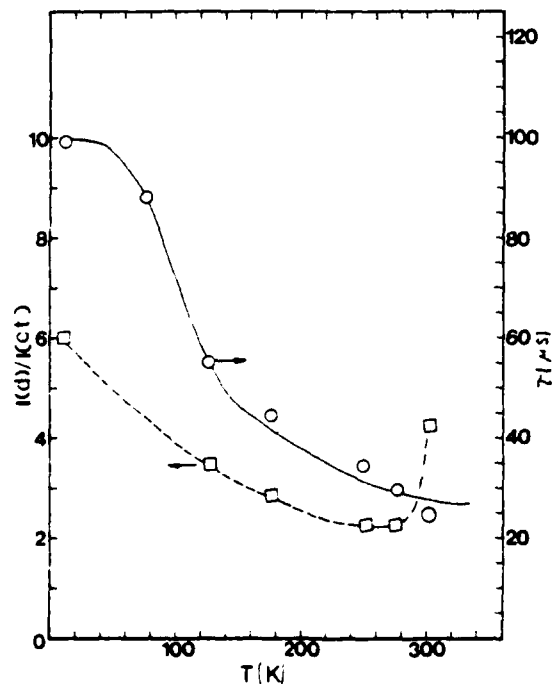


FIG. 9. Temperature dependences of the fluorescence lifetime of the  $d$  emission and the ratios of the integrated intensities of the  $d$  and charge transfer emission for KCl:Ru. See the text for explanation the theoretical curve.

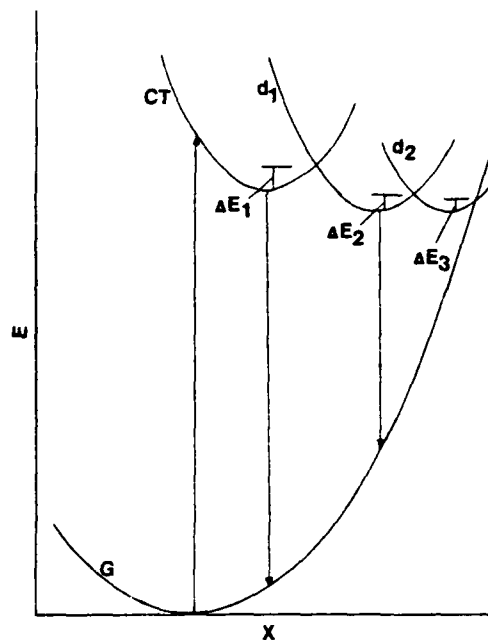


FIG. 10. Simplified single configuration coordinate model for interpreting the experimental results.

### III. INTERPRETATION

The spectroscopic results described in the last section are quite complex and obviously involve dynamic interactions among several different types of charge transfer and  $d$  levels. The exact details of these interactions can not be determined without more extensive experimental results but the general spectroscopic features can be interpreted in terms of the simplified single configuration coordinate model shown in Fig. 10. The manifold of crystal field split charge transfer states are represented by one potential curve and the system of  $d$  levels is represented by one ground state and two excited state potential curves. At low temperatures the absorption transition is followed by radiationless relaxation to the bottom of the charge transfer potential well. The majority of the emission occurs from this relaxed state. As temperature is raised, higher energy vibrational levels of the charge transfer state are occupied and when an energy  $\Delta E_1$  is reached, crossover occurs to the higher energy  $d$  level. Transfer to the lower  $d$  level occurs at a temperature consistent with  $\Delta E_2$  and fluorescence emission occurs from the bottom of both the  $d$  potential wells. At temperatures above that consistent with an energy  $\Delta E_3$  radiationless decay to the ground state occurs. The temperature dependencies of the relative intensities and lifetimes depend on the energies  $\Delta E_1$ ,  $\Delta E_2$ , and  $\Delta E_3$ .

The intensity of the fluorescence emission from each level is proportional to the concentration of ions in the level,  $n_i$ . Representing all of the charge transfer states by one level and all of the excited  $d$  states by one level, the rate equations of the excited state populations are

$$\begin{aligned} \frac{dn_{ct}}{dt} &= W_{ct} - \tau_{ct}^{-1}n_{ct} - \beta n_{ct}, \\ \frac{dn_d}{dt} &= W_d - \tau_d^{-1}n_d + \beta n_{ct}, \end{aligned} \quad (1)$$



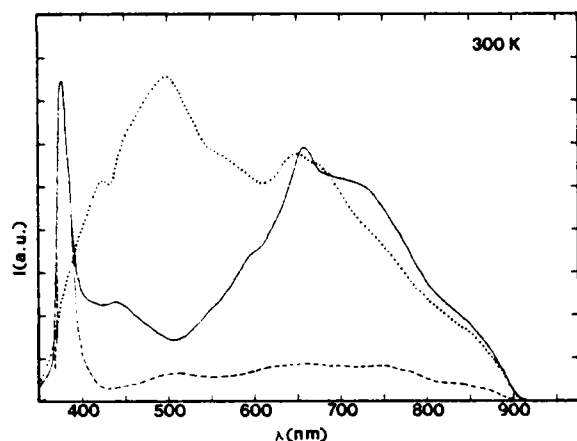


FIG. 4. Fluorescence spectra of KBr:Rh at 300 K after pulsed  $N_2$  laser excitation. --- untreated sample; — irradiated sample; ... annealed sample.

continues to increase with temperature. The solid lines in the figure represent the best fits to the data using the model discussed below.

### B. KBr:Rh $^{2+}$

Figure 4 shows the emission spectra of KBr:Rh $^{2+}$  at room temperature for an as-grown sample, a crystal that has been exposed to a radiation dose of  $10^5$  rad of electrons, and a sample that was annealed by heating to 600 °C and fast cooling on a copper block. Again both charge transfer and spin allowed doublet  $d$  emission bands are observed. Both radiation and heat treatment enhance the  $d$  emission with respect to the charge transfer emission. The former treatment tends to preferentially increase the lower energy  $d$  band

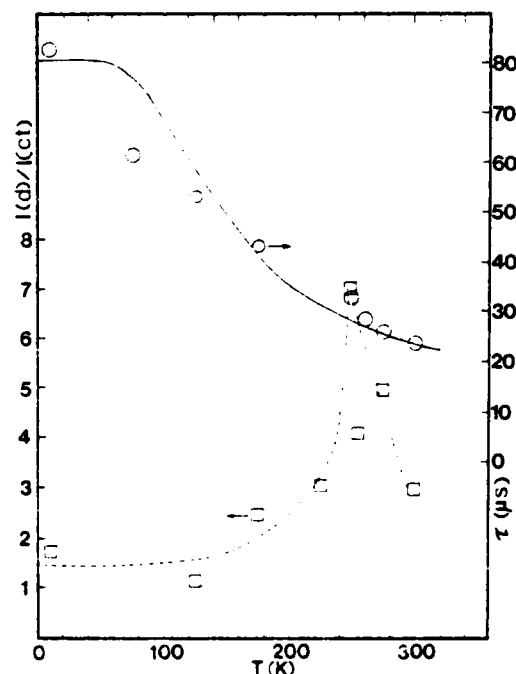


FIG. 5. Temperature dependencies of the fluorescence lifetime of the  $d$  emission and the ratios of the integrated intensities of the  $d$  and charge transfer emissions for KBr:Rh. See the text for explanation of the theoretical curve.

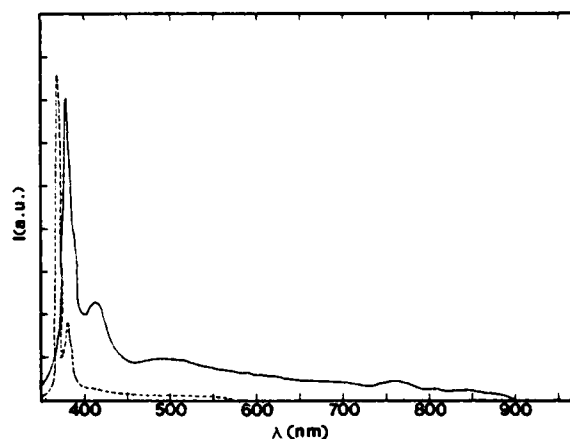


FIG. 6. Fluorescence spectra of KCl:Ir after pulsed  $N_2$  laser excitation at 10 K (---) and room temperature (—) of a freshly cleaved, unirradiated sample.

while the latter preferentially increases the higher energy  $d$  band.

Figure 5 shows the temperature dependences of the relative intensities and fluorescence lifetime of the  $d$  emission. The trends are similar to those discussed above for Pt except that the intensity ratios show a more pronounced maximum near 250 K. The solid line represents the theoretical fit discussed below while the dashed line simply shows the general trend of the intensity ratios. Again the lifetime of the charge transfer emission is less than 20 ns and no change with temperature could be observed within the time resolution of our instrumentation.

### C. KCl:Ir $^{2+}$

Figures 6 and 7 show the spectra and temperature de-

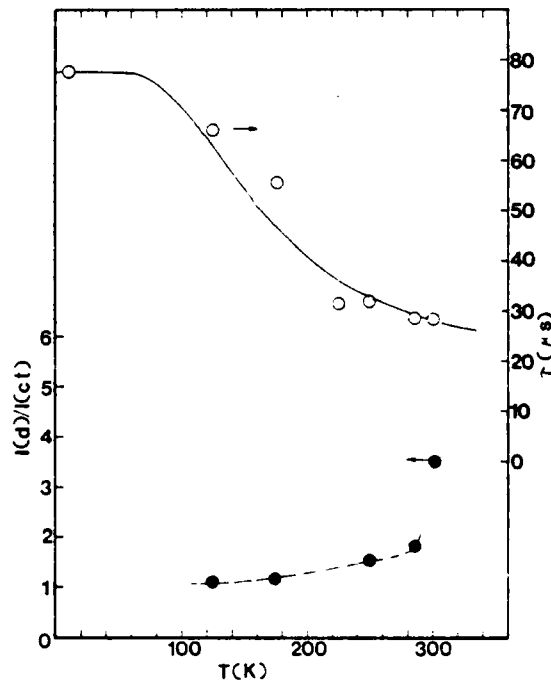


FIG. 7. Temperature dependencies of the fluorescence lifetime of the  $d$  emission and the ratios of the integrated intensities of the  $d$  and charge transfer emissions for KCl:Ir. See the text for explanation of the theoretical curve.

## B. Experimental apparatus

Measurements of the fluorescence spectra and lifetimes were made using a pulsed nitrogen laser for excitation. This provided a pump pulse at 337.1 nm which was about 10 ns in duration and 1 Å in half-width. The samples were mounted in a cryogenic refrigerator capable of controlling the temperature between about 10 K and room temperature. The fluorescence was focused onto the entrance slit of a 1 m monochromator with the slits set for 20 Å resolution. The signal was detected by a cooled RCA C31034 photomultiplier tube and analyzed by a boxcar integrator before being displayed on a strip chart recorder.

To measure lifetimes the window of the boxcar was set in the scanning mode with a time resolution of about 50 ns. The fluorescence spectra were recorded at fixed times after the excitation pulse. Both fast and slow emission bands were observed in these materials and this time-resolved fluorescence technique can be used to emphasize either one of these two types of emissions. Examples of the observed spectra are presented in the following section. Because of the large difference in lifetimes, it is difficult to show both types of emissions on the same spectra. To overcome this problem, the spectra shown in the figures were obtained at 50  $\mu$ s after the laser pulses using a 1 M  $\Omega$  load resistance which distorts the timing of the spectra and allows both types of bands to be easily seen. Thus the absolute magnitudes of the spectral bands in these figures are not meaningful but the relative changes in intensities between samples or with different experimental conditions are accurate.

In the absorption spectra of these samples, it was not possible to detect any bands due to the doping ions. Only the normal absorption edges of the host crystals near 250 nm were observed. Excitation spectra taken with a xenon lamp and 1/4 m monochromator showed the major absorption in all of the samples to occur as a triple peaked band between about 280 and 400 nm. The Ir doped sample exhibited additional excitation bands in the 500 to 600 nm region of the spectrum.

A 2 MeV van de Graaff accelerator was used for radiation treatment of the samples.

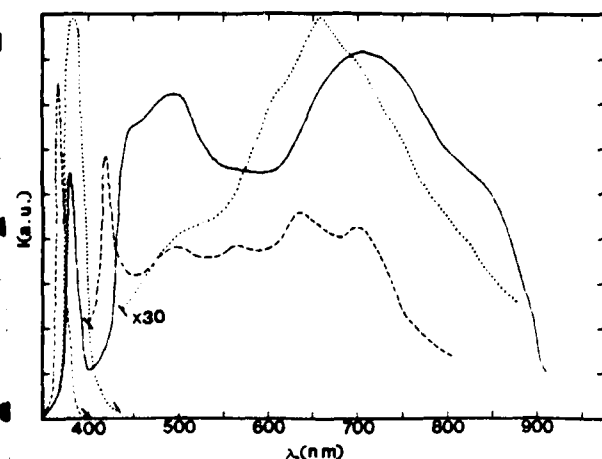


FIG. 2. Fluorescence spectra of KBr:Pt after pulsed  $N_2$  laser excitation. — 300 K, freshly cleaved samples; --- 10 K freshly cleaved sample; ... 300 K aged sample. (All samples unirradiated.)

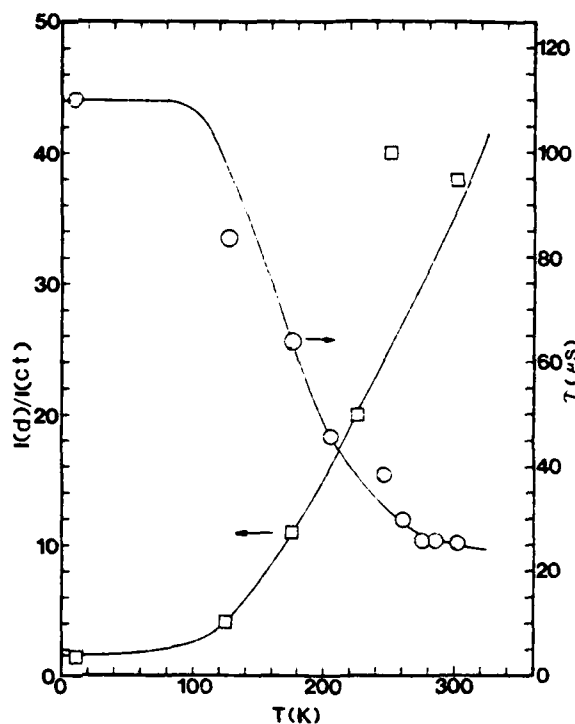


FIG. 3. Temperature dependences of the fluorescence lifetime of the  $d$  emission and the ratios of the integrated intensities of the  $d$  and charge transfer emission for KBr:Pt. See the text for explanation of the theoretical lines.

## II. EXPERIMENTAL RESULTS

### A. KBr:Pt<sup>2+</sup>

Figure 2 shows the fluorescence spectra obtained for Pt<sup>2+</sup> in KBr crystals at room temperature and 10.2 K for a freshly cleaved surface and at room temperature for an aged surface. There are two distinct spectral regions: the relatively narrow band at 380 nm and the broad, structured band between about 425 and 850 nm. The former has a fluorescence lifetime of less than 20 ns independent of temperature and is attributed to emission from the charge transfer state, whereas the latter band has a temperature dependent lifetime in the microsecond time regime and is attributed to transitions between triplet  $d$  levels. The structure in the broadband shows the presence of several different  $d$  to  $d$  transitions split into two major bands. The relative intensities of the fluorescence band show that the fraction of the total emission occurring in the  $d$  to  $d$  transitions decreases with respect to that originating from the charge transfer state as the sample surface ages. At the same time the lower energy  $d$  emission band increases relative to the higher energy  $d$  emission band. These relative intensities also vary with temperature with the  $d$  to  $d$  emission relative to the charge transfer emission decreasing as temperature is lowered.

Figure 3 shows the temperature dependencies of the emission intensities and lifetime for this sample. The ratio of the total emission from the  $d$  levels to that of the charge transfer level increases with temperature reaching a maximum at 250 K. Although both major  $d$  emission bands increase in intensity with temperature up to 250 K, the higher energy band increases more rapidly. Above this temperature the higher energy band decreases while the low energy band

# Spectroscopy of 4d and 5d transition metal ions in alkali halide crystals

Richard C. Powell, Robert H. Schweitzer, Joel J. Martin, George E. Venikouas, and Charles A. Hunt

Physics Department, Oklahoma State University, Stillwater, Oklahoma 74078

(Received 6 January 1984; accepted 2 April 1984)

The fluorescence spectra and lifetimes of divalent Rh, Ru, Pt, and Ir ions in alkali halide crystals are measured using pulsed nitrogen laser excitation. Emission from both the charge transfer states and the excited *d* levels is observed. Changes in the relative intensities and lifetimes are monitored as a function of temperature, annealing, and radiation treatment. The results are interpreted in terms of the possible application of these materials for tunable solid state lasers.

## I. INTRODUCTION

There is currently a significant amount of interest in identifying new materials for use as tunable solid state lasers. Thus far most of the research and development in this area has involved either 3d transition metal ions such as Cr, Co, and Ni in oxide hosts or color centers in alkali halide and oxide crystals. Another class of ions which may be useful in this application is the 4d and 5d transition metals and research is underway to survey the spectroscopic properties of these ions in different types of host crystals. This paper describes the results obtained on crystals of  $\text{KCl:Ru}^{2+}$ ,  $\text{KBr:Rh}^{2+}$ ,  $\text{KCl:Ir}^{2+}$ , and  $\text{KBr:Pt}^{2+}$ . Fluorescence intensities and lifetimes were measured as a function of temperature, annealing, and radiation treatment. The results are interpreted in terms of emission from both charge transfer states and excited *d* levels.

Extensive literature exists on the spectroscopic properties of 3d and 4d transition metal ions in chemical complexes.<sup>1-4</sup> Systematic studies have been performed on the spectral changes that occur with changes in the ligands and the structure of the chemical complex. Emission has been observed from charge transfer states, spin-allowed transitions from excited *d* levels, and spin-forbidden transitions from excited *d* levels. The two series of ions exhibit a variety of broad emission bands throughout the visible region of the spectrum. However very little work has been done on these ions as dopants in single crystals.<sup>5-7</sup> The goal of this work is to begin to understand the properties of 4d and 5d transition metal ions in crystals and to develop techniques for enhancing *d* level emission compared to charge transfer emission.

### A. Samples

The crystals used in this project were grown by the Czochralski method of pulling from the melt. All growth was carried out in a dry nitrogen atmosphere in an internally heated furnace. Fisher Scientific reagent grade KBr and KCl were used for the host starting materials. The  $\text{PtCl}_2$  (99.9%),  $\text{RhCl}_3$  (99.9%),  $\text{IrCl}_3$  (99.95%), and  $\text{RuCl}_3$  (99.9%) anhydrous dopants were obtained from the Gallard-Schlesinger Co. The melts were contained in high purity alumina crucibles. After the crystals were grown, they were slowly cooled to room temperature over a 16 h period. Samples were cleaved from the boule perpendicular to the growth axis so as to ensure uniform doping.

Example crystals were analyzed with an EDXA attachment on an electron microscope to determine the concentration and distribution of the doping ions and to detect the presence of other impurities. In addition, electron paramagnetic resonance measurements were made on example samples to determine the valence of the optically active ions. The results of these measurements indicate that the dopant ions are distributed uniformly at concentrations of around 200 ppm. No significant amount of other optically active impurities or other valence states of the dopant ions were detected.

The ions of interest in this study are  $\text{Rh}^{2+}(4d^6)$ ,  $\text{Ru}^{2+}(4d^6)$ ,  $\text{Pt}^{2+}(5d^8)$ , and  $\text{Ir}^{2+}(5d^7)$ . Partial crystal field energy level diagrams for these *d<sup>n</sup>* electron configurations<sup>8</sup> are shown in Fig. 1. The figure is restricted to the lowest sets of energy levels in the strong crystal field region since this area contains the transitions of interest in interpreting the observed spectra. For each case there is a low lying set of excited states which can give rise to spin-forbidden transitions to the ground state and a higher set of states which can produce spin-allowed transitions to the ground state. Interactions between the transition metal ion and its ligands result in charge transfer states which lie at higher energies with respect to the *d* levels shown in the figure.

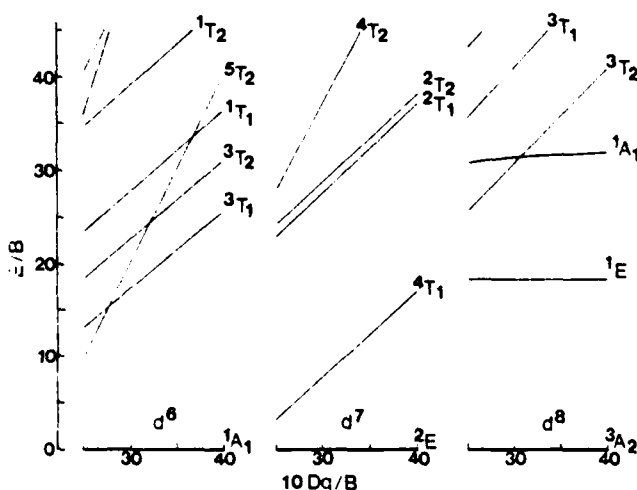


FIG. 1. Portions of crystal field energy level diagrams for  $d^6$ ,  $d^7$ , and  $d^8$  ions in octahedral environments.

### III. DEVELOPMENT OF NEW VIBRONIC LASER MATERIALS

A significant amount of time and effort in this thrust area was spent developing crystal growth methods for doping various host crystals with 4d and 5d transition metal ions. After this was accomplished, a spectroscopic survey was performed on a wide variety of different ions of these classes in different host materials.  $\text{RbCaF}_3:\text{Rh}^{2+}$  was identified as the best candidate for a tunable vibronic laser material. A good optical quality single crystal of this material was synthesized and its laser properties were investigated. Tunable laser action was observed around 710 nm with a high peak cross section. These results are described in the first three manuscripts of this section.

The third manuscript also contains a brief description of laser Raman microprobe results on  $\text{Al}_2\text{O}_3:\text{Ti}^{3+}$  crystals which helped in the identification and elimination of scattering centers in this important type of tunable vibronic laser material.

The fourth manuscript presents a summary of our analysis of  $\text{Mn}_2\text{SiO}_4$  as a possible tunable laser material.

The final manuscript of this section describes the first observation of four-wave mixing in alexandrite crystals.  $\text{BeAl}_2\text{O}_3:\text{Cr}^{3+}$  is an important tunable vibronic laser material and the third order nonlinear optical properties observed in this work may be important in determining the characteristics of the material in high power laser operation. The mathematical background developed in the Appendix is helpful in analyzing some of these results.

- <sup>1</sup>V. M. Kenkre, in *Exciton Dynamics in Molecular Crystals and Aggregates*, edited by G. Hohler (Springer, Berlin, 1982), p. 1.
- <sup>2</sup>C. B. Harris and D. S. Zwemer, *Ann. Rev. Phys. Chem.* **29**, 473 (1978).
- <sup>3</sup>R. Silbey, *Ann. Rev. Phys. Chem.* **27**, 203 (1976).
- <sup>4</sup>N. F. Mott, *Adv. Phys.* **16**, 49 (1967).
- <sup>5</sup>J. Koo, L. R. Walker, and S. Geschwind, *Phys. Rev. Lett.* **38**, 858 (1977); S. Chu, H. M. Gibbs, S. L. McCall, and A. Passner, *Phys. Rev. Lett.* **45**, 1715 (1980).
- <sup>6</sup>K. Godzik and J. Jortner, *J. Chem. Phys.* **38**, 227 (1979); *Chem. Phys. Lett.* **63**, 3 (1979).
- <sup>7</sup>G. Huber, in *Current Topics in Materials Science*, edited by E. Kaldis (North-Holland, Amsterdam, 1980), Vol. 4, p. 1.
- <sup>8</sup>J. M. Flaherty and R. C. Powell, *Phys. Rev. B* **19**, 32 (1979).
- <sup>9</sup>R. C. Powell, D. P. Neikirk, J. M. Flaherty, and J. G. Gualtieri, *J. Phys. Chem. Solids* **41**, 345 (1980).
- <sup>10</sup>M. M. Broer, D. L. Huber, W. M. Yen, and W. K. Zwickler, *Phys. Rev. Lett.* **49**, 394 (1982).
- <sup>11</sup>R. M. Shelby and R. M. Macfarlane, *Phys. Rev. Lett.* **45**, 1098 (1980).
- <sup>12</sup>C. M. Lawson, R. C. Powell, and W. K. Zwickler, *Phys. Rev. Lett.* **46**, 1020 (1981); *Phys. Rev. B* **26**, 4836 (1982); J. K. Tyminski, R. C. Powell, and W. K. Zwickler, in *Lasers '82*, edited by R. C. Powell (STS, McLean, Virginia, 1983), p. 105. R. D. Plattner, W. W. Kruhler, W. K. Zwickler, T. Kovats, and S. R. Chinn, *J. Cryst. Growth* **49**, 274 (1980).
- <sup>14</sup>H. G. Danielmeyer and H. P. Weber, *IEEE J. Quant. Electron.* **QE-8**, 805 (1972).
- <sup>15</sup>H. G. Danielmeyer, in *Festkörperprobleme*, edited by H. J. Queisser (Pergamon, New York, 1975), Vol. 15, p. 253.
- <sup>16</sup>H. P. Weber, *Opt. Quantum Electron.* **7**, 431 (1975).
- <sup>17</sup>D. M. Pepper, *Opt. Eng.* **21**, 156 (1982).
- <sup>18</sup>J. K. Tyminski, Ph.D. dissertation, Oklahoma State University, 1983.
- <sup>19</sup>H. Kogelnik, *Bell System Tech. J.* **48**, 2909 (1969).
- <sup>20</sup>M. D. Fayer, in *Spectroscopy and Excitation Dynamics of Condensed Molecular Systems*, edited by V. M. Agranovich and R. M. Hochstrasser (North-Holland, Amsterdam, 1983), p. 185; J. R. Salcedo, A. E. Siegman, D. D. Dlott, and M. D. Fayer, *Phys. Rev. Lett.* **41**, 131 (1978).
- <sup>21</sup>H. J. Eichler, J. Eichler, J. Knof, and Ch. Noack, *Phys. Status Solidi A* **52**, 481 (1979).
- <sup>22</sup>P. F. Liao, L. M. Humphrey, D. M. Bloom, and S. Geschwind, *Phys. Rev. B* **20**, 4145 (1979).
- <sup>23</sup>P. F. Liao and D. M. Bloom, *Opt. Lett.* **3**, 4 (1978).
- <sup>24</sup>D. S. Hamilton, D. Heiman, J. Feinberg, and R. W. Hellwarth, *Opt. Lett.* **4**, 124 (1979).
- <sup>25</sup>Y. M. Wong and V. M. Kenkre, *Phys. Rev. B* **22**, 3072 (1980).
- <sup>26</sup>V. M. Kenkre, *Phys. Rev. B* **18**, 4064 (1978).
- <sup>27</sup>V. M. Agranovich and M. D. Galanin, *Electronic Excitation Energy Transfer in Condensed Matter* (North-Holland, Amsterdam, 1982).
- <sup>28</sup>V. M. Agranovich and Yu. V. Konobeev, *Fiz. Tverd. Tela (Leningrad)* **5**, 1373 (1963) [*Sov. Phys.—Solid State* **5**, 999 (1966)]; **6**, 831 (1964) [**6**, 644 (1964)]; *Phys. Status Solidi* **27**, 435 (1968); *Opt. Spectrosc.* **6**, 155 (1959).
- <sup>29</sup>A. Szabo and M. Kroll, *Opt. Lett.* **2**, 10 (1978).
- <sup>30</sup>H. Eichler and H. Stahl, *J. Appl. Phys.* **44**, 3429 (1973); H. Eichler, G. Salje, and H. Stahl, *ibid.* **44**, 5383 (1973).
- <sup>31</sup>S. R. Chinn and W. K. Zwickler, *J. Appl. Phys.* **49**, 5892 (1978).
- <sup>32</sup>A. Yariv and D. M. Pepper, *Opt. Lett.* **1**, 16 (1977).
- <sup>33</sup>A. E. Seigmen, *J. Opt. Soc. Am.* **67**, 545 (1977).
- <sup>34</sup>R. L. Abrams and R. C. Lind, *Opt. Lett.* **2**, 94 (1978); **3**, 205 (1978).
- <sup>35</sup>*Optical Phase Conjugation*, edited by R. A. Fisher (Academic, New York, 1983).
- <sup>36</sup>N. C. Kothari, M. Yoshizawa, and T. Kobayashi, *Opt. Commun.* **45**, 211 (1983).
- <sup>37</sup>F. Auzel, D. Meichenin, and J. C. Michel, *J. Lumin.* **18-19**, 97 (1979); F. Auzel, J. Dexpert-Ghys, and C. Gautier, *J. Lumin.* **27**, 1 (1982).
- <sup>38</sup>J. E. Rives and R. S. Meltzer, *Phys. Rev. B* **16**, 1808 (1977); G. D. Dixon, J. E. Rives, and R. S. Meltzer, in *Lasers '82*, Ref. 12.
- <sup>39</sup>P. Reineker and R. Kuhne, *Phys. Rev. B* **21**, 2448 (1980).
- <sup>40</sup>J. L. Skinner, H. C. Anderson, and M. D. Fayer, *Phys. Rev. A* **24**, 1994 (1981).
- <sup>41</sup>P. F. Liao, H. P. Weber, and B. C. Torfield, *Solid State Commun.* **16**, 881 (1975).
- <sup>42</sup>A. Lempicki, *Opt. Commun.* **23**, 376 (1977).
- <sup>43</sup>W. Lenth, G. Huber, and D. Fay, *Phys. Rev. B* **23**, 3877 (1981); D. Fay, G. Huber, and W. Lenth, *Opt. Commun.* **28**, 117 (1979).
- <sup>44</sup>G. Huber, J. P. Jeser, W. W. Kruhler, and H. G. Danielmeyer, *IEEE J. Quantum Electron.* **QE-10**, 766 (1974).
- <sup>45</sup>H. P. Weber and P. F. Liao, *J. Opt. Soc. Am.* **64**, 1337 (1974); P. F. Liao, H. P. Weber, and B. C. Tofield, *Solid State Commun.* **16**, 881 (1973).
- <sup>46</sup>S. Singh, D. C. Miller, J. R. Potopowicz, and L. K. Shick, *J. Appl. Phys.* **46**, 1191 (1975).

model needed to obtain a tractable expression for comparing with experimental results, make it impossible to obtain an exact fit to the data as shown in Sec. V. It appears to be difficult to modify Kenkre's generalized master-equation approach to include the possibility of time-dependent interaction parameters, and thus it may be better in this case to start from the stochastic Liouville equation as done by other workers.<sup>39,40</sup> This is an important problem for future theoretical work.

The ion-ion-interaction rate in neodymium pentaphosphate has been estimated in different ways and ranges from  $2.4 \times 10^7 \text{ s}^{-1}$ , obtained from nearest-neighbor dipole-dipole interaction,<sup>41</sup> to  $9.0 \times 10^8 \text{ s}^{-1}$ , obtained from a spreading-wave-packet calculation.<sup>42</sup> The experimental value for  $j$  obtained in this work is close to the former estimate. The value for the exciton scattering rate cannot be determined as specifically from the experimental data as discussed in Sec. V. The range of possible values of  $\alpha$  between  $10^4$  and  $3 \times 10^6 \text{ s}^{-1}$  is consistent with the dephasing rate of  $5 \times 10^4 \text{ s}^{-1}$  measured by coherent transient spectroscopy methods<sup>11</sup> on the similar stoichiometric rare-earth crystal  $\text{EuP}_5\text{O}_{14}$ . The observation that acoustic phonons are not active in scattering the migrating exciton is not surprising since the wavelengths of acoustic phonons are much greater than the nearest-neighbor ion separations. This means that this type of phonon will modulate the energy levels of ions in neighboring sites simultaneously and will not be effective in causing scattering as the energy-transfer interaction occurs between these ions. The determination of the exact mechanism causing the exciton scattering is an important area for future research. The fact that the acoustic phonons are not effective in scattering excitons does not imply that they do not effect the overall characteristics of the exciton dynamics of the system. It is obvious from the results that the presence of phonons can effect the ion-ion-interaction rate in several ways.

The diffusion length of the excitons given by  $L = \sqrt{2D\tau}$  is found from these results to be of the order of  $1 \mu\text{m}$ , which is a significant fraction of the peak-to-valley grating spacing as required for transient-grating experiments. The exciton mean free path given by  $\Lambda = v_g/\alpha$  ranges from about  $1 \mu\text{m}$  to values over 2 orders of magnitude smaller than this, depending of the value used for  $\alpha$ . Thus the lower-limit value for  $\alpha$  predicts the excitons moving with no scattering during their lifetimes, i.e., completely coherent motion, whereas using the upper limit for  $\alpha$  predicts hundreds of scattering events during the migration of the excitons. The overall results of this investigation are more consistent with the latter type of exciton migration.

The general consistency of the experimental results and the theoretical model presented here does not give conclusive proof that the observed oscillatory grating decay pattern is produced by partially coherent exciton migration. It is important to emphasize that these oscillations were observed only under very special experimental conditions and that these conditions are consistent with the required conditions of the Wong-Kenkre theory for predicting this type of decay pattern. Under different experimental conditions neither the Wong-Kenkre theory nor

other theories<sup>20,39,40</sup> predict the appearance of oscillations and none are observed. It is possible that some other type of physical process is responsible for these results. However, no other mechanism consistent with the experimental results has been discussed in the literature, and therefore this question can only be answered through further experimental investigations.

The four-wave-mixing transient-grating spectroscopy technique employed here monitors the spatial migration of energy. The results show this energy migration to be very efficient and essentially independent of temperature. Other techniques monitoring the spectral diffusion of energy show these processes to be much less efficient and temperature dependent.<sup>8-10</sup> Techniques employing activator ions as traps can also detect spatial energy migration although the results may be difficult to interpret exactly due to the presence of trapping effects. Research of this type on rare-earth-doped neodymium pentaphosphate crystals has been interpreted in terms of fast diffusion of energy among the  $\text{Nd}^{3+}$  ions.<sup>43,44</sup> The coherent transient spectroscopy work mentioned earlier indicates that the exciton wave function in  $\text{EuP}_5\text{O}_{14}$  may be spread out over several lattice spacings, indicating strong resonant energy transfer. Other earlier studies of energy transfer in  $\text{NdP}_5\text{O}_{14}$  crystals resulted in conflicting conclusions concerning the extent of the energy migration.<sup>45,46</sup> Some of the apparent inconsistencies between early work and recent work may be due to the significant improvement in sample quality during this time interval.<sup>13</sup> Furthermore, different techniques may probe different types of physical processes. Spectral diffusion measurements may not be able to detect resonant ion-ion energy transfer in highly concentrated crystals under certain conditions. Thus it may be that transient-grating spectroscopy and site-selection spectroscopy are providing complementary information concerning the characteristic of this material instead of conflicting results. The interpretation of the results of the power dependence of  $D$  in terms of a power-broadening effect is consistent with the fact that this experimental technique is probing long-range resonant energy migration and is not sensitive to short-range spectral diffusion effects.

In conclusion, this work demonstrates the power of four-wave-mixing transient-grating spectroscopy in probing the details of spatial energy migration in highly concentrated solids. Along with the development of more detailed theoretical models discussed above, it is important to extend this type of experimental investigation to other types of materials. In addition, the work on  $\text{NdP}_5\text{O}_{14}$  should be extended to include even lower temperatures and to better define the transition from the high-mobility region of resonant excitation to the lower-mobility region of vibronic excitation.

#### ACKNOWLEDGMENTS

This work was supported by the U. S. Army Research Office, and National Science Foundation under Grant No. DMR-82-16551.

TABLE II. Scattering efficiency parameters at  $T = 300$  K and  $\theta = 10^\circ$ .

Parameters	High flux		Low flux	
	$x = 1.0$	$x = 0.2$	$x = 1.0$	$x = 0.2$
$\lambda_x$ (nm)	575	575	514.5	575
$R$	1.0	1.0	0.01	0.01
$\delta_1$	4.5	4.9	7.2	5.3
$\delta_2$	0.1	0.1	0.1	0.1
$\alpha_1$ ( $\text{cm}^{-1}$ )	50	10	50	10
$\alpha_2$ ( $\text{cm}^{-1}$ )	45	9	45	9
$I_{01}$ ( $\text{W}/\text{cm}^2$ )	$4.0 \times 10^3$	$4.0 \times 10^3$	$3.9 \times 10^3$	$4.0 \times 10^3$
$I_{02}$ ( $\text{W}/\text{cm}^2$ )	$5.0 \times 10^3$	$5.0 \times 10^3$	$5.0 \times 10^3$	$5.0 \times 10^3$
$\Delta$	$6.0 \times 10^{-11}$	$1.0 \times 10^{-6}$	$6.0 \times 10^{-7}$	$2.0 \times 10^{-5}$

would be to use expressions for Gaussian wave fronts<sup>33</sup> instead of the simplified plane-wave approximation used here. This difference between real and approximated wave fronts may be less for the measurements made with the more highly focused beams, which would account for the better fit between theory and experiment for this case.

## VII. DISCUSSION AND CONCLUSIONS

The preceding sections described the results of an extensive investigation of  $\text{Nd}_x\text{La}_{1-x}\text{P}_5\text{O}_{14}$  crystals using four-wave-mixing spectroscopy. The most significant results of this work can be summarized as follows. Under appropriate experimental conditions, both population and thermal gratings can be established. The nonlinear interaction between the laser fields in the material which creates these gratings cannot be described by a simple two-level-system susceptibility model. Spatial exciton migration contributes to the destruction of the population grating, and characteristics of the exciton dynamics can produce different grating decay patterns. The energy migration can be enhanced through vibronic processes which populate the upper crystal-field component of the metastable state and through excitation processes which selectively excite higher-concentration subsets of ions within the inhomogeneous spectral profile. The dominant scattering mechanism which limits the exciton mean free path appears to be scattering from defects and boundaries in the crystals.

The theory of four-wave-mixing interactions in solids is still in the process of being developed. The multiple-energy-level system treated here allows the inclusion of excited-state absorption and dispersion effects not present in a simple two-level system. Although there is no *a priori* justification of using a linear combination of susceptibilities as done in Sec. VI, this is the simplest way of treating a multilevel system and is meant only to be a first approximation in the development of this type of model. The theory predicts a strong deviation from the quadratic dependence of scattering efficiency on pump power predicted by a two-level-system model, which is consistent with the experimental results. Future development of this model should involve more sophisticated methods for treating the susceptibility of a multilevel system, the effects of Gaussian wave fronts,<sup>33</sup> and the effects of beam depletion. Some progress in the latter area has been reported recently.<sup>36</sup>

Vibronic excitation has been employed in previous investigations of energy transfer and electron-phonon interactions of ions in crystals.<sup>37</sup> The results described in Sec. IV show the potential usefulness of this technique for studying the role played by phonons in the processes contributing to the establishment and decay of the population grating in four-wave mixing. The increase in the population of the upper crystal-field component of the metastable state, due to the selective generation of phonons whose energy is identical with that of the crystal-field splitting, is similar to the observations reported by Rives *et al.*<sup>38</sup> in other types of experiments. Since the resonant transition in this case actually involves several overlapping crystal-field components, it might be expected that several vibronic enhancement peaks should be seen. For example, these should appear near 5735 and 5748 Å. Although there appears to be some increase in  $D$  in the former location, both of these wavelengths are in the region where direct absorption begins to occur. It is not possible to develop a greater understanding of the vibronic processes without having available more detailed information concerning the phonon properties of the host crystal.

It is important to define the term coherence since it is commonly used in different ways to describe energy transfer in solids.<sup>1-3</sup> Some authors reserve the term coherence for describing the case where the ion-ion interaction is so strong that the energy transfer must be described by a spreading wave packet using Schrödinger's equation. Others have used the term to describe the case where an exciton moves as a quasiparticle with a given momentum so that it travels over many lattice spacings, maintaining its phase memory before scattering occurs. If numerous scattering events occur within the lifetime of the exciton, this can still be described by a diffusion equation. The use of the term coherence in Sec. V is associated with this type of long-mean-free-path exciton motion.

The observation of experimental results which may be interpreted in terms of partially coherent exciton migration reported here is extremely important since it can provide an opportunity to experimentally study the characteristics of this type of quasiparticle motion. Theoretical models of this type of energy transfer have been developed previously without any possibility of experimental verification. The work of Kenkre<sup>25,26</sup> provides the theoretical model most closely describing the experimental situation of this study. However, approximations made in Kenkre's

$$\left| \frac{\rho}{\zeta} \right| = \frac{\sum_{j=1,2} \left[ \sum_{i=1,2} F_{j,i} \frac{R_i \alpha_{0i}}{(1+\delta_i^2) I_{si}} \frac{(I_2 I_4)^{1/2} [1 + (I_2 + I_4)/I_{si}]}{[1 + (I_2 + I_4)/I_{si}]^2 - 4 I_2 I_4 / I_{si}^2} \right]^2}{\sum_{j=3,4} \left[ \sum_{i=1,2} F_{j,i} \frac{R_i \alpha_{0i}}{1+\delta_i^2} \frac{[1 + (I_2 + I_4)/I_{si}]^2 - 2 I_2 I_4 / I_{si}^2}{[1 + (I_2 + I_4)/I_{si}]^2 - 4 I_2 I_4 / I_{si}^2} \right]^2} \quad (16)$$

Here

$$\begin{aligned} F_{1,i} &= \cos\Delta - \delta_i \sin\Delta, \quad F_{3,i} = 1, \\ F_{2,i} &= \sin\Delta - \delta_i \cos\Delta, \quad F_{4,i} = \delta_i, \\ \Psi_{E_0} &= (2L/\cos\theta) \sum_{i=1,2} R_i \alpha_{0i} / (1 - \delta_i^2). \end{aligned} \quad (17)$$

Under more restrictive simplifying assumptions this expression reduces to the one obtained previously.<sup>12</sup> Although it is rather cumbersome to work with such a complicated equation in fitting experimental data, any further assumptions mask the results of some of the physical processes underlying the mechanisms of four-wave mixing in a multilevel medium. Figures 11 and 12 show the results of measuring scattering efficiency versus laser-pump power for both samples at room temperature with the excitation wavelength in the direct-transition spectral region. Measurements were made in two different ranges of power densities by changing the focused-beam cross-section area in the sample. The results change significantly for the two different measurement conditions, indicating that scattering efficiency is sensitive to power density as well as total pump power. It is immediately obvious that the results do not obey a simple quadratic dependence as predicted by a simple two-level-system model.<sup>23</sup> Instead, the curves are almost s-shaped with the curvature being more enhanced for the  $x=1.0$  sample and being greater for lower power densities.

The solid lines in the figures represent the best fits to the data using Eq. (15) and treating  $R$ ,  $\delta_i$ ,  $\alpha_i$ ,  $I_{0i}$ , and  $\Delta$  (with  $i=1,2$ ) as adjustable parameters. This was done on a Digital Equipment Corporation LSI-11 computer using

a multiple-parameter, nonlinear-regression, least-squares-fitting routine. Although with a complex expression such as Eq. (15) involving eight adjustable parameters it should be possible to generate a variety of different curve shapes, it turns out in this case that to obtain any better fits to the data than those shown in the figure requires unphysical values for one or more of the fitting parameters. Table II lists the values of these parameters used to obtain the fittings shown in the figures. The fitting is good for the  $x=0.2$  sample with high-power-density conditions, but for the low-power-density conditions it does not predict a curvature as strong as that observed in the experimental data. For the  $x=1.0$  sample the fits are reasonably good for both power-density conditions in the regions of low total power, but significant disagreement between theory and experiment occurs in the high-total-power region.

Although there is no way to obtain exact values for the parameters in Table II from independent measurements, the values obtained from the fitting procedure are physically reasonable. It is interesting to note that for both samples the value of  $R$  required to obtain the best fit to the data is significantly greater in the high-power-density case compared to the low-power-density case. This would be expected if the multilevel model proposed here is valid. The fact that there is some discrepancy between theory and experiment shows that there are other physical processes occurring which are not taken into account in the model used here. One possible effect that might be important is beam depletion in the sample. This would be more important in the highly concentrated material, which is consistent with the poorer fit between theory and experiment obtained in the  $x=1.0$  sample compared to the  $x=0.2$  sample. Another improvement of the model

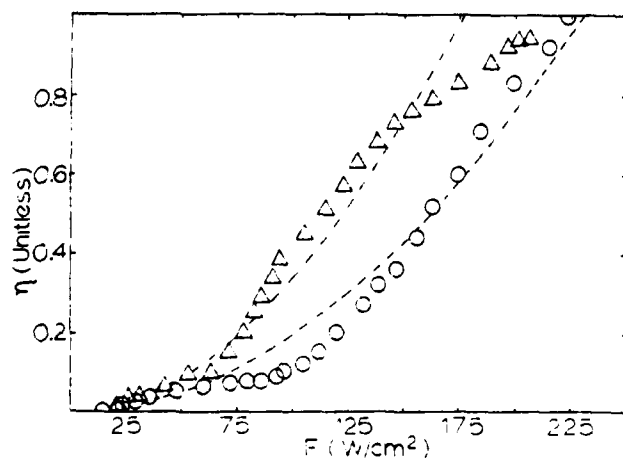


FIG. 11. Variation of scattering efficiency with pump-beam power at low-flux levels at  $T=300$  K and a crossing angle of  $10^\circ$ .  $\Delta$  is for  $x=1.0$  and  $\lambda_{exc}=5145$  Å.  $\circ$  is for  $x=0.2$  and  $\lambda_{exc}=5750$  Å. See text for explanation of theoretical lines.

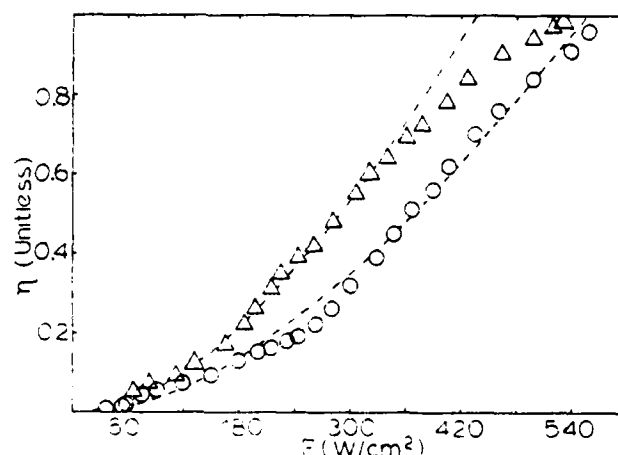


FIG. 12. Variation of scattering efficiency with pump-beam power at high-flux levels at  $T=300$  K and a crossing angle of  $10^\circ$ .  $\Delta$  is for  $x=1.0$  and  $\lambda_{exc}=5750$  Å.  $\circ$  is for  $x=0.2$  and  $\lambda_{exc}=5750$  Å.



or from d-d transitions after intersystem crossing. The relative importance of these two types of emission depends on the specific environment of the  $\text{Rh}^{2+}$  ion in the host crystal.<sup>8</sup> In  $\text{RbCaF}_3$  crystals the  $\text{Rh}^{2+}$  emission comes entirely from spin allowed d-d transitions.

Figures 1 and 2 show the fluorescence emission spectra and lifetimes obtained at room temperature after excitation by the frequency tripled output of a mode-locked  $\text{Y}_2\text{Al}_5\text{O}_{12}:\text{Nd}$  laser. The excitation was at 354.7 nm with a 30 ps pulse. Similar results were obtained using a nitrogen laser which provides a 10 ns pulse at 337.1 nm. A 1/4-m monochromator with a PAR silicon diode array detector and optical multichannel analyzer were used to monitor the emission spectra, while the lifetimes were detected with an RCA C31034 phototube and photographed on a storage oscilloscope. For low energy excitation, the fluorescence spectrum appears as a broad band peaked at 710.0 nm with a full width at half maximum of about 16 nm and a fluorescence decay time of 9.0  $\mu\text{s}$ . At high energy excitation, the position of the emission band remains unchanged but the halfwidth narrows to about 7 nm and the lifetime shortens to about 0.13  $\mu\text{s}$ .

The abrupt lifetime shortening and spectral narrowing at a specific threshold pump energy are indicative of the onset of stimulated emission. In order to directly measure the effects of this "laser action", single pass gain measurements were performed using the experimental setup illustrated in Fig. 3. The tripled output from the  $\text{Y}_2\text{Al}_5\text{O}_{12}:\text{Nd}$  laser operating above threshold was used as the pump source and the output from a nitrogen laser-

pumped tunable dye laser was used as a probe beam. The dye used was a mixture of rhodamine 610 and oxazine 725 since this provided the ability to tune across the entire fluorescence emission band. A storage scope was used to measure the change in the probe beam intensity when the pump beam was turned on. Gain was observed in the tuning range from approximately 700 to 720 nm as shown in Fig. 1.

The results described above give the fundamental laser properties of  $\text{RbCaF}_3:\text{Rh}^{2+}$  summarized in Table I. The peak gain coefficient was measured to be  $\gamma = 0.54 \text{ cm}^{-1}$ . This can be used to determine the population inversion at threshold from the expression

$$\Delta N = 8\pi\Delta\nu\tau\gamma n^2/\lambda^2. \quad (1)$$

Here  $\Delta\nu$ ,  $\tau$ , and  $\lambda$  are the half-width, radiative lifetime, and peak position of the fluorescence band, respectively. Using the measured values for these parameters yields  $\Delta N = 3.4 \times 10^{17} \text{ cm}^{-3}$ . This number can be independently verified from the measured value of the pulsed pumping threshold energy density,  $E_{th} = 0.063 \text{ J/cm}^2$ , which is related to the threshold population inversion by

$$\Delta N = E_{th}/h\nu. \quad (2)$$

From this approach, a value of  $\Delta N = 2.3 \times 10^{17} \text{ cm}^{-3}$  is determined which is consistent with the value obtained from gain measurements. For simplification, an intermediate value of  $\Delta N = 3 \times 10^{17}$  is listed in Table I and used to calculate the peak stimulated emission cross section from the relationship

$$\sigma_p = \gamma/\Delta N. \quad (3)$$

This is also given in the table. The value of the cross section obtained from these measurements is consistent with the value

predicted from spectral parameters using the equation

$$\sigma_e = \lambda_p^2 / [8\pi c n^2 \Delta \tilde{\nu} \tau_f]. \quad (4)$$

The exact values of the laser parameters listed in Table I must be considered as only rough estimates due to several factors. These include perturbations associated with scattering losses because of poor sample quality, feedback due to cleaved sample faces, and unknown properties such as the exact value of the quantum efficiency. Despite these uncertainties, the measured values of gain and cross section are very favorable compared to those of other vibronic laser systems based on 3d transition metal ions. The symmetric shape of the emission band and tuning curve indicates that excited state absorption does not effect the stimulated emission properties of this material.

The results reported here are unique in two aspects: This is the first observation of stimulated emission and tunable gain in a crystal with a 4d transition metal as the active ion, and the first solid state laser system pumped through a charge transfer band. This suggests that many different 4d and 5d transition metal ions as well as other charge transfer molecular ions in solids may be useful in tunable solid state laser systems.<sup>8</sup> The future potential of these materials depends on the development of improved crystal quality which should reduce scattering losses and increase the fluorescence lifetime. When such samples are obtained, an attempt will be made to flashlamp pump the system.

ACKNOWLEDGMENTS. This work was sponsored by the U.S. Army Research Office and by the Office of Naval Research.

TABLE I. Spectral and Laser Parameters for  $\text{RbCaF}_3:\text{Rh}^{2+}$  Crystals

Spectral Parameters	Laser Parameters
$\lambda_p(\text{nm}) \approx 710$	$E_{th}(\text{J}/\text{cm}^3) = 0.063$
$\Delta\lambda_{1/2}(\text{nm}) = 17$	$\Delta N_{th}(\text{cm}^{-3}) = 3 \times 10^{17}$
$\tau_f(\mu\text{s}) = 9.0$	$\gamma(\text{cm}^{-1}) = 0.54$
$\sigma_e(\text{cm}^2) = 1.1 \times 10^{-18}$	$\sigma_p(\text{cm}^2) = 1.8 \times 10^{-18}$
	Tuning Range: 700-720 nm

## REFERENCES

1. P.F. Moulton, "Tunable Paramagnetic Ion Lasers", in Laser Handbook, Vol. 4, M. Bass and M. Stitch, eds. (North Holland, Amsterdam, in press).
2. L.F. Johnson, R.E. Dietz, and H.J. Guggenheim, Phys. Rev. Lett. **11**, 318 (1963) and Appl. Phys. Lett. **5**, 21 (1964); L.F. Johnson, H.J. Guggenheim, and R.A. Thomas, Phys. Rev. **149**, 179 (1966); F. Johnson, H.J. Guggenheim, D. Bahnck, and A.M. Johnson, Opt. Lett. **8**, 371 (1983); L.F. Johnson and H.J. Guggenheim, J. Appl. Phys. **38**, 4837 (1967); B.C. Johnson, R.F. Moulton, and A. Mooradian, Opt. Lett. **10**, 116 (1984); and P.F. Moulton, A. Mooradian, and T.B. Reed, Opt. Lett. **3**, 164 (1978).
3. M.L. Shand and J.C. Walling, IEEE J. Quantum Electron. **QE-18**, 1829 (1982); J. Walling, O.G. Peterson, H.P. Jenssen, R.C. Morris, and E.W. O'Dell, IEEE J. Quantum Electron. **QE-16**, 1302 (1980).
4. S.T. Lai and M.L. Shand, J. Appl. Phys. **54**, 5642 (1983).
5. U. Brauch and U. Durr, Opt. Lett. **9**, 441 (1984) and Opt. Comm. **49**, 61 (1984); U. Durr, U. Brauch, W. Knierim, and C. Schiller, in "Proc. First Tunable Solid State Laser Conference, La Jolla, June 1984" (Springer-Verlag, Berlin, in press).
6. J. Drube, B. Struve and G. Huber, Appl. Phys. **B28**, 235 (1982); ibid, **B30**, 117 (1983) and Opt. Comm. **50**, 45 (1984).
7. P.F. Moulton, Opt. News **8**, 9 (1982).
8. R.C. Powell, R.H. Schweitzer, J.J. Martin, G.E. Venikouas,

and C.A. Hunt, J. Chem. Phys. 81, 1178 (1984); R.C. Powell, J.J. Martin, R.H. Schweitzer, G.C. Gilliland, G.E. Venikouas, and C.A. Hunt, in "Proc. Conf. on Lasers and Applications, 1983", ed. R.C. Powell, (STS Press, Mclean, VA, in press); and R.C. Powell in "Proc. First Tunable Solid State Laser Conference, La Jolla, June 1984" (Springer-Verlag, Berlin, in press).

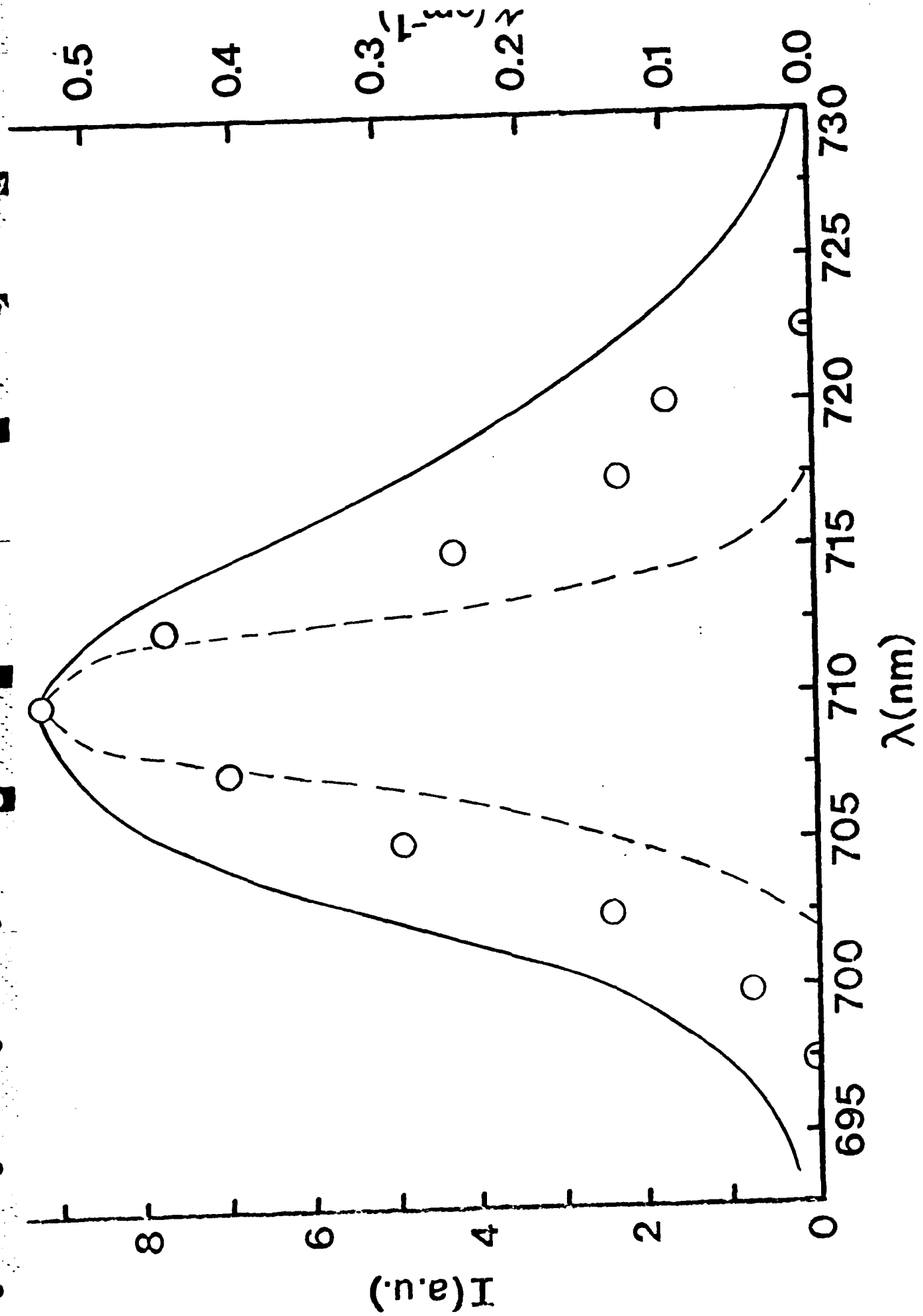
9. F.A. Modine, E. Sonder, W.P. Unruh, C.B. Finch, and R.D. Westbrook Phys. Rev. B 10, 1623 (1974).

# FIGURE CAPTIONS

FIG. 1. Room temperature emission spectra and gain of a  $\text{RbCaF}_3:\text{Rh}^{2+}$  crystal. The solid line is the fluorescence emission with peak pumping pulse energy density below threshold while the dashed broken curve is the fluorescence after pumping above threshold. The circles are the results of single pass gain measurements.

FIG. 2. Room temperature fluorescence decay time of  $\text{RbCaF}_3:\text{Rh}^{2+}$  as a function of peak pumping pulse energy at 354.7 nm.

FIG. 3. Block diagram of experimental setup for single pass gain measurements.





$\tau(\mu s)$

10.0

1.0

0.1

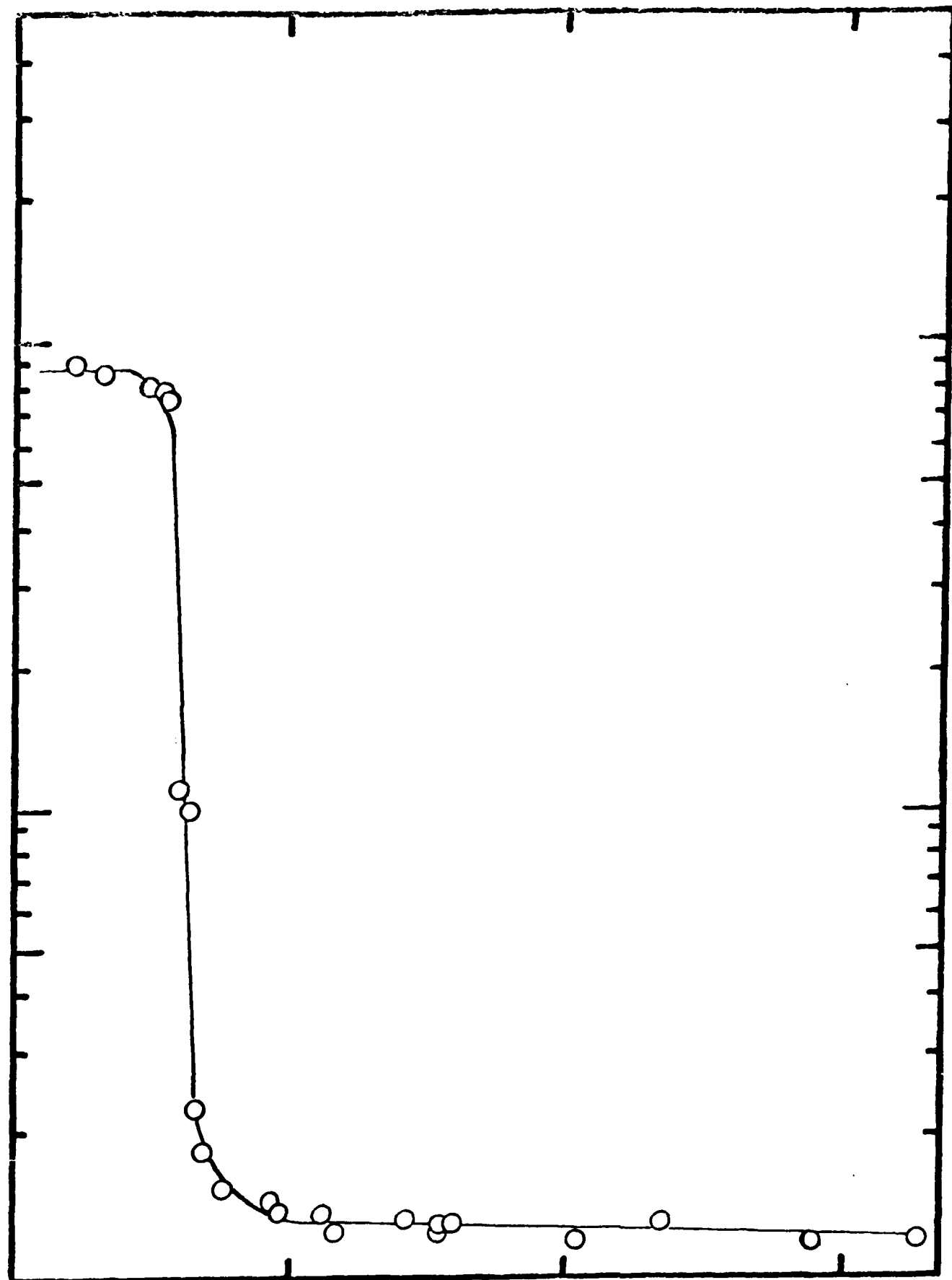
0.0

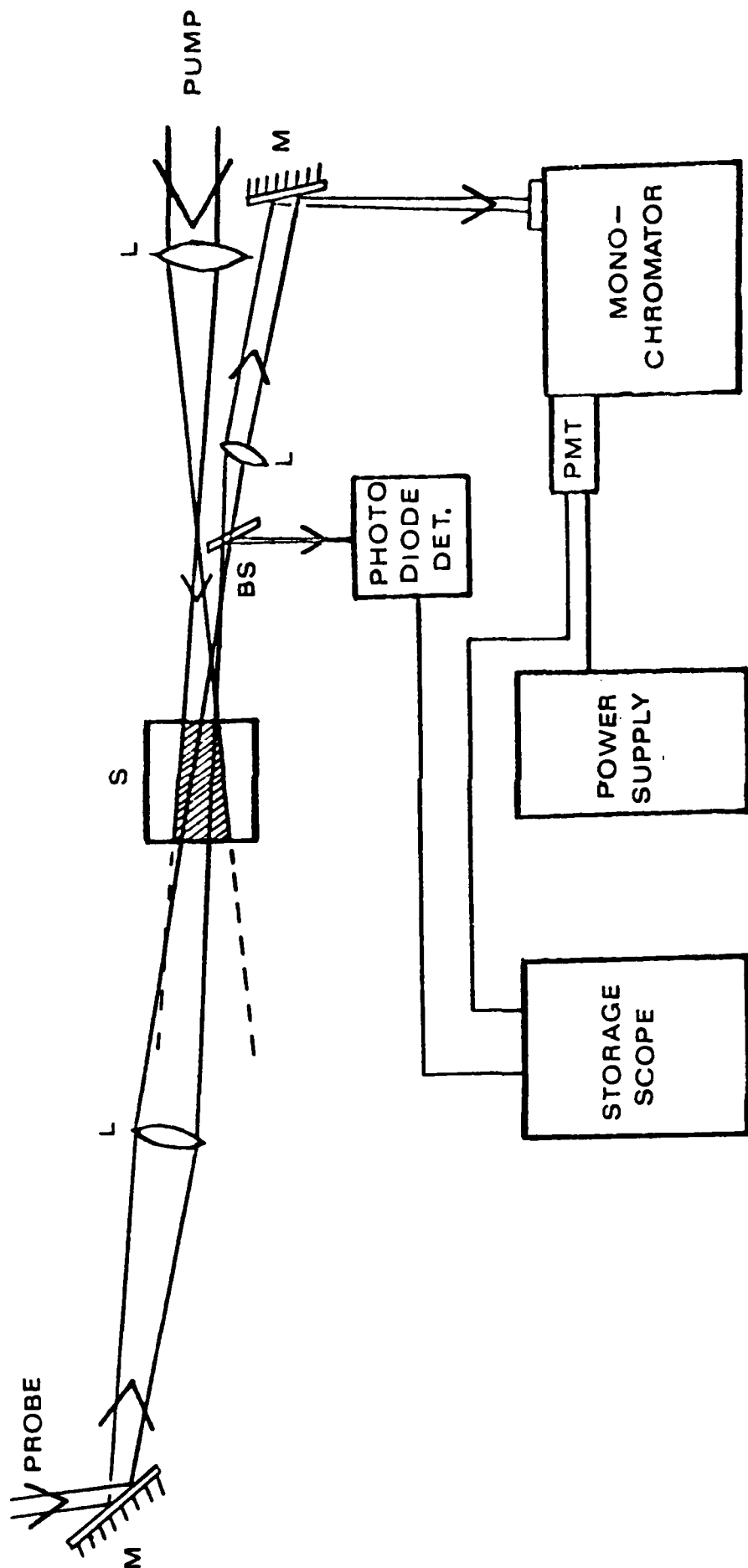
0.5

1.0

1.5

$P(mJ)$





## Recent Results on the Spectroscopy of Transition Metal Ions For Tunable Solid State Lasers

Richard C. Powell  
Department of Physics, Oklahoma State University  
Stillwater, Oklahoma 74078

### I. Introduction

The recent expansion of electro-optic based technology has produced a demand for laser systems having a variety of different operational parameters. In many cases, solid state lasers are the most desirable choice because of their ruggedness and minimum maintenance requirements. Because of this, there is significant interest in research and development on optical materials for use as solid state lasers. Materials which exhibit broad band vibronic emission are of special importance in developing lasers whose wavelength can be tuned continuously over a broad spectral range. Research in this area can be divided into categories: searching for new vibronic laser materials and improving existing vibronic laser materials. This paper summarizes the results obtained so far on several projects currently underway in our laboratory which fall into one or the other of these two categories.

Modern optical spectroscopy techniques provide powerful methods for studying the fundamental properties of a material which are important in characterizing its potential for use in solid state laser systems. The development of different types of laser spectroscopies allows us to probe the properties of a sample with much higher spatial, spectral, and temporal resolution than ever before available as well as allowing us to monitor the response of a material to high power laser radiation and coherent driving fields. The information gained from these experiments can be correlated with crystal growth parameters to help develop improved material quality and in addition can be correlated with laser operational parameters to identify physical reasons for device limitations. The use of several different experimental methods to completely characterize all aspects of the spectral dynamics of a material is important in determining its optimum properties for device applications. A variety of techniques are currently being used in our laboratory including time-resolved site-selection spectroscopy, four-wave mixing spectroscopy, picosecond spectroscopy, nonlinear spectroscopy, and Raman microprobe spectroscopy. Several of these were used in the work described below.

In the following sections, three different projects are discussed. The first involves a survey of the spectroscopic properties of 4d and 5d transition metal ions in different types of host crystals. The second concerns the use of Raman microprobe techniques to identify scattering centers in  $\text{Al}_2\text{O}_3:\text{Ti}^{3+}$  crystals. The final project involves measuring the four-wave mixing properties of alexandrite crystals.

## II. Spectroscopic Survey of 4d and 5d Transition Metal Ions

The currently operating vibronic lasers are all based on 3d transition metal ions such as  $\text{Cr}^{3+}$ ,  $\text{Ti}^{3+}$ ,  $\text{Co}^{2+}$ , and  $\text{Ni}^{2+}$  in various types of host crystals. Another class of ions which have similar unfilled d-electron configurations are the 4d and 5d transition metals. Figure 1 lists the ions of this type in terms of their electron configurations. Under certain conditions, chemical complexes incorporating these ions are known to exhibit efficient broad band fluorescence emission as desired for tunable laser applications. However, little work has been done on studying the spectroscopic properties of these ions as dopants in host crystals. We are presently carrying out an investigation to evaluate the potential of these ions in solid state laser materials. So far, divalent ions of Ru, Rh, Ir, and Pt have been studied and found to have similar spectral properties [1]. In this paper, the spectroscopic properties of  $\text{Rh}^{2+}$  in three different host crystals are compared as an example of the results obtained in this project.

The 4d and 5d transition metal ions of interest to this work have greater than half filled shells. The  $d^5$  through  $d^8$  electron configurations all have low lying excited states strongly coupled to the crystal field of the host. Since the 4d and 5d ions have strong spin-orbit coupling, a simple crystal field analysis of the  $d^n$  states does not provide as accurate a description of the energy levels of these ions in crystals as it does for  $3d^n$  ions [2]. However, it is generally true that there are several excited levels whose energy with respect to the ground state increases significantly as the crystal field increases and whose transitions to the ground state are either dominantly spin allowed or spin forbidden. These properties are favorable for broad band vibronic emission. Figure 2 shows a schematic configuration coordinate diagram for this type of ion. Strong charge transfer (CT) transitions dominate the absorption. After excited state relaxation, either the energy can be emitted from this charge transfer state or intersystem crossing to the d levels can occur. Since there are several different d levels, the energy is distributed among these after which both radiative and radiationless emission occurs. The fluorescence lifetimes of the CT, spin allowed d, and spin forbidden d transitions are of the order of nanoseconds, microseconds, and milliseconds, respectively. This variety of types of levels and transitions results in complex spectral dynamics for these ions.

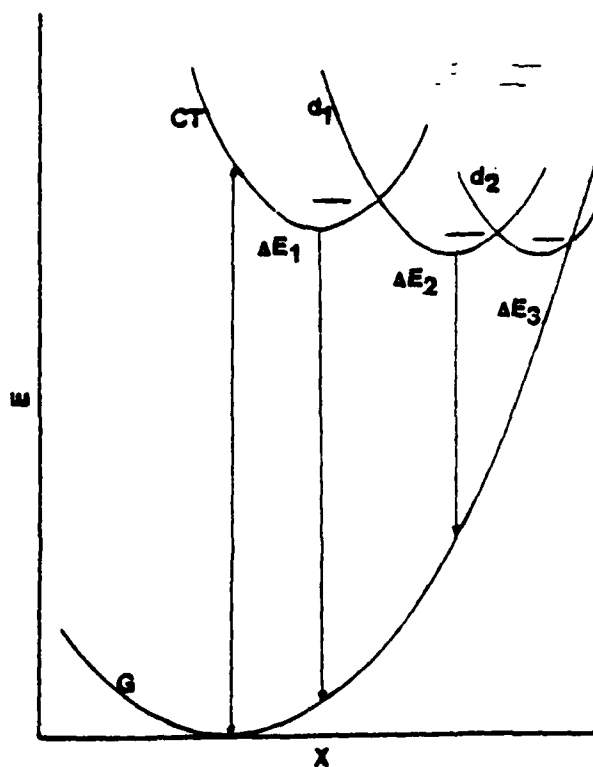
For tunable laser materials, it is desirable to have strong absorption bands and broad emission bands with high peak cross sections. The latter quantity varies directly with quantum efficiency and inversely with the band width and lifetime. Thus the ideal operating scheme for these ions would be to pump into the charge transfer band and have efficient cross over of the excited state energy to the d levels having spin allowed transitions to the ground state with minimum radiationless loss. The CT absorption for each of these ions in all of the host crystals investigated so far was found to occur in the near uv spectral region. The CT absorption bands are strong, broad, and structured with maxima occurring near 320 nm. This makes them ideal for pumping with a  $\text{N}_2$  laser at 337.1 nm. The most important question is which host crystals maximize cross over to the d levels for fluorescence emission.

The first set of host crystals investigated were the alkali halides because of our ability to grow them easily. These were grown by the Czochralski method in a dry nitrogen atmosphere. Good optical quality single crystals were obtained which were cleaved from the boule perpendicular to the growth axis to ensure uniform doping. Time-resolved fluorescence spectra were obtained as a function of temperature to observe the spectral dynamics. The

## DIVALENT &amp; TRIVALENT TRANSITION METAL IONS

$3d^{1(9)}$	$3d^{2(8)}$	$3d^{3(7)}$	$3d^{4(6)}$	$3d^5$
Sc <sup>2+</sup>	V <sup>3+</sup>	V <sup>2+</sup>	Mn <sup>3+</sup>	Mn <sup>2+</sup>
Ti <sup>3+</sup>	(Ni <sup>2+</sup> )	Cr <sup>3+</sup>	(Fe <sup>2+</sup> )	Fe <sup>3+</sup>
(Cu <sup>2+</sup> )	Ti <sup>2+</sup>	(Co <sup>2+</sup> )	(Co <sup>3+</sup> )	
		(Ni <sup>3+</sup> )	Cr <sup>2+</sup>	
$4d^{1(9)}$	$4d^{2(8)}$	$4d^{3(7)}$	$4d^{4(6)}$	$4d^5$
Y <sup>2+</sup>	(Pd <sup>2+</sup> )	(Rh <sup>2+</sup> )	(Ru <sup>2+</sup> )	Ru <sup>3+</sup>
Zr <sup>3+</sup>		(Pd <sup>3+</sup> )	(Rh <sup>3+</sup> )	
(Cd <sup>3+</sup> )				
$5d^{1(9)}$	$5d^{2(8)}$	$5d^{3(7)}$	$5d^{4(6)}$	$5d^5$
La <sup>2+</sup>	(Pt <sup>2+</sup> )	(Ir <sup>2+</sup> )	Re <sup>3+</sup>	Re <sup>2+</sup>
		(Pt <sup>3+</sup> )	(Os <sup>2+</sup> )	Os <sup>3+</sup>
			(Ir <sup>3+</sup> )	

Fig. 1 d electron configurations for divalent and trivalent transition metal ions

Fig. 2 Simplified configuration coordinate model for interpreting the observed spectral dynamics of  $4d^n$  and  $5d^n$  transition metal ions in crystals

experimental apparatus employed  $N_2$  laser pumping and boxcar integrator detection. The details of the system are described elsewhere [1].

Figure 3 shows the fluorescence emission from  $KBr:Rh^{2+}$  at room temperature. The strong, sharp band peaking near 380 nm has a lifetime of the order of 20 ns and is thus attributed to CT emission. The broad, structured band extending throughout the visible spectral region has a lifetime of the order of 25  $\mu$ s and is attributed to emission through spin allowed d-d transitions. As temperature is lowered the fluorescence lifetime of the d emission increases to about 80  $\mu$ s at 10 K while the relative intensity ratio of the d emission to the CT emission increases down to about 250 K and then decreases as temperature is lowered further to 10 K. Analysis of these data allow for the determination of the activation energy for intersystem crossing of the configuration coordinate diagram shown in Fig. 2.

After demonstrating that emission through spin allowed d-d transitions can occur in this material, the next problem is enhancing the fraction of emission occurring in this mode compared to the CT emission. This can be done by shifting the position of the CT configuration coordinate compared to the configuration coordinates of the d levels in order to lower the potential barrier for crossover. Since the CT levels are strongly affected by changes in their ligand environments, the introduction of lattice defects such as vacancies as nearest neighbors to the  $Rh^{2+}$  ions should change the CT levels significantly. Two processes were attempted to accomplish this. The first was thermal annealing. The sample was heated to 600 C and quenched on a copper block. The second process was irradiating the sample with a dose of  $10^5$  rads of electrons from a 2 MeV van de Graaff accelerator. The spectra obtained after each of these treatments are shown in Fig. 3. Both treatments were successful in producing a relative enhancement of the d emission. The radiation treatment results in a greater increase in the low energy part of the d band and the thermal treatment results in a greater increase in the high energy part of this band.

The spectral parameters obtained in this work are summarized in Table 1.  $r$  represents the size of the site occupied by the  $Rh^{2+}$  ion which has an ionic radius of 0.8 Å.  $\lambda_p$  is the peak wavelength of the d emission band and  $\Delta\lambda$  is the full width of the band at half maximum.  $\tau_f$  is the room temperature fluorescence lifetime of the d emission band and  $\sigma_p$  is its peak emission cross section. It can be seen from the table that KBr crystals provide a host for  $Rh^{2+}$  which gives a good possible tuning range and a cross section only slightly smaller than 3d transition metal ions. The major problem is obtaining samples with increased dopant concentrations so that reasonable gain can be achieved in laser operation. Attempts to grow single crystals of alkali halides containing high concentrations of 4d and 5d transition metal ions have been unsuccessful.

In order to work with higher doping concentration, different types of host crystals were investigated. One interesting possibility is using a crystal having a layered structure and diffusing the doping ions into the regions between the layers instead of doping during the growth process. For this purpose, samples of  $Na_{1.67}Mg_{0.67}Al_{10.33}O_{17}$  (8") were obtained from Oak Ridge National Laboratory. These Na  $\beta$ "-alumina crystals have layers with the spinal crystal structure bridged by  $Na^+$  ions [3]. The spacing between the layers is about 11.27 Å. By heating this crystal for several hours in a moulton solution of  $NaCl-RhCl_3$  with varying concentrations, it was possible to diffuse  $Rh^{2+}$  ions into the open planes and replace the  $Na^+$  ions in

## Four-wave mixing in alexandrite crystals

Ali M. Ghazzawi, Jacek K. Tyminski, and Richard C. Powell

*Physics Department, Oklahoma State University, Stillwater, Oklahoma 74078*

John C. Walling

*Allied Chemical Corporation, Mt. Bethel, New Jersey 07060*

(Received 30 July 1984)

Degenerate four-wave mixing was observed in alexandrite crystals ( $\text{BeAl}_2\text{O}_4:\text{Cr}^{3+}$ ), and the signal beam efficiency and decay rate were measured as functions of pump beam-crossing angle, wavelength, and power. The results are consistent with scattering from excited-state population gratings related to the difference in dispersion of the  $\text{Cr}^{3+}$  ions in the ground and metastable states. These gratings can be selectively established with  $\text{Cr}^{3+}$  ions in the inversion or mirror sites depending on the excitation wavelength. Strong scattering occurs only for pump beams polarized parallel to the  $b$  direction of the crystal.

### I. INTRODUCTION

The most successful type of tunable solid-state laser developed to date is based on alexandrite crystals ( $\text{BeAl}_2\text{O}_4:\text{Cr}^{3+}$ ).<sup>1</sup> Because of this, there has been a significant amount of work done in studying the properties of alexandrite.<sup>2-9</sup> One area that has not yet been thoroughly investigated is the nonlinear optical characteristics of this material. Such characteristics can be important in determining device properties for high-power laser operation. One manifestation of nonlinear interactions of laser beams in a solid is four-wave mixing (FWM) which occurs through the third-order component of the susceptibility tensor. FWM can arise from several different types of physical processes including thermal, excited-state population, and charge-migration effects. It has practical applications in optical information processing and phase conjugation,<sup>10</sup> as well as being a useful spectroscopic tool for studying properties of solids which are difficult to investigate by other methods.<sup>11</sup> We report here the first measurements of four-wave mixing in alexandrite crystals and show that the results are consistent with a model based on excited-state population gratings of  $\text{Cr}^{3+}$  ions in different types of sites.

The sample investigated was an oriented cube of  $\text{BeAl}_2\text{O}_4$  with each edge measuring about 5 mm. It contained 0.0897 at. %  $\text{Cr}^{3+}$  ions with about 78% of these being in mirror sites and the rest in inversion sites. The experimental setup used for degenerate four-wave mixing measurements was described previously<sup>11</sup> and is shown schematically in Fig. 1. The work discussed here was done at room temperature using either an argon-ion laser or a ring dye laser with R6G dye as a source. The powers of the write beams ( $P_1, P_2$ ) and the read beam ( $P_r$ ) are controlled by the variable beam splitter and neutral-density filter (VBS, VND). The write beams cross in the sample at an angle  $\theta$  and their interference forms a sine-wave pattern which acts as an index of refraction grating. A chopper (CH) is used to turn off the write beams. The read beam enters the sample in a direction phase conju-

gate to the write beam  $P_1$  and is partially diffracted by the grating. The Bragg diffraction condition results in the signal beam leaving the sample in a direction phase conjugate to write beam  $P_2$ . The intensity and decay time of the signal beam are related to the modulation depth and relaxation of the grating.

### II. SUMMARY OF RESULTS

Attempts were made to perform the experiments with all combinations of crystal orientations and laser polarizations. Strong FWM signals were only observed with laser beams polarized parallel to the  $b$  axis with propagation occurring along either of the other two crystallographic directions as shown in Fig. 2. Much weaker signals were obtained for light polarized parallel to the  $c$  axis and no FWM signal could be detected for light polarized parallel to the  $a$  axis. Figures 3 and 4 summarize the observed FWM characteristics obtained with the strong signal geometry shown in Fig. 2.

Degenerate FWM measurements were made for three laser wavelengths, 488.0, 514.5, and 579.1 nm. The signal

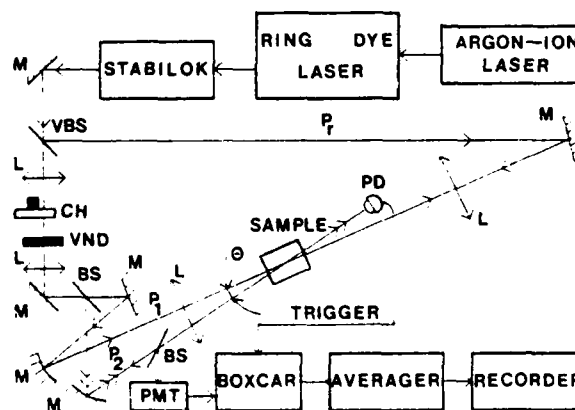
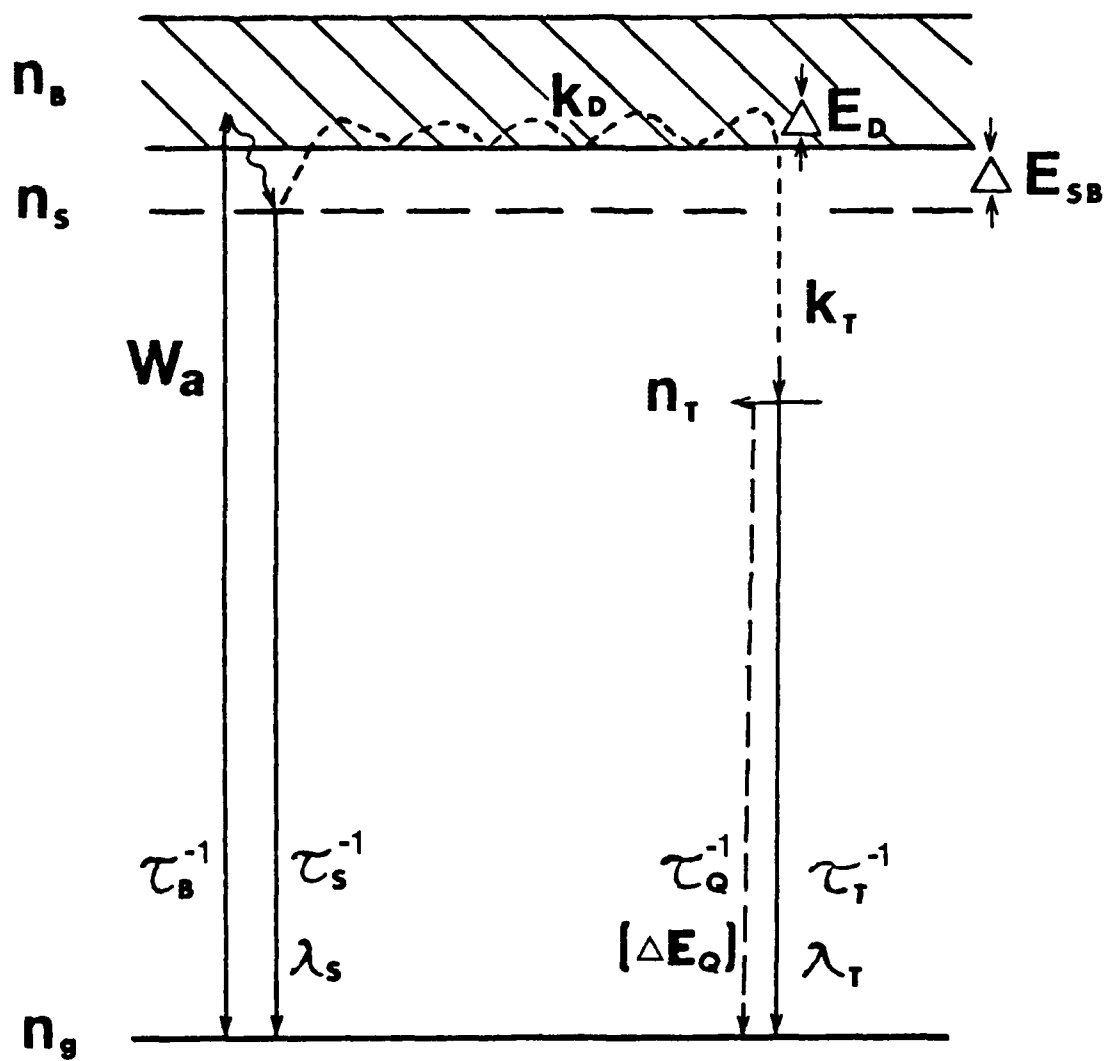


FIG. 1. Block diagram of experimental apparatus used for four-wave mixing.





$I_a/I_s$

$T=150\text{K}$

16

12

8

4

0

0

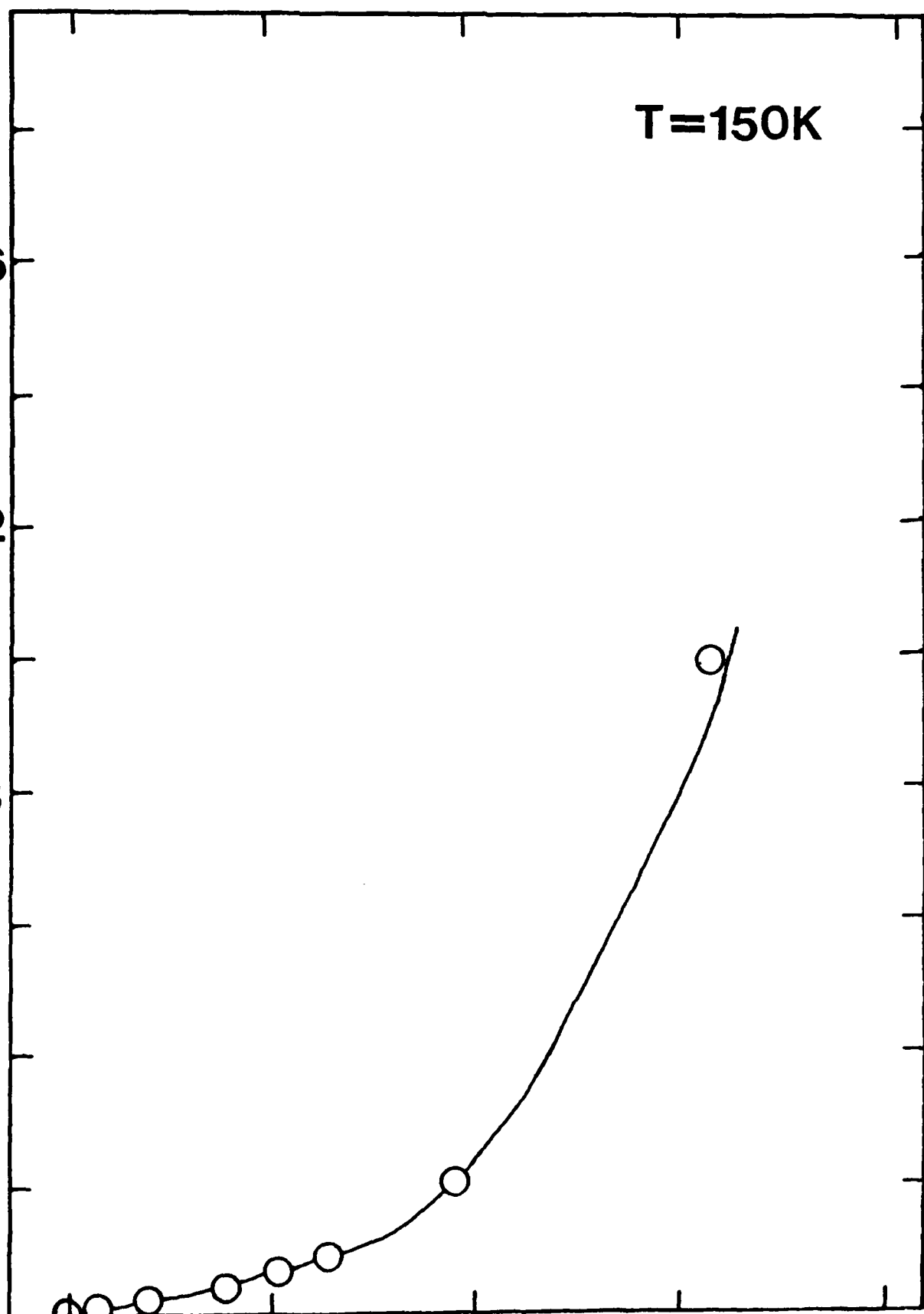
40

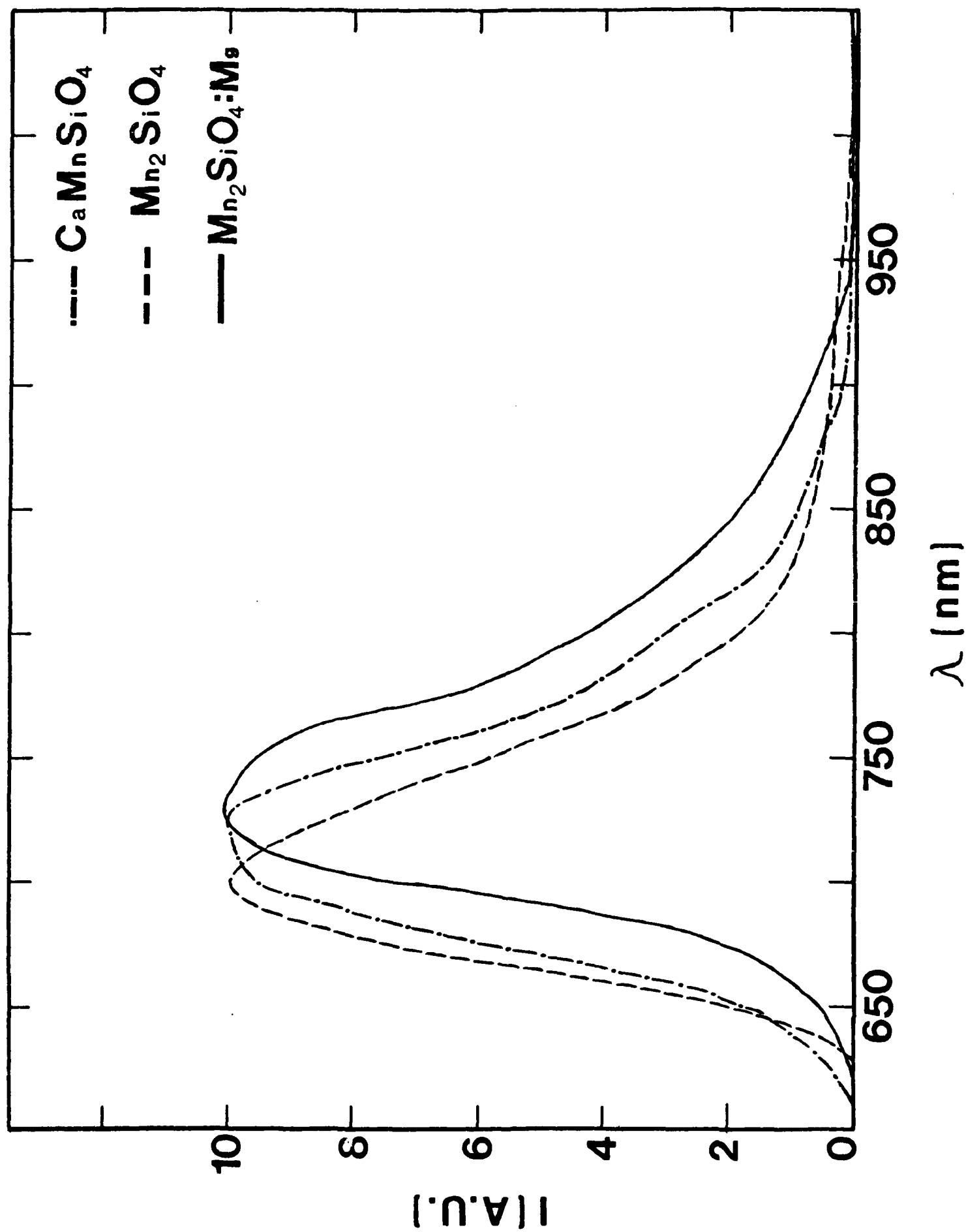
80

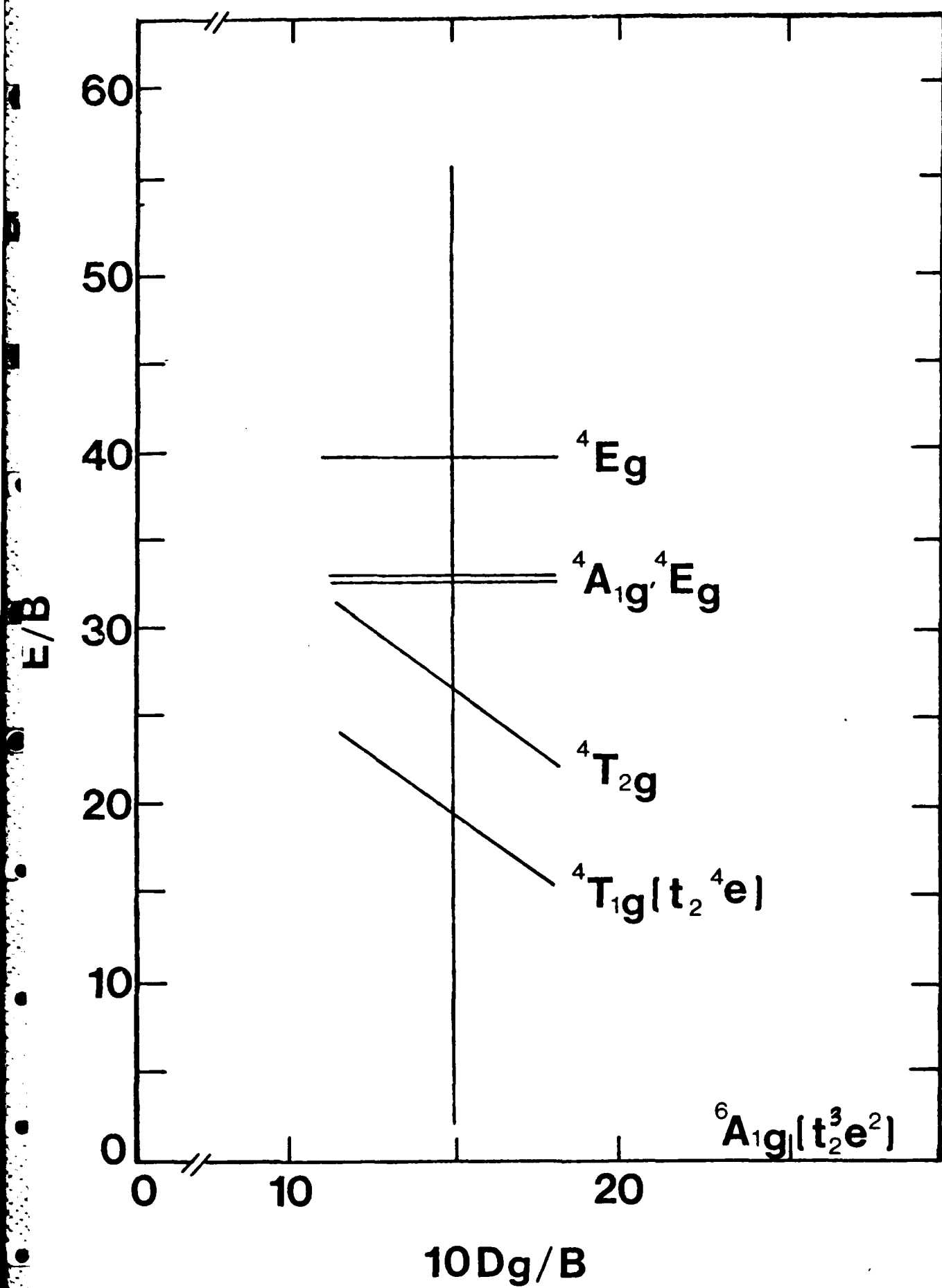
120

160

TIME ( $\mu\text{s}$ )







### References

- (1) K. Goen, B. DiBartolo, M. Alam, R.C. Powell, and A. Linz, Phys. Rev. **177**, 615 (1969).
- (2) E.V. Matyushkin, L.S. Kukushkin, and V.V. Eremenko, Phys. Status. Solidi **22**, 65 (1967); V.V. Eremenko, E.V. Matyushkin, S.V. Petrov, Phys. Status Solidi **18**, 683 (1966); and V.V. Eremenko and E.V. Matyushkin, Opt. i Spektroskopiya **23**, 437 (1967) [English transl.: Opt. Spectry. (USSR) **23** 234 (1967)].
- (3) J. Danko, D. Bacheco, and B. DiBartolo, Phys. Rev. B **28**, 2382 (1983).
- (4) R.L. Green, D.D. Sell, and R.M. White, in "Optical Properties of Ions in Crystals", edited by H.M. Crosswhite and H.W. Moos (Interscience Publishers, New York, 1967), p. 289.

TABLE I. Summary of Results

$\tau_S^0 = 3.17 \text{ ns}$	$\tau_B = 67 \text{ ns}$
$\tau_T^0 = 0.70 \text{ ns}$	$\tau_Q = 21 \text{ ns}$
$k_D^{-1} (150 \text{ K}) = 76 \text{ } \mu\text{s}$	$k_T^{-1} = 4.0 \text{ } \mu\text{s}$
$\Delta E_{SB} = 612 \text{ cm}^{-1}$	$\Delta E_D = 15 \text{ cm}^{-1}$
$\Delta E_Q = 938 \text{ cm}^{-1}$	$N_T/N_S = 0.1$

The relative intensities of the two bands vary significantly with temperature. The fluorescence lifetime of the 700 nm band decreases from about 3.17 ns at 10 K to about 1.33  $\mu$ s at room temperature. The 800 nm band has a lifetime of about 700  $\mu$ s at 50 K and about 1.93  $\mu$ s at room temperature. In addition the long wave length band exhibits a rise time in its emission pattern which decreases from about 107  $\mu$ s at 50 K to about 1.21  $\mu$ s at room temperature.

The time and temperature dependences of the spectral dynamics described above can be interpreted using the model shown in Fig. 4. This is based on the concept of having  $Mn^{2+}$  ions in two nonequivalent types of sites in the lattice. The first are ions in normal lattice sites. These form an exciton band and directly absorb the pump light. At low temperatures, lattice relaxation around the excited ions causes a self-trapping of the exciton and fluorescence is emitted as the 700 nm band. At higher temperatures the exciton can become thermally activated and hop through the lattice until it becomes trapped at a  $Mn^{2+}$  ion with perturbed energy levels due to a neighboring chemical or structural defect. Ions in this type of site are the origin of the 800 nm fluorescence. Using the parameters shown in Fig. 4, rate equations can be written to describe the time dependences of the concentrations of mobile and trapped excitons. The solutions of these equations are proportional to the fluorescence intensities from ions in the two types of sites. These equations can be fitted to the observed experimental data with the energy transfer rate, thermal quenching rate, thermal activation energies, and fractional concentration of defect sites treated as adjustable parameters. In addition, the rise time data provides the information necessary to separate the total transfer rate into its individual components representing the exciton diffusion rate and the trapping rate.

The parameters obtained from the model and fitting approach discussed above are summarized in Table I. The important conclusions from this analysis are: (1) The thermal quenching temperature of  $Mn^{2+}$  ions in normal lattice sites in this material is above room temperature. (2) Fluorescence quenching occurs because of efficient energy migration to  $Mn^{2+}$  ions in trapping sites. In the samples of  $Mn_2SiO_4$  presently available, the concentration of trapping sites is quite high. If future developments in materials preparation are successful in decreasing the amount of chemical and structural defects in the crystals, it should be possible to produce concentrated manganese materials with spectral properties favorable for use in tunable solid state laser applications.

#### Acknowledgements

The OSU part of this research was sponsored by the U.S. Army Research Office.

SPECTROSCOPIC EVALUATION OF  $\text{Mn}_2\text{SiO}_4$  AS A  
POSSIBLE TUNABLE LASER MATERIAL

Lin Xi, Robert H. Schweitzer, and Richard C. Powell  
Physics Department, Oklahoma State University  
Stillwater, OK 74078

and

G.M. Loiacono and G. Mizell  
Philips Laboratories  
Briarcliff Manor, NY 10510

Abstract

$\text{Mn}_2\text{SiO}_4$  is a concentrated manganese system exhibiting broad-band fluorescence at room temperature. Time-resolved spectroscopy results were obtained as a function of temperature and are analyzed to determine the ion-ion interaction and radiationless quenching properties of this material.

$\text{Mn}^{2+}$  ions in crystals are known to have broad fluorescence emission bands.<sup>1-4</sup> The transition producing this emission is between the  ${}^4\text{T}_{1g}$  and  ${}^6\text{A}_{1g}$  levels of the  $3d^5$  electron configuration shown in Fig. 1. Since this involves a redistribution of electrons between the crystal field split d states, the transition energy is sensitive to crystal field modulation and thus appears as a broad vibronic band. In normal  $\text{Mn}^{2+}$  doped crystals, the oscillator strengths of the absorption transitions are so small that the system can not be efficiently optically pumped. One way to overcome this problem is increasing the concentration of manganese ions. However, concentrated manganese systems generally exhibit strong radiationless quenching which leads to the disappearance of fluorescence at room temperature.<sup>1-4</sup>

Figure 2 shows the room temperature fluorescence emission of some concentrated manganese crystals whose spectral properties have not been previously characterized. The appearance of relatively strong room temperature fluorescence indicates weaker radiationless quenching than is present in other stoichiometric manganese crystals. To evaluate the potential usefulness of these materials in optical applications it is important to characterize the complete spectral dynamics of the system. The results of our investigation of the properties of  $\text{Mn}_2\text{SiO}_4$  crystals are summarized below. The laser-excited, time-resolved spectroscopy setup used for this work has been described previously.

The fluorescence emission of  $\text{Mn}_2\text{SiO}_4$  after pulsed laser excitation evolves in time from a band peaked at 700 nm to a band peaked at 800 nm. The time evolution of the ratio of the fluorescence intensities of the two bands at 150 K is shown in Fig. 3.

of crystals. These very different projects demonstrate how optical spectroscopy techniques can be used in vibronic laser research both in the search for new materials and in improving existing materials.

#### Acknowledgments

This work was sponsored by contracts from the Army Research Office and the Office of Naval Research.

#### References

- R.C. Powell, R.H. Schweitzer, J.J. Martin, G.E. Venikouas, and C.A. Hunt: J. Chem. Phys., to be published  
S. Basu and A.S. Chakravarty: Phys. Rev. B 26, 4327 (1982)  
J.B. Bates, J.C. Wang, and N.J. Dudley: Physics Today 35, 56 (1982)  
L. Xi, G.E. Venikouas, R.C. Powell, and J.B. Bates, to be published  
P.F. Moulton: Laser Focus 19, 83 (1983)  
G.J. Rosasco: Adv. in Infrared and Raman Spect. 7, 223 (1980)  
R.C. Powell, J.H. Bowen, A.W. Hounslow and J.L. Caslavsky, to be published  
J.C. Walling: Laser Focus 18, 45 (1982)  
A.M. Ghazzawi, J.K. Tyminski, R.C. Powell, and J.C. Walling, to be published

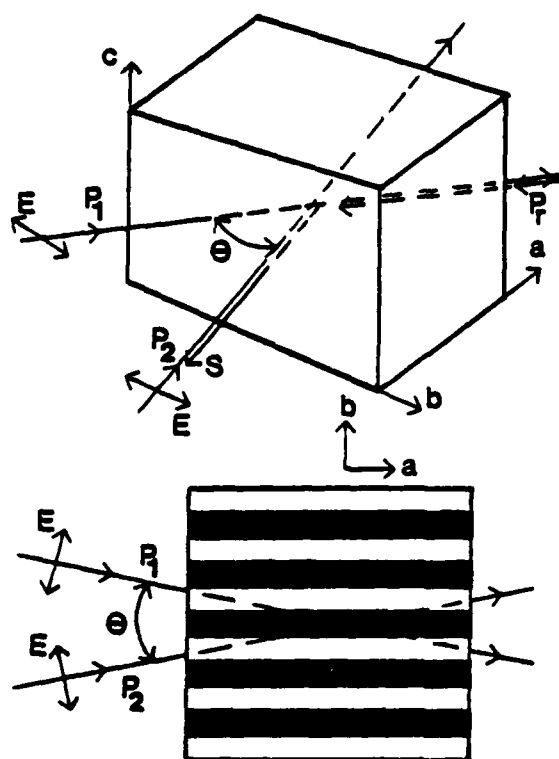


Fig. 6 Geometry of four-wave mixing experiment in alexandrite

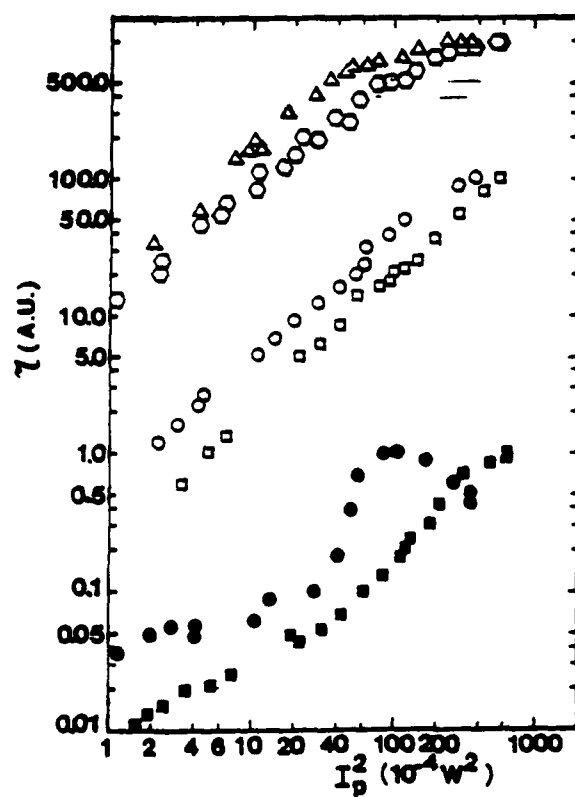


Fig. 7 Power dependence of four-wave mixing efficiency in alexandrite



fluorescence from  $\text{Ti}^{3+}$  was detected. When the laser was focused onto a scattering center the results were significantly different. No background  $\text{Ti}^{3+}$  fluorescence was observed and the Raman peaks shifted to positions similar to those obtained on a sample of  $\text{TiO}_2$ . The latter spectra are shown in Fig. 5.

The results of this work indicate that inclusions of  $\text{TiO}_2$  precipitates are responsible for the scattering centers in  $\text{Al}_2\text{O}_3:\text{Ti}^{3+}$  crystals. Adjusting crystal growth parameters to minimize the formation of these precipitates has resulted in crystals with a greatly reduced concentration of scattering centers.

#### IV. Four-Wave Mixing in Alexandrite Crystals

$\text{BeAl}_2\text{O}_4:\text{Cr}^{3+}$  (alexandrite) has been the most successful tunable solid state laser material to date [8]. To fully understand its operational limitation, it is important to understand all of the physical properties of the material. So far the nonlinear optical properties of alexandrite crystals have not been well characterized and we are currently using degenerate four-wave mixing techniques to do this [9].

This geometry of the experiment is shown in Fig. 6. Two beams from either an argon laser or an argon-pumped dye laser with R6G dye cross at an angle  $\theta$  inside the sample in the  $ab$  plane with horizontal polarization. The interference of these write beams  $P_1$  and  $P_2$  produce a holographic grating in the sample. The probe beam  $P_r$  is aligned conjugate to one of the write beams and Bragg diffracts off of the grating to give the signal beam  $S$ . By chopping the write beams off and monitoring the decay of the signal beam the dynamics of the grating decay can be studied.

We established and probed transient holographic gratings in an alexandrite crystal at three laser wavelengths, 488.0, 514.5, and 579.1 nm. The maximum phase conjugate scattering efficiency was approximately  $10^{-3}$  for each of these wavelengths for the orientation shown in Fig. 6. It was possible to form gratings only in the  $b$  direction. By measuring the grating decay rate as a function of the crossing angle of the write beams, it was found that the grating decay was consistent with the decay of the  $\text{Cr}^{3+}$  ions from the  ${}^2E$  level. This shows that the four-wave mixing is due to an excited state population grating and that no long range energy transfer among  $\text{Cr}^{3+}$  ions occurs. In addition, the results indicate that the 579.1 nm excitation selectively creates a grating with ions in the mirror sites while the other two wavelengths selectively create gratings with ions in the inversion sites. Figure 7 shows the variation of four-wave mixing scattering efficiency with write beam laser power. In general a quadratic dependence is observed as expected. Deviations from this occur for gratings created near the crystal surface. Also at high powers a tendency toward saturation can be observed.

The direct importance of nonlinear optical effects such as those described here to laser performance is not yet clear.

#### V. Summary

The preceding sections describe the use of time-resolved spectroscopy techniques to elucidate the spectral dynamics of 4d and 5d transition metal ions in crystals, laser Raman microprobe spectroscopy to identify crystal defects, and four-wave mixing spectroscopy to characterize nonlinear optical properties

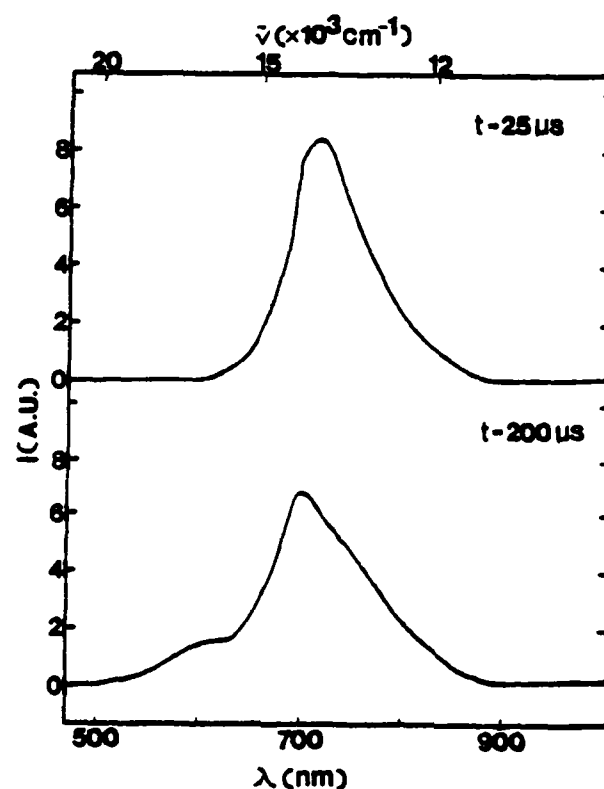


Fig. 4 Room temperature fluorescence spectra of  $\text{Rh}^{2+}$  in  $\text{Na } \beta''$ -alumina crystals at two times after pulsed  $\text{N}_2$  laser excitation

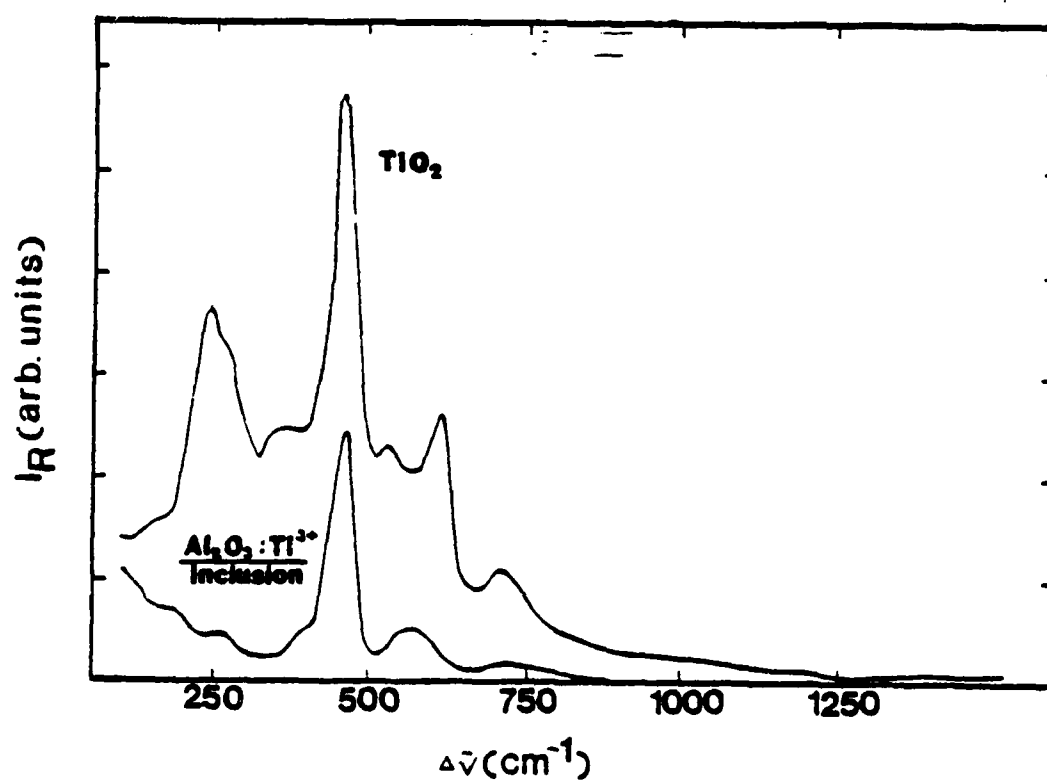


Fig. 5 Laser Raman microprobe spectrum of an inclusion in  $\text{Al}_2\text{O}_3:\text{Ti}^{3+}$  compared to the spectrum of  $\text{TiO}_2$  obtained under similar experimental conditions

concentrations of the order of 1 wt.%.

The  $\text{Rh}^{2+}$  absorption in  $\beta$ "-alumina crystals was again due to a CT band in the near uv region [4]. The fluorescence obtained at room temperature at two times after the  $\text{N}_2$  laser pumping pulse are shown in Fig. 4. The broad fluorescence emission band has a lifetime of about 5.2 ms implying that the dominant emission is from a spin forbidden d-d transition. This results in an extremely small peak emission cross section as listed in Table 1.

$\text{LiNbO}_3$  crystals are another type of host for  $\text{Rh}^{2+}$  ions. As indicated by the results given in Table 1, this material produces a broad emission band peaking near 568 nm and having a fluorescence lifetime of 0.577  $\mu\text{s}$ . This results in a very favorable peak emission cross section. Since laser induced "optical damage" which produces light scattering and absorption is known to be a severe problem in  $\text{LiNbO}_3$  crystals, they are not suitable for laser host materials. However, the spectral trends seen from the data listed in Table 1 may be helpful in identifying an appropriate host crystal for  $\text{Rh}^{2+}$  ions. As the parameter  $r$  decreases the crystal field strength at the  $\text{Rh}^{2+}$  ion site increases. The data show that the positions of the d emission band peaks shift to higher energy with increasing crystal field strength as predicted by the Sugano-Tanabe diagrams and the fluorescence lifetimes become shorter indicating a shift from predominantly spin forbidden to predominantly spin allowed emission. Apparently an optimum host for producing the desired peak emission cross section and accepting a high concentration of dopant ions will be one in which the  $\text{Rh}^{2+}$  ions replace ions having similar ionic radii. Various possibilities are currently being considered.

### III. Laser Raman Microprobe Analysis of $\text{Al}_2\text{O}_3:\text{Ti}^{3+}$ Crystals

Tunable vibronic laser action has been obtained from  $\text{Ti}^{3+}$  ions in  $\text{Al}_2\text{O}_3$  crystals and this material appears to quite promising as a new tunable solid state laser [5]. One problem which has inhibited the development of  $\text{Al}_2\text{O}_3:\text{Ti}^{3+}$  lasers is poor crystal quality. Although new crystal growth methods for sapphire based on heat exchange techniques have greatly improved undoped host crystal quality, doped crystals suffer from the presence of small inclusions or bubbles. These scatter light and thus act as a loss mechanism when the material is used in laser applications. Thus it is important to identify the nature of these scattering centers so crystal growth parameters can be changed in such a way to minimize their concentration.

Laser Raman scattering has been developed as a useful spectroscopic tool for identifying different chemical species. Used in conjunction with a microscope, laser Raman microprobe spectroscopy can be used to study micron size regions of a sample [6]. We recently applied this technique to the study of inclusions in  $\text{Al}_2\text{O}_3:\text{Ti}^{3+}$  crystals using a Spectra Physics argon ion laser with an Instruments SA microscope, monochromator, and computer system [7].

The samples used in this work were grown by Dr. J. L. Caslavsky using the VSOM method. A significant concentration of scattering centers could be seen visually. Laser Raman microprobe spectra were obtained both in the normal region of the sample and by focusing the laser on one of the scattering centers.

In the perfect region of the crystal the Raman peaks coincided closely with those observed in undoped sapphire crystals and a strong background

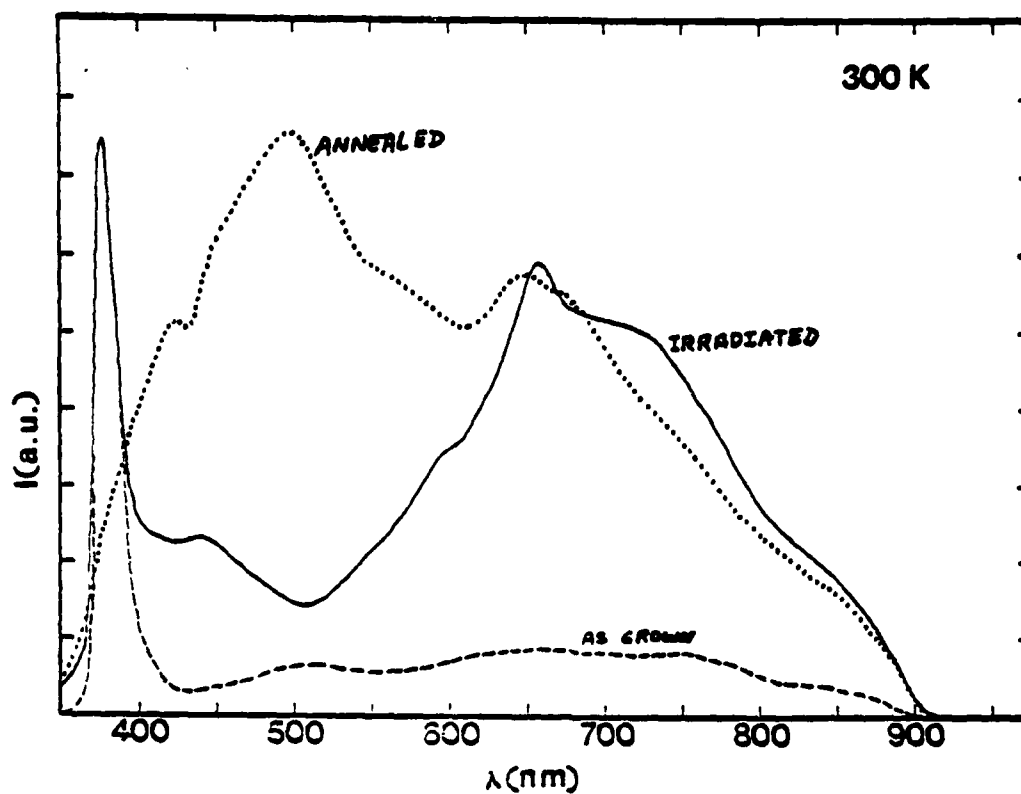


Fig. 3 Fluorescence spectra of  $\text{KBr:Rh}^{2+}$  at 300 K after pulsed  $\text{N}_2$  laser excitation. ---- untreated sample; — irradiated sample; . . . . . annealed sample.

Table 1.  $\text{Rh}^{2+}(4d^7)$  Spectroscopic Parameters

PARAMETER	HOST CRYSTAL		
	Na $\beta''$ -Alumina	KBr	$\text{LiNbO}_3$
$r[\text{\AA}]$	11.27	1.33	0.60
$\lambda_p [\text{nm}]$	700	650	568
$\Delta\lambda [\text{nm}]$	130	270	72
$\tau_f [\mu\text{s}]$	5200	25	0.577
$\sigma_p [10^{-21} \text{cm}^2]$	0.047	2. ]0	627

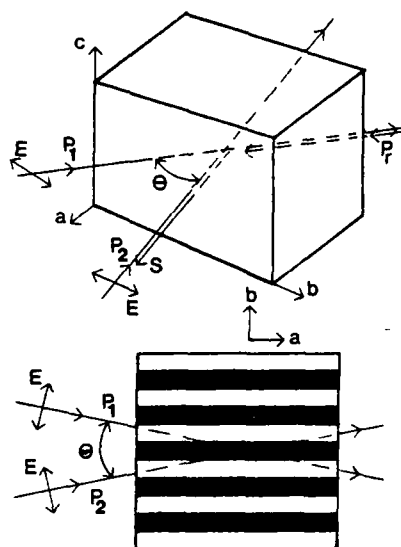


FIG. 2. Geometry of the laser-beam directions and polarizations with respect to the crystallographic axes for obtaining a strong FWM signal in alexandrite crystals.

beam decay rate  $K$  and scattering efficiency  $\eta$ , were determined at various write-beam crossing angles between  $1.75^\circ$  and  $26.5^\circ$  with various laser powers between about 2 and 400 mW for each write beam. The signal decay was purely exponential for all measurements in the time regime investigated. The decay rate was found to be independent of pump beam crossing angle  $\theta$  for all three wavelengths as shown in Fig. 3(a). The magnitude of the decay rate was significantly different for long wavelength pumping compared to pumping with the two shorter wavelengths. For each case it was approximately equal to twice the fluorescence decay rate shown as solid points at  $\theta=0^\circ$ . The grating decay rates were also found to be independent of the power in the write beams as shown in Fig. 3(b).

For the long-wavelength dye laser pumping the relative fraction of the probe beam converted to the signal beam varied quadratically with laser power for all conditions investigated. Pumping with the higher power argon-ion laser at shorter wavelengths also produced quadratic dependences of FWM signal efficiencies at high write-beam crossing angles, but saturation effects were observed for small crossing angles as seen in Fig. 4. If the write beams are oriented to cross near the surface of the sample, significant deviations from quadratic behavior and saturation effects are observed.

### III. DISCUSSION AND CONCLUSIONS

These results can be interpreted in terms of the model of FWM (Refs. 12 and 13) based on scattering from a laser-induced, transient population grating. The interference of the Gaussian wave fronts of the write beams in the region of their crossing forms a sinusoidal pattern resulting in a similar spatial distribution of  $\text{Cr}^{3+}$  ions in the excited state. Because of the difference in the absolute

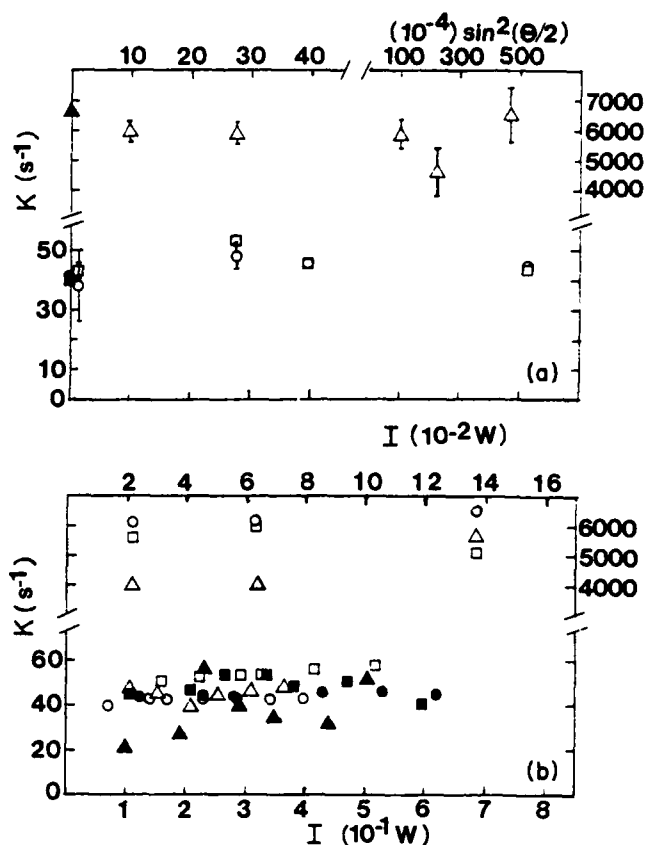


FIG. 3. (a) FWM signal decay rate versus pump beam crossing angle:  $\lambda_x = 579.1$  nm ( $\Delta$ );  $488.0$  nm ( $\circ$ ); and  $514.5$  nm ( $\square$ ). The solid points represent twice the fluorescence decay rates. (b) FWM signal-decay rate versus total pump beam power. Upper scale for  $\lambda_x = 579.1$  nm:  $\theta = 3.5^\circ$  ( $\circ$ );  $\theta = 11.5^\circ$  ( $\Delta$ );  $\theta = 17.3^\circ$  ( $\square$ ). Lower scale for  $\lambda_x = 488.0$  nm:  $\theta = 1.75^\circ$  ( $\Delta$ );  $\theta = 6.0^\circ$  ( $\blacksquare$ );  $\theta = 26.5^\circ$  ( $\bullet$ ); and for  $\lambda_x = 514.5$  nm:  $\theta = 1.75^\circ$  ( $\Delta$ );  $\theta = 6.0^\circ$  ( $\square$ );  $\theta = 26.5^\circ$  ( $\circ$ ).

value of the complex dielectric constant of the material when the  $\text{Cr}^{3+}$  ions are in the ground or excited states, this sinusoidal excited-state population distribution acts as a diffraction grating which scatters the read beam. When the Bragg condition is satisfied, this becomes the FWM signal beam which can be theoretically expressed as<sup>4</sup>

$$\eta(t) \propto [\Delta N(I)]^2 = \eta_p e^{-Kt}, \quad (1)$$

where  $\Delta N$  is the difference in the concentration of excited  $\text{Cr}^{3+}$  ions between the peak and valley regions of the grating and  $I$  is the power of the laser write beams. The decay rate  $K$  contains terms describing all physical processes contributing to the grating relaxation. The term related to the fluorescence decay of the excited ions is  $2/\tau$ , where  $\tau$  is the fluorescence decay time of the ions in the excited state. Other terms depend on  $\theta$  (such as long-range energy migration) or on laser power (such as stimulated emission). The fact that the results obtained here exhibit exponential decays with  $K=2/\tau$  independent of  $\theta$  and  $I$  shows that the gratings created are excited-state-population gratings and that no effects of long-range ener-

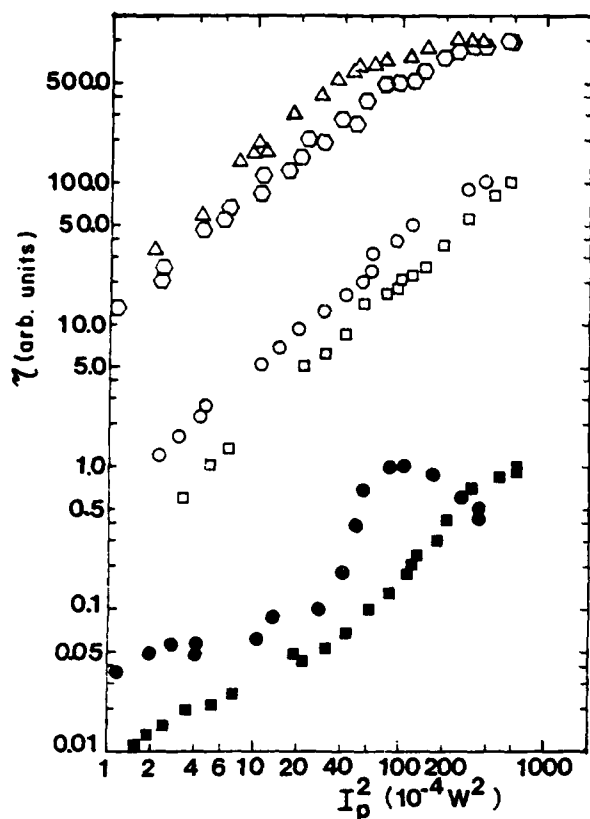


FIG. 4. Fraction of probe beam converted to FWM signal as a function of the product of the powers of the laser pump beams. Bulk:  $\lambda=488.0$  nm,  $\theta=6^\circ$  (○);  $\lambda=514.5$  nm,  $\theta=6^\circ$  (△);  $\lambda=488.0$  nm,  $\theta=26.5^\circ$  (□);  $\lambda=514.5$  nm,  $\theta=26.5^\circ$  (○). Surface:  $\lambda=488.0$  nm,  $\theta=26.5^\circ$  (■);  $\lambda=514.5$  nm,  $\theta=26.5^\circ$  (●).

gy transfer or stimulated emission are contributing to the grating decay.

The fact that the decay rates are significantly different for the two different types of laser excitation can be understood from the absorption and fluorescence spectra shown in Fig. 5. The dye laser excitation at 579.1 nm efficiently excites  $\text{Cr}^{3+}$  ions in the mirror sites as demonstrated by the dominance of the two  $R_m$  lines in the fluorescence spectrum. The measured fluorescence decay rate is consistent with that of the coupled emission from the  $^2E$  and  $^4T_2$  levels of  $\text{Cr}^{3+}$  ions in this type of site.<sup>2</sup> On the other hand, the 488.0- and 514.5-nm excitation wavelengths of the argon laser excite a significant number of  $\text{Cr}^{3+}$  ions in the inversion sites as seen by the enhancement of the  $R_i$  lines from these sites in the fluorescence spectrum. The smaller fluorescence decay rate is consistent with the weaker transition strengths of ions in this type of site.<sup>2</sup> Excitation spectra for the ions in the two types of sites verify the existence of different absorption bands associated with these ions which result in the selective excitation for the three different wavelengths used.<sup>14</sup>

The strength of the FWM signal depends on the difference of the concentration of ions in the excited state between the peak and valley regions of the grating  $\Delta N$  and on the difference in the complex dielectric constant of the

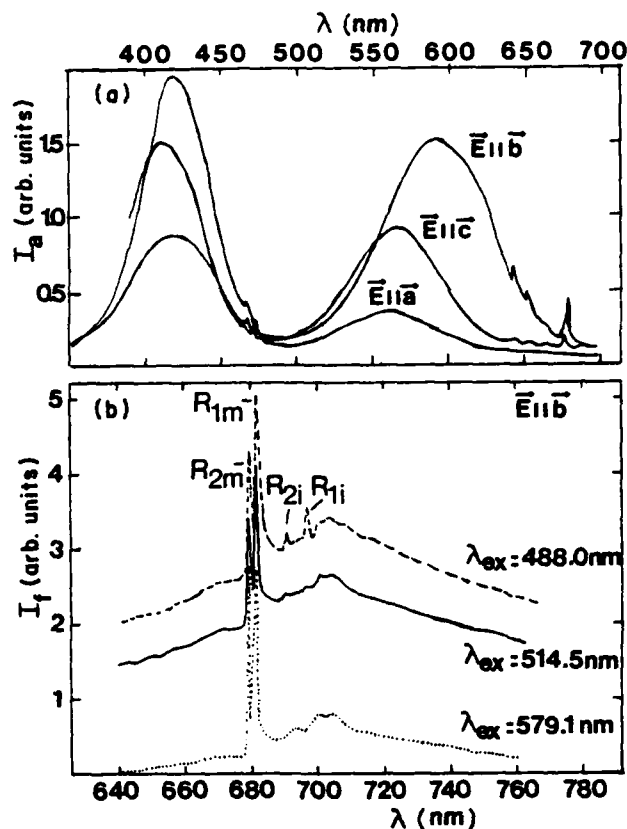


FIG. 5. Absorption and fluorescence spectra of  $\text{BeAl}_2\text{O}_4:\text{Cr}^{3+}$ .

material when the ions are in the excited state and when they are in the ground state. The former depends on the cross section of the  $^4A_2 \rightarrow ^4T_2$  transition which is seen in Fig. 5(a) to be large for  $\vec{E}||\vec{b}$ , medium for  $\vec{E}||\vec{c}$ , and small for  $\vec{E}||\vec{a}$ . This is consistent with the fact that a strong FWM signal is only observed with the first of these polarization orientations, a weak signal with the second, and no signal with third.

The complex dielectric constant is  $\epsilon = \epsilon_r + i\epsilon_i$ . The change in  $\epsilon$  can be associated with either a difference in the absorption coefficient,  $\Delta\alpha = \frac{1}{2}(2\pi/\lambda)\Delta\epsilon_i/(\epsilon_r)^{1/2}$ , or a difference in the refractive index,  $\Delta n = \frac{1}{2}\Delta\epsilon_r/(\epsilon_r)^{1/2}$ . In a simple two-level model, the expression for FWM scattering efficiency is given by<sup>12</sup>

$$\eta = e^{-2\alpha\Gamma} [\sinh^2(\Delta\alpha\Gamma/2) + \sin^2(\pi\Delta n\Gamma/\lambda)], \quad (2)$$

where  $\Gamma = d/\cos\theta$  with  $d$  being the sample thickness and  $\bar{\alpha}$  is the average absorption coefficient at the laser wavelength  $\lambda$ . Absorption gratings are associated with differences in the absorption cross sections of ions in the ground and excited states. The peak-to-valley difference in the absorption coefficient grating is<sup>15</sup>

$$2\Delta\alpha = \frac{2[N_0 I_0 \sigma_1 (\sigma_2 - \sigma_1)]}{2I_0 \sigma_1 + (h\nu)\tau_{21}^{-1}}, \quad (3)$$

where  $N_0$  is the total concentration of active ions,  $I_0$  is the energy density of the laser pump beams with photon

energy ( $h\nu$ ), and  $\tau_{21}$  is the fluorescence decay time of the excited state.

Under optimum conditions, the scattering efficiency is measured to be approximately  $10^{-3}$ . Using Eq. (3) and the excited-state absorption results reported in Ref. 8, the numerator in Eq. (2), which represents the contribution to the scattering due to an absorption grating, can be calculated. Then using this result and the measured value for  $\eta$  in Eq. (2), the denominator, which represents the contribution to the scattering due to a dispersion grating, can be estimated. For the three laser pump wavelengths used in this work, the ratios of the absorption grating term to the dispersion grating term are  $3.0 \times 10^{-4}$  (488.0 nm), 0.0 (514.5 nm), and  $3.0 \times 10^{-6}$  (579.1 nm). These results indicate that for these excitation wavelengths the FWM signal is due mainly to scattering from a dispersion grating. The parameters obtained from this work are summarized in Table I.

It is difficult to theoretically calculate the contribution to the FWM signal due to dispersion changes since this involves the sum over all possible transitions of the  $\text{Cr}^{3+}$  ions in both the ground and metastable states. Using a simple two-oscillator model for dispersion, the change in the index of refraction between the peak and valley regions of the grating can be approximated as<sup>16</sup>

$$2\Delta n = (N_{2p}/n_0) \{ f_1' (1 - \omega/\omega_1) / [4(\omega_1 - \omega)^2 + \gamma_1^2] + f_2' (1 - \omega/\omega_2) / [4(\omega_2 - \omega)^2 + \gamma_2^2] \}. \quad (4)$$

Here  $f_i'$  is the effective oscillator strength of the  $i$ th transition,  $\gamma_i$  is the width of the transition, and  $\omega_i - \omega$  is the detuning from the center of the transition.  $n_0$  is the index of refraction of the unperturbed sample.  $N_{2p}$  represents the number of ions in the excited state in the peak region of the grating which is given by

$$N_{2p} = 2I_0 N_0 \sigma_1 / [2I_0 \sigma_1 + (hc/\lambda\tau_{21})]. \quad (5)$$

Taking the two transitions originating from the ground and metastable states closest to resonance with the incident laser frequency, Eqs. (4) and (5) predict values of  $\Delta n$  three orders of magnitude smaller than those listed in Table I. The required values of  $\Delta n$  can be obtained from this simple model only if the high oscillator strength charge-transfer transitions in the near uv spectral region are included. This latter conclusion is important in developing a general understanding of the FWM signal in materials such as transition-metal and rare-earth-doped crystals.

The fact that saturation of the scattering efficiency versus power occurs at small pump beam crossing angles and not at large angles may be due to the efficiency of coupling the light laser power level in Fig. 4, the effective

TABLE I. Summary of results of FWM measurements on alexandrite.

Parameter	Excitation wavelength (nm)		
	488.0	514.5	579.1
$\eta$	$\sim 10^{-3}$	$\sim 10^{-3}$	$\sim 10^{-3}$
$I_0$ (W/cm <sup>2</sup> )	60	60	12
$\lambda_{21}$ (ms)	49.1	50.3	0.30
$\bar{\alpha}$ (cm <sup>-1</sup> )	0.36	0.54	2.80
$N_{2p}$ (cm <sup>-3</sup> )	$8.74 \times 10^{17}$	$1.31 \times 10^{18}$	$5.3 \times 10^{16}$
$\Delta\alpha$ (cm <sup>-1</sup> )	$2.62 \times 10^{-3}$	0.00	$-8.70 \times 10^{-4}$
$\Delta n$	$6.74 \times 10^{-5}$	$7.78 \times 10^{-5}$	$2.72 \times 10^{-4}$

power inside the sample is significantly greater for the  $\theta = 6^\circ$  data than for the  $\theta = 26.5^\circ$  data. The values of  $N_{2p}$  listed in Table I for the three excitation wavelengths represent 13% (488.0 nm), 19% (514.5 nm), and 0.22% (579.1 nm) of the ions available. Thus a significant number of  $\text{Cr}^{3+}$  ions are in the  $^2E$  level in these experiments but the total saturation level of 50% is not reached. Note that Eq. (5) shows that  $N_{2p}$  depends on the absorption cross section, the laser power, and the metastable-state lifetime. For  $\text{Cr}^{3+}$  ions in the inversion sites the first of these factors is small but the latter two are large compared to the ions in the mirror sites. This explains why  $N_{2p}$  can be large for pumping with argon laser wavelengths which fall in the valley between the two major absorption bands shown in Fig. 5.

The FWM signal efficiency for alexandrite is approximately the same as that of a similar sample of ruby. FWM in ruby has been investigated by several workers<sup>13,15,17-19</sup> and the signal has been attributed to a  $\text{Cr}^{3+}$  population grating as proposed here. There is some disagreement as to whether scattering is due to an absorption or dispersion grating. Thermal gratings with shorter, angle-dependent decay rates were also observed in ruby<sup>19</sup> and will be the subject of a future investigation of alexandrite. For both ruby and alexandrite crystals the laser-induced changes in the dielectric constant are significantly greater for the population gratings created through pumping the  $\text{Cr}^{3+}$  ions than for intrinsic host-crystal properties investigated by off-resonance pumping.<sup>20</sup> The nonlinear properties of the type investigated here are known to affect laser operational properties in ruby<sup>21</sup> and thus may also be important in alexandrite laser operation.

#### ACKNOWLEDGMENTS

This work was sponsored by grants from Allied Chemical Corporation, the U.S. Army Research Office, and the National Science Foundation under Grant No. DMR 82-16551.

<sup>1</sup>J. C. Walling, *Laser Focus* 18, 45 (1982).

<sup>2</sup>J. C. Walling, O. G. Peterson, H. P. Jenssen, R. C. Morris, and E. W. O'Dell, *IEEE J. Quant. Elect.* QE-16, 1302 (1980).

<sup>3</sup>J. C. Walling, H. P. Jenssen, R. C. Morris, E. W. O'Dell, and O. G. Peterson, *Opt. Lett.* 4, 182 (1979).

<sup>4</sup>J. C. Walling and L. Horowitz, in *Lasers 80*, edited by C. B. Collins (STS, McLean, Virginia, 1980), p. 534.

<sup>5</sup>J. C. Walling and O. G. Peterson, *IEEE J. Quant. Elect.* QE-16, 119 (1980).

<sup>6</sup>C. F. Cline, R. C. Morris, M. Dutoit, and P. J. Harget, *J.*

- Mater. Sci. 14, 941 (1979).
- <sup>7</sup>M. L. Shand, J. Appl. Phys. 54, 2602 (1983).
- <sup>8</sup>M. L. Shand, J. C. Walling, and R. C. Morris, J. Appl. Phys. 52, 953 (1981).
- <sup>9</sup>B. K. Sevast'Yanov, Yu. I. Remigailo, V. P. Orekhova, V. P. Matrosov, E. G. Tsvetkov, and G. V. Bukin, Dokl. Akad. Nauk SSR 256, 373 (1981) [Sov. Phys.—Dokl. 26, 62 (1981)].
- <sup>10</sup>J. Feinberg, in *Optical Phase Conjugation*, edited by R. A. Fisher (Academic, New York, 1983), p. 417.
- <sup>11</sup>C. M. Lawson, R. C. Powell, and W. K. Zwicker, Phys. Rev. B 26, 4836 (1982); Phys. Rev. Lett. 46, 1020 (1981); and J. K. Tyminski, R. C. Powell, and W. K. Zwicker, Phys. Rev. B 29, 6074 (1984).
- <sup>12</sup>H. Kogelnik, Bell Syst. Tech. J. 48, 2909 (1969).
- <sup>13</sup>H. J. Eichler, J. Eichler, J. Knof, and Ch. Noack, Phys. Status Solidi A 52, 481 (1979).
- <sup>14</sup>L. Xi, X. Gang, R. C. Powell, and J. C. Walling, (unpublished).
- <sup>15</sup>K. O. Hill, Appl. Opt. 10, 1695 (1971).
- <sup>16</sup>K. A. Nelson, R. Cassalegno, R. J. D. Miller, and M. D. Fayer, J. Chem. Phys. 77, 1144 (1982).
- <sup>17</sup>D. S. Hamilton, D. Heiman, J. Feinberg, and R. W. Hellwarth, Opt. Lett. 4, 124 (1979).
- <sup>18</sup>P. F. Liao, L. M. Humphrey, D. M. Bloom, and S. Geschwind, Phys. Rev. B 20, 4145 (1979); P. F. Liao and D. M. Bloom, Opt. Lett. 3, 4 (1978).
- <sup>19</sup>H. Eichler, G. Salje, and H. Stahl, J. Appl. Phys. 44, 5383 (1973).
- <sup>20</sup>M. J. Weber, D. Milam, and W. L. Smith, Opt. Eng. 17, 463 (1978).
- <sup>21</sup>H. Eichler, P. Glozbach, and B. Kluzowski, Z. Angew. Phys. 28, 303 (1970).



#### IV. INVESTIGATION OF THE SPECTRAL DYNAMICS OF LASER MATERIALS UNDER MULTIPHOTON EXCITATION

The manuscript in this section describes the results of studying the spectral dynamics of the important laser material  $\text{Y}_3\text{Al}_5\text{O}_{12}:\text{Nd}^{3+}$  following excitation by a high-power, picosecond pulse. This type of excitation produces transitions not observed with normal flashlamp pumping of Nd-YAG. This work resulted in the identification and characterization of the properties of new multiphoton absorption transitions, new metastable states, and new radiationless relaxation processes in this material. This information may be useful in developing new excitation schemes for Nd-YAG lasers involving u.v., high power, or cascade pumping techniques.

## Spectroscopy of $\text{Y}_3\text{Al}_5\text{O}_{12}:\text{Nd}^{3+}$ under high-power, picosecond-pulse excitation

George E. Venikouas, Greg J. Quarles, John P. King,\* and Richard C. Powell

*Department of Physics, Oklahoma State University, Stillwater, Oklahoma 74078*

(Received 7 March 1984)

High-power, picosecond-pulse excitation was used to study the dynamics of the pumping and decay processes in  $\text{Y}_3\text{Al}_5\text{O}_{12}:\text{Nd}^{3+}$ . The observed fluorescence spectral lines are assigned to transitions from three different metastable states excited by both single-photon and two-photon absorption. The branching ratios, lifetimes, and quantum efficiencies of the metastable states are obtained from the data as well as the two-photon absorption cross sections. The results provide useful information concerning ultraviolet pumping efficiencies of the Nd-YAG (Nd-doped yttrium aluminum garnet) laser transition and the  $5d-4f$  nonradiative decay rate for this material. In addition, the time-resolved spectroscopy method employed here is shown to be an extremely sensitive technique for obtaining two-photon absorption cross sections.

### I. INTRODUCTION

Despite the importance of  $\text{Y}_3\text{Al}_5\text{O}_{12}:\text{Nd}^{3+}$  (Nd-YAG) as a solid-state laser material, there are still some aspects of its spectroscopic properties which are not well characterized.<sup>1</sup> One area in which very little work has been done is in studying the pumping and relaxation dynamics of the higher-energy electronic states of the  $\text{Nd}^{3+}$  ion.<sup>2-4</sup> These states can be reached by ultraviolet, x-ray, electron-beam, or high-power multiphoton visible laser excitation. For some specific applications, these pumping sources may be preferable to the standard visible flashlamp pumping and thus it is important to understand the spectral dynamics of these upper energy levels.

We report here the results of an investigation of the spectroscopic properties of a Nd-YAG crystal after excitation by high-power picosecond pulses from the various harmonics of a Nd-YAG laser. The time-resolved fluorescence spectra, fluorescence lifetimes, and rise times were measured as a function of laser power for frequency-doubled, -tripled, and -quadrupled Nd-YAG laser lines. The results are consistent with emission from three metastable states after single-photon and two-photon pumping. Models are proposed to describe the observed spectral dynamics, and comparing their predictions to the experimental results provides information such as the quantum efficiencies and branching ratios for the metastable states as well as the two-photon absorption cross sections. The results provide the first measured value for the  $5d-4f$  radiationless decay rate for this system. In addition, it is shown that the time-resolved spectroscopy technique employed here is a very sensitive way to determine two-photon cross sections.

### II. EXPERIMENTAL PROCEDURE

A block diagram of the experimental setup is shown in Fig. 1. A passively mode-locked, Nd-YAG oscillator provides a train of pulses and a pulse-switching network selects a single pulse from the train. This is sent through

an amplifier resulting in a pulse of about 30 ps in duration and 25 mJ energy. Frequency-doubling, -tripling, or -quadrupling crystals are used to obtain the desired wavelength for sample excitation.

The sample investigated was cut from a commercial laser rod and contained 0.87 at. %  $\text{Nd}^{3+}$ . The quantum efficiency of the  $^4F_{3/2}$  level was previously measured to be about 60%.<sup>5</sup>

The sample fluorescence is analyzed by a  $\frac{1}{4}$ -m monochromator and detected by an RCA C31034 photomultiplier tube. The signal is processed by a boxcar integrator triggered by the laser to obtain time-resolved spectra. The signal-to-noise ratio is improved by a signal averager before the results are displayed on a chart recorder. A beam splitter picks off part of the pulse to monitor the shot-to-shot intensity variation of the laser.

The energy levels of the  $4f^3$  electronic configuration of  $\text{Nd}^{3+}$  are shown in Fig. 2. Additional states belonging to

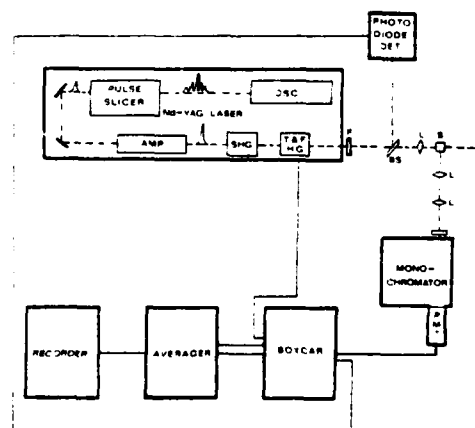


FIG. 1. Experimental apparatus for high-power, picosecond-pulse excitation experiments. The laser is a passively mode-locked Nd-YAG system with a single-stage amplifier and frequency-doubling, -tripling, and -quadrupling crystals. F, filter; BS, beam splitter; L, lens; S, sample.

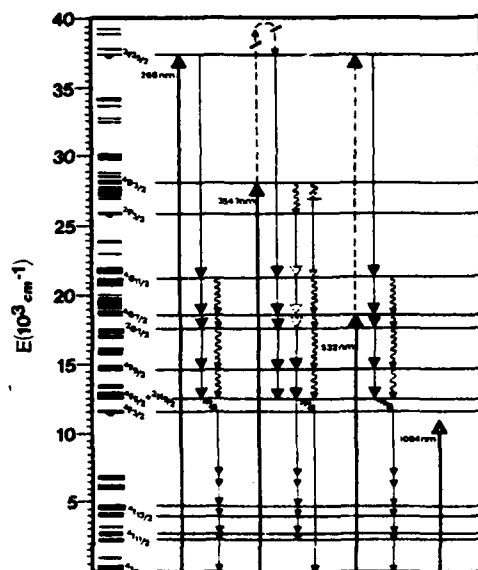


FIG. 2. Energy levels of the  $4f^3$  configuration of  $\text{Nd}^{3+}$  with important multiplets labeled, approximate crystal-field splittings indicated by linewidths, and the observed metastable states in YAG indicated as semicircles. (The highest metastable state is referred to as either  $^2(F2)_{5/2}$  or  $\beta^2F_{5/2}$  in the literature;<sup>2,3</sup> we have arbitrarily chosen to use the former notation.) The important absorption and emission transitions for the different excitation wavelengths used in this work are also shown. The solid arrows with straight shafts represent radiative transitions, and those with dashed shafts represent two-photon transitions; the wavy shafts represent radiationless transitions. Arrows with open heads represent infrared transitions which are implied but not directly observed in this work.

the  $4f^25d$  configuration are found at higher energy beginning at about  $40\,000\text{ cm}^{-1}$ . Typical spectroscopic studies have involved excitation in the visible region of the spectrum, resulting in fast radiationless relaxation to the  $^4F_{3/2}$  metastable state after which fluorescence emission occurs in the near-infrared spectral region. The four Nd-YAG-laser harmonic lines used for pumping are shown in the figure. Attempts to excite fluorescence with multiphoton absorption of the primary 1064-nm radiation were unsuccessful. The doubled output at 532 nm resulted in

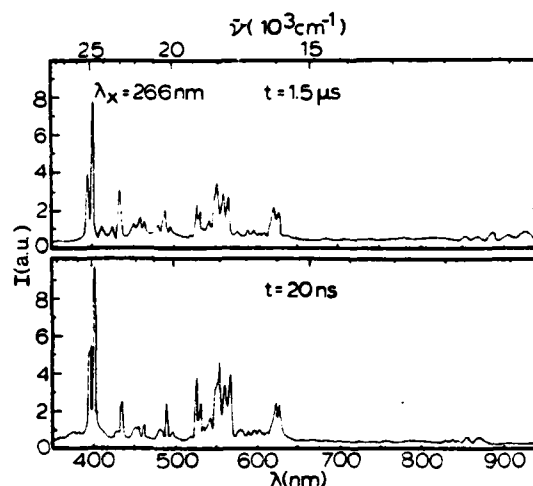


FIG. 3. Fluorescence spectra of Nd-YAG at two times after the excitation pulse at 266 nm.

single-photon absorption in the  $^4G_{7/2}$  level and two-photon absorption to the  $^2(F2)_{5/2}$  level<sup>2,3</sup> (or  $\beta^2F_{5/2}$ ). The tripled output at 354.7 nm gives single-photon absorption in the  $^4D_{3/2}$  level and two-photon absorption in the  $5d$  levels. The quadrupled output at 266 nm results in single-photon absorption in the  $^2(F2)_{5/2}$  level and no observed two-photon absorption. The properties of the fluorescence emission observed after these different types of pumping are discussed in the following sections.

### III. RESULTS FOR 266-nm PUMPING

Figure 3 shows the fluorescence spectra obtained at two times after the excitation pulse for quadrupled Nd-YAG-laser pumping at 266 nm. For this excitation wavelength, the emission intensity of all of the lines in the spectrum are found to vary linearly with pump power, indicating that single-photon absorption is responsible for exciting all of these transitions. The spectral lines can be divided into two distinct groups according to their lifetimes as seen by the spectra recorded at two different times after the pulse as shown in Fig. 3. These are associated with fluorescence emission transitions from two dif-

TABLE I. Characteristics of metastable states in Nd-YAG.

Parameter	$^4F_{3/2}$	State $^2P_{3/2}$	$^2(F2)_{5/2}$
$\tau_f$ ( $\mu\text{s}$ )	220	0.32	3.02
$\eta$	0.60	0.96	0.99
$\Delta E$ ( $\text{cm}^{-1}$ )	4600	2150	3400
$B_1$	$^4I_{9/2}$ : 0.366 $^4I_{11/2}$ : 0.500 $^4I_{13/2}$ : 0.130 $^4I_{15/2}$ : 0.004	$^4I_{11/2}$ : $2.4 \times 10^{-4}$ $^4I_{13/2}$ : $1.44 \times 10^{-4}$ $^4F_{3/2}$ : $1.36 \times 10^{-4}$ $^4F_{9/2}$ : $2.8 \times 10^{-4}$ ir: 0.9992	$^4F_{3/2}$ : 0.23 <sup>a</sup> $^4F_{9/2}$ : 0.03 $^2G_{7/2}$ : 0.03 $^4G_{7/2}$ : 0.43 $^4G_{11/2}$ : 0.28

<sup>a</sup>Also includes transitions to the  $^2H_{9/2}$  levels.

ferent metastable states. Figure 2 shows that this excitation wavelength directly pumps the  $^2(F2)_{5/2}$  level. The lines appearing in the fluorescence spectrum with a lifetime of  $3.02 \mu\text{s}$  are associated with transitions from this level to the various crystal-field-split components of the  $^4G_{11/2}$ ,  $^4G_{7/2}$ ,  $^2G_{7/2}$ ,  $^4F_{9/2}$ , and  $^4F_{5/2} + ^2H_{9/2}$  multiplets after which fast radiationless decay occurs to the  $^4F_{3/2}$  level. This is followed by the well-known near-infrared emission transitions having a lifetime of  $220 \mu\text{s}$ .

Thus from the time-resolved spectra after 266-nm excitation, the  $^2(F2)_{5/2}$  level is identified as a second metastable state for  $\text{Nd}^{3+}$  emission in YAG crystals. The branching ratios for the emission transitions from this level to the different terminal multiplets are given by

$$B_i = \sum_j I_{ij} / \sum_{i,j} I_{ij}, \quad (1)$$

where  $i$  represents the different free-ion-term values and  $j$  represents the different crystal-field components within each term. The branching ratios for this upper metastable state are found from the spectra shown in Fig. 3 and listed in Table I.

The time evolution of the spectra shown in Fig. 3 can be described by the simplified rate model shown in Fig. 4.  $n_1$  and  $n_3$  represent the concentration of ions in excited states  $^4F_{3/2}$  and  $^2(F2)_{5/2}$ , respectively,  $\beta_1$  and  $\beta_3$  are the fluorescence decay rates of these levels, and  $W_3$  is the pumping rate for the upper metastable state. The rate equations describing the time evolution of the excited state populations are

$$\frac{dn_1}{dt} = \beta_3 n_3 - \beta_1 n_1, \quad (2)$$

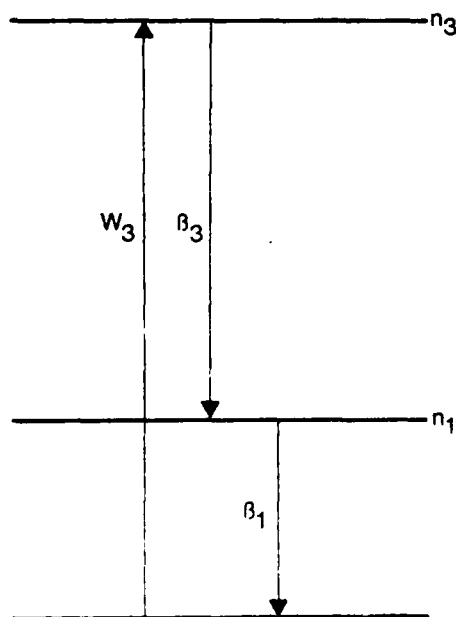


FIG. 4. Model for explaining observed spectral dynamics after 266-nm excitation. See text for definition of parameters.

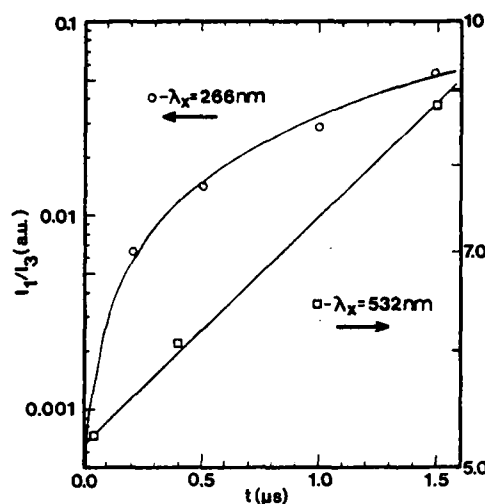


FIG. 5. Time evolution of the ratios of the integrated fluorescence intensities of the emission from the  $^4F_{3/2}$  and  $^2(F2)_{5/2}$  metastable states after 266- and 532-nm excitations. See text for explanation of the theoretical line.

$$\frac{dn_3}{dt} = W_3 - \beta_3 n_3. \quad (3)$$

The basic assumptions of this model are that the  $^4F_{3/2}$  level is pumped only through relaxation from the  $^2(F2)_{5/2}$  level and that the latter level has 100% quantum efficiency and has no radiative transitions that bypass the former level and terminate on levels of the ground-state term or that result in unobserved infrared radiation. The solutions of Eqs. (2) and (3) for  $\delta$ -function excitation can be related to the measured relative fluorescence intensity ratios through

$$I_1(t)/I_3(t) = K [\beta_3/(\beta_3 - \beta_1)] \{ \exp[(\beta_3 - \beta_1)t] - 1 \}, \quad (4)$$

where  $k = \beta_1' B_1 / \beta_3'$ . Here, the  $\beta_i'$  are the radiative decay rates of the two metastable states and  $B_1$  is the branching ratio for the transitions from the lower metastable state to the  $^4I_{9/2}$  ground-state levels. Figure 5 shows the ratios of the integrated fluorescence intensities of all of the  $^2(F2)_{5/2}$  transitions and the visible transitions from the  $^4F_{3/2}$  level shown in Fig. 3. The solid line represents the prediction of Eq. (4) with no adjustable parameters. The excellent fit between theory and experiment indicates that the assumptions underlying the simplified model used here are justified for this case.

#### IV. RESULTS FOR 532-nm PUMPING

Figure 6 shows the fluorescence spectra at two times after the laser excitation pulse for doubled Nd-YAG pumping at 532 nm. The same lines appear in the spectra as seen in Fig. 3, but their relative intensities are different and change with pumping power. As an example of this, Fig. 7 shows the change in the integrated fluorescence intensity of the major emission line at 402 nm as a function of excitation-pulse energy. The observed quadratic depen-

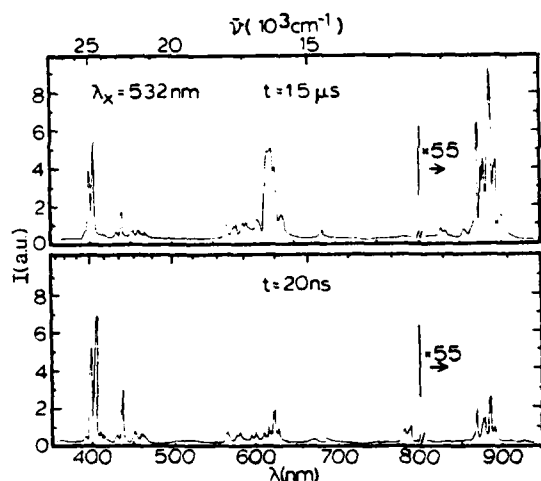


FIG. 6. Fluorescence spectra of Nd-YAG at two times after the excitation pulse at 532 nm.

dence indicates that this excitation wavelength results in two-photon absorption terminating on the  $^2(F2)_{5/2}$  metastable state. The fluorescence from this level is the same as that discussed in the preceding section following single-photon pumping. As seen in Fig. 2, the intermediate state for this two-photon transition is the  $^4G_{7/2}$  level, which is directly pumped through one-photon absorption processes. Only part of the ions excited to this intermedi-

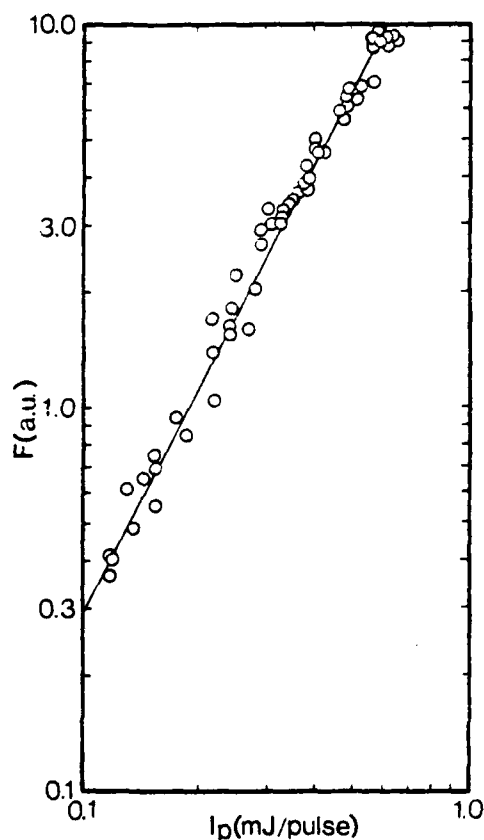


FIG. 7. Integrated fluorescence intensity of the 402-nm spectral line as a function of laser power at 532-nm excitation.

ate state undergo two-photon excitation, while the rest decay radiationlessly to the  $^4F_{3/2}$  metastable state from which the standard emission transitions occur.

The excited-state dynamics for this case can be described by a simplified rate model similar to that shown in Fig. 4, but with an additional parameter  $W_1$  to describe the single-photon pumping rate of the  $^4F_{3/2}$  metastable state through fast radiationless relaxation from the  $^4G_{7/2}$  level and with the two-photon pumping rate of the  $^2(F2)_{5/2}$  metastable state given by  $W'_3$ . The rate equations for this model are

$$\frac{dn_1}{dt} = W_1 + \beta_3 n_3 - \beta_1 n_1, \quad (5)$$

$$\frac{dn_3}{dt} = W'_3 - \beta_3 n_3. \quad (6)$$

The basic assumption of this model is that the cascade nonradiative decay processes from the  $^4G_{7/2}$  state to the  $^4F_{3/2}$  state are very fast and efficient. The ratios of the fluorescence intensities can be obtained from the solutions of Eqs. (5) and (6) as

$$\frac{I_1(t)}{I_3(t)} = [I_1(0)/I_3(0)] \exp[(\beta_3 - \beta_1)t] + K[\beta_3/(\beta_3 - \beta_1)] \{ \exp[(\beta_3 - \beta_1)t] - 1 \}. \quad (7)$$

Figure 5 shows the ratios of the integrated fluorescence intensities of the two metastable states at three times after the excitation pulse for a specific level of laser power. The solid line in the figure represents the best fit to the data using Eq. (7) and treating the ratio of the initial intensities as an adjustable parameter. The excellent fit between theory and experiment indicates the validity of the proposed model and gives the value of  $I_1(0)/I_3(0)$  listed in Table II.

The two-photon absorption cross section can be derived from these results through the expression

$$\begin{aligned} \frac{I_1(0)/\hbar\omega_1}{I_3(0)/\hbar\omega_3} &= \frac{\beta'_1 n_1(0)}{\beta'_3 n_3(0)} \\ &= \frac{\beta'_1 \sigma'_1 I_p n_0 L}{\beta'_3 I_p^2 \sigma_3^{(2)} n_0 L} \\ &= (\beta'_1/\beta'_3)(\sigma'_1/\sigma_3^{(2)})(1/I_p), \end{aligned} \quad (8)$$

where  $I_p$  is the intensity of the laser pulse,  $\sigma'_1$  and  $\sigma_3^{(2)}$  are the relevant one- and two-photon absorption cross sections,  $n_0$  represents the total concentration of  $\text{Nd}^{3+}$  ions,  $L$  is the sample thickness, and  $\hbar\omega_i$  is the average energy of the photons emitted from the  $i$ th metastable state. Using the radiative decay rates determined from the information listed in Table I, the measured value for the fluorescence intensity ratio at an excitation power level of  $I_p = 1.38 \times 10^{28}$  photons/cm<sup>2</sup>s<sup>-1</sup>, and the value for the absorption cross section of the  $^4G_{7/2}$  level from Ref. 6 gives a value of

$$\sigma_3^{(2)} = 3.12 \times 10^{-55} \text{ cm}^4 \text{ s}/(\text{photon ion}).$$

TABLE II. Summary of results.

Parameter	Experimental	Theoretical
$\tau_d^{-1}$ ( $s^{-1}$ )	$5.00 \times 10^8$	
$W_{nr}^e$ ( $s^{-1}$ ): $^2P_{3/2}$		$1.38 \times 10^3$
$^2F_{25/2}$		$3.05 \times 10^3$
$\sigma^{(2)}$ [ $cm^4 s / (\text{photon ion})$ ]: $^2F_{25/2}$	$3.21 \times 10^{-55}$	$1.64 \times 10^{-56}$
$5d^4$	$1.27 \times 10^{-49}$	$3.69 \times 10^{-56}$
$I_1(0)/I_3(0)$ ( $\lambda_x = 532$ nm) <sup>b</sup>	51.6	
$I_2(0)/I_3(0)$ ( $\lambda_x = 354.7$ nm) <sup>b</sup>	3.69	
$K'$	1.058	

<sup>a</sup>Nature of the final states is unknown and may be a high-energy  $4f$  level.

<sup>b</sup>These values are normalized for photon energies and  $I_1(0)$  is corrected for the branching ratio of the observed fraction of the transitions from this level.

### V. RESULTS FOR 354.7-nm PUMPING

Figure 8 shows the fluorescence spectra at two times after the laser pulse for tripled Nd-YAG excitation at 354.7 nm. These spectra contain the same lines as seen in Figs. 3 and 6 as well as numerous additional lines. The new lines all exhibit a faster lifetime of about 0.32  $\mu s$ . The relevant transitions for this pumping wavelength are shown in Fig. 2. The  $^4D_{3/2}$  level is directly excited by the laser pulse. Some of the excited ions undergo rapid radiationless relaxation to the  $^2P_{3/2}$  level, while the rest of the ions undergo two-photon excitation to the  $5d$  levels. After the latter process, radiationless decay back to the  $^2(F_{25/2})$  metastable state occurs followed by the emission processes discussed in the preceding sections. After the former process the  $^2P_{3/2}$  level acts as a new metastable state resulting in the transitions shown in Fig. 2. One important aspect of these new transitions is that only part of them terminate on levels above the  $^4F_{3/2}$  level to give fluorescence from this metastable state while the remainder of the transitions go past this level and terminate on various components of the ground state term.

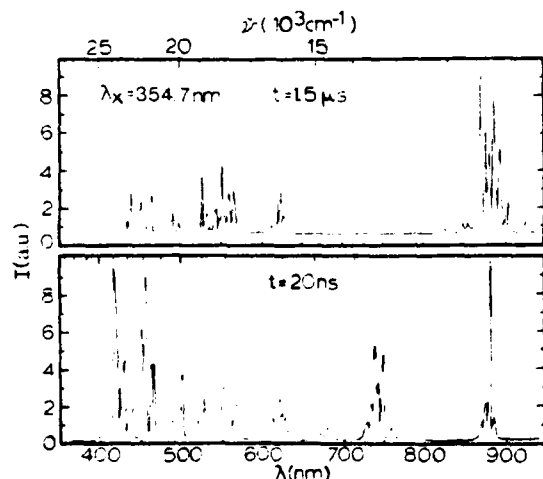


FIG. 8. Fluorescence spectra of Nd-YAG at two times after the excitation pulse at 354.7 nm.

The determination of the branching of these different types of transitions is difficult because of the possible existence of transitions emitting in the infrared spectral region (shown as dashed lines in Fig. 2).

The simplified transition rate model shown in Fig. 9 can be used to describe the excited-state dynamics for this type of pumping. In this case, three rate equations are necessary:

$$\frac{dn_1}{dt} = \beta_3 n_3 + \beta_{21} n_2 - \beta_1 n_1, \quad (9)$$

$$\frac{dn_2}{dt} = W_2 - \beta_2 n_2, \quad (10)$$

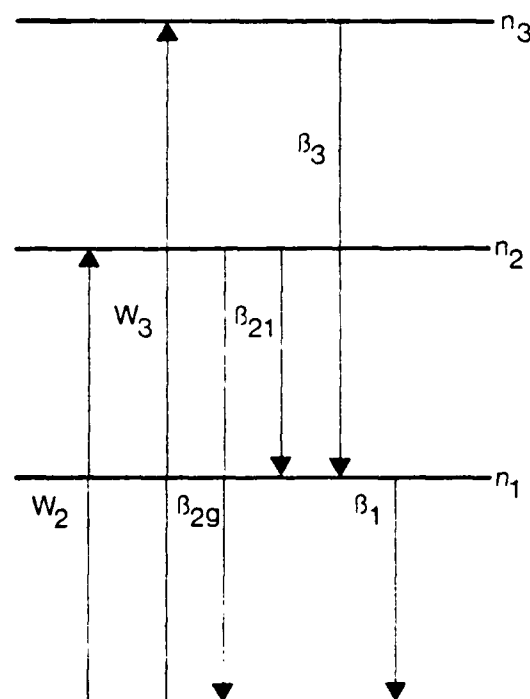


FIG. 9. Model for explaining observed spectral dynamics after 354.7-nm excitation. See text for definition of the parameters.

$$\frac{dn_3}{dt} = W_3'' - \beta_3 n_3. \quad (11)$$

Here  $W_3''$  represents the two-photon pumping rate of the  $^2(F2)_{5/2}$  level through radiationless relaxation from the

$5d$  levels and  $W_2$  is the rate of pumping of the  $^2P_{3/2}$  level by transitions from the  $^4D_{3/2}$  level. The solutions to these equations can be related to two different sets of fluorescence intensity ratios as

$$I_2(t)/I_3(t) = [I_2(0)/I_3(0)] \exp[(\beta_3 - \beta_2)t], \quad (12)$$

$$I_1(t)/I_2(t) = [I_1(0)/I_2(0)] \exp[(\beta_2 - \beta_1)t] + [I_3(0)/I_2(0)] \{ K\beta_3 / [(\beta_3 - \beta_1)(B_{2g} + B_{21})] \} \{ \exp[(\beta_2 - \beta_1)t] - \exp[(\beta_2 - \beta_3)t] \} + \{ \beta_1 B_1 K' / [(\beta_2 - \beta_1)(B_{2g} + B_{21})] \} \{ \exp[(\beta_2 - \beta_1)t] - 1 \}, \quad (13)$$

where  $K' = B_{21} + B_{21}' + W_2''/\beta_2'$ . Here, the branching ratios  $B_{21}$  and  $B_{21}'$  refer to the visible and infrared transitions, respectively, while  $W_2''$  represents the radiationless decay rate of the  $^2P_{3/2}$  metastable state.

Figure 10 shows the measured values of the relevant ratios of the two different sets of integrated fluorescence intensities at three times after the excitation pulse for a specific value of laser intensity. The lines in the figure represent the best fits to the data obtained from Eqs. (12) and (13) treating the initial fluorescence intensity ratios and  $K'$  as adjustable parameters. The excellent fits to the data indicate that the model proposed here is valid. The fitting parameters are given in Table II.

Equation (8) can again be used to determine a value for the relevant two-photon absorption cross sections. In this case  $I_p = 1.3 \times 10^{27}$  photons/cm<sup>2</sup>s<sup>-1</sup> and the value for the absorption cross section of the  $^4D_{3/2}$  level is found from Ref. 6. Using the measured initial ratio of the fluorescence intensities gives  $\sigma_2^{(2)} = 1.27 \times 10^{-49}$  cm<sup>4</sup>s/(photon ion).

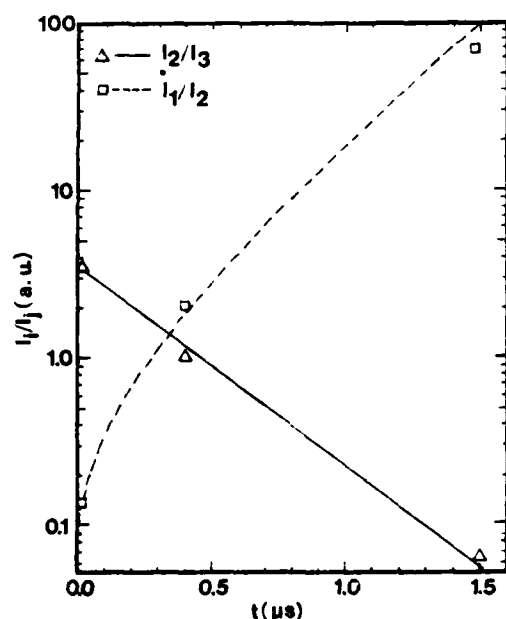


FIG. 10. Time evolution of the ratios of the fluorescence intensities of the emission from the three metastable states populated by 354.7-nm excitation. See text for explanation of the theoretical lines.

One aspect of the data which is not treated by the model discussed above is the observed rise time of approximately 15 ns of the fluorescence from the  $^2(F2)_{5/2}$  level. This does not affect the time-resolved spectroscopy model because of the very different time regime involved. However, this rise time is not observed for the other two pumping wavelengths and thus it can be associated with the nonradiative decay processes from the  $5d$  levels to the  $4f$  levels. In a simple three-level-system model the rise time is given by<sup>7</sup>

$$t_m = \tau_3 \tau_d \ln(\tau_d / \tau_3) / (\tau_d - \tau_3), \quad (14)$$

where  $\tau_d$  is the decay time of the  $5d$  level. Using the measured values for the fluorescence rise time and decay time for the  $^2(F2)_{5/2}$  level gives  $\tau_d^{-1} \approx 5 \times 10^8$  s<sup>-1</sup>.

## VI. DISCUSSION AND CONCLUSIONS

The use of high-power, picosecond-pulse excitation from the various harmonics of a Nd-YAG laser has provided new information concerning the spectral dynamics of Nd<sup>3+</sup> ions in YAG crystals as presented in the preceding sections. The important results of this work can be divided into three categories: characteristics of new spectral transitions, measurements of radiationless decay processes, and measurements of two-photon absorption cross sections. Each of these is discussed below.

### A. New spectral transitions

The high-power, picosecond-pulse excitation at several wavelengths coupled with the time-resolved spectroscopy measurement technique employed here, shows that fluorescence emission lines from Nd<sup>3+</sup> ions in YAG crystals occur throughout the visible and near-uv region of the spectrum as well as in the near-infrared region as usually reported. These lines can be associated with the transitions from three metastable states as shown in Fig. 2, the properties of which are summarized in Tables I and II.

Spectral lines similar to those reported here have been observed previously through our excitation mechanisms.<sup>2-4</sup> X-ray excitation<sup>3</sup> creates free electrons which become bound excitons at lattice-defect sites and can transfer their energy to the Nd<sup>3+</sup> ions. The spectral lines obtained in this way have been interpreted in terms of transitions from the  $^2(F2)_{5/2}$  level to almost all of the

lower-lying levels, including those of the ground-state term. The transition assignments of the lines given here is somewhat different than that proposed previously.<sup>3</sup> One major difference occurs in the uv region of the spectrum where no transitions were observed with Nd-YAG-laser excitation, but where several transitions were observed with x-ray excitation and interpreted as fluorescence originating on the  $^2(F2)_{5/2}$  level and terminating on the various multiplets of the  $^4I_J$  term. It is not clear at the present time why this difference occurs.

Similar spectral lines were also observed using nitrogen-laser-pumped dye-laser excitation in the spectral region around 590 nm.<sup>2</sup> The results were interpreted in terms of three-photon excitation of the  $5d$  level followed by nonradiative relaxation to the  $4f$  levels and fluorescence emission from the  $^2(F2)_{5/2}$  metastable state. The fluorescence lifetime of these transitions was found to be about 3  $\mu\text{s}$ , where is in agreement with the result reported here. Only extremely weak emission lines were observed in the 300-nm region of the spectrum which is consistent with the results reported here and again shows an interesting difference between multiphoton laser excitation and x-ray excitation.

One important result of this work is to clarify the possibility of pumping Nd-YAG lasers in the near-uv spectral region. Pumping at energies of  $37\,500\text{ cm}^{-1}$  or greater leads to very efficient excitation of the  $^4F_{3/2}$  lasing metastable state through fluorescence from the  $^2(F2)_{5/2}$  metastable state. Pumping in the region between  $26\,000$  and  $37\,500\text{ cm}^{-1}$  results in emission from the  $^2P_{3/2}$  metastable state. The determination of the branching ratios and quantum efficiency for this level are discussed in the next section and the results are listed in Table I. These results indicate that pumping in this intermediate metastable state still leads to efficiently populating the lasing metastable state. Further work needs to be done to correlate these results with those on x-ray and electron excitation of rare-earth ions in YAG.<sup>3,8</sup>

### B. Radiationless decay processes

A simple model has been developed to describe multiphonon decay processes in weakly coupled systems and this has been found to give a good fit to experimental data obtained on trivalent rare-earth ions in solids.<sup>9</sup> For decay across an energy gap  $\Delta E$  by the emission of  $p$  phonons of energy  $\hbar\omega$  ( $p = \Delta E/\hbar\omega$ ), the nonradiative decay rate is given by

$$W_{\text{nr}}^p(T) = W(0) \{ \exp(\hbar\omega/kT) / [\exp(\hbar\omega/kT) - 1] \}^p, \quad (15)$$

where

$$W(0) = C \exp(-\alpha\Delta E). \quad (16)$$

Here,  $C$  and  $\alpha$  are parameters involving the electron-phonon-interaction strength and the transition matrix elements. For many cases they have been found to be constants for  $f$ - $f$  transitions of different trivalent rare-earth ions in a specific host and the spontaneous phonon-emission rate  $W(0)$  shows a simple exponential dependence on the energy gaps of the various transitions.

Zverev *et al.*<sup>10</sup> have investigated radiationless relaxation processes of trivalent rare-earth ions in YAG (including the  $^4G_{7/2} \rightarrow ^2G_{7/2}$  transition of  $\text{Nd}^{3+}$ ) and found the results to obey the exponential energy-gap law with the parameters  $C = 9.7 \times 10^7\text{ s}^{-1}$  and  $\alpha = 3.1 \times 10^{-3}\text{ cm}^{-1}$ . Temperature-dependent measurements were fitted with an effective phonon energy of  $700\text{ cm}^{-1}$ , which is somewhat less than the maximum phonon energy in YAG crystals of  $860\text{ cm}^{-1}$ .<sup>11</sup> This is consistent with other phonon effects on the optical spectra<sup>1</sup> and may be due to the fact that the highest-energy phonons are vibrations of  $\text{AlO}_4$  groups which are less strongly coupled to the rare-earth ions than lower-energy lattice phonons.<sup>11,12</sup> Using these values for  $C$ ,  $\alpha$ , and  $\hbar\omega$  in Eqs. (15) and (16) along with the appropriate energy gaps, the room-temperature radiationless decay rates for the  $^2(F2)_{5/2}$  and  $^2P_{3/2}$  metastable states can be calculated. In the former case,  $\Delta E_3 = 3400\text{ cm}^{-1}$  and  $W_{\text{nr}}^p(300\text{ K}) = 3.05 \times 10^3\text{ s}^{-1}$ , while in the latter case,  $\Delta E_2 = 2150\text{ cm}^{-1}$  and  $W_{\text{nr}}^p(300\text{ K}) = 1.38 \times 10^5\text{ s}^{-1}$ .

The calculated value of the nonradiative decay rate can be combined with the measured fluorescence decay rate to find the radiative decay rate of a metastable state through  $\tau_f^{-1} = \beta' + W_{\text{nr}}^p$ . The quantum efficiency of the level is then given by  $\eta = \beta'/\beta_f$ . Applying this analysis to the two upper metastable states of  $\text{Nd}^{3+}$  ions in YAG gives the results listed as theoretical predictions in Table I. For the  $^2(F2)_{5/2}$  level the result agrees quite closely with that obtained from fitting the time-resolved spectroscopy results using the simple rate-equation model discussed in the preceding sections. The value found here of  $\eta_3 = 1.0$  for this level is significantly greater than the value of 0.21 estimated in Ref. 2 using a Judd-Olfelt calculation and absorption spectral data. Since the fluorescence transitions from this metastable state are not the same as the absorption transitions to the level, it is not surprising that this type of analysis does not give an accurate result. The value obtained for the nonradiative decay rate of the  $^2P_{3/2}$  level can be combined with the measured fluorescence decay rates and the value of  $K'$  found from fitting Eq. (13) to experimental data to give the branching ratios for this metastable state as listed in Table I.

Nonradiative decay rates for  $5d$ - $4f$  transitions of trivalent rare-earth ions in YAG crystals have been measured in cases where  $5d$  fluorescence can be observed.<sup>12</sup> Since no  $5d$  fluorescence can be observed for  $\text{Nd}^{3+}$  ions, it has been concluded that the nonradiative decay rates must be very much faster than  $10^7\text{ s}^{-1}$ , which is consistent with the value measured in this study. It should be noted that if the simple model of Eqs. (15) and (16) is employed with the values of  $C$  and  $\alpha$  given above and  $5d$ - $4f$  energy gap of about  $1800\text{ cm}^{-1}$  from Ref. 2, a significantly smaller nonradiative decay rate is predicted than the observed value. This is not surprising since the values of  $C$  and  $\alpha$  are expected to be constant only for similar  $f$ - $f$  transitions. The matrix elements for the  $d$ - $f$  transitions will be significantly greater and should lead to predicted values closer to the observed rate. Performing similar measurements on other YAG samples with different rare-earth ions is necessary to determine values of  $C$  and  $\alpha$  for  $5d$ - $4f$  transitions and checking the validity of the simple nonradiative decay model for these types of transitions.



### C. Two-photon absorption cross sections

The theory of two-photon absorption applied specifically to trivalent rare-earth ions in solids was developed by Apanasevich *et al.*<sup>13</sup> The general expression for the two-photon absorption cross section is

$$\sigma_{if}^{(2)} = (2\pi/\hbar) |A_{if}^{(2)}|^2 \rho_f(E) (\hbar\omega_p)^2, \quad (17)$$

where  $\omega_p$  is the photon frequency,  $\rho_f(E)$  is the density of final states, and  $A_{if}^{(2)}$  is the matrix element for the transition.

$$|A_{if}^{(2)}|^2 = (\hbar/\pi 2n) [(n^2 + 2)/3]^2 [e^2/(mc^2)]^2 [(me^4)/(8\pi^3 c^2 \hbar^4)] (0.069) \\ \times \langle \alpha_f J_f || U^{(2)} || \alpha_i J_i \rangle^2 (2J + 1)^{-1} \left[ \sum_k \langle 4f || r || 5d_k \rangle^2 / [(\hbar\omega_{ik} - \hbar\omega_p) - i\hbar\gamma_{ik}] \right]^2, \quad (19)$$

where  $\gamma_{ik}$  is the half-width of the intermediate state and  $\langle \alpha_f J_f || U^{(2)} || \alpha_i J_i \rangle$  is the reduced matrix element of the tensor operator  $U^{(2)}$  between the initial and final levels of the  $4f$  configuration. The latter have been tabulated for the transitions of interest here.<sup>14</sup> The development of Ref. 13 neglects one-photon resonances and evaluates the sum over intermediate states in Eq. (17) by using an integral over hydrogenlike wave functions. Using their approach along with observed spectral information to estimate the density of final states, the two-photon absorption cross section for 532-nm pumping of the  $^2(F2)_{5/2}$  level is evaluated from Eq. (17) to be  $1.64 \times 10^{-36}$  cm<sup>4</sup>s/(photonion). Considering the rough approximations involved in obtaining this theoretical estimate, the predicted value for the two-photon absorption cross section is very close to that derived from time-resolved spectroscopy data.

Obtaining a theoretical estimate for the two-photon absorption cross section for 354.7-nm pumping is more difficult since the nature of the final state of the transition is unknown. If it is assumed to be  $5d$  level and the sum over intermediate states includes both  $4f$  and  $5d$  levels, the predicted value for  $\sigma_2^{(2)}$  is found to be over 10 orders of magnitude smaller than the observed value. However, it is known that additional  $4f$  levels exist in the high-energy region of the  $5d$  bands,<sup>2</sup> and if one of these is assumed to be the final state of the two-photon transition, the calculation can proceed as described above giving the result  $\sigma_2^{(2)} = 1.11 \times 10^{-36}$  cm<sup>4</sup>s/(photonion). This is much closer to the observed value, but still significantly different indicating the inadequacy of the current theoretical model to treat this specific case.

Both of the two-photon absorption cross sections measured in this work involve real, resonant intermediate states. An unsuccessful attempt was also made to excite fluorescence of Nd<sup>3+</sup> ions in YAG crystals from the fundamental emission of the Nd-YAG laser at 1060 nm. In this case there is no real, resonant intermediate state for a two-photon transition. Such excitation has been used for Nd<sup>3+</sup> ions in other crystals.<sup>15</sup> The fact that no excitation

tion. The density of final states is given by

$$\rho_f(E) = (\hbar\gamma_{if}/\pi) / [(\hbar\gamma_{if})^2 + (\hbar\omega_{if} - 2\hbar\omega_p)^2], \quad (18)$$

where  $\gamma_{if}$  is the half-width of the final state. The major problem in the application of two-photon absorption theories is deciding how to treat the sum over intermediate states in the matrix element for the transition. Apanasevich *et al.*<sup>13</sup> chose the  $5d$  levels as the intermediate states and derived an expression for the matrix element of the transition given by

could be achieved with the primary laser output at higher powers than used with the various harmonics shows the importance of the enhancement achieved with a real intermediate state. The multiphoton excitation spectra in Ref. 2 also exhibited enhancements at real intermediate state resonances. The theory of Ref. 12 used here does not account for the effects of single-photon resonances with intermediate  $4f$  levels. However, models for evaluating the matrix elements using two sequential  $4f$ - $4f$  transitions or a  $4f$ - $4f$  transition followed by a  $4f$ - $5d$  transition predict theoretical values for the cross sections many orders of magnitude smaller than the experimentally observed values. It appears that the difference in magnitude of the two types of two-photon cross sections measured here is associated with the factors of photon energy and density of final states in Eq. (17), not with differences in the transition matrix elements. It is important to note that the values of  $\sigma^{(2)}$  reported here are much smaller than those that can generally be measured by transmission experiments.<sup>16</sup>

### D. Conclusions

In summary, the use of high-power, picosecond laser excitation of Nd<sup>3+</sup> ions in YAG crystals has provided new information about the excited-state dynamics of this system. These results have practical applications with regard to pumping Nd-YAG lasers as well as fundamental interest in the areas of multiphoton absorption and radiationless relaxation processes. The time-resolved spectroscopy technique provides a very sensitive way to characterize the properties of different metastable states of a system and to quantitatively determine two-photon absorption cross sections and  $5d$ - $4f$  radiationless decay rates.

### ACKNOWLEDGMENTS

This work was sponsored by the U.S. Army Research Office and by the National Science Foundation under Grant No. DMR-82-16551.

\*Permanent address: Physics Department, Central State University, Edmond, OK 74008.

- <sup>1</sup>R. C. Powell, in *Nd-YAG Lasers*, edited by L. G. DeShazer (Springer, Berlin, 1984).
- <sup>2</sup>M. A. Kramer and R. W. Boyd, *Phys. Rev. B* **23**, 986 (1981).
- <sup>3</sup>A. Niklas and W. Jelenski, *Phys. Status Solidi A* **77**, 393, (1983).
- <sup>4</sup>N. S. Rooze and N. A. Anisimov, *Opt. Spectrosc.* **38**, 356 (1975).
- <sup>5</sup>R. C. Powell, D. P. Neikirk, and D. Sardar, *J. Opt. Soc. Am.* **70**, 486 (1980).
- <sup>6</sup>W. F. Krupke, *IEEE J. Quantum Electron.* **QE-7**, 153 (1971).
- <sup>7</sup>B. DiBartolo, *Optical Interactions in Solids* (Wiley, New York, 1968).
- <sup>8</sup>D. J. Robbins and P. J. Dean, *Adv. Phys.* **27**, 499 (1977).
- <sup>9</sup>L. A. Riseberg and M. J. Weber, *Prog. Opt.* **14**, 89 (1977).
- <sup>10</sup>G. M. Zverev, G. Ya. Kolodnyi, and A. M. Onishchenko, *Zh. Eksp. Teor. Fiz.* **60**, 920 (1971) [*Sov. Phys.—JETP* **33**, 497 (1971)].
- <sup>11</sup>G. A. Slack, D. W. Oliver, R. M. Chrenko, and S. Roberts, *Phys. Rev.* **177**, 1308 (1969).
- <sup>12</sup>M. J. Weber, *Solid State Commun.* **12**, 741 (1973).
- <sup>13</sup>P. A. Apanasevich, R. I. Gintoft, V. S. Korolkov, A. G. Makhanev, and G. A. Skripko, *Phys. Status Solidi B* **58**, 745 (1973).
- <sup>14</sup>W. T. Carnall, P. R. Fields, and K. Rajnak, *J. Chem. Phys.* **49**, 4424 (1968).
- <sup>15</sup>S. Singh and J. E. Geusic, in *Optical Properties of Ions in Crystals*, edited by H. M. Crosswhite and H. W. Moos (Interscience, New York, 1967), p. 493.
- <sup>16</sup>M. Ito and N. Mikami, *Appl. Spectrosc. Rev.* **16**, 299 (1980).

AD-A151 731

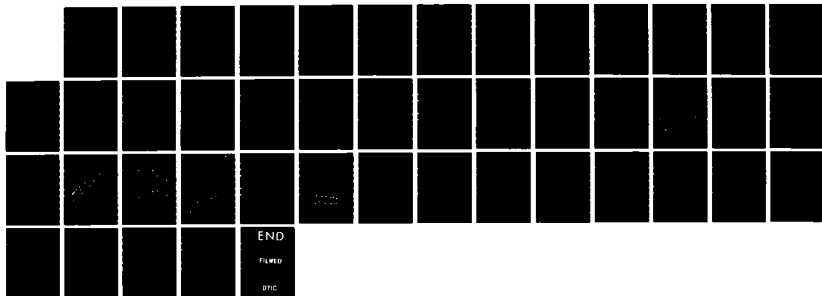
SPECTROSCOPIC INVESTIGATION OF MATERIALS FOR FREQUENCY  
AGILE LASER SYSTEMS(U) OKLAHOMA STATE UNIV STILLWATER  
DEPT OF PHYSICS R C POWELL JAN 85 ARO-18677.11-PH  
DARG29-82-K-0041

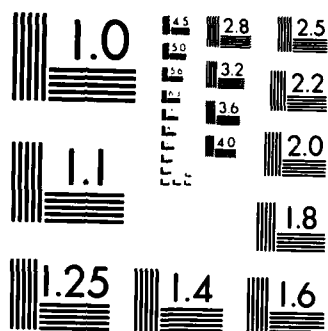
2/2

UNCLASSIFIED

F/G 20/5

NL





## V. DETERMINATION OF CHARGE RELOCATION DYNAMICS IN PHOTOREFRACTIVE CRYSTALS

The manuscript in this section describes the results of characterizing the photorefractive effect (PRE) in  $\text{LiNbO}_3$  crystals using holographic grating techniques. The optical results obtained in our laboratory on the PRE properties of crystals with different types of thermal, radiation, and crystal growth histories were correlated closely with the defect properties of the same samples determined by electron paramagnetic resonance. The most important result is the development of a model to describe the charge relocation dynamics involved in the PRE. This work demonstrates the presence of two types of charge carriers and the importance of trap modulated mobility in determining the PRE characteristics of this type of material.

ANALYSIS OF THE DECAY DYNAMICS OF LASER-INDUCED GRATINGS  
IN  $\text{LiNbO}_3$

Jacek K. Tyminski and Richard C. Powell

Department of Physics, Oklahoma State University

Stillwater, OK 74078

Laser-induced refractive index gratings were created and probed in "nominally pure"  $\text{LiNbO}_3$  crystals. The time dependence of the probe beam scattered from the grating during erasure was measured as a function of the crossing angle of the write beams for samples with different thermal annealing histories and as a function of sample temperature. Biexponential grating decay curves were observed and the characteristic decay times are interpreted in terms of two types of charge carrier dynamics contributing to the photorefractive effect. Using a simple charge relocation model, the charge carrier densities, relocation rates and relative trap concentrations contributing to the two grating decay components were obtained from the data and their changes with sample temperature and annealing treatment were determined. Measurements of energy transfer through two-wave mixing on both oxidized and reduced samples were used to confirm the two charge carrier model.

## I. INTRODUCTION

The creation of laser-induced refractive index changes (photorefractive effect, PRE) in  $\text{LiNbO}_3$  crystals has been an important topic for research for many years.<sup>1-4</sup> The macroscopic, laser-induced non-uniformities of the refractive index act as "optical damage" centers if the material is used for applications such as beam modulation and wave guiding.<sup>5,6</sup> However, they also form the basis for using the material in optical information processing applications such as optical storage or phase conjugation. Thus it is important to understand the fundamental processes producing the PRE properties so materials can be tailor made to either maximize or minimize the effect depending on the desired application. Despite the significant amount of research done in characterizing the PRE in  $\text{LiNbO}_3$ , the basic solid state defect physics and charge migrational properties underlying this effect are still not well understood.

The source of the material's photorefractive response is the macroscopic relocation of charge along the crystallographic  $c$ -direction. There are two fundamental problems of interest in characterizing the photorefractive properties of  $\text{LiNbO}_3$ . The first is identifying the defects acting as charge donors, acceptors, and traps contributing to the photocurrents in the material.<sup>7-14</sup> The second is characterizing the dynamics of the charge transport in the photorefractive medium.<sup>4,15-18</sup>  $\text{LiNbO}_3$  exhibits a large bulk photovoltaic effect<sup>19,20</sup> which complicates the dynamics of charge migration processes leading to the PRE in the material.<sup>4</sup> In the volume of the material exposed to the laser beam, the photocurrent is influenced by diffusion,<sup>19,21,22</sup>

the photovoltaic effect,<sup>19,22,23</sup> and a static electric field.<sup>19,21-23</sup> This static field, developed as a result of the charge migration along the c-axis, produces changes in the extraordinary refractive index<sup>2</sup> depending on the material's electro-optic tensor.<sup>6</sup>

Two methods have been developed to probe refractive index changes in photorefractive materials. The first measures the changes in the birefringence of the crystal using a polarization compensator technique.<sup>20,24</sup> The second method is a holographic technique which uses the interference between two laser beams to produce periodic refractive index variations in the material.<sup>4,20,24</sup> In this technique, the sinusoidal interference pattern of the light produces changes in the index of refraction which act like a hologram in the shape of a grating. The properties of the refractive index changes can be investigated by monitoring the scattering of a probe beam off of this grating.

Previous investigations have dealt mostly with determining the macroscopic characteristics of the PRE in a material without attempting to relate the observed results to microscopic properties of defects and charge dynamics. The studies that have been done on the microscopic processes underlying the PRE have involved purposely doped materials. The intentional substitution of chemical impurities into the sample may alter the distribution of structural defects in the lattice significantly and introduce other perturbations in the material. Therefore the results on microscopic charge relocation processes in doped samples may not pertain to undoped samples. Thus there is still much to be



learned about the charge dynamics underlying the PRE in undoped  $\text{LiNbO}_3$ . Because of this, the work reported in this paper focuses on the task of relating the dynamics of the photorefractive response to the charge transport properties of "nominally pure"  $\text{LiNbO}_3$ . The success of this work in obtaining new information on this material is based on the recent development of a new theoretical model for analyzing grating decay data<sup>25</sup> and on the results of recent electron paramagnetic resonance (EPR) experiments characterizing the different types of defects in "nominally pure" samples.<sup>26</sup>

By subjecting a sample of "nominally pure"  $\text{LiNbO}_3$  to a series of thermal annealing treatments, the concentration of defects in the crystal was altered. After each anneal, laser-induced gratings were formed and the decay patterns of the gratings erasure were measured. The most important aspect of this work is the demonstration of a method for analyzing the time response of the scattered probe beam during erasure in holographic grating experiments to obtain independent information about charge carrier types and concentrations, trap concentrations, and charge relocation dynamics in the PRE. The results of these measurements are related to information about the relative concentration of impurities in the sample determined by electron paramagnetic resonance (EPR) measurements.<sup>26</sup> The erase patterns exhibit two decay components. Our analysis of these curves show for the first time that charge carriers having two different types of relocation dynamics and different concentrations contribute to the PRE in this type of material. The annealing treatments cause different changes in the contributions

of the two different types of charge dynamics which can be related through EPR results to changes in the concentrations of different types of defects. The measurement of energy transfer in a two-wave mixing experiment is used to corroborate these results. Finally, measurements of grating decay patterns as a function of sample temperature show for the first time the importance of shallow traps in the charge relocation dynamics of this material. The combination of different experimental approaches used here has allowed the development of a model relating the microscopic charge relocation dynamics to the macroscopic PRE properties in "nominally pure"  $\text{LiNbO}_3$ . This has not previously been possible because the experimental results in the literature have been obtained by different techniques on different samples in different laboratories making consistent interpretation of the data impossible.

## II. EXPERIMENTAL

The sample used in these experiments was a good optical quality single crystal of "nominally pure" lithium niobate obtained from Union Carbide. The absolute concentration of the transition metal ion impurities in the sample was between 25 and 50 ppm. The individual concentrations of specific types of defects in the material are difficult to determine at this low level and have been obtained only for a limited number of types of imperfections.<sup>26</sup> Their relative concentration was varied by subjecting the sample to a series of thermal annealing treatments.<sup>26</sup> To reduce the sample at a given temperature, it was annealed in a vacuum of approximately  $2 \times 10^{-6}$  torr for one hour.

described below. The sample was placed in a furnace so that the signal could be monitored at elevated temperatures. In addition, the transfer of energy between the two beams writing the hologram was measured to determine the amount of phase shift between the light pattern and the induced hologram.

### III. THEORY OF HOLOGRAPHIC GRATING DECAY

Kogelnik<sup>27</sup> derived an expression for describing the first order Bragg diffraction from a thick hologram refractive index grating. In the case of shallow gratings, his result simplifies to

$$I_s \propto |\Delta n|^2 \quad (1)$$

where  $I_s$  is the intensity of the scattered signal beam and the "grating depth"  $|\Delta n|$  is the difference in the refractive index  $n$  between the peak and valley regions of the grating.

Equation (1) is useful in relating the results obtained in the holographic grating experiments to the changes in  $n$  produced by the PRE in the material. The next step in interpreting the results is based on models relating the depth of the index of refraction grating with the parameters describing the electrodynamic properties of the material. The bulk of the theoretical efforts to establish such models have focused on the steady state properties of the photorefractive gratings.<sup>4,15-23,2830</sup> Recently Valley<sup>31</sup> presented a model discussing the transient behavior of the photorefractive response under short pulse excitation and erasure conditions. However, his description does not address the question of charge relocation over distances comparable to the grating spacing which is the condition required to completely

erase the grating. Given this we can not use his approach to analyze our data.

Feinberg, et al.<sup>25</sup> developed an expression for describing the depth of the static field grating based on a model of the charge dynamics in a photorefractive medium. Their result and Eq. (1) can be used together in interpreting the data from holographic grating experiments to obtain information concerning the dynamics of photocarrier redistribution. The model of Feinberg, et al.<sup>25</sup> involves the following assumptions: (1) the grating is sinusoidal; (2) the charge migration involves only nearest neighbor relocation; (3) the migration of the charge can be described by a single parameter, i.e. the trap-to-trap relocation rate; and (4) the grating wavelength is greater than the relocation distance. These assumptions set the limits of applicability of the Feinberg model. Also, the generation and the erasure of photorefractive gratings consist of charge detrapping, migration, and retrapping processes. Therefore, two different factors are important in characterizing the photorefractive effect: the rates of excitation and de-excitation of the charge to and from its mobile state, and the dynamics of charge migration between trapping sites. Modeling the detrapping-migration-retrapping sequence by a single parameter related to the average relocation rate gives only a rough description of the complex microscopic processes taking place. Despite these limitations, the Feinberg model provides the best available method for relating measurements of the photorefractive response of the medium to the microscopic charge relocation dynamics.

The Feinberg model predicts an exponential decay of the

scattered signal intensity during the erasing of the grating,<sup>25</sup>

$$I_g = I_0 \exp(Kt). \quad (2)$$

The decay rate has the form

$$K = K_0 + K_g \sin^2(\theta/2) \quad (3)$$

where  $\theta$  is the crossing angle of the two write beams used to generate the grating. The first term in Eq. (3) has the form  $K_0 = 2Rd^2Nq^2/(\epsilon\epsilon_0k_B T)$  where  $\epsilon$  is the material's dielectric constant,  $\epsilon_0$  is the dielectric constant of a vacuum,  $k_B$  is Boltzmann's constant,  $T$  is temperature,  $N$  is the average concentration of the photocarriers contributing to the photorefractive response of the material,  $q$  is their charge and  $R = I_0 D$  is the rate of charge relocation over a distance  $d$  where  $D$  is the diffusion coefficient. This term describes the contribution to the erasure rate of the photorefractive grating due to the rates of trapping and detrapping the charges. It is the dominant contribution in the limit in which charge migration distances are negligible compared to the grating wavelength. The parameter  $K_g$  in the second term in Eq. (3) has the form  $K_g = 2Rd^2(4\pi/\lambda)^2$ . This describes the charge relocation rate over the distance  $\lambda/2\pi$  where the grating wavelength is given by  $\Lambda = \lambda/[2\sin(\theta/2)]$ .

After measuring  $K$  as a function of  $\sin^2(\theta/2)$ , the slope and intercept of the experimental data can be used to obtain independent values of  $K_0$  and  $K_g$  for specific sample conditions. The ratio of these two parameters is given by

$$K_0/K_g = Nq^2\lambda^2/[16\pi^2\epsilon\epsilon_0k_B T] \quad (4)$$

and the slope  $dK/d[\sin^2(\theta/2)]$  has the form

$$dK/d[\sin^2(\theta/2)] = 32\pi^2 R d^2 / \lambda^2. \quad (5)$$

Within the limits of the model, Eq. (4) gives an estimate of the concentration of the photocarriers contributing to the photorefractive effect  $N$  and Eq. (5) can be used to obtain an estimate for the product  $Rd^2$  which is related to the rate of the charge relocation.

#### IV. RESULTS AND DISCUSSION

The time dependence of the signal beam intensity during erasing of photorefractive holograms was monitored for different crossing angles of the write beams after a series of reducing thermal annealing treatments. Figure 2 shows examples of the typical non-exponential signal decay curves obtained for crossing angles of  $3.5^\circ$  and  $10^\circ$  for an oxidized sample at room temperature. The data were analyzed by approximating the decay profiles as double exponential shapes. Examples of the angular dependences of the fast and slow components of the decay rates for different sample conditions are shown in Fig. 3. The data demonstrate the significant changes in the angular dependences of the grating decay rates caused by different thermal annealing conditions.

The two components of the decay curves can be interpreted as originating from the presence of two different gratings having different types of charge dynamics. The different decay rates are related to differences in the detrapping, migration, and retrapping rates of the photocarriers creating the gratings. The data can be analyzed using Eq. (2). The slopes of the plots of the decay rates versus the crossing angle of the write beams are different for the fast and slow components of the decay curves

indicating different relocation rates for the two charge-trap systems producing the two types of gratings. In addition, the intercepts of these plots are different indicating different concentrations for the two types of charge carriers.

For the results obtained on the fast component of the decay of the grating in the oxidized sample, departure from the predicted linear behavior of the data is seen in Fig. 3. This occurs when the relocation distance approaches the grating wavelength,

$$2\pi d/\lambda \approx 1. \quad (6)$$

This departure occurs at  $\theta = 14^\circ$ , which places a lower limit of approximately  $2 \times 10^{12} \text{ cm}^{-3}$  on the density of traps at the fast component of the grating decay. This is consistent with the fact that scattering efficiency measurements indicate this trap concentration to be of the order of  $10^{16} \text{ cm}^{-3}$ .

Similar departures from the linear dependence of  $K$  on  $\sin^2(\theta/2)$  were not observed for the vacuum annealed samples within the range of variation of  $\theta$  measured. The data obtained on the angular dependences of  $K$  were analyzed to obtain values of  $K_0$  and  $K_1$  for each annealing condition. Using Eqs. (4) and (5), estimates were obtained for the concentrations of the photocarriers involved in the fast and the slow decay components of the grating and for the product  $Rd^2$  which can be interpreted as the charge relocation parameter. The results of this analysis are shown in Fig. 4. It is important to note that the magnitudes of the charge carriers and the charge relocation parameters are dependent on the properties of the erase beam which in this case means a flux of  $0.2 \text{ W/cm}^2$  at  $442 \text{ nm}$ .

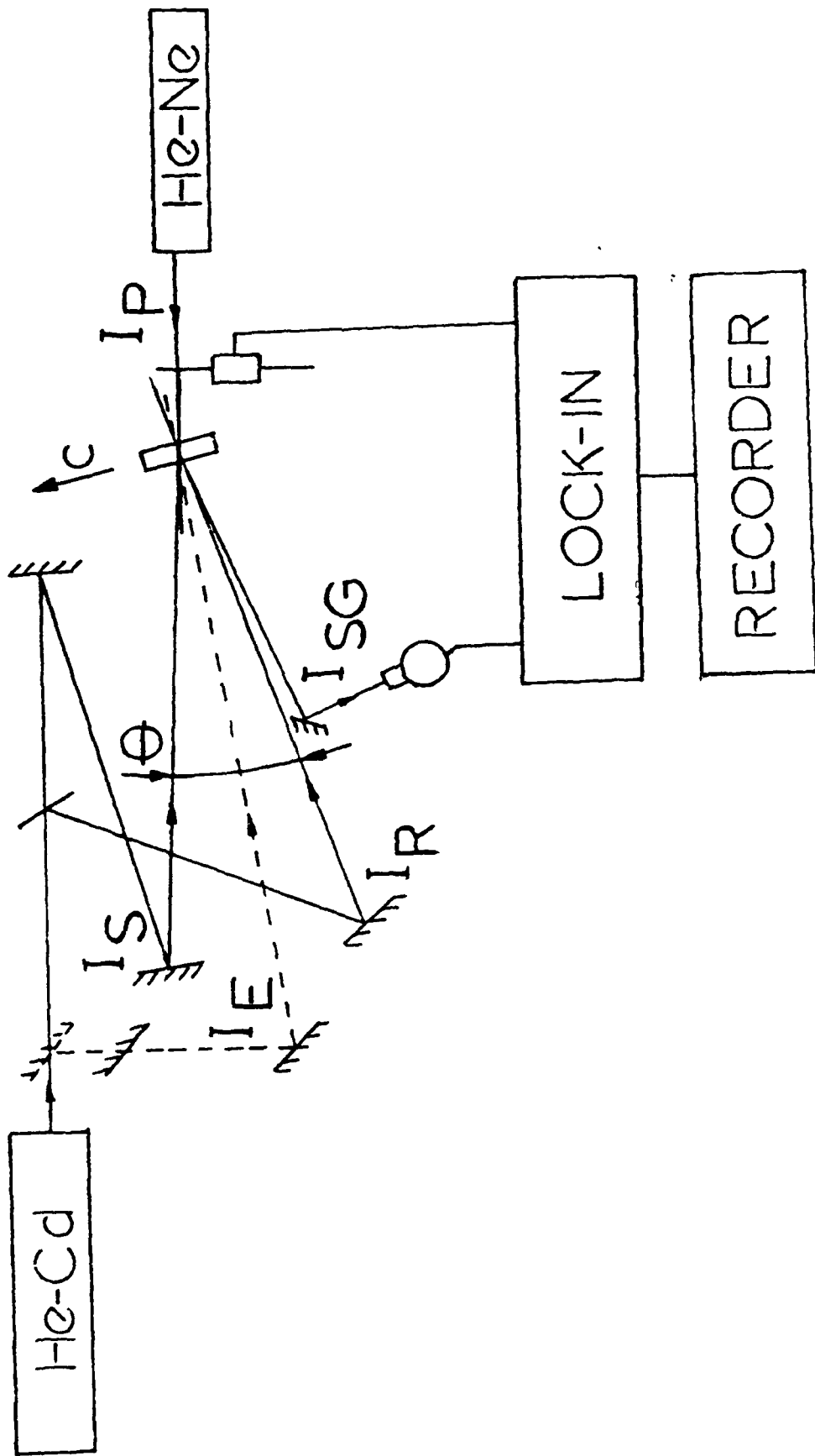
Figure 4 shows that the concentrations of the photocarriers

contributing to the fast and slow components of the grating decay both decrease as annealing temperature is increased with the latter showing a much greater change. However,  $N = p_d W$  where  $p_d$  is the donor trap density and  $W$  is the absorption coefficient. Annealing in a vacuum changes the defect composition of the sample which affects both of these factors. The observed decrease in the values of  $N$  is probably due primarily to the simultaneous increase in the absorption which occurs throughout the visible spectral region with annealing.<sup>4,32</sup> This new type of absorption does not create charge carriers which contribute to the PRE and thus, after vacuum annealing at high temperatures fewer photons in the laser beams excite the photocarriers contributing to the PRE. Because of this, it is impossible to directly relate the measured concentration of the charge carriers contributing to the PRE to the concentration of the donors present in the sample.

The charge relocation parameter  $Rd^2$  was measured to be constant with annealing temperature for the fast grating decay component and to increase for the slow component as shown in Fig. 4 (B). Since  $R$  is dependent on the light intensity and the effective value for  $I_0$  decreases with annealing temperature as discussed above, the results shown in Fig. 4 (B) indicate that the relocation distance  $d$  is increasing with higher annealing temperatures for both the fast and slow components.

Estimates of the relative trap densities were obtained by analyzing the shapes of the biexponential signal decay curves for write beam crossing angles of about  $10^\circ$ . This gives  $I_{f0}/I_{s0}$ , the





400 C.

Fig. 7. Proposed model for the PRE charge relocation dynamics  
in "nominally pure"  $\text{LiNbO}_3$ .

# FIGURE CAPTIONS

Fig. 1. Experimental setup for holographic grating measurements of the photorefractive effect.

Fig. 2. Decay patterns for the scattered probe beam during grating erasure for the oxidized sample at room temperature. The erase beam flux is  $0.2\text{W}/\text{cm}^2$ .

Fig. 3. Angular dependences of the erase rate of the grating obtained at room temperature.  $\circ$  -oxidized sample, fast component;  $\bullet$  -oxidized sample, slow component;  $\triangle$  -sample annealed in a vacuum at  $250^\circ\text{C}$ , fast component;  $\blacktriangle$  -sample annealed at  $250^\circ\text{C}$ , slow component;  $\square$  -sample annealed at  $400^\circ\text{C}$ , fast component (no slow component observed).

Fig. 4. Variation of photocarrier concentration (A) and relocation constant (B) with vacuum annealing temperature. Data taken at room temperature with  $\square$  and  $\circ$  found from the fast components of the grating decay curves and  $\blacksquare$  and  $\bullet$  found from the slow components.

Fig. 5. Ratio of the concentrations of traps contributing to the fast and slow grating decay components as a function of annealing temperature.

Fig. 6. Temperature dependences of the grating decay rates.  $\bullet$  and  $\blacksquare$  represent data obtained from the slow decay component of the oxidized sample with  $\theta=10^\circ$  and  $3.5^\circ$ , respectively.  $\circ$  and  $\square$  represent data obtained from the fast decay component of the oxidized sample with  $\theta=10^\circ$  and  $3.5^\circ$ , respectively.  $\triangle$  represents data obtained from the fast decay component at  $\theta=3.5^\circ$  after annealing the sample in a vacuum at

30. V.G. Brokovich and B.I. Sturman, JETP Lett. 37, 550 (1983).
31. G.C. Valley, IEEE J. Quant. Electron. QE-19, 1637 (1983).
32. M.B. Clark, F.J. DiSalvo, A.M. Glass, and G.E. Peterson, J. Chem. Phys. 59 6209 (1973).
33. D.L. Steabler and J.J. Amodi, J. Appl. Phys. 43, 1042 (1972).
34. R. Orlowski and E. Kratzig, Solid State Comm. 27, 1351 (1978).

16. W. Josch, R. Munser, W. Ruppel, and P. Wurfe., J. Ferroelect. 21, 623 (1978).
17. M.G. Mohoram, T.K., Gaylord, R. Magnusson, and L. Young, J. Appl. Phys. 50, 5642 (1978).
18. Y. Shiozaki and T. Mitsui, J. Phys. Chem. Solids 24, 1057 (1963).
19. A.M. Glass, D. von der Linde, and T.J. Negran, Appl. Phys. Lett. 25, 232 (1974).
20. M.E. Lines and A.M. Glass, "Principles and Application of Ferroelectrics and Related Materials", (Oxford Univ. Press, Oxford, 1979).
21. L. Young, W.K.Y. Wong, M.L.W. Thelwalt, and W.D. Cornish, Appl. Phys. Lett. 24, 264 (1974).
22. L. Young, G.M. Mohoram, F.E. Guilaly, and E. Lun, J. Appl. Phys. 50, 4201 (1979).
23. R. Grusson, M. Henry, S. Malick, and S.L. Xu, J. Appl. Phys. 54, 3012 (1982).
24. A.M. Glass, Opt. Eng. 17, 420 (1978).
25. J. Feinberg, D. Heiman, A.R. Tanguay, Jr., and R.W. Hellwarth, J. Appl. Phys. 51, 1279 (1980); J. Appl. Phys. 52, 537 (1980).
26. J.L. Ketchum, K.L. Sweeney, L.E. Halliburton, and A.F. Armington, Phys. Lett. 94A, 450 (1983); K.L. Sweeney and L.E. Halliburton, Appl. Phys. Lett. 43, 336 (1983).
27. H. Kogelnik, Bell Sys. Tech. J. 48, 2909 (1969).
28. N.V. Kukhtarev, V.B. Markov, S.G. Odulov, M.S. Soskin, and V.L. Vinetskii, J. Ferroelect. 22, 949 (1979).
29. J.J. Amodai, Appl. Phys. Lett 18, 22 (1971).

# REFERENCES

1. A. Ashkin, G.D. Boyd, J.M. Dziedzic, and R.G. Smith, Appl. Phys. Lett. 9, 72 (1966).
2. F.S. Chen, J. Appl. Phys. 40, 3389 (1969).
3. W.D. Johnston, Jr., J. Appl. Phys. 41, 3279 (1970).
4. P. Gunter, Phys. Repts. 93, 199 (1982).
5. G.E. Peterson, A.A. Ballman, P.V. Lenzo, P.M. Bridenbaugh, and Appl. Phys. Lett. 5, 62 (1964).
6. P.V. Lenzo, E.B. Spencer, and K. Nassau, J. Opt. Soc. Am. 56, 633 (1966).
7. A. M. Glass, G.E. Peterson, and T.J. Negran, Nat. Bur. Std. Special Pub. #327, 15 (1972).
8. D.L. Steabler and W. Phillips, Appl. Opt. 13 788 (1974).
9. H. Kurz, J. Ferroelect. 13, 291 (1976).
10. Yu. V. Vladimister, V.A. Golenishchev-Kutuzov, S.A. Migachev, and N.A. Shamukmov, Sov. Phys. Solid State 20 1994 (1978).
11. H.J. Levinstein, A.A. Ballman, R.T. Denton, A. Ashkin, J. Dziedzic, J. Appl. Phys. 38, 3101 (1967).
12. R.L. Hollman, P.J. Cressman, and J.F. Revelli, Appl. Phys. Lett. 32, 280 (1978).
13. J. Jackel, A.M. Glass, G.E. Peterson, C.E. Rice, D.A. Olson, and J.J. Veselka, J. Appl. Phys. 55, 269 (1984).
14. D.A. Bryan, R. Gerson, and H.E. Tomaschke, to be published in Appl. Phys. Lett.
15. G.A. Alphonse, R.C. Alig, D.L Steabler, and W. Phillips, RCA Review 36, 211 (1975).

TABLE 1. PRE Parameters for  $\text{LiNbO}_3$ 

Parameter	Sample		Annealed (400 C)
	Oxidized (fast)	Oxidized (slow)	
$K_O (\text{sec}^{-1})$	0.012	0.008	0.004
$K_\theta (\text{sec}^{-1})$	0.53	0.26	0.57
$N (10^{14} \text{cm}^{-3})$	1.4	1.9	0.4
$Rd^2 (10^{-15} \text{cm}^2 \text{sec}^{-1})$	3.3	1.6	3.5
$\Delta E (\text{cm}^{-1})$	850- 2500	90	850
$P_f/P_s$	1.0		9.9
$\Delta I_R/I_R (\%)$	9.0		12.5

In summary, the work reported here demonstrates the use of grating decay pattern measurements for determining the charge dynamics of the PRE. The technique described here allows the separate determination of charge carrier concentrations, relocation rates, and donor and acceptor trap concentrations. The contributions from different types of charge carriers can be measured and the effects of shallow traps determined. Applying this technique to both oxidized and annealed samples provided some new information concerning the charge relocation dynamics and traps contributing to the PRE in "nominally pure"  $\text{LiNbO}_3$  crystals. The model based on the data involves trap modulated mobility of two types of charge carriers interacting with donor and acceptor impurities. Specific properties of trap concentration and occupancy were shown to be altered by thermal annealing treatments. Future measurements of this type will be made on doped  $\text{LiNbO}_3$  and other photorefractive materials.

ACKNOWLEDGMENTS: The authors gratefully acknowledge the benefits of helpful discussions with L.E. Halliburton and K.L. Sweeney and the assistance of R.E. Schweitzer in making experimental measurements. This work was sponsored by the U.S. Army Research Office.



in relocation parameters indicates that the diffusion coefficient for electrons is larger than that for holes. The result of this is that the deviation of  $K$  from a linear dependence on  $\sin^2(\theta/2)$  appears at smaller angles for the electron contribution to the PRE than for the hole contribution. The magnitudes of the charge carrier densities contributing to the PRE found in this work are consistent with estimates made previously.<sup>2</sup>

The weak temperature dependence of  $K$  for the slow decay component of the oxidized sample indicates that shallow traps about  $90 \text{ cm}^{-1}$  above the valance band modulate the hole conductivity. The strong temperature dependence of the fast decay component shows that shallow traps near the conduction band with activation energies distributed between  $850$  and  $2500 \text{ cm}^{-1}$  modulate the electron conductivity.

The reducing annealing treatment causes the contribution to the grating of  $\text{Fe}^{2+}$  ions to be an order of magnitude greater than that of the  $\text{Fe}^{3+}$  ions and the change in relative intensities of the fast and slow grating decay components as well as the change in energy transfer in the two-wave mixing experiment show that the contribution of electrons to the grating erasure conductivity becomes much greater than that of holes. The charge relocation parameter increases which is associated with the increase in  $d$  resulting from the decrease in  $\text{Fe}^{3+}$  concentration.

The temperature dependences of  $K$  for different sample conditions show that the shallow trap states affect the grating decay dynamics through controlling the concentration of mobile charge carriers. The relocation parameters have no sample temperature dependence in the range investigated.

context of the model described above are associated with the establishment of sinusoidal spatial distributions of  $\text{Fe}^{2+}$  or  $\text{Fe}^{3+}$  defect concentrations and erasing the grating returns these uniform distributions to their normal random state. The nonexponential decay patterns observed for grating erasure can be caused by several different effects such as trap modulated mobility, statistical distribution of the charge relocation distances, trap saturation, and different types of charge carriers with different dynamics leading to their relocation. The first two effects may be present but can not explain the observed changes in decay dynamics as a function of write beam crossing angle, annealing temperature, and sample temperature. In addition, the observed difference in the energy transfer in the two-beam mixing experiment for the oxidized and reduced sample indicates the presence of both positive and negative charge carriers in the conduction process. The charge carriers associated with the fast grating decay component are electrons and those associated with the slow decay component are holes.

In the oxidized sample the relative intensities of the two decay components indicate that the grating consists of approximately equal concentrations of  $\text{Fe}^{3+}$  and  $\text{Fe}^{2+}$  ions, and the saturation observed in the crossing angle dependence of  $K$  gives an estimate of the concentration to be of the order of  $10^{19} \text{ cm}^{-3}$ . The angular dependence of  $K$  also shows the concentration of holes contributing to the grating erasure is slightly larger than the contribution of electrons in the oxidized sample while the relocation parameters differ by about a factor of 2. This difference

unambiguously identified but could be due to various ionization states of the known defects or to  $\text{Nb}^{4+}$ . The concentrations of these defects are of the order of tens of parts per million and they vary differently with annealing temperatures.

Table 1 summarizes the values of the parameters measured in this investigation. The results are consistent with a model such as that shown in Fig. 7. In general there can be four types of defect centers contributing to the observed PRE properties. The first type of center is a donor which can absorb a laser photon to produce a mobile electron in the conduction band. This is a deep trap which can not be emptied through thermal activation in the temperature range investigated here. The second type of defect center is an acceptor which can absorb a laser photon to produce a mobile hole in the valance band. This is also a deep trap. Acceptors act as trapping centers for the migrating electrons while the donors act as traps for the migrating holes. In addition there can be two types of shallow traps, one near the conduction band and one near the valance band. These contribute thermally activated electrons and holes, respectively, to the conduction process with the occupancy of these shallow traps being in thermal equilibrium with the density of free charge carriers in the bands. This results in "trap-modulated mobility" of the migration of photo-excited carriers. The specific nature of the different types of defects can not be identified from the results obtained here. We discuss our results in terms of the proposed model using  $\text{Fe}^{2+}$  and  $\text{Fe}^{3+}$  as examples of possible donor and acceptor impurities in the material.

The refractive index gratings created in this study in the

beam increased in intensity by approximately the same amount. The percentage of intensity change  $\Delta I_R/I_R$  was about +9.0% for the oxidized sample and +12.5% for the annealed sample. The presence of this energy transfer between beams shows that there is a component of the refractive index grating which is phase shifted with respect to the light beam interference pattern. The direction of the phase shift and thus the direction of the energy transfer between beams is the result of the interplay between the concentration, sign, and mobility of the charge carriers and the photovoltaic effect. The presence of carriers with different signs decreases the amount of transfer as shown by Orlowski and Kratzig.<sup>34</sup> The results of the experiments performed here are consistent with their data. They indicate that negative charge carriers dominate the conductivity process with a greater contribution from positive charge carriers being present in the oxidized sample than in the annealed sample.

#### V. SUMMARY AND CONCLUSIONS

The photorefractive properties of  $\text{LiNbO}_3$  are known to vary significantly depending on the wavelength and power of the laser excitation source and on the chemical and structural defect composition of the sample. The results described in this study are associated with low power 442 nm excitation of "nominally pure" samples. Electron paramagnetic resonance (EPR) measurements on these samples was used to determine the concentrations of both chemical and structural defects after the various annealing treatments.<sup>26</sup> This work revealed the presence of Fe impurities, oxygen vacancies, and other bands which are not

$$K = K' \exp[-\Delta E / (k_B T)]. \quad (8)$$

The values of the activation energies found from fitting Eq. (8) to the data in Fig. 6 are listed in Table 1. They are approximately the same for both conditions. At higher temperatures the curves for the fast component of the oxidized sample deviate from a simple exponential shape indicating the presence of higher activation energies. Fitting Eq. (8) to this high temperature region gives the larger value of  $\Delta E$  listed in the table.

The fact that the values of  $K$  for two different crossing angles change in the same way with temperature indicates that  $Rd^2$  remains constant while  $N_f$  changes. Thus the temperature dependence of  $K$  can be attributed to a change in the detrapping rate of the charges, and the measured activation energy can be associated with the energy depths of the traps contributing to the PRE. Since the activation energies determined by the temperature dependent measurements are much smaller than the energy of the laser photons, the origin of the charge carriers from the two excitation processes must be different.

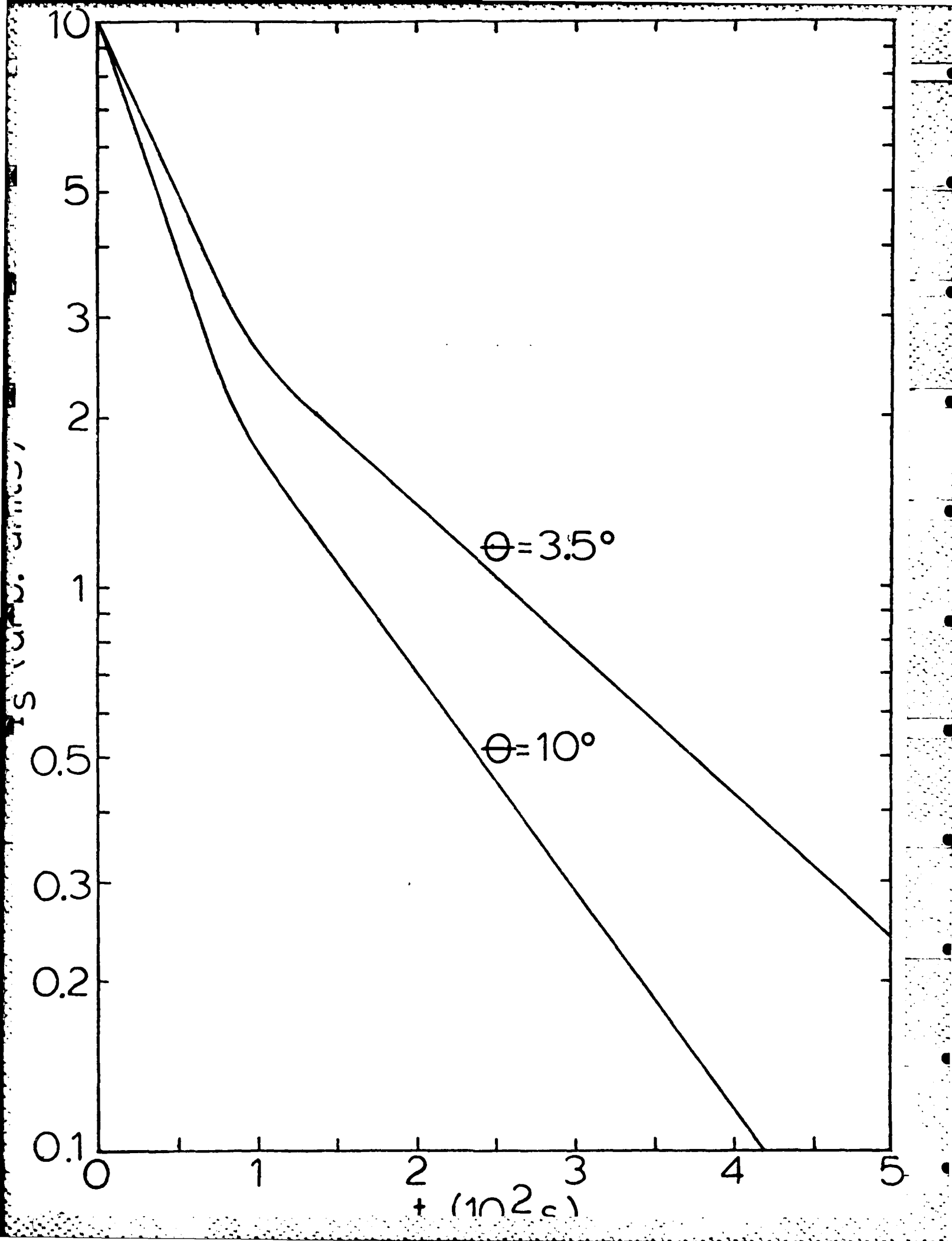
The final experiment performed in this investigation was the measurement of energy transfer between write beams. This technique, called two-wave mixing, can be used to probe the phase shift between light interference pattern and the index of refraction grating.<sup>4,25,33,34</sup> The measurement was made at a crossing angle of  $10^\circ$  on the sample in the oxidized condition and after vacuum annealing at 400 C. The He-Cd write beams entered the sample with equal intensities and exited the sample with the beam toward the poled C direction decreased in intensity and the other

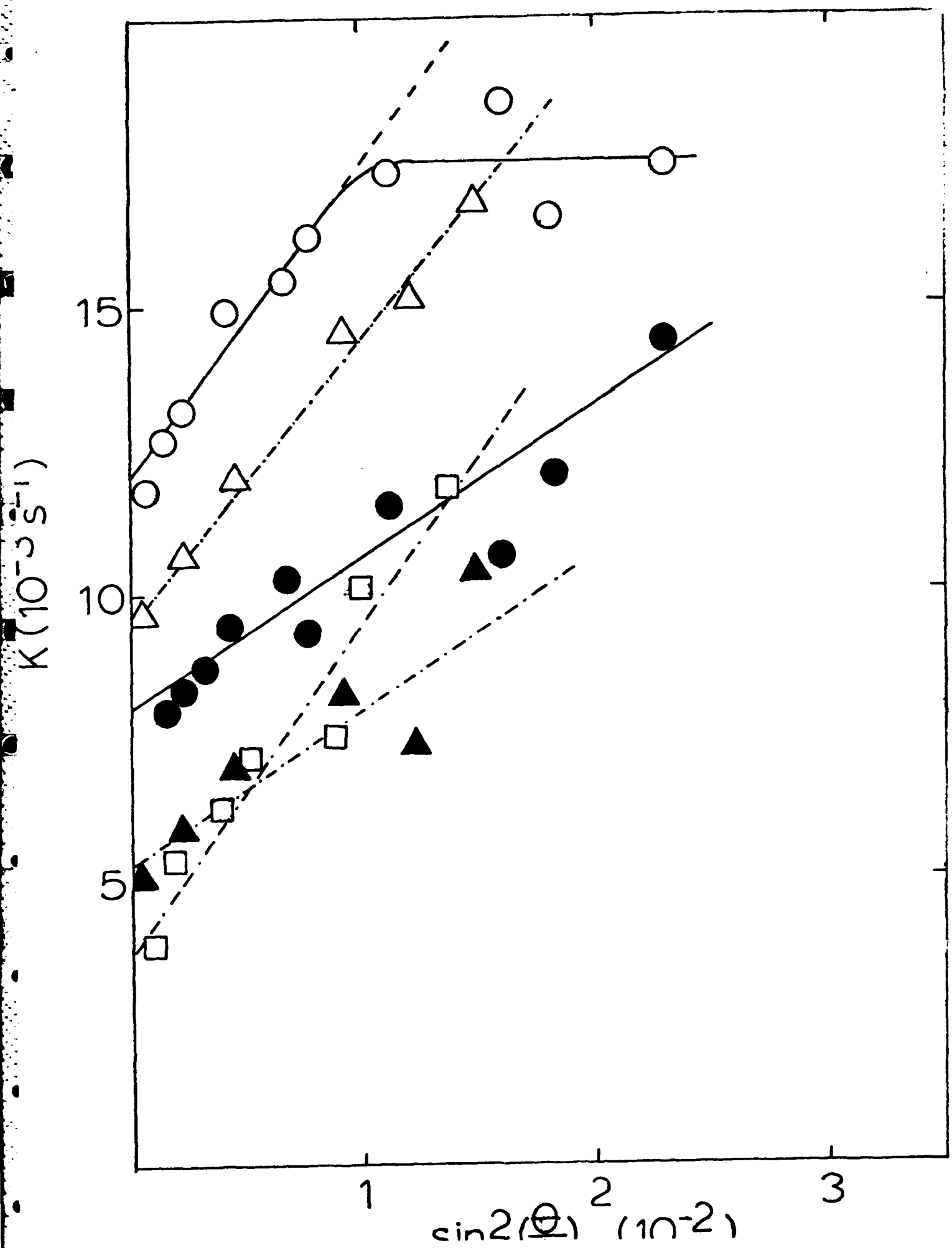
ratio of the maximum intensities of the light scattered from the two types of trapping centers contributing to the grating. This is assumed to be proportional to the square of the ratio of the densities of charges trapped in the two types of trapping centers. Under steady state conditions, the ratio of concentrations of charges trapped in the fast decaying and slow decaying trapping centers is proportional to the ratio of the concentrations of the two types of trapping centers,  $\rho_f/\rho_s$ . Thus, Eq. (1) gives

$$\rho_f/\rho_s = [I_{f0}/I_{s0}]^{1/2}. \quad (7)$$

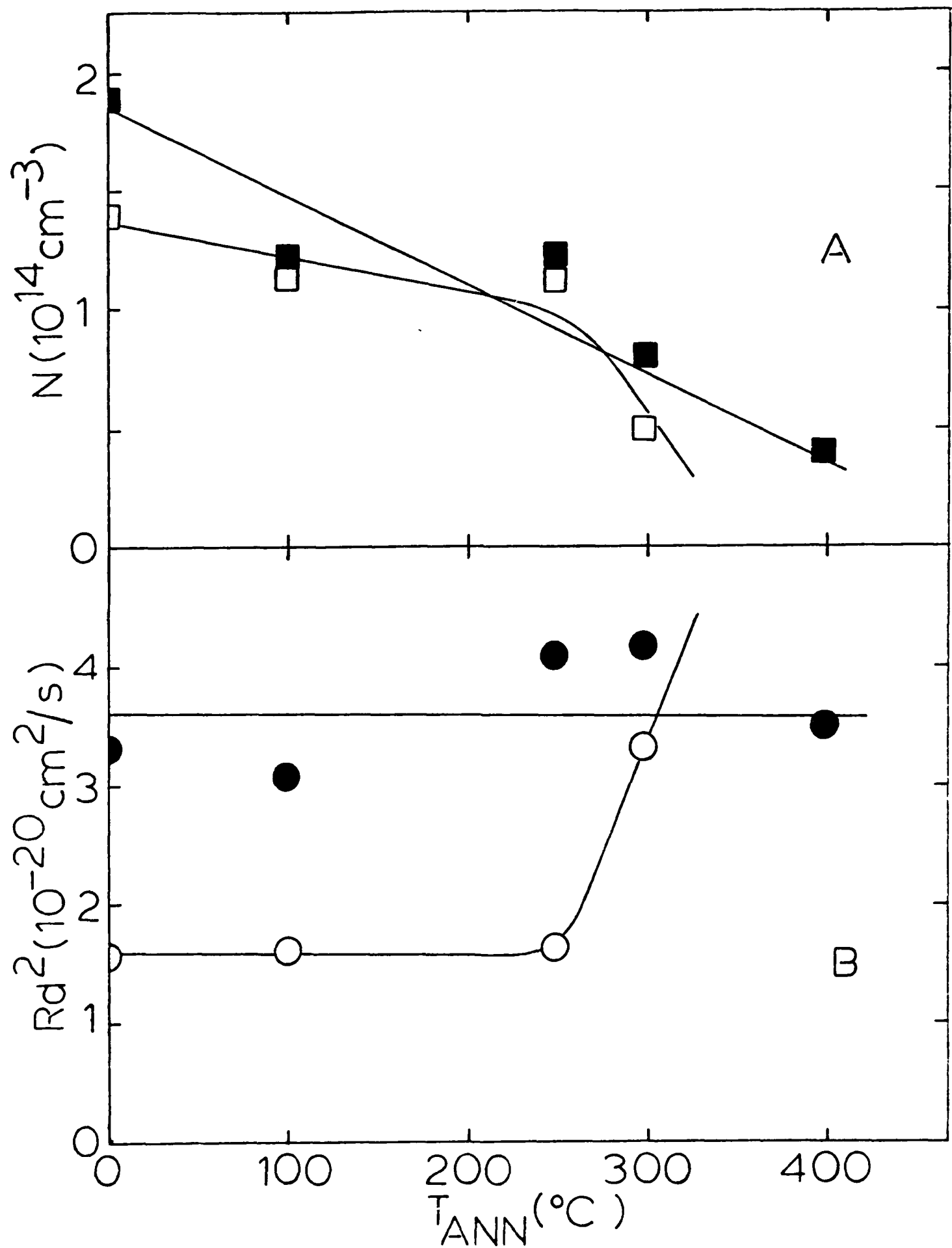
Figure 5 shows the ratio of the concentrations of the two types of traps as a function of thermal annealing temperature. The concentration of the trapping centers contributing to the fast signal decay component increases by an order of magnitude compared to that of the other type of trapping center as annealing temperature increases. This explains the observation that the photorefractive response of  $\text{LiNbO}_3$  becomes faster with higher annealing temperatures.

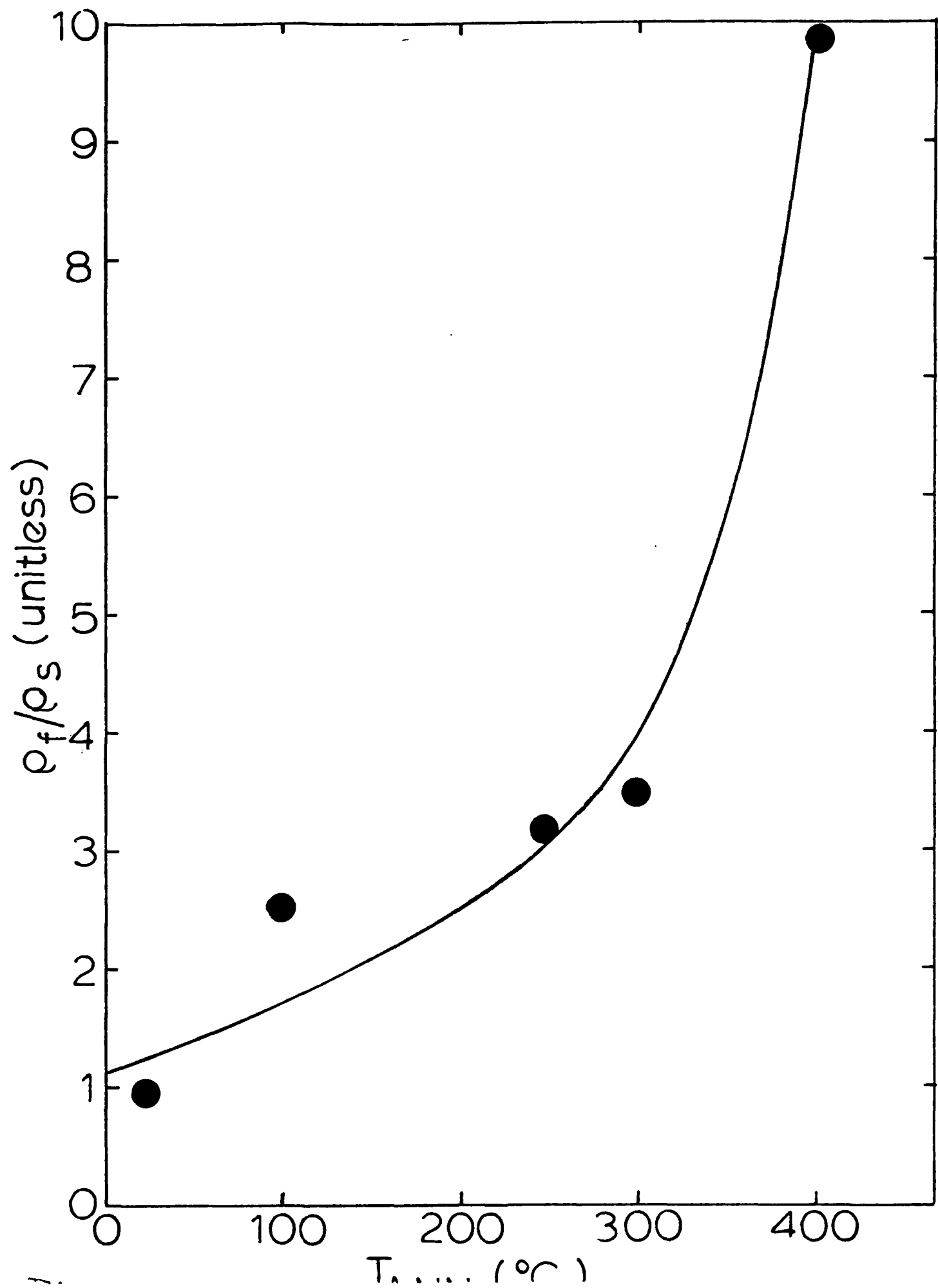
The temperature dependence of the grating decay rate was also monitored for the sample in the oxidized state and after vacuum annealing at a temperature of 400 C. The results are shown in Fig. 6. The fast components of the grating decay rate increased significantly as temperature was increased for both sample conditions. The slow components of the grating decay rates of the oxidized sample increased only slightly with temperature in the same range. In the temperature range between 20 and 70 C, the temperature dependence of the decay rates are described by

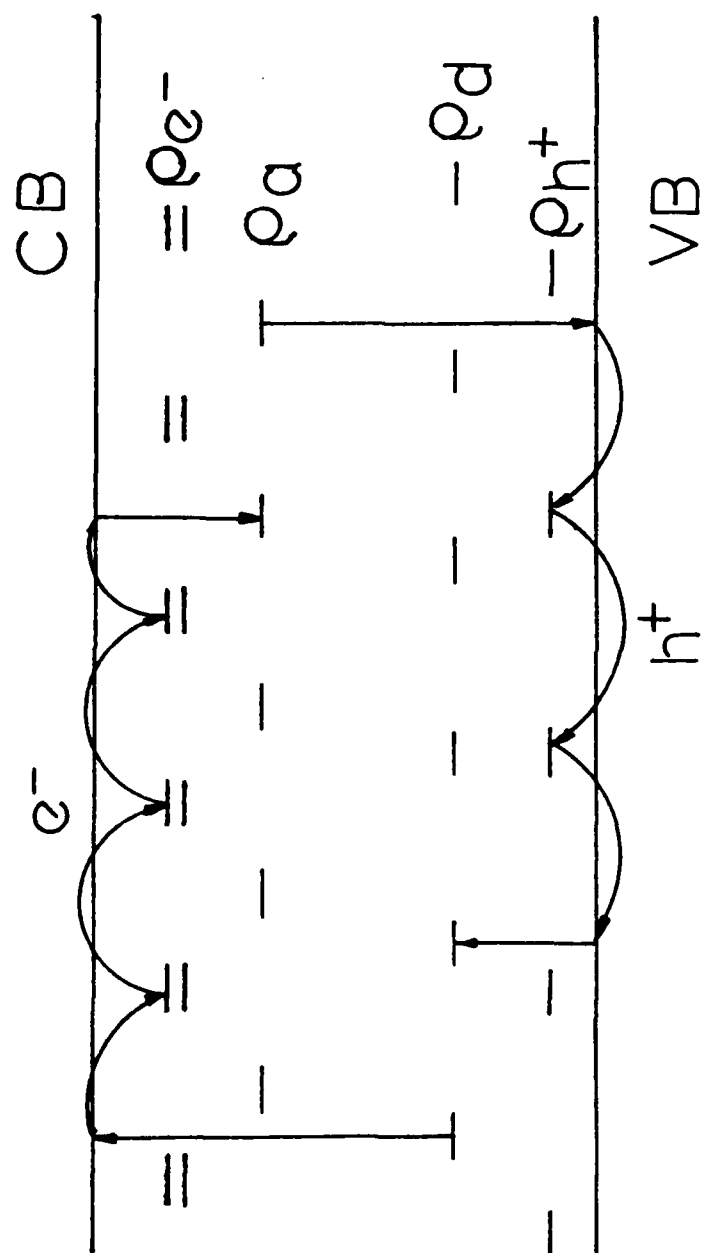


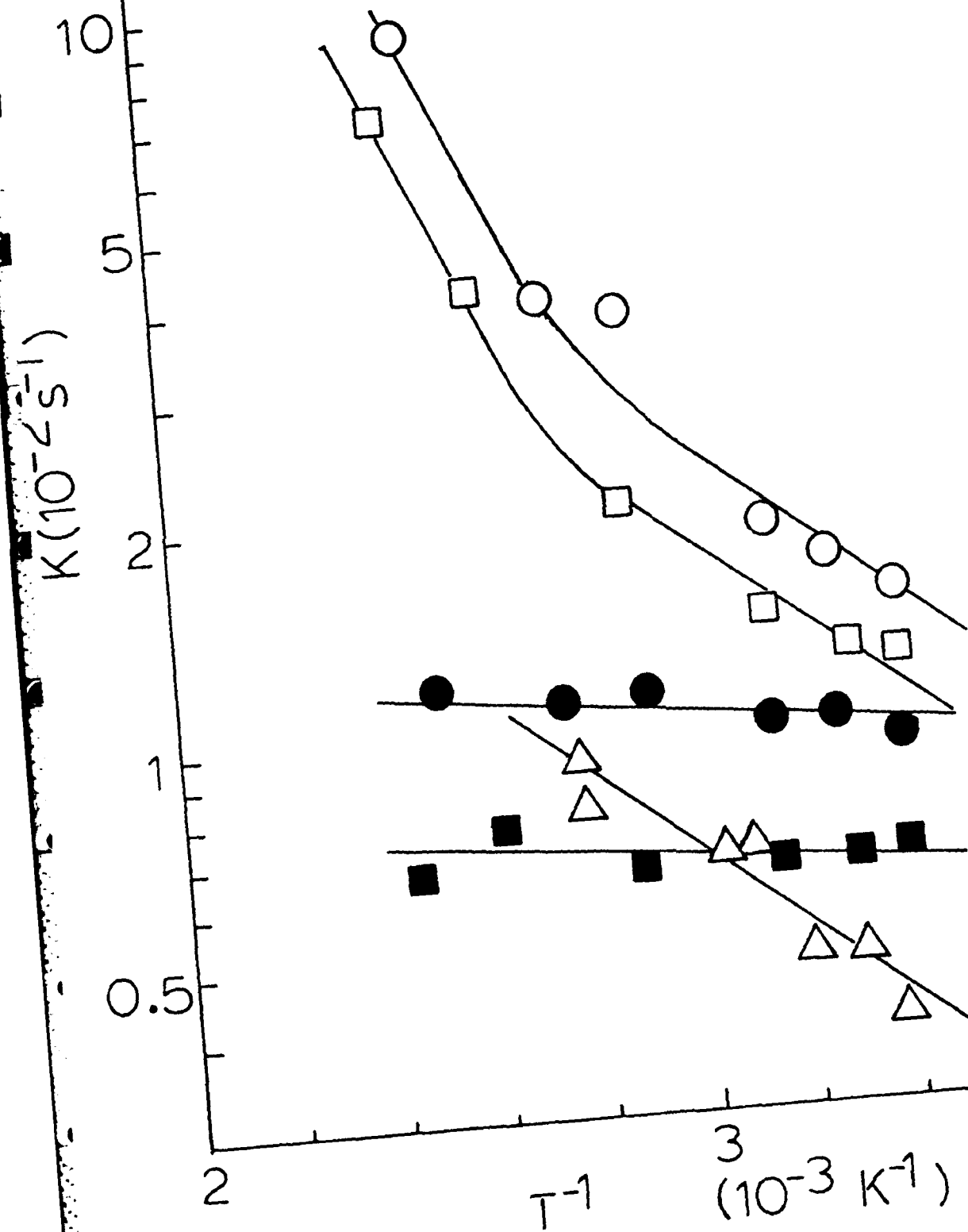












## APPENDIX

The susceptibility of the two level system as derived by Lawson in Section II.1 takes the form

$$\chi = \frac{2\alpha_0}{k} \frac{1 + \delta}{(1 + \delta + \left| \frac{E}{E_s} \right|^2)} \quad (\text{A-1})$$

where  $\delta$  is the normalized detuning between the excitation wavelength and the ground-excited states gap,  $\alpha_0$  is the absorption line small signal excitation field attenuation coefficient, and  $E_s$  is the line saturation field.

If the susceptibility of the three level system is assumed to take the form of a linear combination of two, two level systems (see Figure 1 and related comments in Section II.3), then the resultant susceptibility takes the form

$$\chi(E) = \frac{R}{R+1} \chi_1 + \frac{1}{R+1} \chi_2 \quad (\text{A-2})$$

The meaning of the symbols in the above formula is identical to those in Section II.3.

According to the definition, the polarization of the material  $\bar{P}(\bar{E})$  can be expressed as

$$\bar{P}(\bar{E}) = \epsilon_0 \left[ \sum_{1,2} R_i \chi_i(E) \right] \bar{E} \quad (\text{A-3})$$

where  $\bar{E}$  is the electric field interacting with the isotropic medium.

In the Four-wave mixing experiment when the energy migration process is investigated, the configuration of beams is arranged as in Fig. 2 Sec. II.1. Given the fact that the Four Wave Mixing experiment utilizes nonlinear response of the material, it is advantageous to set the beam intensities such that the pump field  $E_0$  is much bigger than the probe-scattered  $\Delta E_0$  part of the Four-wave mixing configuration (see definitions in Sec. II.3 of the mixing fields).

Given this, it is possible to expand  $\chi(E)$  around  $E_0$  in formula (A-3) giving Eq. 13, Sec. II.3, if the nonlinear terms of  $\Delta E$  are truncated.

After straightforward differentiation and the application of the slow varying envelope of beams assumption (see Sec. II.1) and the application of the non-depleting pump beams assumption (see Sec. II.1), we have

$$\begin{aligned} & \cos\theta \exp(-i\vec{k}_1 \cdot \vec{r}) \partial_z A_1(z) + \exp(-i\vec{k}_3 \cdot \vec{r}) \partial_z A_3(z) \\ &= \sum_{1,2} R_{12} \alpha_{01} I_{s1} (1 - i\delta_1) \left[ \frac{E_0}{I_{s1} + |E_0|^2} + \frac{\Delta E}{(I_s + |E_0|^2)^2} \right. \\ & \quad \left. - \frac{E_2 \Delta E^*}{(I_{s1} + |E_0|^2)^2} - \frac{|E_0|^2 \Delta E}{(I_{s1} + |E_0|^2)^2} \right] \end{aligned} \quad (A-4)$$

where  $I_{s1} = |E_{s1}|^2 / (1 + \delta_1)$  and  $A_i(z)$ ,  $i = 1, 2, 3, 4$  are the envelopes of the beams.

Comparing the synchronous terms on the left and right side of equation (A-4) (see ref. 15, Sec. II.1) where the above procedure is demonstrated in great detail), a set of equations is obtained

$$\cos\Theta \partial_z A_1(z) = \sum_{1,2} R_i \frac{\alpha_{oi} |E_{si}|^2 (1 - i\delta_i)}{(I_{si} + |E_o|^2)^2} [(I_{si} + \zeta) A_1(z) - A_2^*(z) A_4(z) A_3(z)] \quad (A-5)$$

$$\partial_z A_3(z) = \sum_{1,2} R_i \frac{\alpha_{oi} |E_{si}|^2 (1 - i\delta_i)}{(I_{si} + |E_o|^2)^2} [(I_{si} + \zeta) A_3(z) - A_2(z) A_4^*(z) A_1(z)] \quad (A-6)$$

where  $\zeta = A_2(z) A_4(z) \exp[ik(1-\cos\Theta)z]$

(The asterisk in the above formula designates the conjugate value).

Given the fact, that in the Four Wave Mixing configuration  $|A_1| > |A_3|$  the probe beam intensity is higher than the scattered beam intensity, and as long as the pump beams are weaker than the saturation fields

$$I_s \ll |A_2(z) A_4^*(z)| \quad (A-7)$$

the set of equations (A-5)-(A-6) simplifies to

$$\cos\Theta \partial_z A_1(z) = \sum_{1,2} R_i \frac{\alpha_{oi} |E_{si}|^2 (1 - i\delta_i)}{(I_{si} + |E_o|^2)^2} (I_{si} + \zeta) A_1(z) \quad (A-8)$$

$$\partial_z A_3 = \sum_{1,2} R_i \frac{\alpha_{oi} |E_{si}|^2 (1 - i\delta_i)}{(I_{si} + |E_o|^2)^2} [(I_{si} + \zeta) A_3(z) - A_2(z) A_4^*(z) A_1(z)] \quad (A-9)$$

Phases  $\psi_i$  can be defined by formula

$$E_i = |E_i| (\cos\psi_i + i \sin\psi_i) \quad (A-10)$$

and, according to definitions in Sec.II.3, the following is obtained

$$\psi_1 - \psi_2 = -ik(1-\cos\theta)z + \Delta$$

where

$$\Delta = \operatorname{actg} \frac{\operatorname{Im}(A_2(z))}{\operatorname{Re}(A_2(z))} - \operatorname{arctg} \frac{\operatorname{Im}(A_4(z))}{\operatorname{Re}(A_4(z))} \quad (\text{A-11})$$

The above formula give

$$|E_0|^2 = I_2 + I_4 + 2|A_2 A_4| \cos[k(1-\cos\theta)z + \Delta] \quad (\text{A-12})$$

After the introduction of the symbols

$$D_{01} = I_{s1} + I_2 + I_4 \quad (\text{A-13})$$

$$a = |A_2(z)A_4(z)| \quad (\text{A-14})$$

the set of equations (A-8)-(A-9) takes the form

$$\partial_z A_1(z) = \sum_{1,2} R_1 \frac{\alpha_{01} |E_{s1}|^2 (1 - i\delta_1)}{\cos\theta} \frac{[I_{s1} + a \exp[ik(1-\cos\theta)z + \Delta]]}{D_0 + 2a \cos[k(1-\cos\theta)z + \Delta]} A_1(z) \quad (\text{A-15})$$

$$\begin{aligned} \partial_z A_3(z) = & \sum_{1,2} \{ R_1 \alpha_{01} |E_{s1}|^2 (1 - i\delta_1) \frac{I_{s1} + a \exp[ik(1-\cos\theta)z + \Delta]}{[D_{01} + 2a[k(1-\cos\theta)z + \Delta]]^2} A_3(z) \\ & - R_1 \alpha_{01} |E_{s1}|^2 (1 - i\delta_1) \frac{a \exp(i\Delta)}{[D_{01} + 2a[k(1-\cos\theta)z + \Delta]]^2} A_1(z) \end{aligned} \quad (\text{A-16})$$

Defining the following quantities

$$\beta = k(1 - \cos\theta) \quad (\text{A-17})$$

$$R(z) = - \sum_{1,2} R_1 \frac{\alpha_{01} |E_{s1}|^2 (1 - i\delta_1)}{\cos\theta} \frac{I_{s1} + a \exp(\beta z + i\Delta)}{[D_{01} + 2a \cos(\beta z + \Delta)]^2} \quad (\text{A-18})$$



$$P(z) = - \sum_{1,2} R_i \alpha_{oi} |E_{si}|^2 (1 - i\delta_i) \frac{I_{si} + a \exp(-i\beta - i\Delta)}{[D_{oi} + 2a \cos(\beta z + \Delta)]^2} \quad (A-19)$$

$$Q(z) = - \sum_{1,2} R_i \alpha_{oi} |E_{si}|^2 (1 - i\delta_i) \frac{a \exp(i\Delta) A_1(z)}{[D_{oi} + 2 \cos(\beta z + \Delta)]^2} \quad (A-20)$$

one can obtain from the set (A-15)-(A-16) the following equations

$$\partial_z A_1(z) - R(z) A_1(z) = 0 \quad (A-21)$$

$$\partial_z A_3(z) - P(z) A_3(z) = Q(z) \quad (A-22)$$

which describes the response of the medium in the FWM experiment.

Case I:  $\theta$  angle is large

If the angle of the pump beam crossing is wide enough that the probe-scattered part of the mixing field does not change substantially over the length of the pump part oscillation  $\lambda_{osc} = \frac{\lambda}{1-\cos\theta}$  then it is possible to approximate the set of equations (A-21)-(A-22) by their forms "averaged" over the  $\lambda_{osc}$ . This leads to the set of equations

$$\partial_z A_1(z) + \langle R(z) \rangle A_1(z) = 0 \quad (A-23)$$

$$\partial_z A_3(z) + \langle P(z) \rangle A_3(z) = \langle Q(z) \rangle A_1(z) \quad (A-24)$$

In particular the formula

$$\frac{1}{\lambda_{osc}} \int_{-\lambda_{osc}/2}^{\lambda_{osc}/2} dz \frac{I_{si} + a \cos \beta z + i a \sin \beta z}{(D_{oi} + 2a \cos \beta z)^2} = \frac{D_{oi} I_{si} - 2a^2}{(D_{oi}^2 - 4a^2)^{3/2}} \quad (A-25)$$

which is valid if the assumption of non-depleting pump field holds is used to obtain

$$\langle R(z) \rangle = - \sum_{1,2} R_1 \frac{\alpha_{oi} |E_{si}|^2 (1 - i\delta_i)}{\cos\theta} \frac{D_{oi} I_{si} - 2a^2}{(D_{oi}^2 - 4a^2)^{3/2}} \quad (A-26)$$

$$\langle P(z) \rangle = - \sum_{1,2} R_1 \alpha_{oi} |E_{si}|^2 (1 - i\delta_i) \frac{D_{oi} I_{si} - 2a^2}{(D_{oi}^2 - 4a^2)^{3/2}} \quad (A-27)$$

$$\langle q(z) \rangle = - \sum_{1,2} R_1 \alpha_{oi} |E_{si}|^2 (1 - i\delta_i) \frac{D_{oi} a \exp(i\Delta)}{(D_{oi}^2 - 4a^2)^{3/2}}$$

Calculated from set (A-23) and (A-24) the envelopes of the fields take the form

$$A_1(z) = A_1(L) \exp[-\langle P(z) \rangle (z-L)] \quad (A-28)$$

$$A_3(z) = \frac{\langle q(z) \rangle A_1(z)}{\langle P(z) \rangle (\cos^{-1}\theta - 1)}$$

$$\left\{ \exp\left[-\frac{\langle P(z) \rangle (z-L)}{\cos\theta}\right] - \exp[-\langle P(z) \rangle (z-L)] \right\} \quad (A-29)$$

From the above, it is straightforward to obtain

$$I_3(0) = |A_3(0)|^2 = \left| \frac{\langle q(z) \rangle}{\langle P(z) \rangle} \right|^2 \frac{|A_1(L)|^2}{(\cos^{-1}\theta - 1)^2} \left\{ \exp(-2\zeta_R L) + \exp\left(-\frac{2\zeta_R L}{\cos\theta}\right) - 2 \exp[-\zeta_R (1 + \cos^{-1}\theta)L] \right. \\ \left. \cos[\zeta_I (1 - \cos^{-1}\theta)L] \right\} \quad (A-30)$$

$$I_1(0) = |A_1(0)|^2 = |A_1(L)|^2 \exp(-2\zeta_R L) \quad (A-31)$$

where

$$\zeta_R = \text{Re}[-\langle P(z) \rangle] \quad (\text{A-32})$$

$$\zeta_I = \text{Im}[-\langle P(z) \rangle] \quad (\text{A-33})$$

The scattering efficiency in the Four-wave mixing experiment is defined as

$$\eta = \frac{I_3(0)}{I_1(0)} \bigg|_{E_0 = 0} \quad (\text{A-34})$$

this leads to the formula

$$\eta = \left| \frac{\rho}{\zeta} \right|^2 \frac{\exp(-\Psi_{E_0})}{(\cos^{-1}\theta - 1)^2} \left\{ \exp(-2\zeta_R L + \exp(-\frac{2\zeta_R L}{\cos\theta})) - 2 \exp[-\zeta_R L (1 + \cos^{-1}\theta)] \cos[\zeta_I L (1 - \cos^{-1}\theta)] \right\} \quad (\text{A-35})$$

where

$$\left| \frac{\rho}{\zeta} \right| = \frac{\sum_{j=1,2} \left\{ \sum_{i=1,2} F_{j,i} \frac{R_{i^3 o1}}{(1 + \delta_i)^2 I_{si}} \frac{\sqrt{I_2 I_4} (1 + \frac{I_2 + I_4}{I_{si}})}{[(1 + \frac{I_2 + I_4}{I_{si}})^2 - 2 \frac{I_2 I_4}{I_{si}^2}]^{3/2}} \right\}^2}{\sum_{j=3,4} \left\{ \sum_{i=1,2} F_{j,i} \frac{R_{i^3 o1}}{(1 + \delta_i)^2} \frac{(1 + \frac{I_2 + I_4}{I_{si}})^2 - 2 \frac{I_2 I_4}{I_{si}^2}}{[(1 + \frac{I_2 + I_4}{I_{si}})^2 - 4 \frac{I_2 I_4}{I_{si}^2}]^{3/2}} \right\}^2} \quad (\text{A-36})$$

$$F_{1,1} = \cos\Delta + \delta_1 \sin\Delta ; F_{3,1} = 1 \quad (\text{A-37})$$

$$F_{2,1} = \sin\Delta - \delta_1 \cos\Delta ; F_{4,1} = \delta_1$$

$$\Psi_{E_0} = \frac{2L}{\cos\theta} \sum_{1,2} \frac{R_{i^3 o1}}{(1 + \delta_i)^2} \quad (\text{A-38})$$

$$\zeta_R = - \sum_{1,2} \frac{R_i I_{si} \alpha_{oi}}{(1 + \delta_i)^2} \frac{D_{oi} I_{si} - 2a^2}{(D_{oi}^2 - 4a^2)^{3/2}} \quad (A-39)$$

$$\zeta_I = \sum_{1,2} \frac{R_i I_{si} \alpha_{oi}}{(1 + \delta_i)^2} \frac{D_{oi} I_{si} - 2a^2}{(D_{oi}^2 - 4a^2)^{3/2}} \quad (A-40)$$

The formula (A-34)-(A-40) express the scattering efficiency in the Four Wave Mixing experiment in the case of a large angle.

Case II: The pump field is far from saturation level.

If the pump field is far from saturation level in the Four Wave Mixing experiment, then the following relationships will be satisfied

$$\begin{aligned} \frac{a}{I_{si}} &\ll 1 \\ \frac{I_2}{I_{si}} &\ll 1 \quad ; \quad i = 1, 2 \\ \frac{I_4}{I_{si}} &\ll 1 \end{aligned} \quad (A-41)$$

Expanding the expressions of the type

$$\frac{I_{si} + a \exp(i\beta_2 - i\Delta)}{[I_{si} + I_2 + I_4 + 2 \cos(\beta_2 + \Delta)]^2}$$

into the power series of  $\frac{I_2}{I_{si}}$ ,  $\frac{I_4}{I_{si}}$  and  $\frac{a}{I_{si}}$  and truncating nonlinear terms obtains the following formula:

$$\begin{aligned} R(z) = \sum_{1,2} R_i \frac{a_{oi}(1 - i\delta_i)}{(1 + \delta_i)^2 \cos\theta} \left[ 1 - \frac{3a}{I_{si}} \cos(\beta z + \Delta) \right. \\ \left. + i \frac{a}{I_{si}} \sin(\beta z + \Delta) - 2 \frac{I_2 + I_4}{I_{si}} \right] \end{aligned} \quad (A-42)$$

The above formula together with equation (A-21) leads to

$$\begin{aligned}
 A_1(z) = A_1(L) \exp \left\{ \sum_{1,2} - \frac{R_1 \alpha_{01} \delta_1}{(1 + \delta_1)^2 \cos \theta} \left[ (z - L) \left( 1 - 2 \frac{I_2 + I_4}{I_{s1}} \right) \right. \right. \\
 \left. \left. - \frac{6a}{8I_{s1}} \sin \frac{\beta(z-L)}{2} \cos \frac{\beta(z+L) + 2\Delta}{2} \right. \right. \\
 \left. \left. - \frac{12a}{8I_{s1}} \sin \frac{\beta(z+L) + 2\Delta}{2} \sin \frac{\beta(z-L)}{2} \right] \right\} \quad (A-43)
 \end{aligned}$$

Using the same approximation the following is also obtained

$$Q(z) = - \sum_{1,2} \frac{R_1 \alpha_{01} (1 - i\delta_1)}{(1 + \delta_1)^2 I_{s1}} a \exp(i\Delta) A_1(z) \quad (A-44)$$

$$\begin{aligned}
 P(z) = - \sum_{1,2} \frac{R_1 \alpha_{01} (1 - i\delta_1)}{(1 + \delta_1)^2 I_{s1}} \\
 \left[ 1 - \frac{3a}{I_{s1}} \cos(\beta z + \Delta) - i \frac{a}{I_{s1}} \sin(\beta z + \Delta) - 2 \frac{I_2 + I_4}{I_{s1}} \right] \quad (A-45)
 \end{aligned}$$

The solution of equation (A-23) together with formulae (A-44), and (A-45) gives

$$A_3(z) = e^{f(z)} \left( C_1 + \int_0^z Q(z') e^{-f(z')} dz' \right) \quad (A-46)$$

which allows to evaluate  $f(z)$  as

$$f(z) = - \int_0^z P(z') dz' + C_2 \quad (A-47)$$

and leads to

$$f(z) = \sum_{1,2} \frac{R_1 \alpha_{01} (1 - i\delta_1)}{(1 + \delta_1)^2 I_{s1}} \left[ z \left( 1 - 2 \frac{I_2 + I_4}{I_{s1}} \right) - \frac{3a}{\beta I_{s1}} \sin(\beta z + \Delta) + i \frac{a}{I_{s1}} \cos(\beta z + \Delta) \right] \quad (A-48)$$

Introducing a function  $F(z)$  such that

$$F(z) = \int_0^z Q(z') e^{-f(z')} dz' \quad (A-49)$$

it is possible to express

$$A_3(z) = e^{f(A)} [F(z) - F(L)] \quad (A-50)$$

what gives intensity of scattered light on the face  $L=0$  as:

$$I_3 = |A_3(0)|^2 = |e^{f(0)}|^2 |F(0) - F(L)|^2 \quad (A-51)$$

for  $|e^{f(0)}|^2$  expressed as:

$$|e^{f(0)}|^2 = \exp \left[ -6 \sin \Delta \frac{\sqrt{I_2 I_4}}{\beta} \sum_{1,2} \frac{R_1 \alpha_{01}}{(1 + \delta_1)^2 I_{s1}} - 2 \cos \Delta \frac{\sqrt{I_2 I_4}}{\beta} \sum_{1,2} \frac{R_1 \alpha_{01} \delta_1}{(1 + \delta_1)^2 I_{s1}} \right] \quad (A-52)$$

$$\begin{aligned}
|F(0) - F(L)|^2 = L^2 |A_1(L)|^2 \frac{I_2 I_4}{\cos^2 \theta} & \left[ \left( \sum_{1,2} \frac{R_1 \alpha_{oi} \delta_i}{(1+\delta_i)^2 I_{si}} \right)^2 \right. \\
& + \left( \sum_{1,2} \frac{R_1 \alpha_{oi}}{(1+\delta_i)^2 I_{si}} \right)^2 \left[ LB_R \cos^2 \frac{\theta}{2} \right. \\
& - \frac{L^2}{6} (B_R^2 + B_L^2) \cos \theta - 1 \left. \right]^2 \\
& \left. + (LB_I \cos^2 \frac{\theta}{2} - \frac{L^2}{3} B_R B_I \cos \theta)^2 \right\} \quad (A-53)
\end{aligned}$$

$$B_R = \sum_{1,2} \frac{R_1 \alpha_{oi}}{(1+\delta_i)^2 \cos \theta} \quad (A-54)$$

$$B_I = - \sum_{1,2} \frac{R_1 \alpha_{oi} \delta_i}{(1+\delta_i)^2 \cos \theta} \quad (A-55)$$

The intensity of the probe beam, while the pump field is turned off is

$$I_1 = |A_1(0)|^2 \Big|_{E_o = 0} = |A_1(L)|^2 \exp \left[ - \frac{2L}{\cos \theta} \sum_{1,2} \frac{R_1 \alpha_{oi}}{(1+\delta_i)^2} \right] \quad (A-56)$$

The formula (A-53)-(A-56) allows one to express the scattering efficiency in Four-wave mixing as:

$$\eta = S_1 I_2 I_4 \exp (-S_2 \sqrt{I_2 I_4}) \quad (A-57)$$

$$\begin{aligned}
S_1 = & \frac{L^2}{\cos^2 \theta} \left\{ \left[ \sum_{1,2} \frac{R_{i\alpha oi} \delta_i}{(1+\delta_i)^2} \right]^2 + \left[ \sum_{1,2} \frac{R_{i\alpha oi}}{(1+\delta_i)^2} \right]^2 \right\} \\
& \exp \left[ \frac{2L}{\cos \theta} \sum_{1,2} \frac{R_{i\alpha oi}}{(1+\delta_i)^2} \right] \left\{ \left[ L \cos^2 \frac{\theta}{2} \sum_{1,2} \frac{R_{i\alpha oi}}{(1+\delta_i)^2 \cos \theta} \right. \right. \\
& - \frac{L^2}{6} \cos \theta \left( \left( \sum_{1,2} \frac{R_{i\alpha oi}}{(1+\delta_i)^2 \cos \theta} \right)^2 + \right. \\
& + \left. \left. \left( \sum_{1,2} \frac{R_{i\alpha oi} \delta_i}{(1+\delta_i)^2 \cos \theta} \right)^2 - 1 \right] + \left[ \frac{L \cos^2 \frac{\theta}{2}}{\cos \theta} \sum_{1,2} \frac{R_{i\alpha oi} \delta_i}{(1+\delta_i)^2} \right. \right. \\
& \left. \left. - \frac{L^2}{3 \cos \theta} \left( \sum_{1,2} \frac{R_{i\alpha oi} \delta_i}{(1+\delta_i)^2} \right) \left( \sum_{1,2} \frac{R_{i\alpha oi}}{(1+\delta_i)^2} \right) \right]^2 \right\} \quad (A-58)
\end{aligned}$$

$$S_2 = \frac{2}{\sqrt{\beta}} \cos \Delta \sum_{1,2} \frac{R_{i\alpha oi} \delta_i}{(1+\delta_i)^2 I_{s1}} + 3 \sin \Delta \sum_{1,2} \frac{R_{i\alpha oi}}{(1+\delta_i)^2 I_{s1}} \quad (A-59)$$

Formulae (A-57)-(A-59) describes the scattering process in the Four-wave mixing experiment while the intensity of the pump field is below its saturation level.



**END**

**FILMED**

**5-85**

**DTIC**